The Muon-Induced Neutron Indirect-Detection EXperiment: MINIDEX

Matteo Palermo

München 2016

The Muon-Induced Neutron Indirect-Detection EXperiment: MINIDEX

Matteo Palermo

Dissertation
an der Fakultät für Physik
der Ludwig–Maximilians–Universität
München

vorgelegt von
Matteo Palermo
aus Perugia

München, den 20. April 2016

Erstgutachter: Prof. Dr. Jochen Schieck
Zweitgutachter: Prof. Dr. Otmar Biebel
Tag der mündlichen Prüfung: 6. Juni 2016

Contents

Zusammenfassung

Ein neues Experiment zur Messung von myoninduzierten Neutronen wird vorgestellt. Das Konzept des "Muon-Induced Neutron Indirect Detection EXperiment", MINIDEX, wird erläutert und sein Aufbau und seine Inbetriebnahme im "Tübingen Shallow Underground Laboratory" beschrieben. Resultate der ersten Datennahmeperiode, "run I", werden präsentiert. Myoninduzierte Neutronen sind nicht nur ein interessantes Thema an sich, sie sind auch von besonderer Bedeutung als Untergrundquelle für Suchen nach möglichen seltenen Phänomenen wie neutrinolosem Doppelbetazerfall oder direkt beobachtbaren Wechselwirkungen von dunkler Materie. Diese Themen sind von großer Bedeutung für das Verständnis des frühen Universums. Deswegen wird eine neue Generation von Experimenten geplant, die bei einer aktiven Masse auf der Skala einer Tonne extrem niedrige Untergründe erreichen müssen. Zuverlässige Monte Carlo Simulationen sind notwendig, um die Untergründe und Sensitivitäten solcher Experimente abzuschätzen. Der durch myoninduzierte Neutronen hervorgerufene Untergrund ist schwer vorherzusage, weil bisherige Messungen zum Teil inkonsistent sind und Monte Carlo Vorhersagen und Daten oft nicht übereinstimmen. Insbesondere fehlen ausreichende Daten zur Neutronenproduktion in Materialien mit hohem Z. MINIDEX wurde genau in Bezug auf diese Fragestellung konzipiert. Bereits die Daten der ersten fünf Monate sind wertvoll für das Verständnis von Produktion und Transport von Neutronen in Blei. Erste Vergleiche mit Vorhersagen von zwei auf GEANT4 basierten Monte Carlo Paketen werden vorgestellt. Die Daten zeigen eine 70–100% höhere Neutronenproduktionsrate als von den Monte Carlos vorhergesagt. Die Monte Carlos sagen auch eine zu schnelle Entwicklung des Neutronensignals voraus. Allerdings wurde die Gesamtzeit, über die sich das Signal erstreckt, korrekt vorhergesagt. Es ist vorgesehen, dass MINIDEX viele Jahre betrieben wird, in verschiendenen Tiefen und mit verschiedenen Materialien. Die Resultate werden helfen, die myoninduzierte Produktion von Neutronen in Materialien mit hohem Z und die Folgen für Experimente mit geringem Untergrund zu verstehen.

Abstract

A new experiment to measure muon-induced neutrons is introduced. The design of the Muon-Induced Neutron Indirect Detection EXperiment, MINIDEX, is presented and its installation and commissioning in the Tübingen Shallow Underground Laboratory are described. Results from its first data taking period, run I, are presented. Muon-induced neutrons are not only an interesting physics topic by itself, but they are also an important source of background in searches for possible new rare phenomena like neutrinoless double beta decay or directly observable interactions of dark matter. These subjects are of great importance to understand the development of the early universe. Therefore, a new generation of ton-scale experiments which require extremely low background levels is under consideration. Reliable Monte Carlo simulations are needed to design such future experiments and estimate their background levels and sensitivities. The background due to muon-induced neutrons is hard to estimate, because of inconsistencies between different experimental results and discrepancies between measurements and Monte Carlo predictions. Especially for neutron production in high-Z materials, more experimental data and related simulation studies are clearly needed. MINIDEX addresses exactly this subject. Already the first five months of data taking provided valuable data on neutron production, propagation and interaction in lead. A first round of comparisons between MINIDEX data and Monte Carlo predictions are presented. In particular, the predictions of two Monte Carlo packages, based on GEANT4, are compared to the data. The data show an overall 70–100% higher rate of muon-induced events than predicted by the Monte Carlo packages. These packages also predict a faster time evolution of the muon-induced signal than observed in the data. Nevertheless, the time until the signal from the muon-induced events is completely collected was correctly predicted by the Monte Carlos. MINIDEX is foreseen to run for many years at different depths and with different target materials. The results will help to understand muon-induced neutron production in high-Z materials and the consequences for low-background physics.

Introduction

In this thesis, a new experiment to measure muon-induced neutrons is presented. The data of its first run in 2015 (from July 15 until November 25, 2015), a first analysis and the results are discussed. The work is set in the context of low-background physics. The quest to find evidence for direct dark matter interactions and neutrinoless double beta decay are of great importance for the physics community. Several experiments have been built in deep underground locations in the last decades to search for such fundamentally new phenomena. The next generation of these experiments requires ton-size detectors and very low background levels in order to improve the current sensitivities for direct dark matter and neutrinoless double-beta-decay searches.
The presence of intense fluxes of cosmic rays at the earth surface makes the choice to perform these experiments underground unavoidable. Nevertheless, high-energy muons can penetrate into the overburden of these experiments and are a source of background. In particular, muon-induced neutrons represent one of the main background sources for such experiments. Reliable Monte Carlo simulations are needed to predict the background level for these low-background experiments, with particular interest on the muon-induced background. Test facilities for Monte Carlo validations are highly important to the scientific community, especially concerning neutron yield in high-Z materials, for which the current studies are still controversial.
The Muon-Induced Neutron Indirect Detection EXperiment (MINIDEX), described in this thesis is well suited to provide valuable data for Monte Carlo validation. It will provide data-samples for selected target materials, which will help to solve the current controversy of the muon-induced neutron yield as a function of the muon energy. This thesis includes a simulation study of MINIDEX run I performed with GEANT4. The predictions from the simulation are compared to the first experimental results.

The first goal was to design a compact and flexible experiment which could provide benchmarks for Monte Carlo simulations. As aforementioned, MINIDEX will help the physics community to address the muon-induced neutron yield in high-Z materials. The second goal was to build such an experiment and develop the analysis strategy. The third goal was to develop a simulation framework and generate simulated data to be compared to experiment. These goals were achieved. MINIDEX is expected to run for many years. The work presented here represents the first milestone of the MINIDEX endeavor.

The thesis is structured as follows.
In *Chapter 1*, the field of low-background physics is briefly introduced. Particular attention is given to dark matter and neutrinoless double-beta-decay searches. A summary of the principles and the state of art of these research areas are shortly discussed.
In *Chapter 2* and *3*, the main background sources for these research areas are discussed. *Chapter 3* describes the cosmic rays induced background, which is of interest for this thesis.
In *Chapter 4*, the MINIDEX setup is described in detail. The data analysis strategy is presented and the results obtained for MINIDEX run I are discussed.
In *Chapter 5*, the simulation of MINIDEX run I performed with GEANT4 is presented. Detailed information on the geometry as described in the simulation and the input parameters of the simulation are given.
In *Chapter 6*, the results obtained with simulations are presented and discussed. Furthermore, a comparison of Monte Carlo to data is discussed.
Finally, in *Chapter 7*, the experimental and simulated results of MINIDEX run I are summarized. Possible sources of uncertainty of the simulation are highlighted. An outlook to future developments for the MINIDEX project as foreseen and partially already initiated completes the thesis.

Chapter 1

Low-Background Physics

The *Standard Model*, SM, of particle physics is a very successful model. It describes with great accuracy the interactions between the elementary particles. The recent experimental discovery of the Higgs boson at the Large Hadron Collider (LHC) [1, 2] is the most recent proof of the validity of the SM.
Nevertheless, the SM provides a description of only a small percentage of our universe. There are still several unresolved issues in seemingly different fields of physics, like particle physics, astrophysics and cosmology, which are, however, linked. The intrinsic nature of neutrinos together with their masses, the origin of the universe and its composition, the strong interaction within nucleons and the origin of extragalactic high-energy cosmic rays are just a few examples of these presently unresolved issues. Some of these issues are addressed within the so called *low-background physics* framework as they are connected to searches for very rare processes. The common feature of such experiments to search for rare processes is that they all require extremely low background-levels and they all need very precise and sophisticated detection techniques. A deep understanding of the background sources is necessary to successfully carry out these experiments.
The searches for direct dark matter (DM), neutrinoless double beta decay (NDBD or $0\nu\beta\beta$), low-energy neutrino interactions and proton decay have played a crucial role in the past decades [3, 4, 5, 6, 7, 8].
In this chapter, a brief introduction to NDBD and DM searches is given.

1.1 Neutrinoless Double-Beta-Decay Searches

Neutrinos were first postulated by Wolfgang Pauli in 1930 in order to explain β^- decay spectra. Since then, neutrinos have been of great interest in particle physics. In 1956, Reines and Cowan observed them for the first time directly [9]. Many experiments were carried out to measure neutrino fluxes of different origins like solar neutrinos [10, 11, 12, 13, 14, 15, 16] and atmospheric neutrinos [17, 18, 19, 20], as well as some of their properties [21]. Neutrinos were originally described in the SM as massless fermions of spin 1/2. However, the discovery of neutrino oscillations [22, 23] has proved that at least two of the neutrinos described in the SM have mass. This discovery made a modification and extension of the SM necessary and further experiments to measure their properties were performed [24, 25, 26, 27, 28, 29]. Currently, experiments are running [26, 30, 31, 32, 33, 34] to further improve the accuracy of the measurement of the relevant parameters of neutrino oscillations. All these experiments have greatly improved the understanding of neutrinos. Nevertheless, there are still some very fundamental questions about neutrinos which have not been answered yet:

- are neutrinos their own antiparticles?
- which is the correct neutrino mass hierarchy?
- what is the absolute mass scale for neutrinos?
- why are neutrino masses so small compared to the masses of other elementary particles?
- are there additional heavy or sterile neutrinos?

NDBD is considered the most promising process to address the first two of the above open questions [35, 36].
In general, double beta decay is a nuclear process in which two neutrons simultaneously decay into two protons. This kind of process only occurs in even-even (thus spin zero) isotopes, for which single beta decay is energetically forbidden. This is due to the nuclear pairing force which makes the even-even isotopes lighter than the odd-odd isotopes (see Fig. 1.1).

Two different processes can be distinguished:

$$(Z, A) \rightarrow (Z + 2, A) + 2e^- + 2\bar{\nu_e} \tag{1.1}$$

$$(Z, A) \rightarrow (Z + 2, A) + 2e^- \tag{1.2}$$

where Z and A are the number of protons (also called atomic number) and the sum of protons and neutrons in the nucleus, respectively. The former process is referred to as *neutrino-accompanied double beta decay* or $2\nu\beta\beta$ decay while the latter represents the NDBD. Figure 1.2 shows the Feynman diagrams for these two processes.

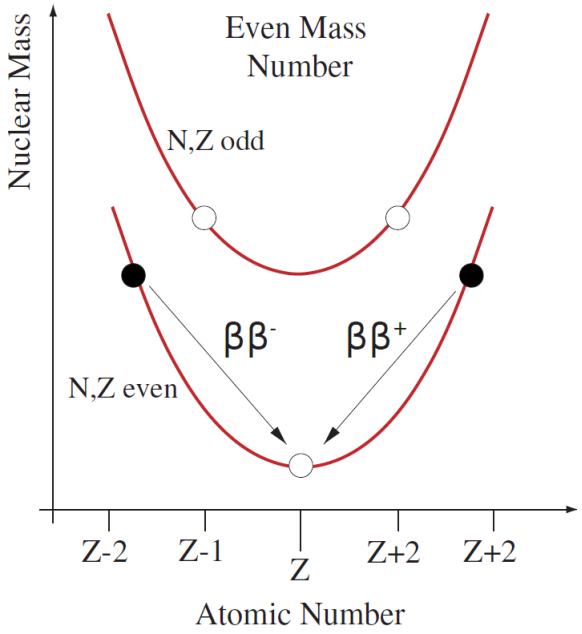

Figure 1.1: Nuclear mass as a function of the number of protons, Z, in the nucleus around an even Z, for which isotopes with $Z \pm 2$ and an even number of neutrons, N, cannot decay to isotopes with $Z \pm 1$. Taken from [38].

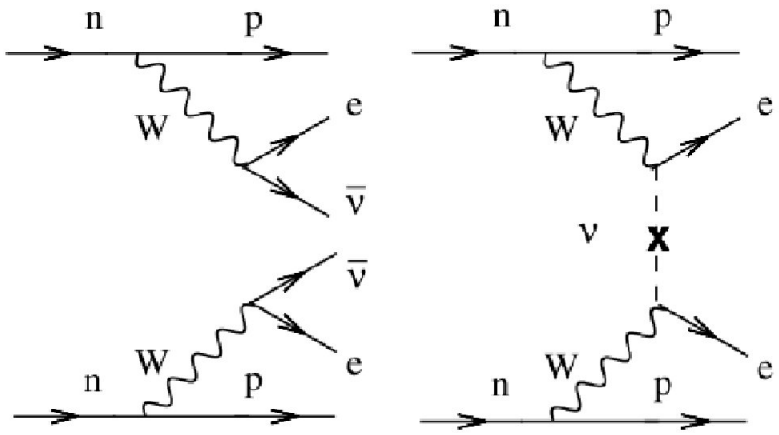

Figure 1.2: Feynman diagrams for $2\nu\beta\beta$ decay (left) and $0\nu\beta\beta$ decay (right).

$2\nu\beta\beta$ decay is a SM process and has been observed in many isotopes [37]. NDBD has not been observed. It is considered the most likely lepton-number violating process. Its observation would give information about the intrinsic nature of the neutrinos, their absolute mass and the mass hierarchy (see [38] and references therein). Although there are

theoretically other processes mediating NDBD, the process depicted in Fig. 1.2 (right), representing NDBD mediated via light neutrinos, is currently the theory for NDBD which is discussed the most [38]. This process would reveal the Majorana nature of neutrinos [39]. According to Fermi's golden rule, the rate of NDBD can be expressed as:

$$\frac{1}{{T_{1/2}}^{0\nu}} = G_{0\nu}(Q,Z,N)|M_{0\nu}|^2 {m_{\beta\beta}}^2 \ , \tag{1.3}$$

where:

- $G_{0\nu}(Q,Z,N)$ represents the phase-space factor, which is a function of the Q-value[1] of the reaction and the isotopic composition;
- $M_{0\nu}$ is the nuclear matrix element (NME);
- $m_{\beta\beta}$ is the so called *effective Majorana neutrino mass.*

The *effective Majorana neutrino mass* is defined as:

$$m_{\beta\beta} = |\sum_i {U_{ei}}^2 m_i| \tag{1.4}$$

where m_i are the mass-eigenstates of the neutrinos and U_{ei} are elements of the mixing-matrix, U, between the neutrino flavor-eigenstates and neutrino mass-eigenstates, known as the Pontecorvo-Maki-Nakagawa-Sakata (PMNS) matrix [40]. In case of only three generations of neutrinos, a common representation of the PMNS matrix is:

$$\begin{aligned} U = &\begin{pmatrix} 1 & 0 & 0 \\ 0 & cos\theta_{23} & sin\theta_{23} \\ 0 & -sin\theta_{23} & cos\theta_{23} \end{pmatrix} \times \begin{pmatrix} cos\theta_{13} & 0 & sin\theta_{13}\, e^{-i\delta_{CP}} \\ 0 & 1 & 0 \\ -sin\theta_{13}\, e^{-i\delta_{CP}} & 0 & cos\theta_{13} \end{pmatrix} \\ &\times \begin{pmatrix} cos\theta_{12} & sin\theta_{12} & 0 \\ -sin\theta_{12} & cos\theta_{12} & 0 \\ 0 & 0 & 1 \end{pmatrix} \times \begin{pmatrix} e^{i\alpha_1/2} & 0 & 0 \\ 0 & e^{i\alpha_2/2} & 0 \\ 0 & 0 & 1 \end{pmatrix} \end{aligned} \tag{1.5}$$

where θ_{ij} are the mixing angles, δ_{CP} is the so called *Dirac phase* and α_1 and α_2 are the so called *Majorana phases*. A value of $\delta_{CP} \neq 0$ would lead to CP-violating neutrino oscillations. With the nomenclature of Eq. 1.5, the *effective Majorana neutrino mass* becomes

$$m_{\beta\beta} = |m_1\,|U_{e1}|^2 \ + \ m_2\,|U_{e2}|^2\, e^{i(\alpha_2-\alpha_1)} \ + \ m_3\,|U_{e3}|^2 e^{-i(\alpha_1+2\delta_{CP})}| \ . \tag{1.6}$$

[1] Energy released by a specific reaction.

This demonstrates that finite *Majorana phases* would influence the NDBD rate.
Figure 1.3 shows the allowed regions for $m_{\beta\beta}$ as a function of the lightest neutrino mass, $m_{lightest}$. These regions represent the predictions on $m_{\beta\beta}$ from the results of the neutrino oscillation experiments [41] and the constraints on $m_{lightest}$ due to the latest cosmological surveys [42, 43, 38].

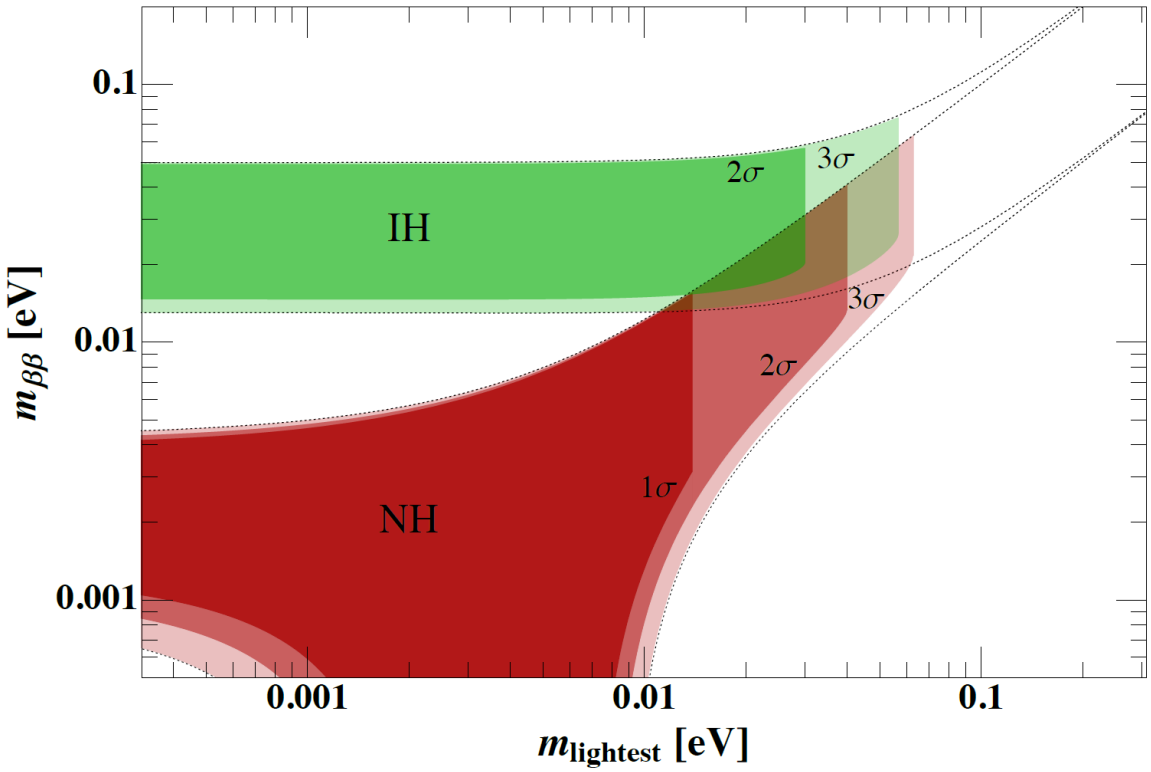

Figure 1.3: Allowed regions of $m_{\beta\beta}$ as a function of $m_{lightest}$ for both the inverted-hierarchy (IH) and normal-hierarchy (NH) scenarios. The latest constraints from oscillation experiments and cosmological surveys are included. The dotted contours represent the 3σ regions allowed considering oscillations only. The shaded areas show the effect of the inclusion of the cosmological constraints at different C.L. Figure taken from [43].

The values of $m_{\beta\beta}$ are sensitive to the neutrino mass configuration, i.e. the inverted-hierarchy (IH) and normal-hierarchy (NH) scenarios can be distinguished.
Particular attention is devoted by the community to the evaluation of the nuclear matrix elements . Historically, this was always the main source of uncertainty on the evaluation of the NDBD decay rate, thus on the upper bounds on $m_{\beta\beta}$. Many theoretical models have been developed. Currently, the main source of uncertainty is considered to be the quenching factor of the axial vector coupling constant. Further details can be found in [38] and references therein.

The main background sources for the NDBD searches are:

- environmental radioactivity;
- cosmic rays;
- *neutrino accompanied double beta decay.*

The latter is experimentally unavoidable, since it comes from the same isotope that could undergo NDBD. As shown in Fig. 1.4, the spectrum from the two electrons emitted in NDBD is (ideally) a monoenergetic line at the Q-value of the reaction, while a continuous spectrum is observed for $2\nu\beta\beta$ decay.

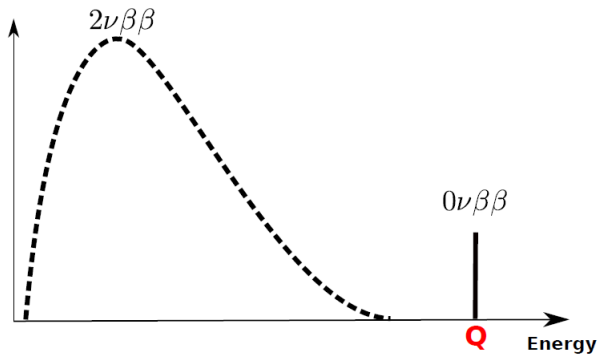

Figure 1.4: Schematic view of the $2\nu\beta\beta$ and $0\nu\beta\beta$ spectra.

NDBD searches are not feasible for all isotopes that could undergo double-beta-decay. In particular, an isotope should meet the following requirements [38]:

- high Q-value, to avoid as much natural background as possible and to have a larger phase-space factor;
- high isotopic abundance;
- compatibility with detection techniques;
- scalability of technology to bigger experiments.

Table 1.1 lists the isotopes which are currently used in NDBD searches together with their Q-values and abundances. There is no isotope, among those listed in Tab. 1.1, which is a priori the best.
Many experiments aimed to measure NDBD are currently ongoing and more are planned. These experiments fall in two main categories: those in which the source coincides with the detector and those in which the source and the detector are separate volumes. The former category includes Germanium detectors [6, 45], bolometers [46, 47, 48], liquid scintillators

Isotope	Natural Abundance [%]	Q-value [MeV]
^{48}Ca	0.187	4.263
^{76}Ge	7.8	2.039
^{82}Se	9.2	2.998
^{96}Zr	2.8	3.348
^{100}Mo	9.6	3.035
^{116}Cd	7.6	2.813
^{130}Te	34.08	2.527
^{136}Xe	8.9	2.459
^{150}Nd	5.6	3.371

Table 1.1: Isotopic abundance and Q-value for the isotopes candidate for NDBD search. Taken from [44].

[49, 50] and time projection chambers (TPC) [51, 52, 53, 54]. The latter relies instead on good tracking capabilities to reconstruct the event topology [55, 56]. In general, all experiments are performed deep underground and a big effort is made to reduce the background due to the materials used in the experiment. It can be shown that a limit on the NDBD half-life, ${T_{1/2}}^{0\nu}$, is [57]:

$$ {T_{1/2}}^{0\nu} \propto a \cdot \sqrt{\frac{M \cdot t}{B \cdot \Delta E}} \, , \tag{1.7} $$

where a is the isotopical abundance, M the mass of the isotope, t the measurement time, ΔE is the search window and B is the background index expressed in counts/(kg $\cdot$ keV $\cdot$ y). This limit requires that no peak in the region of interest (ROI) is observed and the background scales linearly with time. The main experimental challenges are the reduction of the background B while increasing the *exposure* $M \cdot t$. A good energy resolution allows for a small ΔE.
Currently, the best lower limits on ${T_{1/2}}^{0\nu}$ are given by the Germanium-based experiment GERDA (${T_{1/2}}^{0\nu} > 2.1 \cdot 10^{25}$ y at 90% C.L.) [58] and the Xenon-based experiments EXO-200 (${T_{1/2}}^{0\nu} > 1.1 \cdot 10^{25}$ y at 90% C.L.) [51] and KamLAND-Zen (${T_{1/2}}^{0\nu} > 1.9 \cdot 10^{25}$ y at 90% C.L.) [49]. These limits can be translated into upper limits on $m_{\beta\beta}$ according to Eq. 1.3.

The community is now moving towards large-scale experiments to increase the exposure to probe lower values of the *effective Majorana neutrino mass*. Two different shielding approaches have been adopted so far, i.e. high-Z shielding materials [45] and low-Z shielding materials [6]. The latter approaches have different impact on the background level of the experiments. A deeper understanding of background sources will drive the choice of the shielding approach for future generation experiments.

1.2 Dark Matter Searches

A well established result of observational cosmology and astrophysics is the existence of non-luminous matter in the universe. The first historical evidence for the existence of DM was the measurement of galactic rotation curves [59]. The observation of gas clouds in galaxies has shown that the rotational velocity tends to remain constant as the distance from the galactic center increases. If visible matter, i.e. stars, would be the only contribution to the mass of the galaxy, then the rotational velocity would decrease as $1/\sqrt{r}$, r being the distance from the galactic center.
This disagreement implies the existence of a dark halo[2] with a mass distribution $M(r) \propto r$.
Another evidence for the presence of DM is the observation of large galactic masses through their gravitational strength. This method relies on the so called *gravitational lensing* effect, in which light coming from sources in the background is deflected by the gravitational field of the foreground galaxy [60].
More recently, a strong confirmation of the existence of DM came from cosmological estimates of the baryonic-matter abundance in the universe. The most accurate method to measure the baryonic-matter abundance is based on the formation of light nuclei during the Big Bang Nucleosynthesis[3]. Recent measurements of the deuterium/hydrogen ratio [61], together with nucleosynthesis predictions, estimate a baryonic-matter contribution of $\Omega_B \sim 0.03$. This is also in agreement with measured nuclei abundances for ^{3}He, ^{4}He and ^{7}Li [62]. The cosmic density of optically luminous matter is $\Omega_{lum} \sim 0.003 \ll \Omega_B$. This indicates that most of the baryons are optically dark, they probably form a diffuse intergalactic medium. By comparing Ω_{lum} and Ω_B to the measured total matter contribution to the universe $\Omega_M \sim 0.3$ [42], it emerges that most of the matter in the universe is not only invisible, but it also has a non-baryonic nature.
Furthermore, DM played a significant role in the evolution of the universe, in particular in structure formation [63]. One of the simplest models for the generation of cosmological structures is gravitational instability acting on small initial fluctuations, whose origin can be explained by the theory of inflation[4]. Immediately after the Big Bang, all matter was relativistic (hot). During the expansion, the universe cooled down until it reached the temperature, at which DM particles decoupled (froze-out) from the rest. DM, being heavy and non-relativistic, started to arrange in gravitational structures: the galactic halos. When baryons decoupled, they were gravitationally attracted inside the DM aggregations to form galaxies. This scenario is based on the so called *Cold Dark Matter* (CDM) [64].
The scenario with dominant relativistic particles (Hot Dark Matter, HDM) is disfavored, both by observation and numerical calculations. The small structure of the universe would have been dissolved by HDM.

[2] A dark matter halo is a hypothetical component of a galaxy, which extends well beyond the edge of the visible galaxy and dominates the total mass.

[3] Nucleosynthesis is the process of creating new nuclei from pre-existing nucleons. The primordial nucleons themselves were formed from the quark-gluon plasma of the Big Bang as it cooled below two trillion degrees.

[4] Inflation is an epoch during which the universe grew exponentially.

There are still many unresolved issues about DM, above all, its nature. Many theoretical speculations and experimental efforts are being carried out [65, 66, 67]. Several candidates have been proposed in the past, such as primordial black holes [68], massive neutrinos [69], axions [70] and weakly interacting massive particles (WIMPs). The latter have been considered the most likely candidates by many in the community. The characteristics of the WIMP-DM candidates are:

- non-baryonic nature;
- stable or long lived compared to the age of the universe;
- present as a relic population
- massive, $O(1GeV) \div O(1TeV)$ [71, 72];
- non-relativistic at decoupling;
- very low cross section with ordinary matter, approximately of the order of the weak coupling strength or below;
- electrically neutral;
- colorless.

The DM searches can be grouped essentially in four categories [65, 66, 67]:

- **astrophysical searches**, which include for example the abundance of dwarf galaxies, stellar streams and gravitational lensing (see [73] and references therein);
- **searches at particle colliders:** production of DM particles at colliders like the LHC [66, 74, 75];
- **indirect searches:** mainly the searches for DM annihilation products in cosmic rays [73, 66];
- **direct searches:** direct DM interactions with ordinary matter, mainly elastic scattering off nuclei.

These different approaches provide useful information on every DM scenario. It is very important that the scientific community pursues all these complementary approaches to provide a clearer and stronger picture about dark matter.
In the following, only the direct searches are briefly discussed, since they belong to the low-background physics research field. Specifically, the discussion will focus on WIMP direct searches.

1.2.1 Direct Dark Matter Searches

WIMPs are assumed to be gravitationally trapped inside galaxies, with rotational velocities relative to the galactic center similar to that of stars (∼220 km/s for the solar system). Despite the low cross section for interactions with ordinary matter, at these velocities WIMPS could undergo elastic scattering off nuclei on a non co-moving planet [65]. Direct searches essentially look for the recoil of target nuclei due to the interactions with WIMPs. The expected recoil energies are in the range from sub-keV to 100 keV, depending on the WIMP mass. The expected rates range from 1 to 10^{-3} events per kg of detector and year. Ultra-sensitive low-background detectors are needed for such kind of searches.
Typically, the direct spin 1/2-WIMP interactions with ordinary matter are classified depending on whether the relative orientation of the spin of the particles involved plays a role or not:

- *spin-independent* interactions;
- *spin-dependent* interactions.

Given the aforementioned energy range of the recoil, environmental radioactivity and cosmic-ray induced events are the major background sources for the experiments. Similarly to NDBD, these experiments are performed deep underground and require big efforts in terms of background reduction. Moreover, these experiments will eventually be affected by the so called *ultimate neutrino background*. This background is induced by solar neutrinos, which have low-energies but intense fluxes. These neutrinos can contribute to the electron recoil background, and therefore, depending on the detector's capability to distinguish between nuclear and electron recoils, they represent an irreducible background for direct DM detection. Atmospheric neutrinos can also constitute a background source for WIMP mass above 10 GeV.
In order to detect the energy deposited by the scattered nucleus, the following mechanisms are used experimentally:

- **ionization;**
- **scintillation light;**
- **phonons.**

In current experiments one or two of the above mechanisms are used. A common classification of the experiments is based on the detection technologies used:

- *Cryogenic Solid-State detectors*: experiments operated as bolometers at sub-Kelvin temperatures;
- *Nobel Liquid detectors*: non-segmented, homogeneous, compact and self-shielding experiments which use the ionization and scintillation properties of nobel liquids (usually Xe or Ar);

- *Scintillating Crystal detectors*;
- *Super Heated Liquid detectors*: liquids kept in metastable states which are destroyed by energy deposition. Usually used to study the spin-dependent interactions.
- *Directional detectors*: experiments aimed to infer the WIMPs incoming direction by sensing the direction of nuclear recoils ([67] and references therein).

Table 1.2 lists selected direct DM-search experiments targeting WIMPs together with their experimental technique and detection mechanisms.

Experiment	**Technique**	**Mechanism**
CDMS [76]	Cryogenic Solid-State	ionization+phonons
CRESST [77]	Cryogenic Solid-State	scintillation+phonons
EDELWEISS [78]	Cryogenic Solid-State	ionization+phonons
CDEX[79]	Cryogenic Solid-State	ionization
XENON100[80]	Nobel Liquid (Xe): dual phase TPC	scintillation+ionization
LUX[81]	Nobel Liquid (Xe): dual phase TPC	scintillation+ionization
DarkSide[82]	Nobel Liquid (Ar): dual phase TPC	scintillation+ionization
DAMA/LIBRA[83]	Scintillating Crystal: NaI(Tl)	scintillation
ANAiS[84]	Scintillating Crystal: NaI(Tl)	scintillation
PICASSO[85]	Super Heated Liquid: bubble chamber, C_4F_{10}	ionization
SIMPLE[86]	Super Heated Liquid: bubble chamber, C_2ClF_5	ionization
DRIFT[87]	Directional: multi-wire proportional chamber	ionization

Table 1.2: List of direct DM-search experiments. The experimental techniques and detection mechanisms are also listed.

Figure 1.5 summarizes the current situation for direct DM experiments, showing exclusion limits for WIMP-nucleon cross-section as a function of the hypothetical WIMP mass for spin-independent interactions. Figures 1.6 and 1.7 show equivalent limits for spin-dependent interactions with neutrons and protons, respectively. So far, besides a few controversial claims of DM direct detection, only upper limits have been reported [67].

The scientific community is now moving towards large-scale experiments in order to improve their sensitivity.

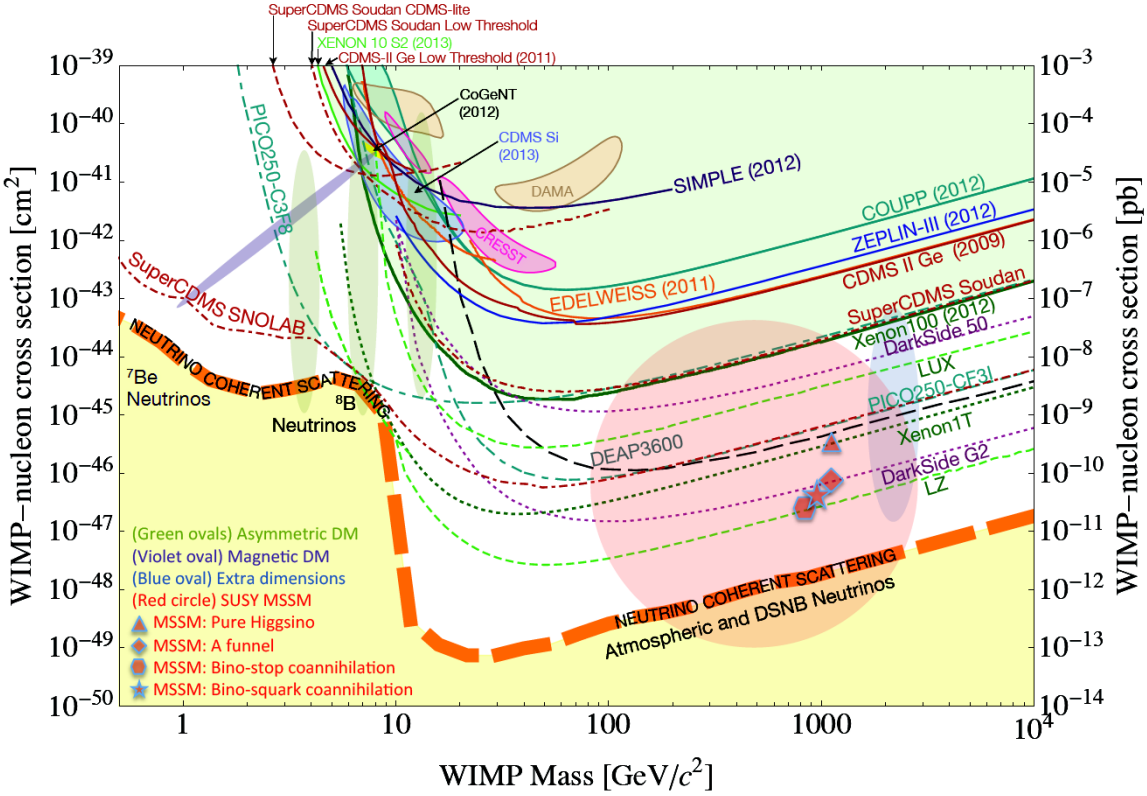

Figure 1.5: WIMP-nucleon spin-independent cross section limits (solid curves) and expectations (dotted curves) vs WIMP mass. The irreducible neutrino background is also shown. The shaded closed contours refer to debated DM signal-detection. A selection of theoretical model predictions is indicated by the shaded regions, with model references included. Figure taken from [67].

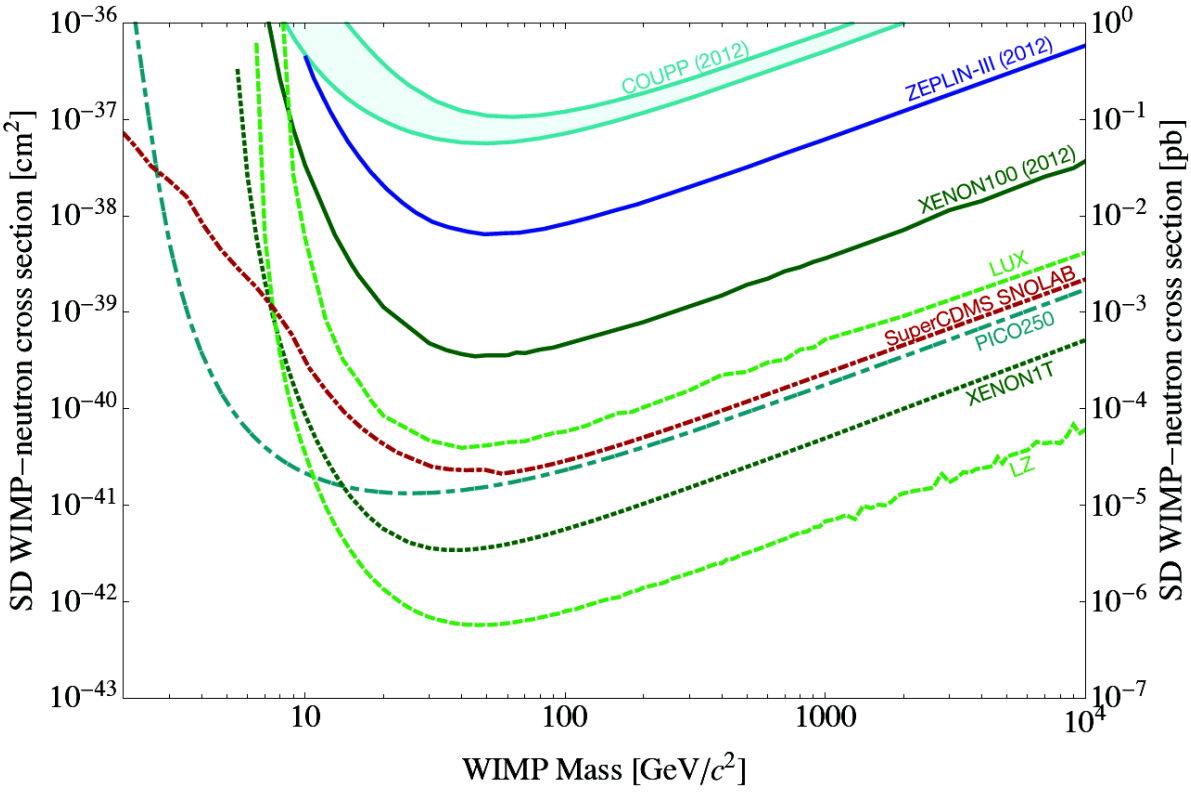

Figure 1.6: WIMP-neutron spin-dependent cross section limits (solid curves) and expectations (dotted curves) vs WIMP mass. Figure taken from [67].

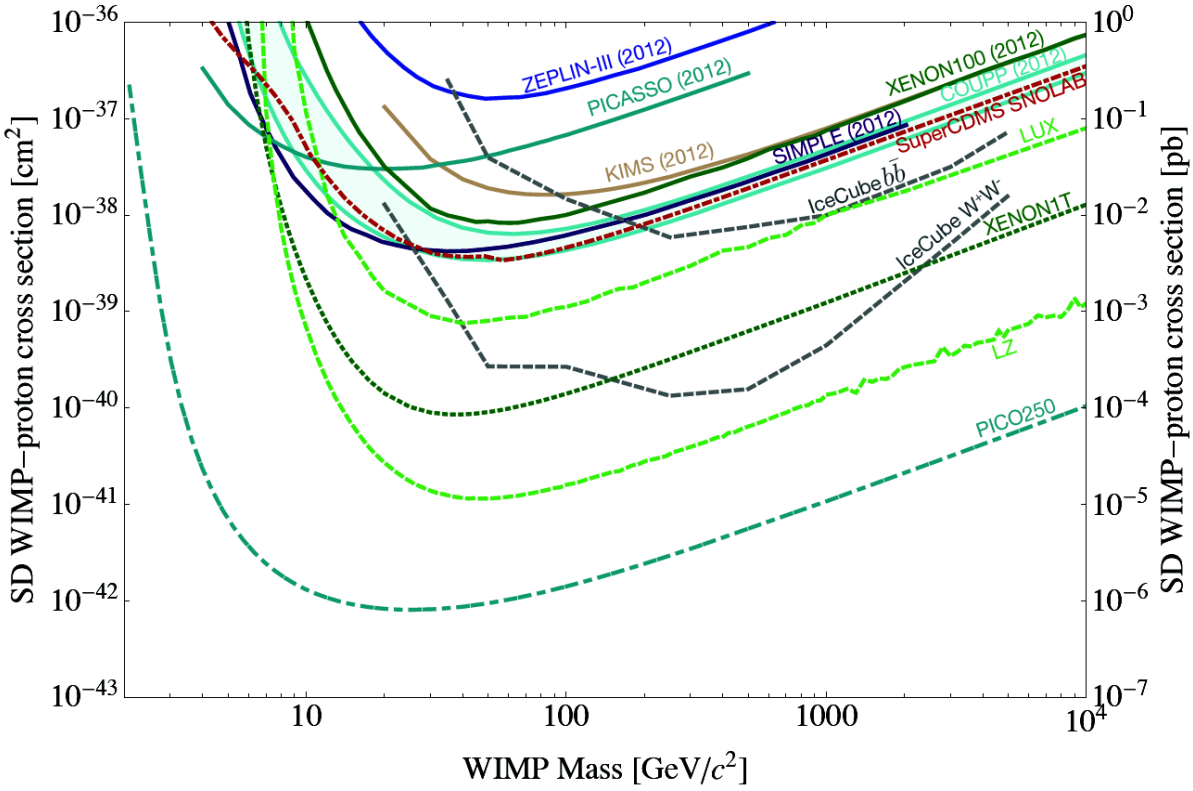

Figure 1.7: WIMP-proton spin-dependent cross section limits (solid curves) and expectations (dotted curves) vs WIMP mass. Figure taken from [67].

Chapter 2

Background Sources for Underground Experiments

In low-background physics, large efforts were made over the last 40 years to understand the different background sources and their impact on the sensitivity of an experiment and thus on its discovery potential [88]. The capability to predict the sensitivity of an experiment, given a certain background level, is crucial to design an experiment. Several techniques, based on Monte Carlo methods, have been developed in this context (see for example [89, 90]). An example of a prediction of sensitivity is shown in Fig. 2.1, left and right, where the expected 90% probability lower limit and the 50% probability to report a discovery on the half-life of neutrinoless double beta decay versus the exposure are plotted.
Calculations as illustrated in Fig. 2.1 can only be used to evaluate the potential of an experiment if the background level is known precisely enough. This requires knowledge on the spectral shape of the background and thus on its nature.

While low-background experiments differ substantially in terms of techniques and physics goals, they are all affected, although in different ways and magnitude, by the same background sources. The relevant common background sources are:

- natural radioactivity in the vicinity of the experiment and its infrastructure;
- intrinsic radioactivity of active volumes and close by materials;
- background induced by the interactions of cosmic rays (see Ch. 3).

In order to reduce the background from cosmic radiation, low-background experiments are performed deep underground. While a large overburden shields an experiment from a big fraction of the cosmic radiation, the intensity of the first two background sources does not depend on the depth of the location, but rather on the composition of the materials.

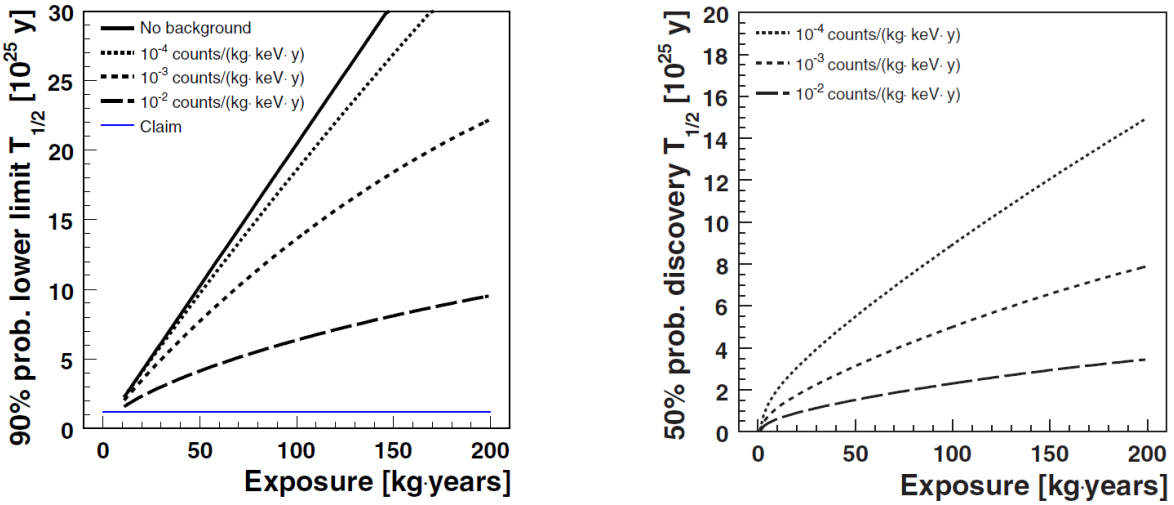

Figure 2.1: The plot on the left shows the expected 90% probability lower limit on the half-life for neutrinoless double beta decay versus the exposure for different background levels. No contribution from the signal is assumed here. For a background level of 10^{-3} counts/(kg · keV · y) and 100 kg · years exposure the expected sensitivity on the half-life of NDBD is $13.5 \cdot 10^{25}$ years. The plot on the right shows instead the half-life for which 50% of the experiments would report a discovery versus the exposure. Both figures are taken from [89] and were provided for the GERDA experiment.

2.1 Natural Radioactivity

The radioactive isotopes present in the rock surrounding an experimental hall as well as in the infrastructure of the experiment itself contribute to its overall background level. The radiation reaching the detectors is mainly in the form of gamma-rays, neutrons and alpha particles. The main contribution to this background source is typically due to the presence of primordial radionuclides[1] in the materials close to the detectors. The contribution from the rock and main support structures is normally reduced by special shields. Dominant are ^{40}K and members of the natural ^{238}U and ^{232}Th α-decay series due to their large abundance [91].
While ^{40}K produces only gammas (at 1460 keV), the uranium and thorium decay sequences are responsible for gammas, neutrons, alpha and beta particles. Figure 2.2 and Fig. 2.3 show the ^{238}U and ^{232}Th decay chains, respectively. In both cases, many radioactive isotopes are created along the sequence before reaching the stable isotopes ^{206}Pb and ^{208}Pb, respectively. The two most problematic gamma emitters generated are ^{208}Tl, which emits

[1]Radioactive isotopes with lifetimes of the order of 10^9 years. These radionuclides were produced by progenitor stars to the solar system and persist until now in the earth.

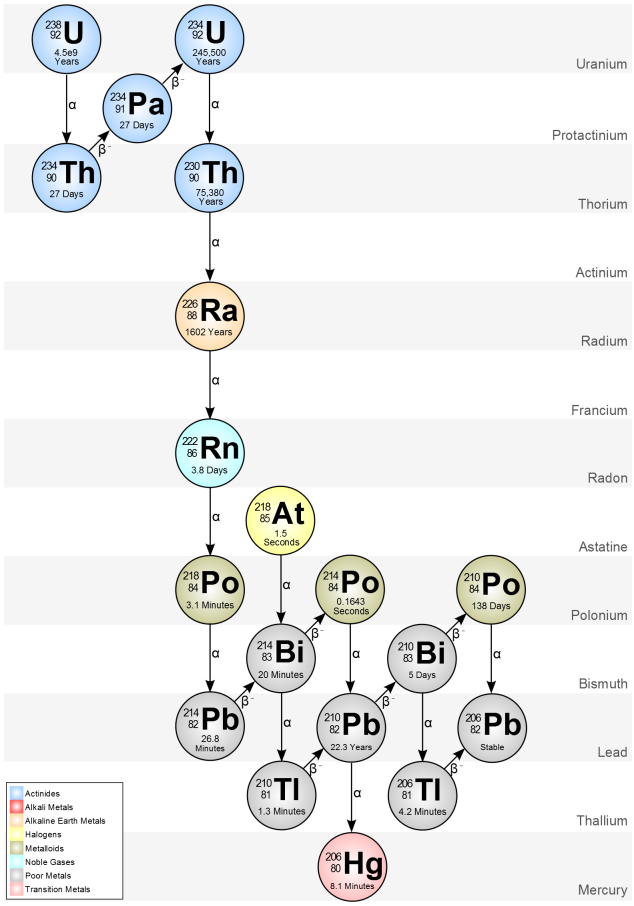

Figure 2.2: Illustration of the ^{238}U decay chain.

gammas at 2.614 MeV, and ^{214}Bi, which emits gammas at 2.204 MeV.

Neutrons are mainly produced via (α,n) reactions[2], which occur inside the rock or other surrounding materials [92, 93]. These (α,n) reactions are more likely to occur on light nuclei, like ^{9}Be and ^{43}Ca, than on heavier but more abundant nuclei, like ^{16}O and ^{28}Si. Hence, the composition of the rock determines the intensity of this neutron source. Neutrons arising from these reactions themselves produce further secondary neutrons. This process also depends on the composition of the materials. Another important process that contributes to the neutron flux from natural radioactivity is spontaneous fission[3] [94, 95]. The three main isotopes that undergo spontaneous fission are ^{235}U, ^{232}Th and, most important, ^{238}U.

The neutrons produced via the mechanisms of natural radioactivity have typically energies below 10 MeV. Figure 2.4 gives an example for a spectrum as predicted from uranium

[2]Neutrons are produced when alpha particles from alpha decays interact with a nucleus.
[3]A natural decay process in which heavy nucleus breaks into two lighter nuclei.

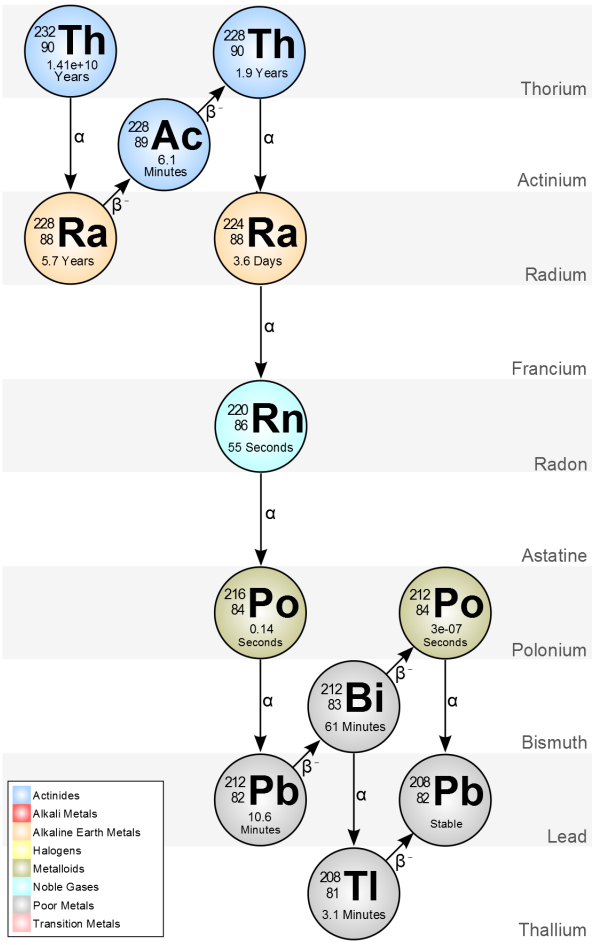

Figure 2.3: Illustration of the ^{232}Th decay chain.

and thorium in LSM[4] rock. Calculations and simulations of this background component are available in the literature (see for example [91, 96, 95, 97] and references therein). Many measurements of these background components are also available in the literature [94, 98, 99, 100, 101, 102, 103, 104].

In many low-background experiments, neutrons are considered one of the most problematic background component. The problem is that they are difficult to identify and hard to shield. When they interact within the detectors they can mimic the signal. For example, in direct dark matter experiments, elastic neutron scattering creates the same signature as WIMP scattering. In neutrino detection experiments, high-energy neutrons can mimic a neutrino deep inelastic event.

In NDBD experiments, gamma rays emitted after inelastic neutron scattering or ther-

[4]Modane Underground Laboratory

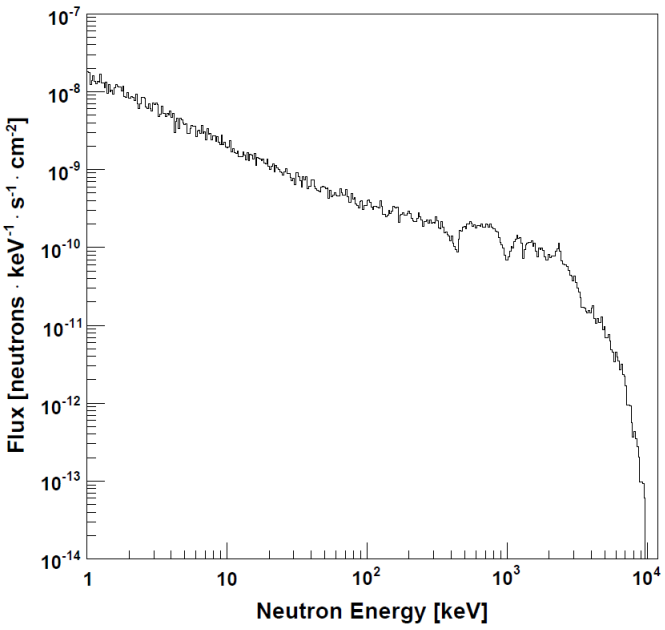

Figure 2.4: Neutron energy spectrum from uranium and thorium in LSM rock as predicted with GEANT4. Figure taken from [96].

mal neutron capture might mimic the double-beta-decay signature or simply enhance the background in the region of interest (ROI). Metastable isotopes can also be created within the detector or its vicinity via transmutation.

The natural radioactivity in the vicinity of the experiment and the intrinsic detector radioactivity contribute to the low-energy background in low-background experiments. Proper shielding techniques [6, 45, 105, 51] and purification methods were used with great success along the past decades to reduce this background. The purity of the shielding materials used is crucial, since these materials themselves often represent the dominant source of neutron background.

Radon

As shown in Fig. 2.2 and Fig. 2.3, the uranium and thorium decay chains include radioactive isotopes of radon. As a nobel gas, radon is able to diffuse through rock and experimental infrastructure and reach the detector. Thus, radon contamination is also a dangerous background source. Its radioactive isotopes, especially ^{222}Rn, can produce alphas and secondary gammas in the vicinity of the detector. It should be noted that radon is not the only airborne background source. Other radionuclides present in the atmosphere or produced via cosmic ray induced spallation, mainly with nitrogen and oxygen, can also play a role [91].

2.2 Intrinsic Radioactivity of Active Volumes and close by Materials

Natural radioactivity in underground experiments does not only come from the surrounding rock or from the experimental infrastructures. The most critical background due to radioactive isotopes comes from the materials close to the active volumes or from these detectors themselves.
The radionuclides can be part of the material itself or can be introduced during the various manufacturing processes. Extensive surveys are necessary. Each piece has to be manufactured from carefully selected and screened batches of material. The screening itself requires low-background facilities. The storage of materials has to be controlled as well as all the manufacturing steps. The machines used have to be cleaned appropriately and all handling has to be controlled. Facilities have to be kept dust and radon free. Radioactive isotopes can also originate from cosmogenic activation during transports above ground. Reducing the above ground exposure of sensitive materials is one of the main challenges for low-background experiments. For future experiments, appropriate manufacturing facilities will have to be set up within the underground laboratories.
Cosmogenic activation due to muon interactions can also occur in deep underground sites [106]. However, the rate is much reduced.
The cosmogenic production rates can be calculated [107, 108, 109, 110]. It is, however, necessary to have exact knowledge of material compositions.

Chapter 3

Cosmic Ray Induced Background

3.1 General Features

The earth atmosphere is constantly struck by intense fluxes of energetic particles. These particles are called *primary cosmic rays*. The study of this cosmic radiation involves many different research fields, from elementary particle physics to astrophysics and cosmology. The cosmic ray spectrum ranges from few MeV to thousands of EeV. Figure 3.1 depicts the spectrum of of primary charged particles..

Primary cosmic rays, charged and neutral, are of galactic and extragalactic origin [112]. Charged cosmic rays are ≈99% protons and nuclei and ≈1% electrons. Neutral cosmic rays are gammas covering the whole electromagnetic spectrum and neutrinos. While neutrinos traverse the earth atmosphere and with high probability the whole planet without interacting, charged particles and high-energy gammas interact with the atoms and nuclei of the atmosphere. From these interactions, electromagnetic and hadronic showers arise and the particles produced by these showers are referred to as *secondary cosmic rays*.

During the last hundred years many experiments have been conceived to measure the fluxes and energy spectra of both primary and secondary cosmic rays [113, 114, 115, 116, 117, 118]. Cosmic rays represent the main component of natural radiation on the earth surface. They are composed mainly of gammas, muons, neutrinos, neutrons and other hadronic particle like pions. The presence of this intense cosmic radiation wipes out any possibility to perform a low-background experiment above ground. By going underground, it is possible to shield most of the cosmic radiation. However, high-energy cosmic muons and neutrinos, penetrate deeply and reach any underground location. The highly energetic muons can interact with the surrounding rock and the infrastructure of the experimental hall as well as with the shielding of the experiment and its sensitive components. The interactions of cosmic muons can produce electromagnetic and hadronic showers. The net effect is the production of high-energy gammas and neutrons which contribute to the overall background.

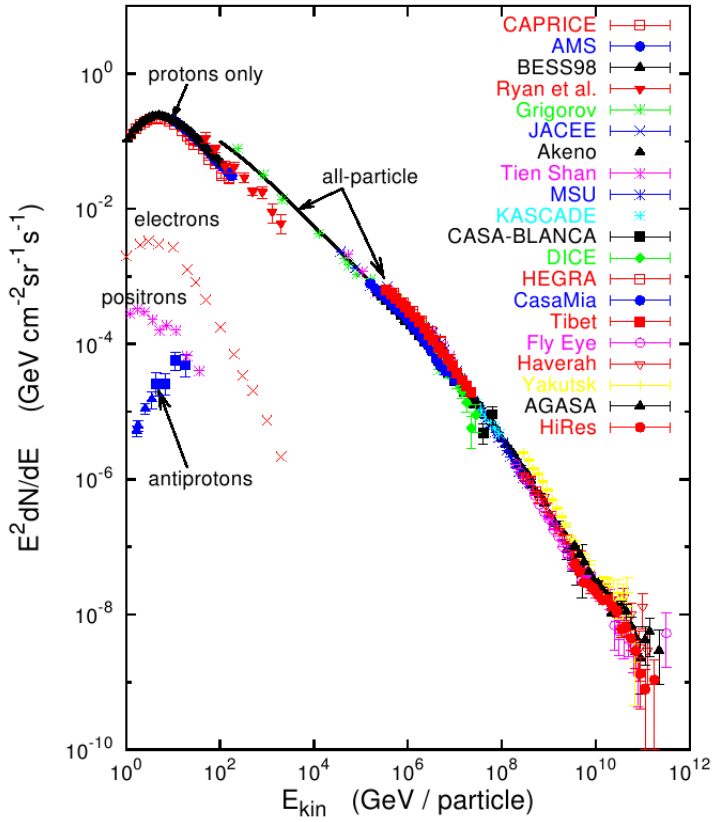

Figure 3.1: Spectrum of charged primary cosmic rays. Taken from [111].

Although the muon-induced neutron flux in deep underground laboratories is typically much smaller than neutron flux from radioactivity in the rock [119, 106, 95], it is often relevant as a source of background for low-background experiments. Examples of the influence of muon-induced neutrons are the annual modulation in the DAMA/LIBRA experiment [120, 121, 122, 123], results from the Palo Verde experiment [124, 125], XENON100 [126] and Kamland [127, 128]. The most energetic muons are produced in the atmosphere by mesons decaying before further interactions. In summer, due to the increase of the temperature of the atmosphere, the fraction of such mesons increases. This temperature variation results in an annual modulation of muon-induced neutrons in deep underground laboratories.

While neutrons produced by natural radioactivity, such as fission or (α,n) reactions, have energies only up to a few MeV (soft energy spectrum), and can be efficiently shielded by hydrogen-rich materials, the energies of muon-induced neutrons extend up to several GeV (hard energy spectrum, see Fig. 3.2). This extended energy range makes it more

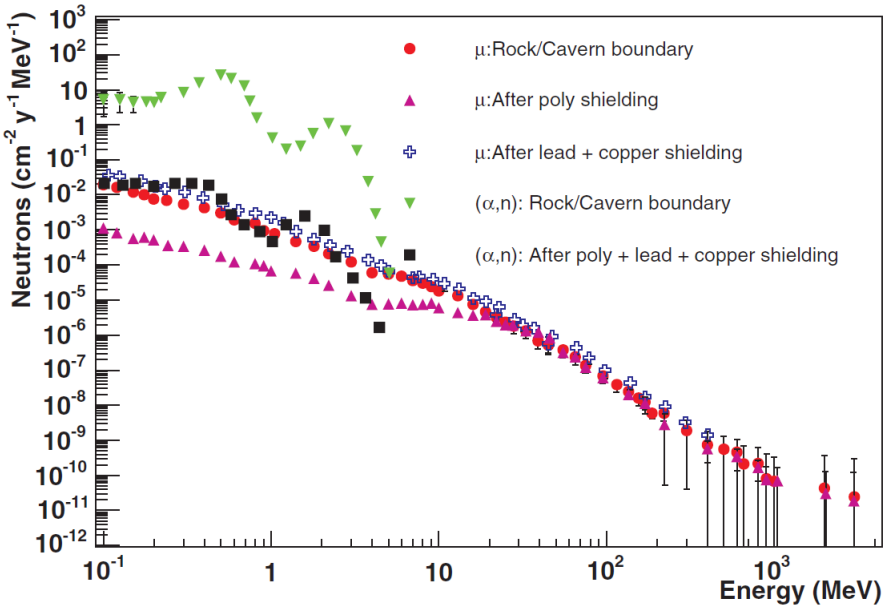

Figure 3.2: Comparison of the energy spectra of muon and (α,n)-induced neutrons. These spectra are predictions from simulations performed with GEANT 3 for the depth of the Gran Sasso underground laboratory in the presence of a shielding as foreseen for the Majorana experiment. It can be seen, how the presence of lead shielding increases the muon-induced neutron component. Details can be found in [106].

difficult to shield against them. Therefore, beside going deeper and deeper underground, muon veto techniques are usually used in low background experiments to further reduce this background component. Typical examples of muon vetoes, such as instrumented water tanks or liquid scintillators like argon or xenon, can be found in GERDA [6] and LZ [129], respectively. However, active veto systems might not be enough. Often, the muon-induced neutrons travel quite some distance from the originating muon track and can, therefore, reach the sensitive components of the experiment, also if the primary muon cannot be tagged. These kind of neutrons are often an irreducible background for low-background experiments. This background is particularly problematic, if metastable particles are produced.
A simulation study of the hadronic shower development in rock is available in Appendix A.
Further simulation studies were done by other authors in the past, both with FLUKA [130] and GEANT4 [131], [132, 119, 133, 106].
As mentioned previously, the interaction of cosmic muons with the shielding materials around the experiment can produce dangerous background neutrons. These neutrons are produced either directly by the interactions of the muons or of the secondary high-energy gammas and other hadrons. The more shielding material is used in a low background

experiment, the higher is the probability that muon-induced neutrons play an important role as a source of background. The shielding materials (often high-Z materials like lead) can be responsible for most of the relevant neutrons [119, 134, 135]. This effect of the shielding materials on the neutron flux is demonstrated in Fig. 3.2. It shows how the presence of high-Z shielding materials enhances the neutron background. The muon-induced background strongly depends on the actual geometry and components of the experimental setup. The (α,n)-induced neutrons are more efficiently attenuated by the presence of shielding materials due to their limited energy. This results in a more significant muon-induced neutron component, even though the unshielded flux is much lower. This has to be taken into account when designing an experiment for a given location. The Majorana design based on high-Z shielding can only be realized at extreme depth.

In general, the muon-induced background can be a limiting factor for underground experiments. A lot of effort was done to understand and reduce this background component [106, 136, 137]. It is very important to have an accurate knowledge of both the muon differential flux and the resulting secondary particles fluxes and spectra (especially neutrons) in order to have a precise background description. Many experiments were performed and calculations were carried out for this purpose in the last decades. A selection of these measurements and calculations, together with some MC studies, are reported in the following.

3.2 Muon Fluxes Underground

Figure 3.3 shows the total muon flux measured at various underground sites as a function of the *equivalent vertical depth relative to a flat overburden*[1] (h_0). The total muon flux is reduced by six orders of magnitude for the deepest site. These results are also summarized in Table 3.1.

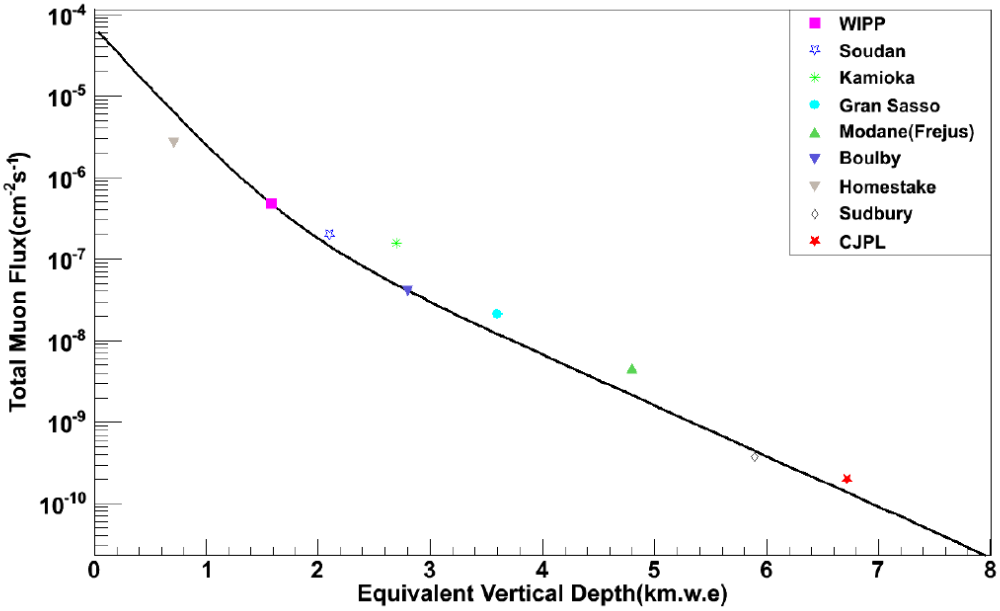

Figure 3.3: Total muon flux vs. depth for different underground sites [138]. The Black curve represents the flat-earth model prediction developed in [106].

The black curve shown in Fig. 3.3 represents the predicted muon flux (in case of a flat overburden) from Mei and Hime [106]. The function that describes the black curve is:

$$I_\mu(h_0) = 67.97 \cdot 10^{-6} \cdot e^{\frac{-h_0}{0.285}} + 2.071 \cdot 10^{-6} \cdot e^{\frac{-h_0}{0.698}} \ , \tag{3.1}$$

where h_0 is expressed in km.w.e. and $I_\mu(h_0)$ is expressed in units of cm^{-2} s^{-1}.

Other measurements [139]-[146] and parametrizations [106, 146, 118] [147]-[150] to predict the muon flux together with its spectral shape are available. However, due to the complexity of these calculations, MC simulations [106, 132, 151, 152] were carried out to have more detailed descriptions of the muon fluxes and their spectra. In general, concerning muons, there is good agreement between data and MC [106, 153, 132].

It is worth to mention that also high-energy neutrinos can produce high-energy muons in deep underground cavities. Therefore, the effect of these neutrino-induced muons can

[1]The depth (h_0) corresponding to a certain muon flux under the assumption of a flat overburden.

Site	Total μ-flux [cm^{-2} s^{-1}]		Depth [km.w.e]
Homestake	$\approx 5 \cdot 10^{-6}$	[154]	0.71
WIPP	$(4.77 \pm 0.09) \cdot 10^{-7}$	[155]	1.59
Soudan	$(2.0 \pm 0.2) \cdot 10^{-7}$	[156]	1.95
Kamioka	$(1.58 \pm 0.21) \cdot 10^{-7}$	[157]	2.05
Boulby	$(4.09 \pm 0.15) \cdot 10^{-8}$	[158]	2.81
Gran Sasso	$(3.22 \pm 0.2) \cdot 10^{-8}$	[159]	2.96
Modane	$(5.47 \pm 0.1) \cdot 10^{-9}$	[160]	4.15
Sudbury	$(3.77 \pm 0.41) \cdot 10^{-10}$	[161]	6.01
CJPL	$(2.0 \pm 0.4) \cdot 10^{-10}$	[138]	6.72

Table 3.1: Total muon flux measurements at different underground sites [154] [155]-[138]. For each site, the equivalent vertical depth relative to a flat overburden is also reported.

contribute to the overall muon-induced background. Figure 3.4 shows the calculated contribution of neutrino-induced muons (shaded area) to the vertical muon total intensity as a function of depth. At the depth of CJPL, three or four of the 60 muons observed per

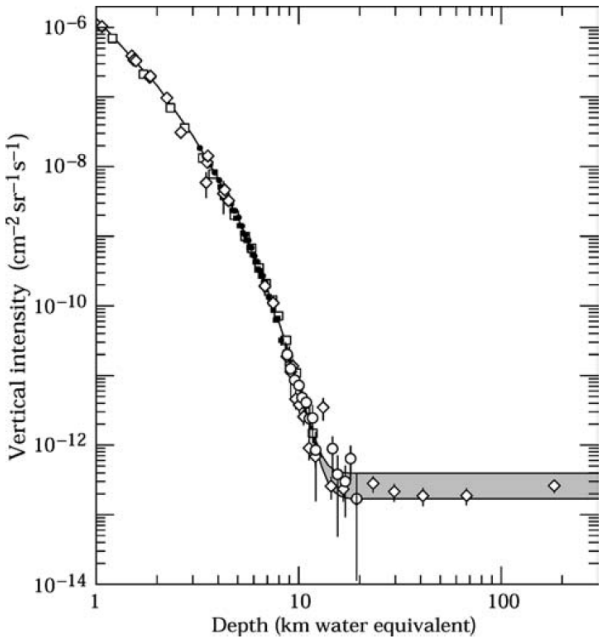

Figure 3.4: Vertical muon intensity as a function of depth. Measured values [160, 162, 146, 163, 164] are plotted together with the neutrino-induced muons of energy higher than 2 GeV. Figure taken from [165].

year are expected to originate from neutrinos.

3.3 Muon-Induced Neutrons

The current situation regarding muon-induced neutrons is controversial. The controversial quantities are the neutron yield, the neutron energy spectrum and the neutron multiplicity. In the literature, calculations [166]-[170] can be found, which are in disagreement, and experimental results [169, 171, 172, 173, 174, 175, 176], which are not always consistent between each other or with calculations. Several MC studies were performed in order to further investigate these unresolved issues [177, 106, 119, 132, 178, 179, 134, 180, 181, 182]. The neutron energy spectra and neutron multiplicities are the least understood quantities and thus are still under debate. The neutron yield as a function of the muon energy is now better understood [134, 181, 183], however, some discrepancies between MC and data are still present. A selection of results obtained by MC studies are discussed in the following. In particular, the individual processes which contribute to muon-induced neutron yield are discussed.

3.3.1 Physics Processes

The main physics processes that contribute to the production of muon-induced neutrons are:

- photonuclear disintegration;
- muon spallation[2];
- hadron spallation;
- muon capture;
- processes initiated by neutrons produced by any of the above.

Photonuclear disintegration

This process refers to the interaction of a high-energy gamma with an atomic nucleus ($\gamma \rightarrow$ N). When such an interaction occurs, the nucleus enters into an exited state, with subsequent emission of nucleons. High-energy muons can produce high-energy gammas through Bremsstrahlung when traversing matter. The gammas will produce electromagnetic showers. The primary or any secondary real gamma has a certain probability to interact with a nucleus through photonuclear disintegration and thus produce neutrons. Measurements and calculations of the photonuclear cross section for different nuclear targets were published [184, 185, 186, 187, 188, 189, 190].

[2]Spallation refers to any process that leads to the fragmentation of the target nucleus.

Muon spallation

Muon spallation refers to the direct interaction between the muon and the target nucleus ($\mu \rightarrow$ N). This inelastic scattering can be explained via the exchange of a virtual photon between the muon and the nucleus, see Fig. 3.5. For high muon energies, also Z-boson exchange can contribute, as well as W-boson exchange. Nuclear fragments, including neutrons, emerge as a result of these neutral current (NC) and charged current (CC) deep inelastic scattering (DIS) processes. At high energies, DIS is well understood. At low

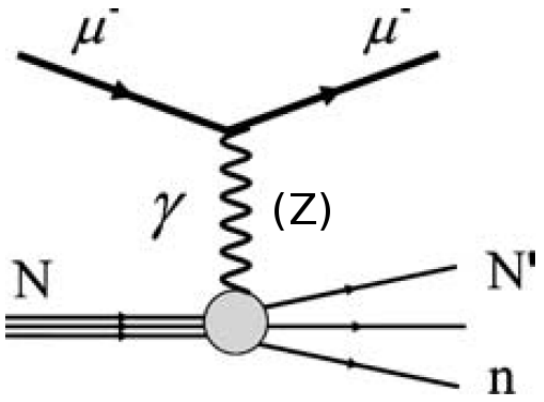

Figure 3.5: Feynman diagram of muon scattering off nucleus via the exchange of a virtual photon or Z-boson.

energies, however, muon spallation is one of the least understood processes concerning muons interactions. Nevertheless, there are theoretical models that allow to calculate the muon spallation cross-section $\sigma_{\mu N}$ by relating it to the real photonuclear cross-section $\sigma_{\gamma N}$ via the following equation:

$$\sigma_{\mu N} = \int dE_\gamma \frac{n_\gamma(E_\gamma)\sigma_{\gamma N}(E_\gamma)}{E_\gamma} \tag{3.2}$$

where $n_\gamma(E_\gamma)$ is the virtual photon energy spectrum. However, this method, called *equivalent photon approximation* [191, 192, 193], breaks down at very low energies when the virtuality of the photon is comparable to the muon momentum.

Hadron spallation

This category includes all the spallation processes initiated by energetic hadrons produced within the muon-induced hadronic shower. When a hadronic shower develops inside a medium, hadronic particles like protons, pions and neutrons are produced. These particles can themselves interact with the nuclei inducing further spallation processes which contribute to the muon-induced neutron yield [119, 181, 194, 135].

Muon capture

When a negative muon is slowed down inside a medium, it can be captured by a nucleus due to its Coulomb field. This leads to the formation of a *muonic atom*. The captured muon is believed to rapidly relax to the *1s* state of muonic atom. Once the muon is in the *1s* state, it either decays into an electron and two neutrinos or undergoes nuclear capture via the semi-leptonic weak process (see Fig. 3.6)

$$\mu^- + N(A, Z) \rightarrow N(Z - 1, A) + \nu_\mu \ , \tag{3.3}$$

in which a proton is transformed into a neutron inside the nucleus. This process, which is the muonic analogous to electron capture, is mediated by a virtual W boson. The re-

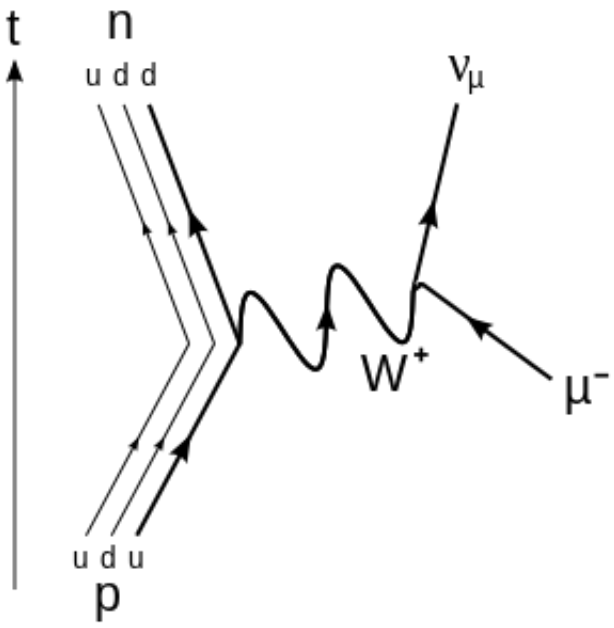

Figure 3.6: Feynman diagram of the muon capture.

sulting nucleus is in an excited state and radiates particles such as gammas and neutrons (*radiative muon capture* [195, 196]), contributing to the total muon-induced background. Many studies were carried out in the past about this process; details can be found in [197, 198, 199, 200, 201, 202, 203, 204, 205] and references therein. The diagram depicted in Fig. 3.6 also contributes to the spallation processes, when due to the high four-momentum-transfer no muonic atom can be formed. In general, the negative muon capture process is relevant only for shallow sites (<100 m w.e.).

3.3.2 Neutron Yield

The neutron yield, Y_n, is defined as the number of neutrons produced per muon per thickness of the target material. In the literature, the definition of Y_n is, however, ambiguous and the comparison between results of different experiments is thus difficult [135, 206], especially because Y_n is very sensitive to the geometry of the experiment, particularly for thin targets. Reports on measurements and MC studies are abundant in the literature [178, 119, 194, 135, 132, 173, 189, 174, 207, 208, 128, 181, 134, 172, 183, 209, 171, 106]. Simulations indicate that most of the neutrons come from the muon-induced electromagnetic and hadronic showers, rather than from direct muon spallation, for which the contribution decreases with increasing muon energy. The higher the muon energy, the higher the contribution of hadronic cascades and secondary processes in general. These results were, recently, confirmed by simulations performed by Horn [194] and Kluck [135]. It should be noted that, since high-energy gammas can produce neutrons via photonuclear disintegration, they could also be an important background source for low-background experiments. An important feature of electromagnetic and hadronic showers is that they reach equilibrium after a certain depth. That means that, once they have fully developed in the medium, the fractions of the different types of particles produced in the showers remain constant. This feature is very useful when performing simulations to predict the particle fluxes in deep underground sites and in general to study the muon-induced particle production in a certain target material. Many comparative studies between data and MC simulations, both with GEANT4 and FLUKA, were performed in the last 15 years [178, 177, 182, 119, 106, 181, 180, 194, 135].
In general, it is possible to state that decent agreement between data and simulations is found concerning the behavior of the neutron yield as a function of the muon energy. However, there are features which are not properly reproduced by the simulations. In addition, different simulation packages do not fully agree. Further studies and improvements are therefore needed.
A selection of relevant simulations concerning the neutron yield is listed in chronological order:

- Wang *et al.* [178] have performed simulations for liquid scintillators with FLUKA [130] and have found an exponential behavior of the neutron yield (Y_n) as a function of the muon energy (E_μ) in reasonable agreement with data.

- Kudryavtsev *et al.* [177] have confirmed the results of Wang *et al.*. However a 10 to 15% underproduction of neutrons by FLUKA compared to data was found. For thin[3] targets, a decent agreement between FLUKA simulations and data was found [210].

[3]Thin targets were probed by the CERN experiment NA55 [210] with 190 GeV muons in order to measure the fast neutron yield due to direct muon spallation. Thin targets were chosen in order to minimize the development of electromagnetic and hadronic cascades, which otherwise would have compromised the possibility to study the direct muon spallation.

- Wulandari *et al.* [182] found an agreement within a factor ≈2 between FLUKA and GEANT4 [131].

- Araújo *et al.* [119] performed multiple comparisons between FLUKA, GEANT4 and experimental data. At high muon energies (E>100 GeV) and for thick targets, GEANT4 was found to produce ≈30% less neutrons than FLUKA. In addition, an underproduction of a factor 2 by GEANT4 with respect to experimental data was found for thick low-Z materials. However, at low muon energies, GEANT4 produces more neutron than FLUKA. The contribution of the electromagnetic and hadronic cascades to the neutron yield is different for GEANT4 and FLUKA. In general, for thick low-Z materials, a factor ≈2 difference between GEANT4 and FLUKA was found. Concerning thin targets, the predictions from both simulation packages were found to be totally inconsistent with the NA55 [210] data; both of them seriously underestimate the neutron yield.

- Mei and Heime [106] have found a ≈35% deficit for FLUKA predictions compared to experimental data for thick liquid scintillators. A too low neutron multiplicity was claimed to be (partially) responsible for that deficit.

- Marino *et al.* [180] performed simulation studies of both neutron yield and neutron transport using GEANT4. They compared their results with the experimental data of NA55 [210] and its FLUKA predictions done by Araújo *et al.* [119]. GEANT4 predicted a too low neutron production by factors that range between 2.1 and 5.9, increasing with the Z of the target material. This substantial underproduction could not be explained. The predictions of the angular distribution were similar for GEANT4 and FLUKA and were both in clear disagreement with the NA55 data. In terms of neutron transport, the GEANT4 results were compared to the data measured at SLAC by Taniguchi *et al.* [211] and its FLUKA simulation [212]. A significantly higher attenuation power than FLUKA, which was in good agreement with the data, was found for GEANT4.

- Different results were obtained by Lindote *et al.* [181, 213] while studying the neutron yield in lead using a liquid scintillator detector. They have found an overproduction (factor ∼1.8) of neutrons in lead of GEANT4 compared to experimental data. Furthermore, FLUKA was found to produce twice the neutrons in lead with respect to GEANT4. This overproduction was explained as an overproduction of neutrons in the hadronic processes compared to GEANT4. These results are clearly in contrast with previous studies. In summary, the heavier the target material, the bigger the discrepancy between data and MC, but also between GEANT4 and FLUKA.

- Abe *et al.* [128] found a systematic underproduction of neutrons in liquid scintillators of both FLUKA and GEANT4 compared to data. GEANT4 was also compared with experimental data over a wide range of muon energies and a too low neutron yield was observed. Furthermore, they found that FLUKA v. 2006-3b produces ≈10% less neutrons than previous studies [106, 119, 178, 177] reported for older versions.

- similar results were obtained by Persiani *et al.* [183] using GEANT4 (≈35% lower neutron yield than measured with the LVD detector).
- According to Empl *et al.* [132], also a recent version of FLUKA (v. 2011.2) underestimates the neutron yield in the liquid scintillator of Borexino [209] by a factor ≈1.2. This discrepancy was explained as a miscalculation of the neutron multiplicity, especially at low values. The reasons for that seems to be related to an underestimate in FLUKA of the number of muons that produce at least one neutron (≈30% less than Borexino data).

The situation is therefore still unclear, especially for heavy materials which are very important for low-background experiments. A better understanding and modeling of the physics processes related to neutron yield and transport is needed. The differences between the simulation packages are mainly due to the different physics models employed in the various simulation packages (see for example Refs. [119, 106, 178, 181, 180, 177]). The need for dedicated data is also obvious.

3.3.3 Neutron Energy Spectrum

The situation regarding the underground neutron spectra is even more controversial than that of the neutron yield. The reason for this controversy in the literature lies experimentally in the complexity of measuring neutron energies with accuracy over a wide range. From the simulations point of view, the lack of detailed models to properly describe all the complex physics processes involved in neutron production is responsible for it. Several measurements [210, 173, 214, 172, 175] and simulation studies [178, 106, 180, 177, 119, 181, 182, 215, 96] disagree on many aspects.

The spectrum of muon-induced neutrons is harder than the spectrum of neutrons due to environmental radioactivity. As already shown in Fig. 3.2, it extends to hundreds of GeV. Simulation studies with both GEANT4 and FLUKA were carried out and were compared with experimental data ([180, 181, 119]). The various processes contributing to the neutron spectrum were also simulated separately [181, 194].
Different measurements and models indicate that the neutron spectra in underground cavities must follow a power law [178], however no agreement on the spectral index has been reached so far.

3.3.4 Cosmogenic Activation

As already mentioned, neutron and muon interactions with the experimental setup and its surrounding can produce long-lived metastable isotopes (*cosmogenic activation*). As their half-lifes can be long compared to the window which is vetoed after a muon is identified, this is a problem even for vetoed muons. The background resulting from their decays is an irreducible background for low-background experiments [106, 128, 209]. The production rate of these isotopes is strongly dependent on the target materials. As an example, two of the most problematic isotopes for NDBD experiments based on Germanium detectors, like GERDA [6] and MAJORANA [45], are ^{77}Ge and ^{77m}Ge. These isotopes are problematic because their Q values, 2.7 MeV and 2.8 MeV respectively, exceed the expected Q value of NDBD of ^{76}Ge (2.039 MeV) and therefore increase the background in the region of interest (ROI) [216].

Chapter 4

MINIDEX

Monte Carlo (MC) methods are typically used to reproduce and predict the performance of an experiment. While the MC capability of reproducing the data is important to understand and interpret the results of an experiment, the ability to make predictions is also very important for the design of an experiment. The availability of a reliable MC plays, therefore, a crucial role when performing an experiment. The MINIDEX apparatus was designed and built in order to provide data to validate the MC framework (MaGe [217], GEANT4 [131]) used to design future NDBD experiments.
The goal of MINIDEX is to provide reliable data on the production of neutrons in different high-Z materials. Only data can help to improve the MC programs. The GEANT4 collaboration [218] constantly implements improved physics processes for neutron and hadron interactions in general, see for example Table 4 of Ref. [134]. Only data can validate these improvements.

In this chapter, the MINIDEX apparatus is presented. First, the basic concept and the experimental setup are described in detail. Then the analysis strategy and the results obtained from MINIDEX run I are presented. A detailed description of the simulations is presented in the next chapter.

4.1 The Working Principle

In the previous chapter, a number of measurements and simulation studies concerning muon-induced neutron yield in low-Z materials such as liquid scintillators were mentioned. The advantage of liquid scintillators is that the target and the detector are identical. Studying muon-induced neutron yield in high-Z materials, and in general in materials which cannot be instrumented, is more challenging. When target and detector are separated, a series of extra sources of systematic uncertainty as well as geometrical detection inefficiencies are introduced.

The detection strategy chosen for the MINIDEX apparatus is the following:

- muons interact with high-Z target;
- neutrons emerging from the high-Z volume are thermalized in water and eventually captured by an hydrogen nucleus;
- the 2.2 MeV gammas emitted after the capture are detected in high-purity germanium (HPGe) detectors within a time window after the muon passed through the target;
- the background is measured outside the time window opened by the passage of muons through the target.

Figure 4.1 depicts the MINIDEX working principle. Indirect neutron detection through a

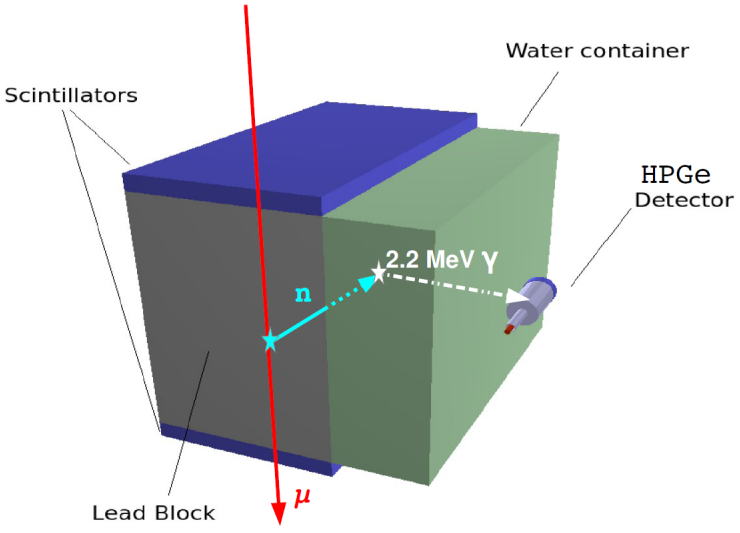

Figure 4.1: Schematic of the MINIDEX working principle. Muon-induced neutrons are measured indirectly via their conversion into gamma rays. Scintillators are used to identify the muons.

thermal capture process on a selected isotope with subsequent gamma ray emission is a

standard technique used to detect neutron interactions [134, 135].
Plastic scintillator panels are used to identify muons passing through the target while, independently, the HPGe detector is used to measure the 2.2 MeV gammas. In this approach, there are no inefficiencies due to time resolution, which can be a problem for experiments using the same detector to identify the muon and the neutrons. Neutrons, observed through a 2.2 MeV gamma, are associated with a passing muon for a certain time window after the muon passed. The accidental rate is measured outside a safe time window.
The target material chosen for the first phase of MINIDEX is lead. The main reason for this choice was that lead is one of the most commonly used passive shielding materials for deep underground experiments [134, 45, 51, 105]. Hence, a good knowledge of the neutron yield in lead is needed to plan future low-background experiments. Moreover, as previously mentioned, the available data could not be consistently described by simulations. Because of its high Z, and thus high A, lead has a high muon-induced neutron yield. This high neutron yield is desirable for MINIDEX, as the efficiency of its indirect measure of neutrons is expected to be low.
Elements typically used to detect neutrons via thermal capture are hydrogen (H), gadolinium (Gd), boron (B) and helium (He). The neutron capture in Gd produces about 3 to 4 gammas, with a summed energy of ≈8 MeV. Since in MINIDEX the gamma detector and the medium that actually converts neutrons into gammas are separate components, the use of gadolinium-doped materials to convert neutrons into gammas are disfavored, because the probability to detect all the emitted gammas would be extremely low for geometric reasons.
Boron is also disfavored due to the low-energy (≈477 keV) of the emitted gammas. This would result in a low signal-to-background (S/B) ratio in the region of interest in the germanium detector spectrum due to the high level of environmental background-gammas around 480 keV.
Finally, a helium-based medium is not suitable, because gamma rays are not produced in the thermal captures of neutrons by He. When a neutron is captured by a nucleus of ^{3}He, a proton and a ^{3}H are produced, but no gammas. Furthermore, the supply of ^{3}He is very limited.
Water has clear advantages over these materials, despite the relatively low thermal neutron capture cross-section of hydrogen [219]. Above all, the energy of the emitted gamma (≈2.2 MeV) is high enough to be above most of the environmental gamma-background and still low enough to ensure a good full absorption probability ($O(10)\%$) in a ≈ 7 x 7 x 7 cm^3 germanium crystal. Moreover, water is very accessible, cheap, and is easier to purify than other materials with high H content such as polyethylene.

4.2 Optimization of Geometry

During the planning phase of MINIDEX, MC simulations were used to optimize the thickness of the water layer to be placed between the HPGe detector and the target material, i.e. lead, within the constraints given by the dimensions of the available equipment and the availability of lead. These studies were performed with MaGe [217], a GEANT4-based simulation package developed and maintained by both the GERDA and MAJORANA collaborations. The optimization of the water thickness was done with a simple geometry. A parallelepiped of lead, 100 x 50 x T_{Pb} cm^3 with variable thickness (T_{Pb}), was placed next to a water volume with same cross section and a variable thickness (T_{H_2O}) as well. Figure 4.2 shows a sketch of the simulated geometry. Positive vertical muons were shot towards the

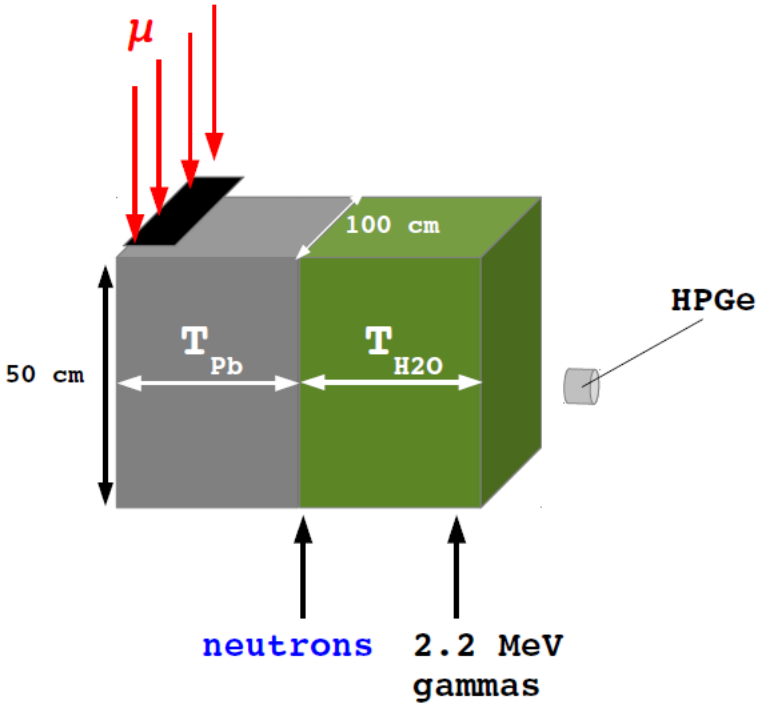

Figure 4.2: Schematic of the simulated geometry for the optimization of the water thickness.

top of the lead slab as shown in Fig. 4.2. The spectrum of the incoming muons is shown in Fig. 4.3. It corresponds to the muon energy spectrum at sea level measured by Rastin et. al. [220]. Whenever a particle produced in the simulation crossed the boundary between one volume to another, for example between the lead and the water or between the water and the surrounding volume, it was recorded with all its characteristics such as particle type, kinetic energy, position, momentum and time after the beginning of the simulated event. This output configuration is referred to as *FLUX output scheme* in the rest of this text. Table 4.1 summarizes the relevant simulation parameters.

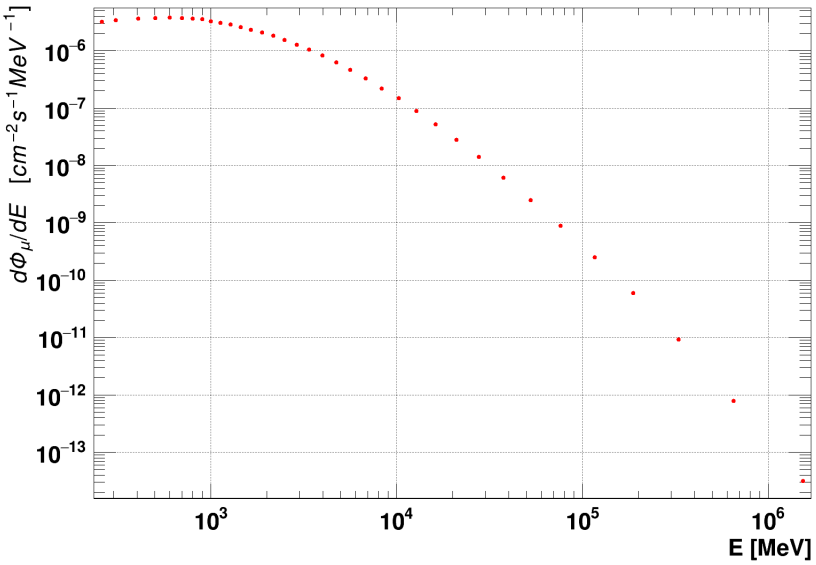

Figure 4.3: Incoming muon spectrum [220] used for the optimization of the water thickness.

GEANT4 version	9.6.2
Particle Type Injected	μ^+
Number of Events Generated	$9.5 \cdot 10^6$ (for each T_{H_2O} and T_{Pb})
Generation Plane	100 x 5 cm^2
Energy Spectrum	YES [220]
Angular Distribution	NO
Output Scheme	*FLUX*

Table 4.1: Information on the simulation done for the optimization of the water thickness.

The ratio between the number of 2.2 MeV gammas exiting the water slab (towards the HPGe) and the number of neutrons exiting the lead surface (towards the water) was calculated for different values of T_{H_2O} and T_{Pb}. As shown in Fig. 4.4, the ratio is maximal at around 10 cm of water thickness. Similar results were obtained when the muons were shot horizontally (from left to right in the reference frame of Fig. 4.2) to the lead slab. The results of these simple studies were taken into account when MINIDEX was designed in its final configuration. The simple approach with slabs was replaced by a closed-volume design to improve geometrical acceptance and shield against environmental radiation.

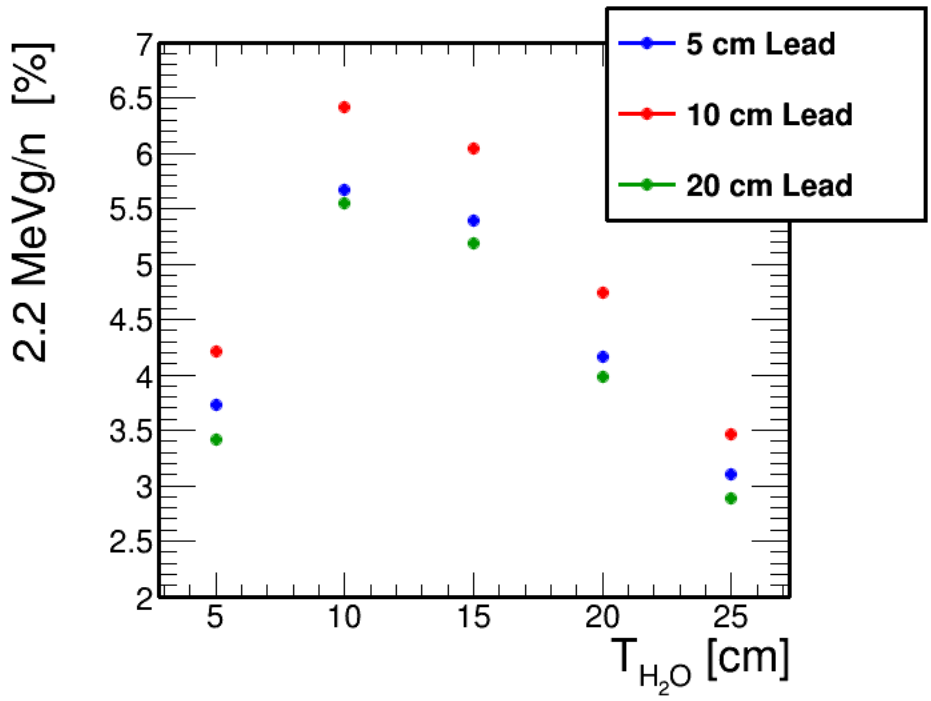

Figure 4.4: Ratio between the number of 2.2 MeV gammas exiting the water slab (towards the HPGe) and the number of neutrons exiting the lead surface (towards the water) as a function of the water thickness T_{H_2O}. Three different values of the lead thickness T_{Pb} were investigated.

4.3 The MINIDEX Apparatus

4.3.1 Geometry

The Muon-Induced Neutron Indirect-Detection EXperiment is a compact apparatus with a foot-print of 65 x 75 cm^2 and a height of 60.5 cm. It consists of a lead castle with outer dimensions of 65 x 75 x 50.5 cm^3. On top of and below the lead castle, 5 cm thick plastic scintillator panels are placed exactly covering the lead surfaces. These two plastic scintillator panels are used to identify muons that pass through the setup. The outer view of the MINIDEX apparatus is depicted in Fig. 4.5. As can be seen in Fig. 4.6, a rectangular

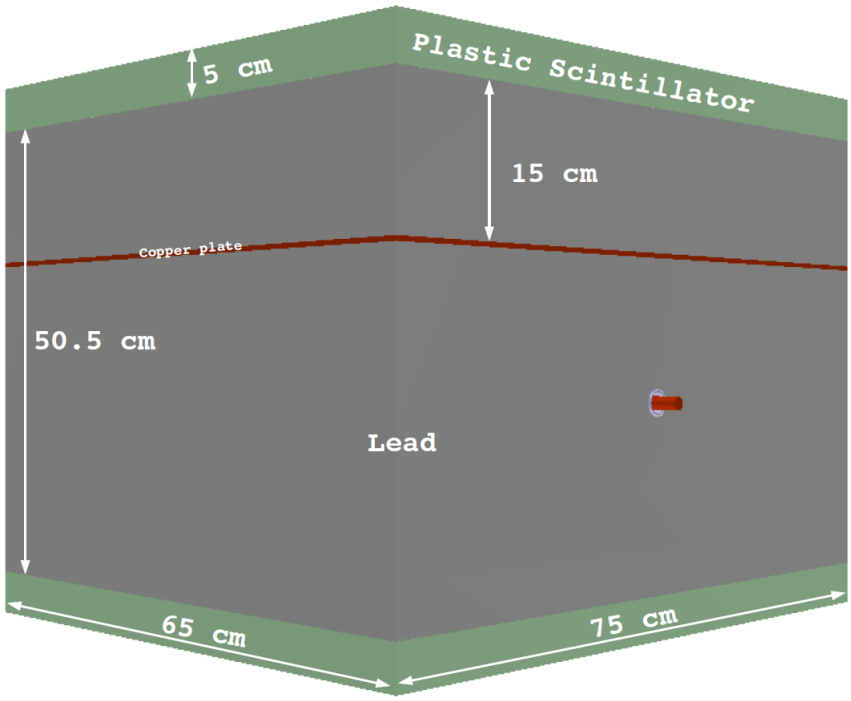

Figure 4.5: Schematic external view of the MINIDEX apparatus.

water container (outer dimensions: 35 x 55 x 30 cm^3) is housed inside the lead castle. The water container has a central hole which runs through the whole length of the container. It has a length of 55 cm, is 13 cm wide and 8 cm high. In this hole, two HPGe detectors are placed symmetrically with respect to the center of the water container. The water container is made of plastic ($C_{10}H_8O_4$) and has a wall-thickness of 1 cm.

The water layer that separates the lead from the HPGe detectors is at least 9 cm thick in every direction. This is close to the optimal value as discussed in Sec. 4.2. The water layer is only missing behind the HPGe detectors. The water container is fully covered by lead, as shown in Fig. 4.6 and Fig. 4.7. As support for the top layer of lead, there is a

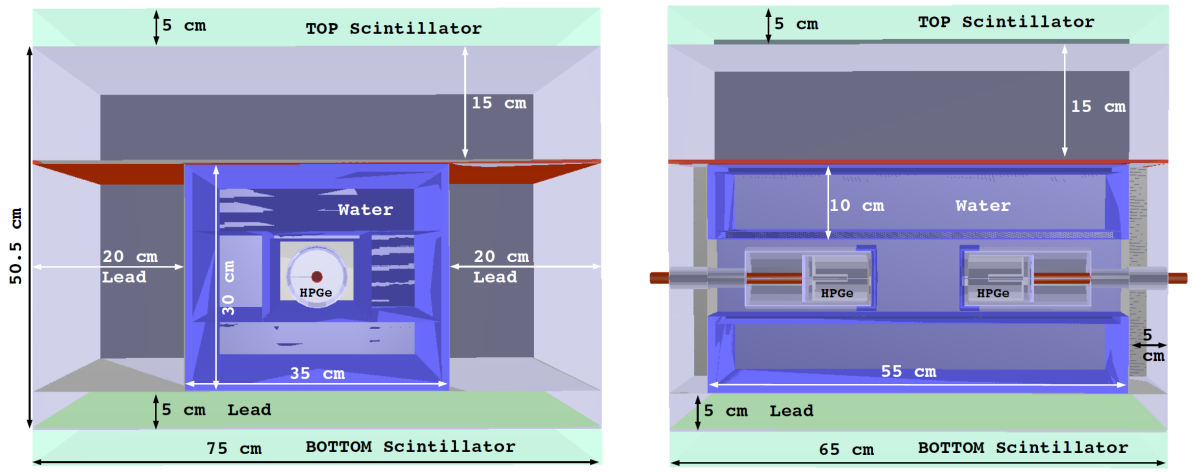

Figure 4.6: Schematic central cuts through MINIDEX as seen from the front (left) and the side (right).

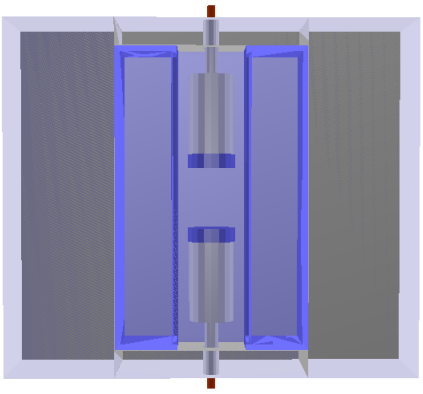

Figure 4.7: Schematic central cut through as seen from the top of the MINIDEX apparatus.

0.5 cm thick copper plate. This copper plate avoids any weight load on the plastic water container. Copper was chosen due to its relative low weight compared to its strength. Furthermore, copper is a common material used in low-background experiments.
This configuration is referred as MINIDEX run I.
Photos of the MINIDEX setup during construction are shown in Fig. 4.8.

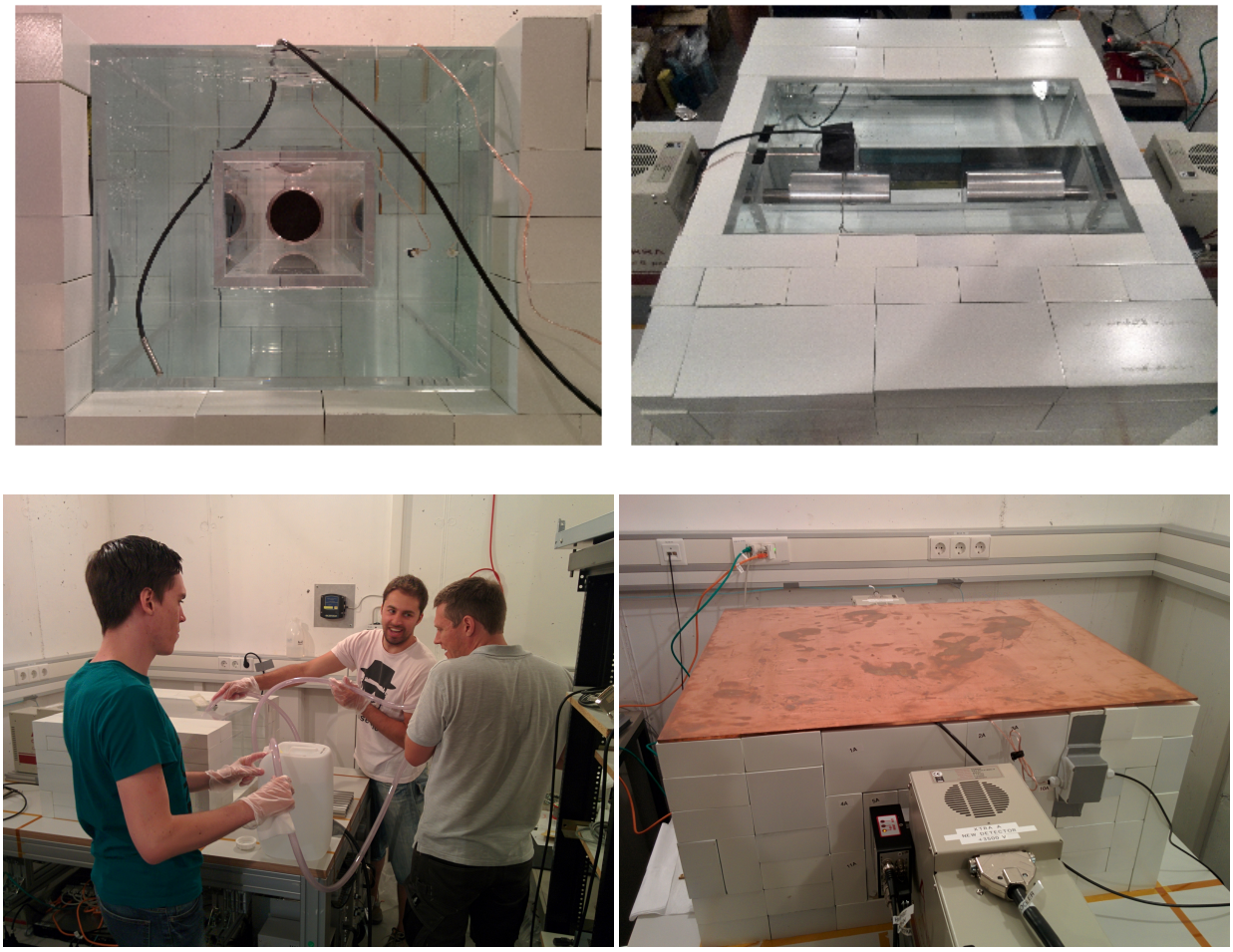

Figure 4.8: Top: Front (left) and top (right) view of the inside of MINIDEX. Bottom: filling of the water tank (left) and view with the copper plate on top (right).

4.3.2 Detectors

The MINIDEX run I is a simple setup with only four detectors to read out: two plastic scintillator panels and two HPGe detectors.
The two scintillator panels, produced by Saint-Gobain Crystals [221], are made of BC-408 (Polyvinyltoluene, $C_{10}H_{11}$), with a density of 1.032 g/cm^3. The wavelength of maximum emission is $\approx$ 425 nm.
As previously mentioned, they are 65 x 75 x 5 cm^3 big and are placed above and below the lead castle. They cover the entire top and bottom lead surface. Their efficiency is essential to identify muons that cross the setup.
As shown in Fig. 4.9, both the Photomultiplier Tube (PMT) and the PMT HV base (model HV2520AN) are embedded inside the panel volume and no wavelength shifters are used to collect the light of the scintillators onto the PMT photocathode. In this way, possible inefficiencies due do the wavelength shifters are avoided. As a draw-back, not all the panel surface is active. The PMT is a 30 mm diameter end window phototube (model 9900B), produced by ET Enterprises [222], with sensitive sidewalls to allow for wide angle light detection. The active diameter is 25 mm wide and the spectral range goes from 280 nm to 680 nm, with a peak quantum efficiency of 26% at around 400 nm. The tube housing the multiplication dynodes is $\approx$9 cm long. The scintillator panels play

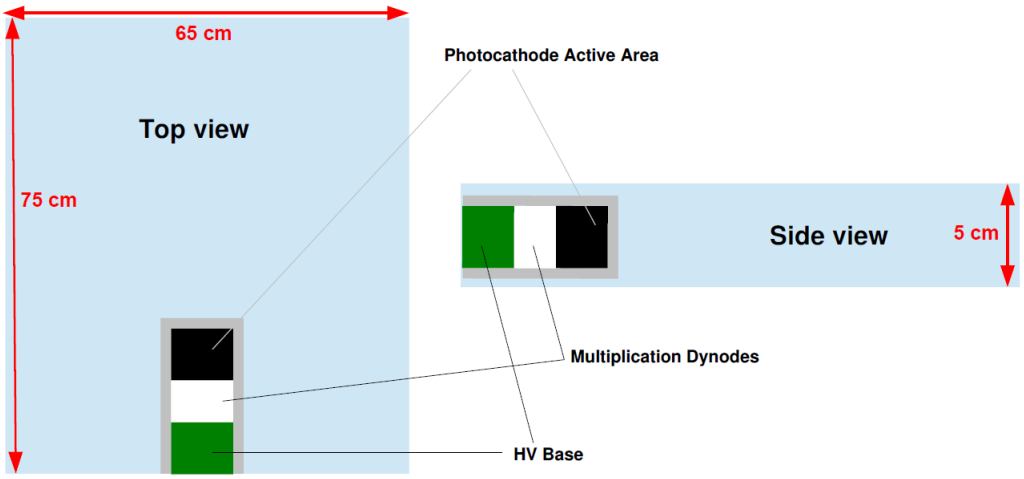

Figure 4.9: Schematic view of a scintillator panel as employed in the MINIDEX setup. The PMT itself together with the PMT HV base are housed inside the volume of the scintillator panel.

a crucial role in MINIDEX because the identification of muons is a key prerequisite to identify muon-induced events. Their efficiency was tested during the *commissioning phase* of MINIDEX, which took place in the Tübingen Shallow Underground Laboratory (TSUL) where MINIDEX was installed.

Scintillator Efficiencies

The overall detection efficiency (ϵ) for muons was measured during the commissioning phase of MINIDEX for both scintillators. These efficiencies are needed to correct the number of 2.2 MeV gammas originating from muon-induced neutrons in the setup at the analysis stage. In order to measure ϵ, each scintillator was placed between two other scintillators used to trigger. The scintillator directly on top is called A, the scintillator under study is called B and the one underneath a 2.5 cm thick lead layer, on which A and B where placed, is called C. The lead was inserted to reduce random coincidences and to ensure that a coincidence between A and C is really caused by a muon passing through both. The coincidence window used was a few tens of ns wide. The efficiency ϵ_B of the scintillator under study is than determined as:

$$\epsilon_B = \frac{S_{ABC}}{S_{AC}} \tag{4.1}$$

where S_{AC} is the number of coincidences between panel A and C (trigger condition) and S_{ABC} is the number of triple coincidences between A, B and C. No energy cuts on the trigger scintillators were made. The TOP and the BOTTOM scintillators of MINIDEX where independently placed in position B. In Tab. 4.2 the results of these measurements are reported. These efficiencies are unexpectedly low for this kind of plastic scintillators.

Scintillator	**HV [V]**	ϵ_B [%]
TOP	1000	86.53 ± 0.10
BOTTOM	801	92.69 ± 0.15

Table 4.2: Efficiencies and operation voltages for the TOP and the BOTTOM scintillators of MINIDEX.

The reasons for the inefficiencies are that having the PMTs embedded inside the panel produces geometrical inefficiency. This is probably because the PMT sidewalls were less sensitive than expected. A detailed investigation revealed that the PMTs were not properly optically coupled. The panels were finally replaced by the company and replaced for the second phase of the experiment: MINIDEX run II.
It should be noted that the uncertainties listed in Tab. 4.2, which appear symmetric, are in principle asymmetric and were evaluated using the Bayesian approach described by M. Paterno [223]. The uncertainties were evaluated as the smallest interval with a probability content of 68% of the posterior distribution $P(\epsilon_B|S_{ABC}, S_{AC})$ of the probability that the true efficiency is between ϵ_B and $d\epsilon_B$. Under the assumption that this is a binomial process, $P(\epsilon_B|S_{ABC}, S_{AC})$ is expressed using the Bayes' Theorem [224] as:

$$P(\epsilon_B|S_{ABC}, S_{AC}) = \frac{P(S_{ABC}|\epsilon_b, S_{AC}) \cdot P(\epsilon_b|S_{AC})}{Z_N} \ , \tag{4.2}$$

where:

$$P(S_{ABC}|\epsilon_b, S_{AC}) = \frac{S_{AC}!}{S_{ABC}!(S_{AC}-S_{ABC})!} \cdot {\epsilon_B}^{S_{ABC}}(1-\epsilon_B)^{(S_{AC}-S_{ABC})} \tag{4.3}$$

is the so called *likelihood*, i.e. the probability to observe S_{ABC} given that the true efficiency is ϵ_B.
$P(\epsilon_b|S_{AC})$ in Eq. 4.2 is the prior probability distribution of the true value of ϵ_B, which is assumed to be flat, i.e. having a constant positive value between 0 and 1. The denominator of Eq. 4.2, Z_N, is the normalization factor, often called *evidence*.

Germanium Detectors

The two HPGe detectors used are commercial Extended Range (XtRa) coaxial germanium detectors, produced by CANBERRA [225]. These kind of detectors are commonly used for gamma spectroscopy due to their excellent energy resolution (nominal resolution ≈2 keV at 1.3 MeV). These two p-type detectors are operated at +3000 V and +3500 V on the n^+ contact, respectively. As shown in Fig. 4.10, these detectors are manufactured from a cylindrical germanium crystals with a radius of 3.5 cm, a length of ≈7 cm and a central bore hole with a length of 4.5 cm. The crystals are housed in cylindrical vacuum chambers made of aluminum. Both germanium detectors are electrically cooled. The detectors are in

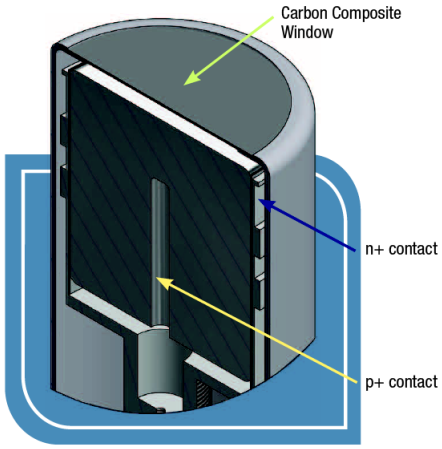

Figure 4.10: Schematic view of a the XtRa HPGe detector. Taken from [226].

thermal contact with copper cooling fingers which extend beyond the lead castle where the electrical cooling units are placed. These components, but the electrical cooling units, are also shown in Fig. 4.6 right. Having electro-cooled germanium detectors makes MINIDEX a maintenance-free setup.

The lead castle is placed on top of an aluminum table (surface of $100 \times 150\,\mathrm{cm}^2$) suitable for heavy loads. A schematic view of the whole setup (table+MINIDEX) is shown in Fig. 4.11.

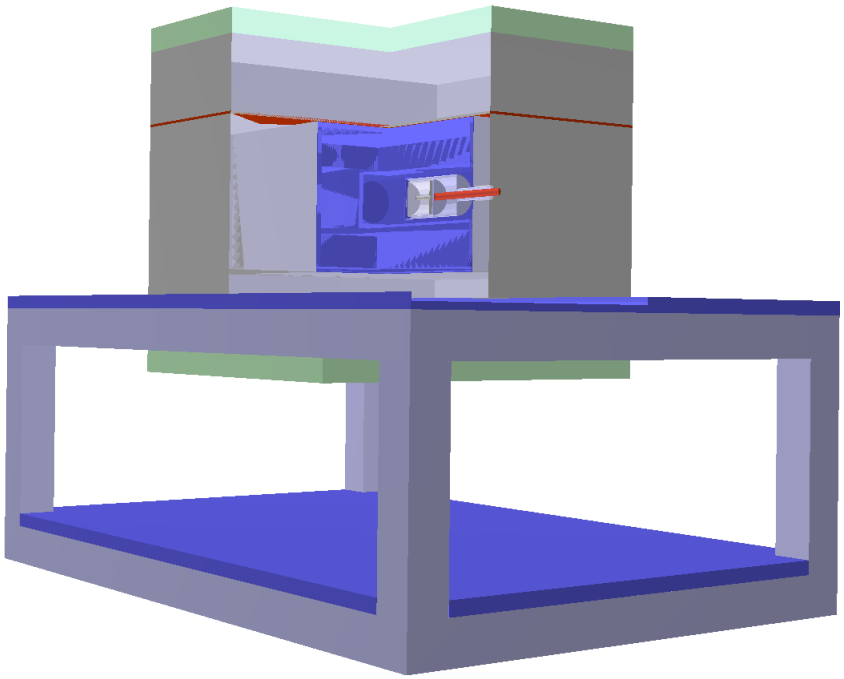

Figure 4.11: Schematic view of the whole setup: MINIDEX on top of its support table. The inside of the apparatus is also partially displayed.

The bottom scintillator is placed underneath the table top, supported by an aluminum structure. It is therefore a few centimeters below the bottom of the lead castle. The lower shelf of the table is used for the data acquisition system (DAQ) and all the electronic devices of MINIDEX.

4.3.3 DAQ and Electronics

The DAQ employed for MINIDEX is a 16 channel VME digitizer card, SIS3316-DT, produced by Struck Innovative System [227]. Each channel can be used independently from the others with a 250 MHz sampling rate. All channels are equipped with a 14 bit resolution ADC, and run in double bank mode to avoid dead time. The time information is distributed to the channels via an internal clock. All detector signals from MINIDEX are recorded independently without a shared trigger. The time correlation between events in different detectors is done offline in the data analysis. Data are written to and stored into a server (sysGen/Supermicro SYS-5018D-MTF [228]) which is placed directly next to the DAQ on the lower shelf of the supporting table.
A NIM crate, also placed on the lower shelf of the table, hosts a 2 channels HV power supply (iseg NHQ 206L), which provides the high voltage for the HPGe detectors, and two preamplifier power supplies for the front-end electronics of the HPGe detectors and for the scintillators. The whole system is being controlled remotely, with the help of a router, which provide access to every single device. To prevent damages to the HPGe from power cuts and to protect, in general, the system from noise due to the power line, MINIDEX is equipped with an Uninterruptible Power Supply, Online XSR3000 PSU.

The completely installed MINIDEX run I setup is shown in Fig. 4.12. This setup was

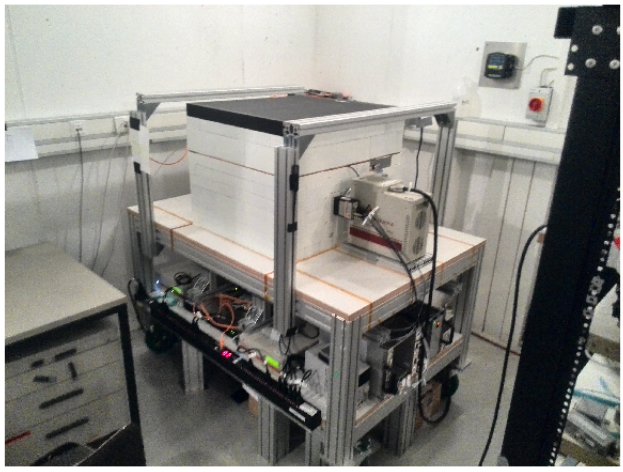

Figure 4.12: The MINIDEX run I setup completely installed in the Tübingen Shallow Underground Laboratory.

successfully installed in the Tübingen Shallow Underground Laboratory on July 15, 2015. Run I continued until January 19, 2016, when the construction and commissioning for MINIDEX run II began. An underground location was chosen for MINIDEX to drastically reduce the cosmogenic neutron flux which, at ground level, would represent a forbidding background source. The TSUL was chosen because it is shallow enough so that the in-

coming muon flux is high enough to have a good signal-to-background ratio. The nominal overburden of the TSUL corresponds to 16 m.w.e.

4.4 Online Monitoring and Detector Performances

The MINIDEX apparatus is being constantly monitored during operation. The energy spectra of the scintillators and the HPGe detectors, together with the temperature of the water and its level inside the tank, are recorded. The online monitoring[1] is available at *https://www.mpp.mpg.de/∼palermo/minidex-monitoring/* and a screenshot of it is shown in Fig. 4.13. The spectra of the HPGe detectors are shown in the bottom left, from which

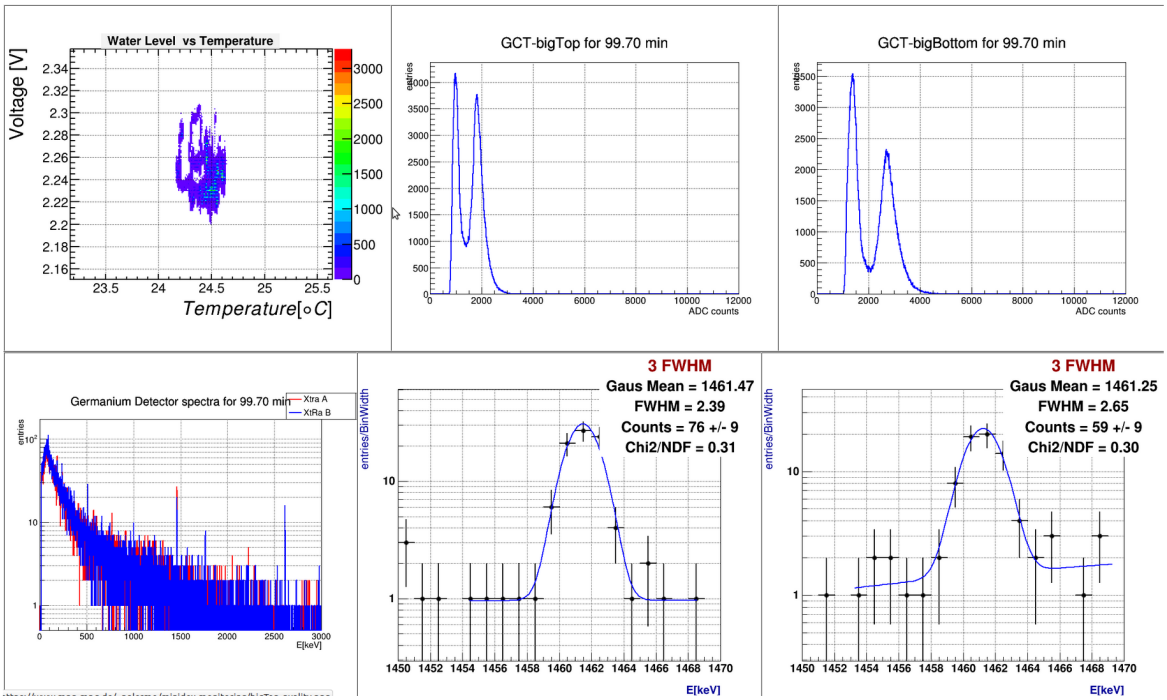

Figure 4.13: A screenshot of the online monitoring page during MINIDEX run I operation. Top left: water level vs water temperature. Top center and top right: uncalibrated spectrum for the TOP and the BOTTOM scintillator, respectively. Bottom left: HPGe spectra. Bottom center and bottom right: the fit of the ^{40}K peak for the two HPGe detectors.

the stability of the calibration factors can be inferred. The energy resolutions for both HPGe detectors at 1460 keV (^{40}K) are continuously measured by fitting the spectra in the

[1] A similar online monitoring was implemented for the GALATEA test-facility [229]. The monitoring has been extremely helpful for safe operation of such a delicate setup.

region around 1460 keV with a Gaussian plus a first order polynomial (see bottom center and right of Fig. 4.13).
Figure 4.14 shows the stability of the energy resolution at 1460 keV as expected from the summed energy spectra of the two HPGe detectors. Each point represents approximately two hours of data taking. The energy resolution was very stable.

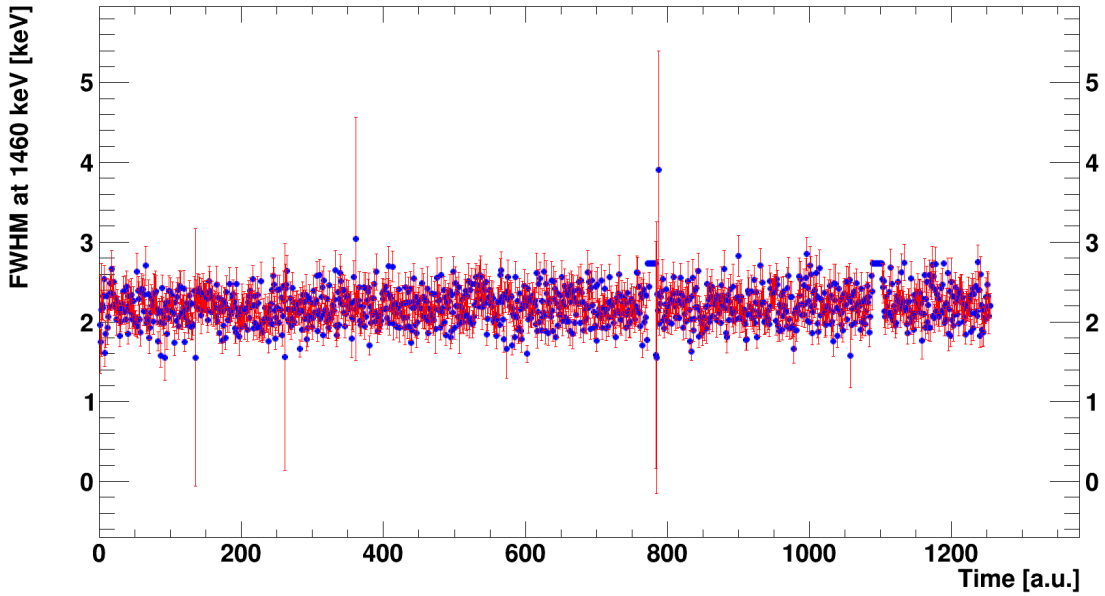

Figure 4.14: The energy resolution at 1460 keV of the summed spectra of the HPGe detectors vs time. Each point corresponds to approximately two hours of data taking. All data collected between the beginning of MINIDEX run I and November, 25, 2015 are included.

The temperature of the water was measured with a PT100 [230] temperature sensor placed inside the water tank. To measure the level of the water inside the tank, MINIDEX was equipped with a liquid level sensor probe, produced by Vegetronix [231] and commercially available. The stability of both temperature and water-level is demonstrated in Fig. 4.15 left and right, respectively. Both temperature and level are stable, not only over the period shown but for the entire data taking period. The water-level sensor was calibrated on site during the commissioning phase of MINIDEX. The signal produced is a voltage and, according to the calibration, a difference of 0.1 V voltage corresponds to a change in water-level of 1 mm.

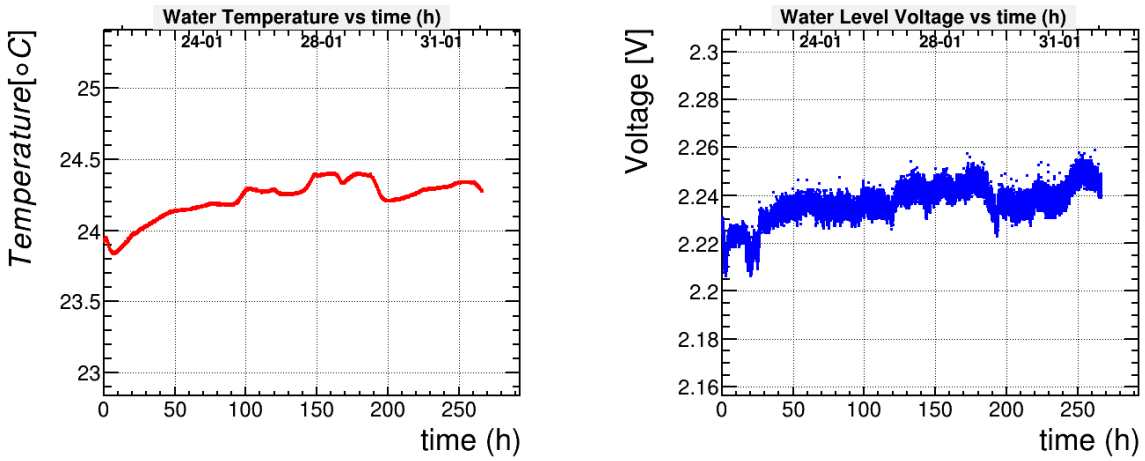

Figure 4.15: Left: Water temperature vs. time. Right: Water level, expressed in voltage, vs time.

4.5 A Simple Setup: Advantages and Disadvantages

MINIDEX for run I was a simple apparatus with only four signal channels being recorded: two scintillator panels and two HPGe detectors. In the following some advantages and disadvantages of such a setup are highlighted.
First of all, MINIDEX is very compact and the target material can easily be exchanged. Therefore, MINIDEX can be used to investigate different materials. Furthermore, the target material is decoupled from the detector. That makes MINIDEX a flexible setup suitable for instance for MC validation. In contrast to experiments which identify both the muons and the muon-induced neutrons using the same detector signal, like those which use liquid scintillator detectors, MINIDEX does not have problems with the time resolution. In other experiments, it can happen that after the detection of the muon the detector is not active for a certain amount of time (dead time) and neutrons are missed. But MINIDEX has no dead time problems, since muons are identified by the scintillator panels while muon-induced events are identified by the HPGe detectors. This is supported by the fact that all detectors in MINIDEX are recorded independently in double bank mode, as previously mentioned.

Disadvantages of the MINIDEX approach are that the separation of target and detection volume introduces some systematic effect due to uncertainties on the neutron transport. In addition, MINIDEX has a relatively low detection probability ($O(10^{-5})$) due to geometrical factors. Only a certain fraction of the muon-induced neutrons produce a 2.2 MeV gamma and not all these gammas reach the HPGe detectors. In addition, due to its simplicity, MINIDEX has no detection redundancy and the number of quantities that can be used to compare data and simulations is limited. Another limitation arises from the fact that for MINIDEX run I data, it is not possible to distinguish between different

muon topologies, i.e. between muons traversing a lead wall vertically and muons traversing the setup diagonally. Thus, the resulting neutrons are the consequence of very different muon path lengths inside the target volume, which makes the results harder to interpret.

However, the sparsity of experimental data for muon-induced neutron yield in high-Z materials and the complexity of some of the previous experiments, which makes them difficult to interpret, make MINIDEX a promising new source of data. In the following section the analysis strategy is presented and it is pointed out how the fact that the detectors are recorded independently allows to have a simultaneous measurement of signal and background.

4.6 Analysis Strategy

The strategy used to analyze the MINIDEX run I data is simple. It relies, first of all, on the capability of the scintillator panels to identify a muon going through the setup. When a muon crosses both the top and the bottom scintillator panels, it releases energy via ionization inside the panels and, therefore, a corresponding signal is recorded for both scintillators. Since the panels are read out independently, the event seen by the top scintillator has, a priori, a different time tag than the one seen by the bottom scintillator: T_{top} and T_{bot}, respectively. A muon-event, referred as *trigger* in the rest of the text, is simply defined as an event for which the time difference $T_{top} - T_{bot}$ lies within the time interval $[-40; +20]$ ns, thus when a coincidence between the two panels occurs. No condition on the energy recorded by each panel is set for the analysis of MINIDEX run I data. The coincidence window was chosen according to the distribution of the time difference $T_{top} - T_{bot}$, shown in Fig. 4.16. As can be seen, a very significant peak distinguishes the triggered muon events from random single hits. For each triggered event, T_{top} is assigned as the time of the passage of the muon (T_{trig}).
Figure 4.17 shows the comparison between the calibrated energy spectra without (blue) and with (red) trigger for the top and the bottom scintillator panel. The minor shift towards lower energies of the spectra of events with trigger is due to geometrical effects. It should be noted that the calibration of the scintillator panels is done on the muon peak by assigning the energy obtained in simulations to the observed ADC value.
Table 4.3 summarizes the information related to the triggers recorded in MINIDEX run I from July 15 to November 25, 2015.
The individual total count rates of the scintillator panels are ${R_{top}}^{single} \approx 49.3$ Hz and ${R_{bot}}^{single} \approx 46.8$ Hz, respectively. Given the width of the coincidence window ($\Delta T_{coinc} = 60$ ns), the accidental triggers rate ${R_{acc}}^{trig}$ is:

$$ {R_{acc}}^{trig} = 2{R_{top}}^{single}{R_{bot}}^{single}\Delta T_{coinc} \approx 2.77 \cdot 10^{-4} \text{ Hz}. \tag{4.4} $$

This value is negligible compared to the measured trigger rate of 8.14 Hz.

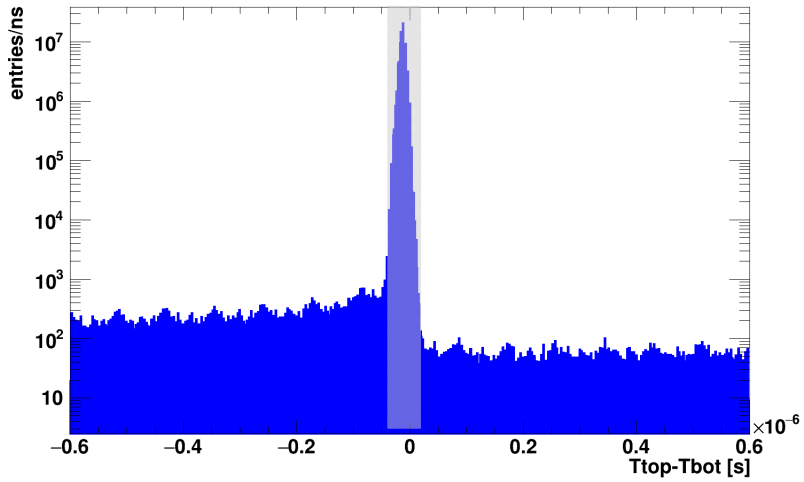

Figure 4.16: Distribution of the time difference $T_{top} - T_{bot}$. The shaded area around the pronounced peak represents the time selection for the trigger events.

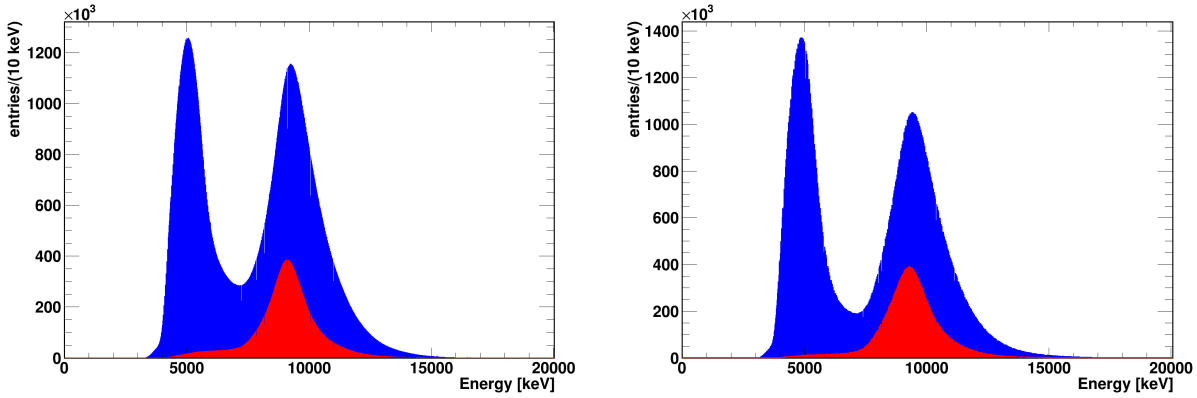

Figure 4.17: Calibrated energy spectra without (blue) and with (red) trigger comparison for the upper (left) and lower (right) scintillator panels.

Triggers	**Run Time [s]**	**Trigger rate [Hz]**
$7.98745 \cdot 10^7$	$9.81359 \cdot 10^6$	8.14

Table 4.3: Summary of the trigger-related information of MINIDEX run I, from July 15 to November 25, 2015. The number of triggers and the trigger rate are as measured and were not corrected for the trigger detection efficiency of the scintillator panels.

Between each pair of triggers, the data recorded for the two HPGe detectors is divided into two time windows:

- *INSIDE*: events recorded in the two HPGe detectors within a time window ΔT_{win} after the occurrence of the trigger at T_{trig};
- *OUTSIDE*: events recorded between the end of ΔT_{win} and the arrival of the next trigger.

Simulations predict that the time distribution of muon-induced 2.2 MeV gammas seen by the germanium detectors extends only up to 1–2 ms after the occurrence of a trigger, see Fig. 4.18. Therefore, for ΔT_{win} long enough, the *INSIDE* spectrum will contain all the

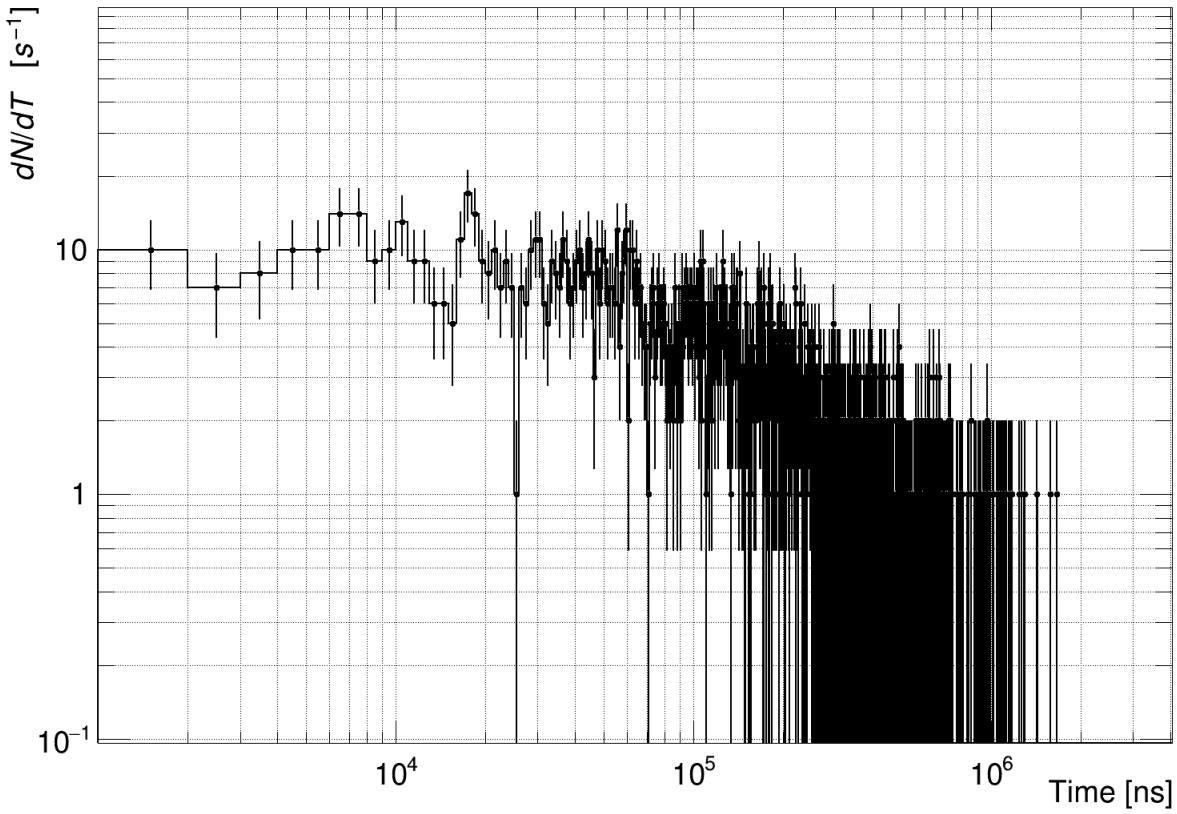

Figure 4.18: Distribution of the time of muon-induced 2.2 MeV gammas seen by the two HPGe detectors, after the occurrence of a trigger T_{trig}. All muon-induced 2.2 MeV gammas are seen by the germanium detectors within ≈2 ms.

muon-induced events in the ROI, which represent our signal. The *OUTSIDE* spectrum

will be completely signal-free; it contains only background events in the ROI. Under the assumption that background events are uniformly distributed over time, i.e. they are not correlated to the occurrence of a trigger, the 2.2 MeV events in the *INSIDE* spectrum represent the sum of the signal and the background. This situation is depicted in Fig. 4.19. In this way, a simultaneous measurement of the signal and the background is performed.

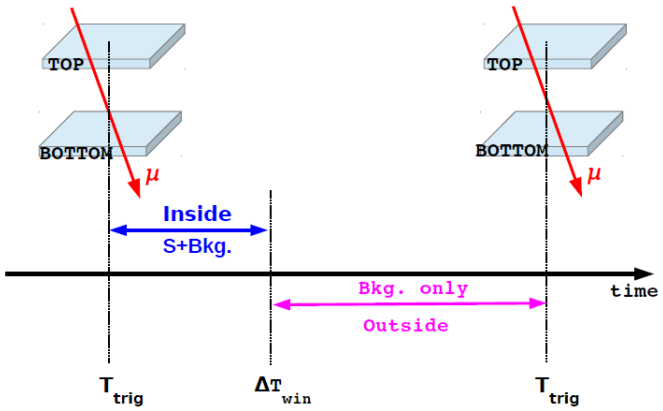

Figure 4.19: Sketch illustrating the analysis strategy adopted for MINIDEX run I. When ΔT_{win} is big enough, the *OUTSIDE* contains only background events.

Recording the detectors independently from each other is crucial for this purpose.
The possibility to vary ΔT_{win} gives access to the time structure of the process.
Furthermore, measuring the muon-induced signals for small ΔT_{win} reduces the background in the ROI. Hence, a better signal-to-background ratio can be achieved.
The analysis was performed for different values of ΔT_{win}. The values chosen are (0.01, 0.02, 0.03, 0.04, 0.05, 0.06, 0.07, 0.08, 0.09, 0.1, 0.11, 0.12, 0.13, 0.14, 0.15, 0.16, 0.17, 0.18, 0.19, 0.2, 0.25, 0.3, 0.35, 0.4, 0.6, 0.8, 1.0, 1.2, 1.4, 1.6, 1.8, 2.0, 2.5, 3.0, 4.0, 5.0, 7.5, 10, 20, 35, 50) ms. It should be noted that the biggest value of ΔT_{win} = 50 ms, is smaller than the average time between two consecutive triggers (≈107 ms) in order to have a low probability that a second trigger occurs within ΔT_{win}.

The goal of the analysis is to measure the muon-induced signal rate, the background rate and the signal-to-background ratio $\rho_{S/B}$, for each value of ΔT_{win}. To do this, the number of counts (N_{peak}) under the 2.2 MeV peak[2] seen by the HPGe detectors for both the *INSIDE* and *OUTSIDE* spectra have to be extracted. Two alternative methods have been used to evaluate the number of 2.2 MeV gammas seen by the HPGe detectors in the *INSIDE* and *OUTSIDE* spectra.

[2]The measured spectra of the HPGe detectors are calibrated to the known energies of two background lines, namely the ^{40}K line at 1460 keV and the ^{208}Tl line at 2614 keV. This is a good choice since the ROI of this analysis lies between the two lines.

4.6.1 FIT Method

This method consists of simply fitting the 2.2 MeV peak region with a Gaussian plus a first order polynomial. The polynomial function is needed to take the Compton background underneath the 2.2 MeV peak into account. The fit is performed between 2210 keV and 2230 keV. This range is wide enough to contain the peak fully as the resolution (FWHM) is 2.8 keV. The lower edge of this fit region clearly avoids the natural background peak at 2.204 MeV originating from ^{214}Bi. An example of an *OUTSIDE* spectrum together with the corresponding fit is shown in Fig. 4.20.
To evaluate N_{peak}, the Gaussian function obtained from the fit is integrated over an ROI of 2.223 MeV $\pm$ 1.8 $\cdot$ FWHM. The width of the ROI was chosen according to the needs of a second method that will be described later. The statistical uncertainty on N_{peak}, $\delta {N_{peak}}^{stat}$, is given by the uncertainty from the fit.
If ΔT_{win} is big enough to contain all the muon-induced events (referred to as signal, S),

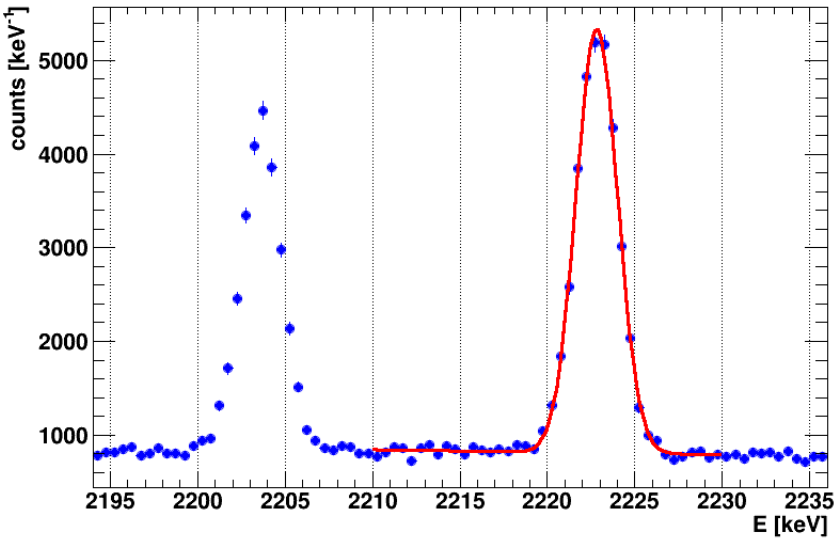

Figure 4.20: *OUTSIDE* spectrum for $\Delta T_{win} = 35$ ms together with the fit. On the left, the natural background peak due to ^{214}Bi is clearly seen. The data shown refer to those recorded in MINIDEX run I, until November 25, 2015.

for the *INSIDE* spectrum, the equation

$$ {N_{peak}}^{inside} = N_S + {N_B}^{inside} \tag{4.5} $$

holds, where N_S is the number of muon-induced 2.2 MeV gammas and ${N_B}^{inside}$ is the number of background 2.2 MeV gammas within ΔT_{win}. For the *OUTSIDE* spectrum, the relation

$$ {N_{peak}}^{outside} = {N_B}^{outside} \text{ holds.} \tag{4.6} $$

The N_B events are generated by interactions of background neutrons, such as neutrons produced in $(\alpha - n)$-reactions in the laboratory environment or neutrons that were produced by muon interactions in the laboratory overburden.

Figures 4.21 and 4.22 show all the fits performed for different ΔT_{win} for the *INSIDE* and the *OUTSIDE* spectra, respectively. It can be seen how, for small ΔT_{win} values, the *INSIDE* spectra are limited by low statistics, while there are no statistics issues for larger values of ΔT_{win}. This behavior reflects the fact that the bigger the ΔT_{win} the more events are collected, both from signal and background. There are no statistics issues for the *OUTSIDE* spectra for any value of ΔT_{win}.

It should be noted that the fit method can either fail or give unreliable results for very small values of ΔT_{win} due to the lack of statistics. For this reason, an alternative method based on the Bayes' Theorem [224] was also adopted.

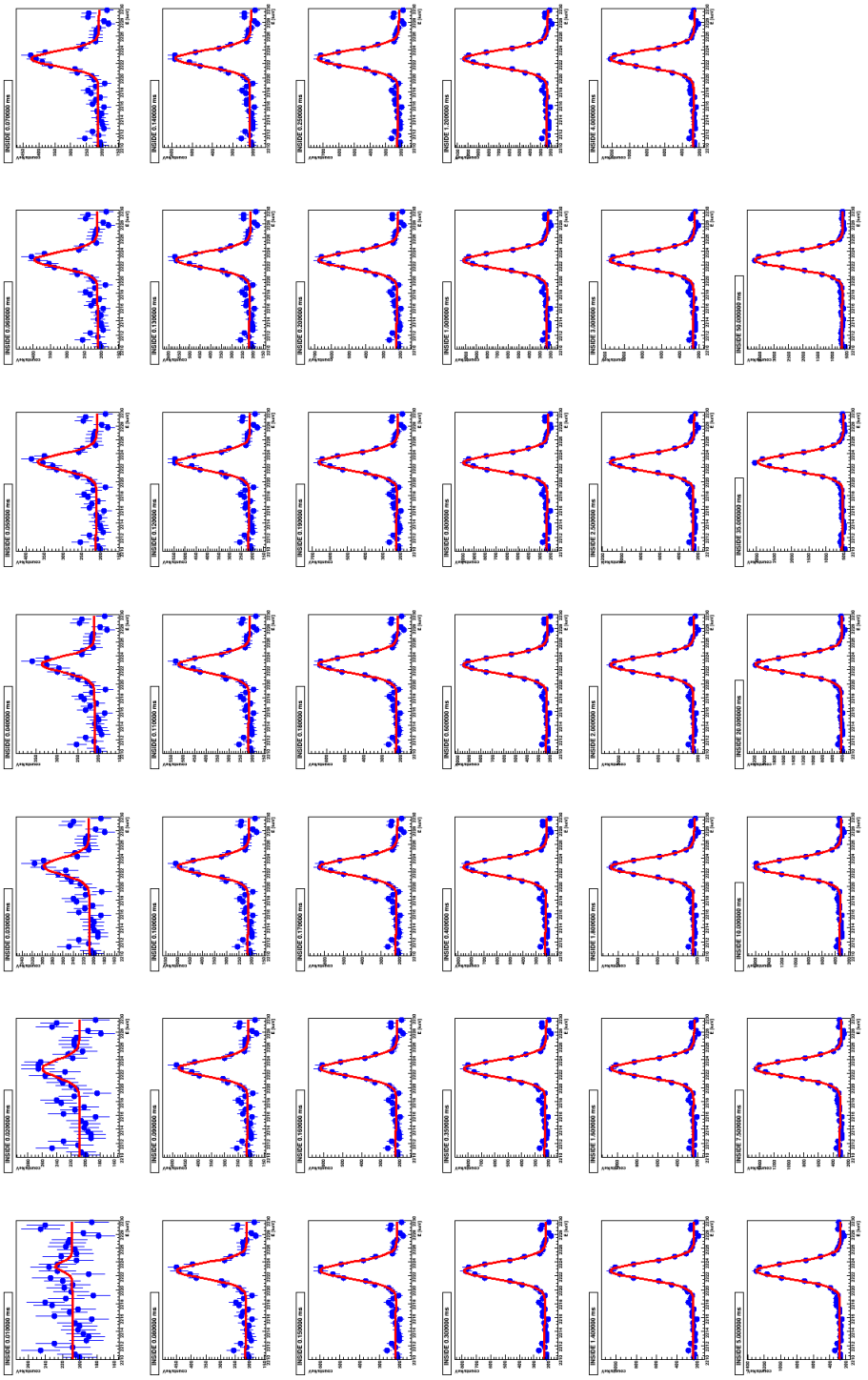

Figure 4.21: Fits of the 2.2 MeV gamma peak in the *INSIDE* spectrum for all the ΔT_{win} values.

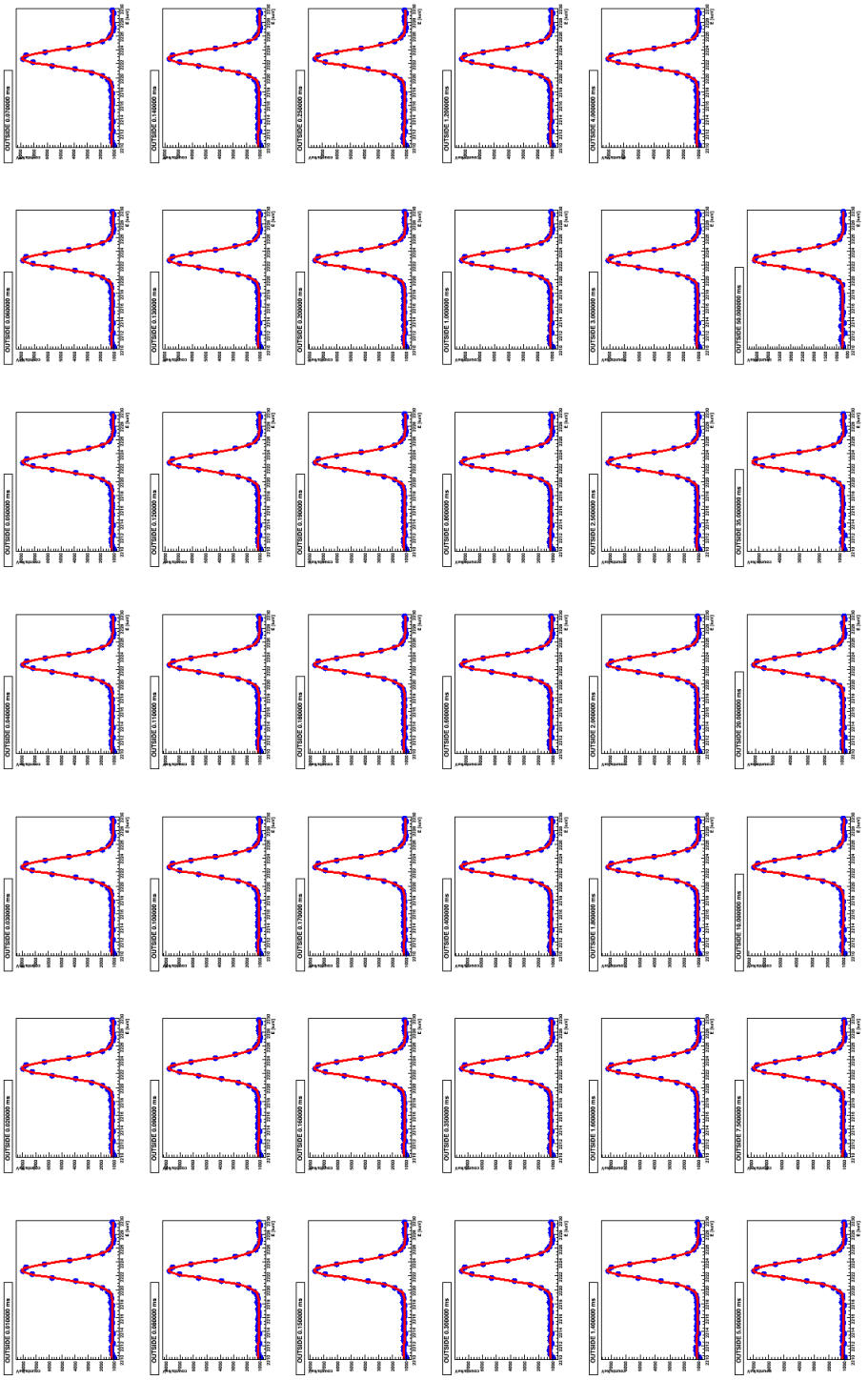

Figure 4.22: Fits of the 2.2 MeV gamma peak in the *OUTSIDE* spectrum for all the ΔT_{win} values.

4.6.2 Bayesian Method, BAT

This method to estimate N_{peak} follows a Bayesian approach. In this case, not only the ROI (2.223 MeV $\pm$ 1.8 $\cdot$ FWHM) is considered, but also the two (equal-width) side bands, to the left and to the right of the ROI. The side bands are used to estimate the contamination of the ROI due to Compton background.
In general, Bayes' Theorem relates the probability (called *posterior* probability $P(\overrightarrow{\lambda}|\overrightarrow{D}, M)$) that a model, M, with parameters $\overrightarrow{\lambda}$, describes the measured data $\overrightarrow{D}$ to the probability of observing $\overrightarrow{D}$ given the model M and its parameters $\overrightarrow{\lambda}$, called *likelihood* $P(\overrightarrow{D}|\overrightarrow{\lambda}, M)$:

$$P(\overrightarrow{\lambda}|\overrightarrow{D}, M) \ \propto \ P(\overrightarrow{D}|\overrightarrow{\lambda}, M) \cdot P(\overrightarrow{\lambda}|M) \ , \tag{4.7}$$

where $P(\overrightarrow{\lambda}|M)$, called *prior* probability, describes the knowledge about the parameters before the experiment is performed. The *posterior* carries the updated knowledge about the parameters $\overrightarrow{\lambda}$ of interest. The Bayes' Theorem also applies to probability distribution functions.
Let n_T be the total number of events in the ROI and n_{CB} the total number of events in the side bands for the energy spectrum under study. While the ROI contains both the 2.2 MeV events and Compton background, the side bands contain only Compton events. Under the assumption that the Compton background is uniformly distributed in the ROI plus the side bands, the measured value n_{CB} can be used to estimate the background content in the ROI. The expected number of Compton events, N_{CB}, in the side bands is

$$N_{CB} = \Gamma_{CB} \cdot W_{bands} \ . \tag{4.8}$$

The total number of total events expected, N_T, in the ROI is:

$$N_T = (\Gamma_{peak} + \Gamma_{CB}) \cdot W_{ROI} \tag{4.9}$$

where Γ_{CB} and Γ_{peak} are the count rates per unit energy of the Compton background and the 2.2 MeV gammas, respectively. W_{bands} and W_{ROI} represent the widths of the bands and the ROI, where:

$$W_{bands} = 2 \cdot W_{ROI} = 2 \cdot 3.6 \cdot FWHM \ . \tag{4.10}$$

Figure 4.23 depicts an example of the situation described above.

The parameter of interest for this analysis method is Γ_{peak} and its possible values are obtained applying Bayes' Theorem. The posterior probability for the parameters of the model, Γ_{peak} and Γ_{CB}, is

$$P(\Gamma_{CB}, \Gamma_{peak}|n_{CB}, n_T) \ \propto \ P(n_T|\Gamma_{CB}, \Gamma_{peak}) \cdot P(\Gamma_{peak}) \cdot P(\Gamma_{CB}|n_{CB}) \ , \tag{4.11}$$

where Eq. 4.7 becomes

$$P(\Gamma_{CB}|n_{CB}) \ \propto \ P(n_{CB}|\Gamma_{CB}) \cdot P(\Gamma_{CB}) \ . \tag{4.12}$$

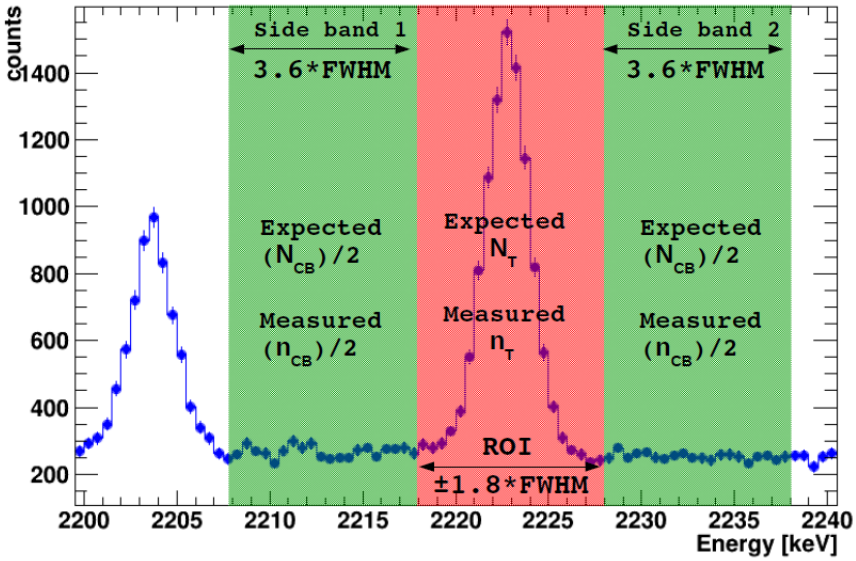

Figure 4.23: *OUTSIDE* spectrum for $\Delta T_{win} = 35$ ms with bands as described in the text for the Bayesian method.

The combination of Eqs. 4.11 and 4.12 gives

$$P(\Gamma_{CB}, \Gamma_{peak}|n_{CB}, n_T) \;\propto\; P(n_T|\Gamma_{CB}, \Gamma_{peak}) \cdot P(n_{CB}|\Gamma_{CB}) \cdot P(\Gamma_{CB}) \cdot P(\Gamma_{peak}) \; . \quad (4.13)$$

Assuming flat priors, $P(\Gamma_{peak})$ and $P(\Gamma_{CB})$,

$$P(\Gamma_{peak}) = \begin{cases} 1 & \text{if } \Gamma_{peak} \in \left[0, \frac{n_T}{W_{ROI}} + \Lambda\right] \\ 0 & \text{otherwise} \end{cases} \quad (4.14)$$

and

$$P(\Gamma_{CB}) = \begin{cases} 1 & \text{if } \Gamma_{CB} \in \left[\frac{n_{CB}}{W_{bands}} - \Lambda', \frac{n_{CB}}{W_{bands}} + \Lambda'\right] \\ 0 & \text{otherwise} \end{cases} \quad (4.15)$$

where Λ and Λ' were chosen such that the phase space for the parameters Γ_{peak} and Γ_{CB} is large enough, Eq. 4.13 reduces to

$$P(\Gamma_{CB}, \Gamma_{peak}|n_{CB}, n_T) \;\propto\; P(n_T|\Gamma_{CB}, \Gamma_{peak}) \cdot P(n_{CB}|\Gamma_{CB}) \; . \quad (4.16)$$

The underlying processes that produce the measured values n_{CB} and n_T are considered to be Poissonian with expectations N_{CB} and N_T, respectively. Therefore the resulting likelihood distributions become

$$P(n_{CB}|\Gamma_{CB}) = \frac{e^{-N_{CB}} \cdot {N_{CB}}^{n_{CB}}}{n_{CB}!} \quad (4.17)$$

and

$$P(n_T|\Gamma_{CB},\Gamma_{peak}) = \frac{e^{-N_T}\cdot {N_T}^{n_T}}{n_T!}\ , \tag{4.18}$$

where N_{CB} and N_T are given by Eqs. 4.8 and 4.9, respectively.
The expected value of Γ_{peak} is given by the most probable value (mode) of its probability distribution $P(\Gamma_{peak}|n_{CB},n_T)$ which is obtained by marginalizing the posterior probability distribution given in Eq. 4.16:

$$P(\Gamma_{peak}|n_{CB},n_T) = \int P(\Gamma_{CB},\Gamma_{peak}|n_{CB},n_T)d\Gamma_{CB}\ . \tag{4.19}$$

The number of 2.2 MeV gammas in the ROI is

$$N_{peak} = \Gamma_{peak}\cdot W_{ROI}\ . \tag{4.20}$$

It should be noted that the normalization factor in the Bayes' Theorem, called *evidence*, was not taken into account in the computation, since the purpose of this method is to find the most probable value of Γ_{peak}, and thus of N_{peak}, rather than the actual value of its associated probability. The smallest interval containing the 68% probability of $P(\Gamma_{peak}|n_{CB},n_T)$ is quoted as the statistical uncertainty interval of the most probable value of Γ_{peak}.
The evaluation of the posterior probability distribution and its marginalization was done with the Bayesian Analysis Toolkit (BAT)[3] [232].

Systematic Uncertainty on N_{peak}

Using two alternative methods to evaluate the number of counts under the 2.2 MeV peak, N_{peak}, allows to estimate the systematic uncertainty associated to the evaluation of ${N_{peak}}^{4}$. A conservative approach was chosen by estimating the systematic uncertainty ${\delta N_{peak}}^{Sys}$ as:

$${\delta N_{peak}}^{Sys} = \mid {N_{peak}}^{FIT} \ - \ {N_{peak}}^{BAT} \mid\ . \tag{4.21}$$

This is added in quadrature to the statistical uncertainty ${\delta N_{peak}}^{Stat}$.

[3] BAT was also used in [233] and [234] to estimate the background content in the region of interest of HPGe spectra for neutrinoless double beta decay.

[4] ${N_{peak}}^{FIT}$ was chosen as reference.

4.6.3 Effective Rates

The ${N_{peak}}^{inside}$ and ${N_{peak}}^{outside}$ were evaluated for each value of ΔT_{win}. The effective measured time of the *INSIDE* spectra is

$$ {ET_{inside}}^{meas} = {N_{trig}}^{meas} \cdot \Delta T_{win} \ , \tag{4.22} $$

where ${N_{trig}}^{meas}$ is the measured number of triggers, and

$$ {ET_{outside}}^{meas} = RT - {ET_{inside}}^{meas} = RT - {N_{trig}}^{meas} \cdot \Delta T_{win} \tag{4.23} $$

is the effective measured time of the *OUTSIDE* spectra, where RT represents the total run time of the measurement. The *effective* rates are, than, defined as:

$$ {\Gamma_{S+B}}^{meas} = \frac{{N_{peak}}^{inside}}{{ET_{inside}}^{meas}} = \frac{{N_{peak}}^{inside}}{{N_{trig}}^{meas} \cdot \Delta T_{win}} \tag{4.24} $$

and

$$ {\Gamma_{B}}^{meas} = \frac{{N_{peak}}^{outside}}{{ET_{outside}}^{meas}} = \frac{{N_{peak}}^{outside}}{RT - {N_{trig}}^{meas} \cdot \Delta T_{win}} \ . \tag{4.25} $$

Figure 4.24 shows the values of ${\Gamma_{S+B}}^{meas}$, which represent the signal-plus-background (effective) rates, obtained with the fit method for each ΔT_{win}.
As already pointed out, *signal* refers to the 2.2 MeV gamma events induced by the interaction of muons, which provided a trigger within the setup. *Background* refers to the 2.2 MeV gammas events with any origin different from the one labeled as *signal*. Figure 4.25 shows the behavior of ${\Gamma_{B}}^{meas}$ vs ΔT_{win} obtained with the fit method. This figure demonstrates how, for small values of ΔT_{win}, some *signal* events are still being collected in the *OUTSIDE* spectra. When all the *signal* events are collected by the *INSIDE* spectra, a constant *background* rate is observed up to $\Delta T_{win} \approx 20$ ms.
For very long ΔT_{win}, namely 35 and 50 ms, ${\Gamma_{B}}^{meas}$ rises. This is expected as the probability of close-by passage of non-triggered muon increases with time. Furthermore, muons are known to arrive in *bundles* [235] but mostly only one of the muons generates a trigger in the MINIDEX setup. This enhances the effect, which was neglected for this first analysis. Thus, very long ΔT_{win} were not suitable to measure the background (effective) rate.
As a result, $\Delta T_{win} = 4$ ms was chosen,

$$ {R_{B}}^{meas} \ = \ [{\Gamma_{B}}^{meas}]_{\Delta T_{win}=4\,ms} \ = \left[\frac{{N_{peak}}^{outside}}{RT - {N_{trig}}^{meas} \cdot \Delta T_{win}} \right]_{\Delta T_{win}=4\,ms} \ , \tag{4.26} $$

which is sufficiently short to avoid undetected muons and sufficiently long to go beyond the end of signal collection, observed to be around ≈1 ms in agreement with predictions.

The uncertainties shown in Fig. 4.24 and 4.25 are purely statistical and were treated as uncorrelated[5].

[5]Considering the uncertainties as uncorrelated clearly is a simplification since every ΔT_{win}-data set contains the events present in smallerΔT_{win}-data sets.

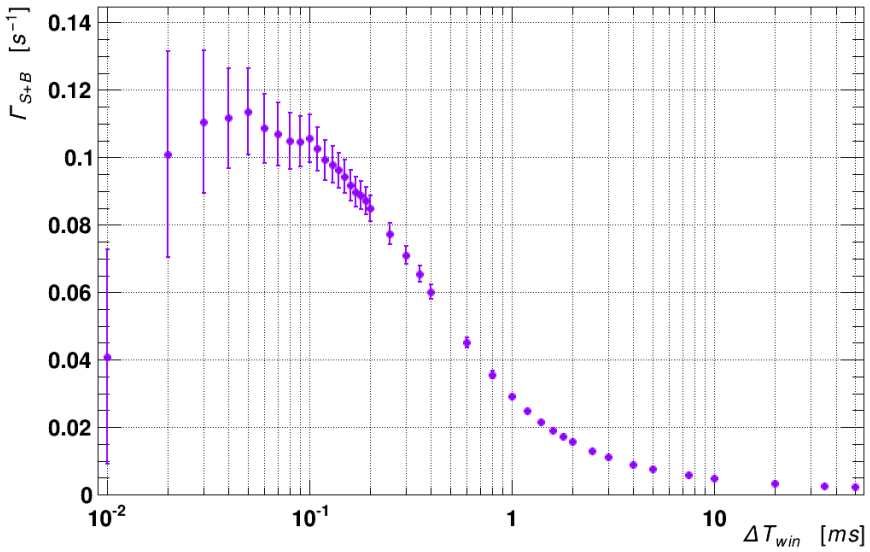

Figure 4.24: The signal-plus-background *effective* rate, ${\Gamma_{S+B}}^{meas}$, obtained with the fit method vs ΔT_{win}. The error bars represent the statistical uncertainties.

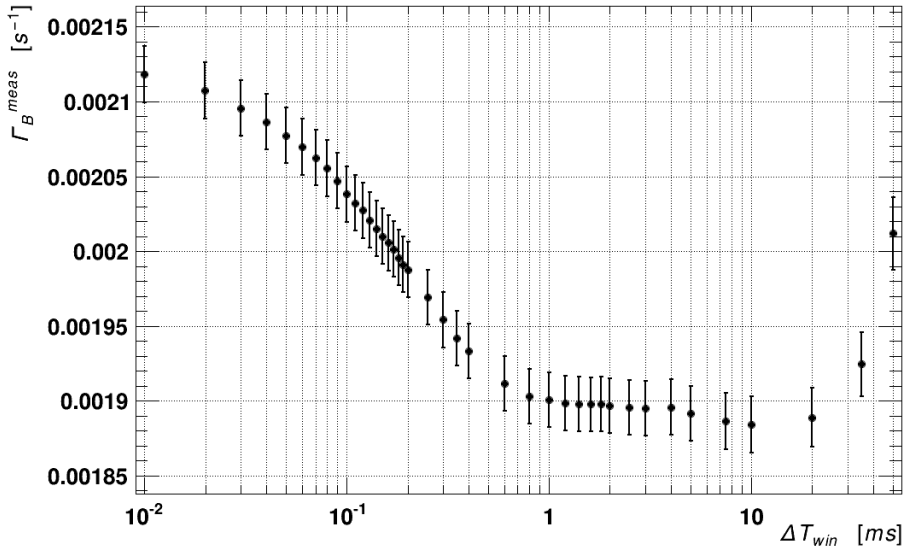

Figure 4.25: The *effective* rate, ${\Gamma_B}^{meas}$, of events which occurred in the ROI of the *OUTSIDE* spectra obtained with the fit method vs ΔT_{win}. The error bars represent the statistical uncertainties.

The measured signal *effective* rate was evaluated for each ΔT_{win} as:

$$R_S{}^{meas} = \Gamma_{S+B}{}^{meas} - R_B{}^{meas} . \tag{4.27}$$

However, the efficiency of the scintillator panels to trigger muons has to be included in the analysis.

4.6.4 Correction for the Inefficiency of the Muon Trigger

The measured detection efficiencies of the scintillator panels, ϵ_{TOP} and ϵ_{BOT} respectively, were relatively low. Hence, the trigger efficiency cannot be neglected. The trigger detection efficiency is the product of ϵ_{TOP} and ϵ_{BOT}

$$\epsilon_{trig} = \epsilon_{TOP} \cdot \epsilon_{BOT} = 0.802 \pm 0.002 . \tag{4.28}$$

The relation between the measured number of triggers and the number of muons that could have satisfied the trigger condition is

$$N_{trig}{}^{meas} = \epsilon_{trig} \cdot N_{trig}{}^{corr} . \tag{4.29}$$

Table 4.4 represents the version of Tab. 4.3 corrected according to Eq. 4.29.

Triggers^{corrected}	**Run Time** [s]	**Trigger rate**^{corrected} [**Hz**]
$(9.96 \pm 0.03) \cdot 10^7$	$9.81359 \cdot 10^6$	10.15± 0.03

Table 4.4: Summary of the trigger-related information of MINIDEX run I, until November 25, 2015. The number of triggers, and therefore also the trigger rate, reported in this table were corrected for the trigger detection efficiency of the scintillator panels, ϵ_{trig}. In this work, the corrected number of triggers as well as the corrected trigger rate were considered without uncertainty.

Similarly, Eqs. 4.22 and 4.23 can be written in terms of the corrected values

$$ET_{inside}{}^{meas} = \epsilon_{trig} \cdot ET_{inside}{}^{corr} , \tag{4.30}$$

$$ET_{outside}{}^{corr} = RT - ET_{inside}{}^{corr} = RT - \frac{ET_{inside}{}^{meas}}{\epsilon_{trig}} . \tag{4.31}$$

The important quantities that have to be evaluated are the corrected signal effective rate, $R_S{}^{corr}$, and the corrected background effective rate, $R_B{}^{corr}$, for which the following relation holds:

$$R_S{}^{corr} = \Gamma_{S+B}{}^{corr} - R_B{}^{corr} . \tag{4.32}$$

Since the ϵ_{trig} only lets events migrate from signal to background, the total rate Γ_{S+B} does not change, namely:

$$\Gamma_{S+B}{}^{corr} = \Gamma_{S+B}{}^{meas} = \Gamma_{S+B} \ . \tag{4.33}$$

Thus, the corrected background rate becomes

$$R_B{}^{corr} = \left[\frac{R_B{}^{meas} \cdot ET_{outside}{}^{meas} - (N_{trig}{}^{corr} - N_{trig}{}^{meas}) \cdot \Gamma_{S+B} \cdot \Delta T_{win}}{ET_{outside}{}^{corr}} \right]_{4\,ms} \tag{4.34}$$

where $R_B{}^{meas} \cdot ET_{outside}{}^{meas}$ is the measured number of background counts and $(N_{trig}{}^{corr} - N_{trig}{}^{meas}) \cdot \Gamma_{S+B} \cdot \Delta T_{win}$ represents the number of counts which, due to inefficiency, ended up in the *OUTSIDE* spectrum instead of the *INSIDE*.

Figure 4.26 shows the behavior of the corrected *effective* rate of the signal, $R_S{}^{corr}$, obtained with the FIT method for MINIDEX run I data. As before, the uncertainties displayed are purely statistical and are treated as uncorrelated.

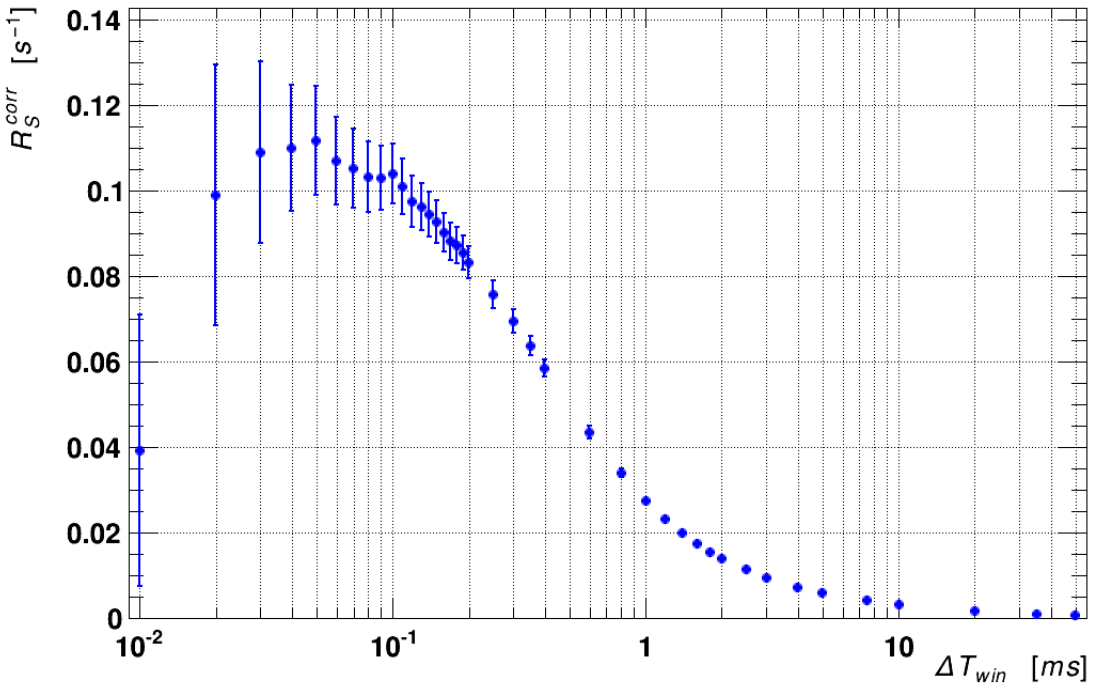

Figure 4.26: The *effective* rate of the signal, $R_S{}^{corr}$, obtained with the FIT method vs ΔT_{win}. The error bars represent statistical uncertainties only.

It can be seen how the number of signal events that occurred within ΔT_{win} increases substantially for small ΔT_{win} until ≈0.1 ms. Then, the importance of the signal gradually

decreases compared to the background. Fig. 4.27, which shows the corrected signal-to-background ratio

$$\rho_{S/B} = \frac{{R_S}^{corr}}{{R_B}^{corr}} \tag{4.35}$$

obtained with the FIT method. This figure demonstrates how after the collection of the signal the background becomes important for long ΔT_{win}.

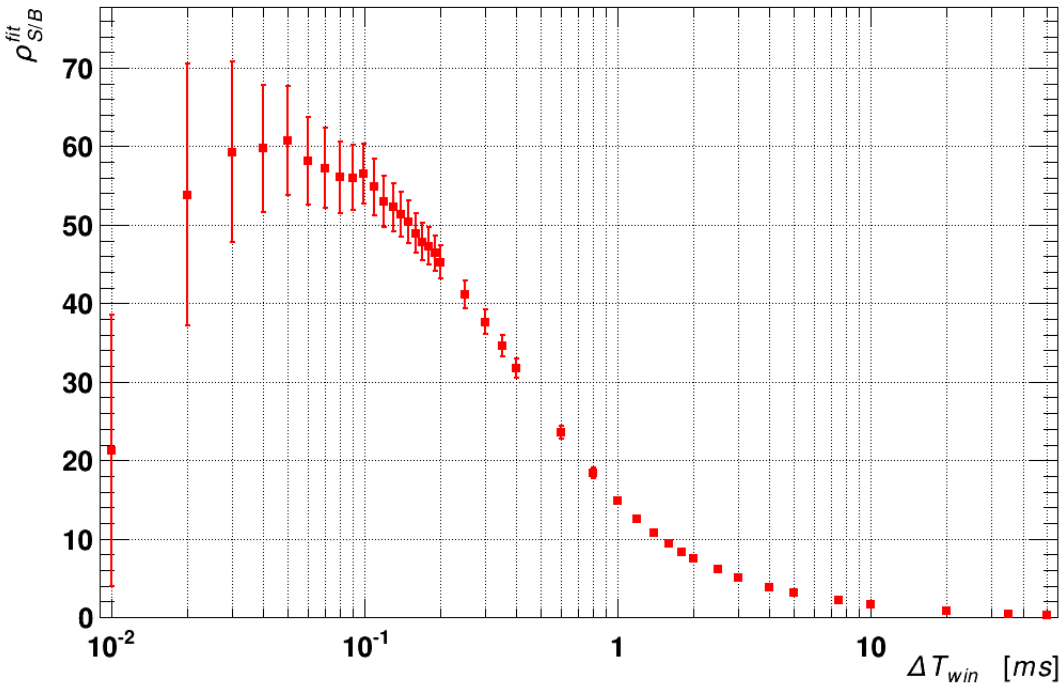

Figure 4.27: The corrected signal-to-background ratio, ${\rho_{S/B}}^{corr}$, obtained with the FIT method vs ΔT_{win}. Both the signal and background rate rates were corrected for the trigger detection efficiency.

Once again, the uncertainty bars displayed are purely statistical and were treated as uncorrelated. For details on the uncertainty propagation refer to Appendix B, specifically to Secs. B.1 and B.2 for the fit and BAT method, respectively.

4.7 Comparison of FIT and BAT Method

Figure 4.28 shows the measured, not corrected, *effective* rate observed in the *OUTSIDE* spectra (${\Gamma_B}^{meas}$) vs ΔT_{win} obtained with the FIT (blue triangles) and the BAT (red circles) method, respectively. As defined in Sec. 4.6.2, the difference between the results

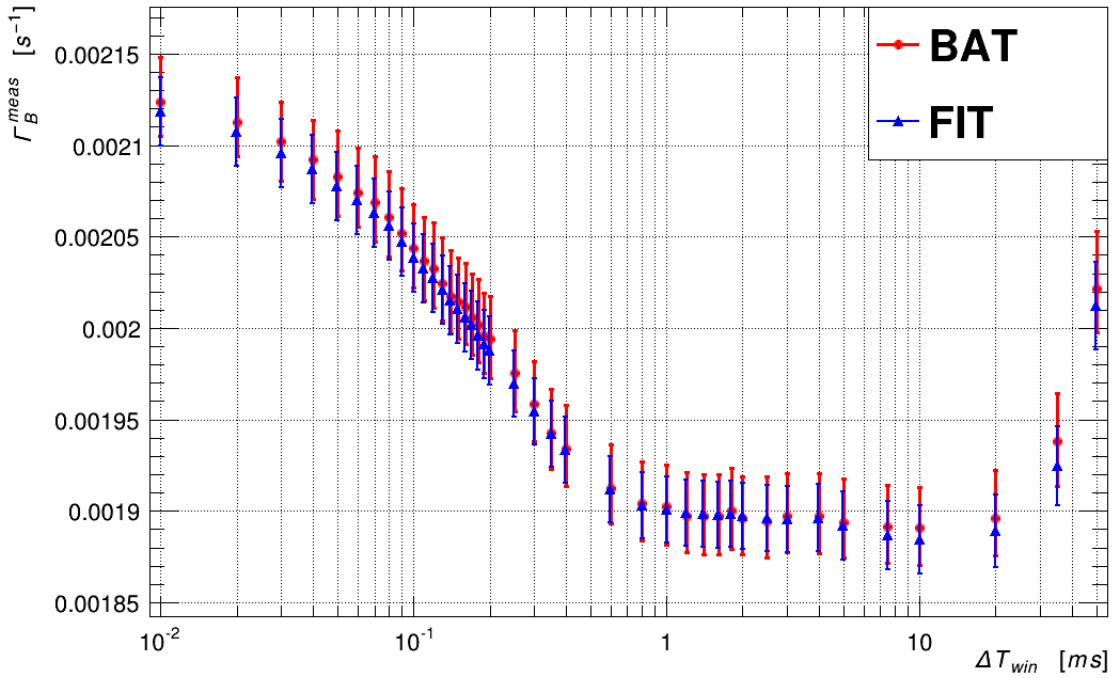

Figure 4.28: The *effective* rate, ${\Gamma_B}^{meas}$, of events observed in the ROI of the *OUTSIDE* spectra, obtained with the FIT (blue triangles) and the BAT (red circles) method vs ΔT_{win}.

obtained with the two methods is taken as the systematic uncertainty (see Eq. 4.21, for example). Figure 4.29 shows these systematic uncertainties (black circles) together with the statistical uncertainties obtained either with the FIT (blue triangles) or the BAT (red triangles) method. The statistical uncertainties correspond to the full size of the uncertainties depicted in Fig. 4.28, while the systematic values correspond to $2 \cdot \delta^{Sys}$. Statistical and systematic uncertainties were added in quadrature. The result for the FIT method is shown in Fig. 4.30. A comparison between the background rate before, ${R_B}^{meas}$, and after the correction, ${R_B}^{corr}$, for the trigger efficiency for both the FIT and the BAT method is given in Tab. 4.5. The results agree very well between the two methods. Similar comparisons are provided in Figs. 4.31, 4.32 and 4.33 for the signal *effective* rate ${R_S}^{corr}$ and in Figs. 4.34, 4.35 and 4.36 for the signal-to-background ratio ${\rho_{S/B}}^{corr}$.

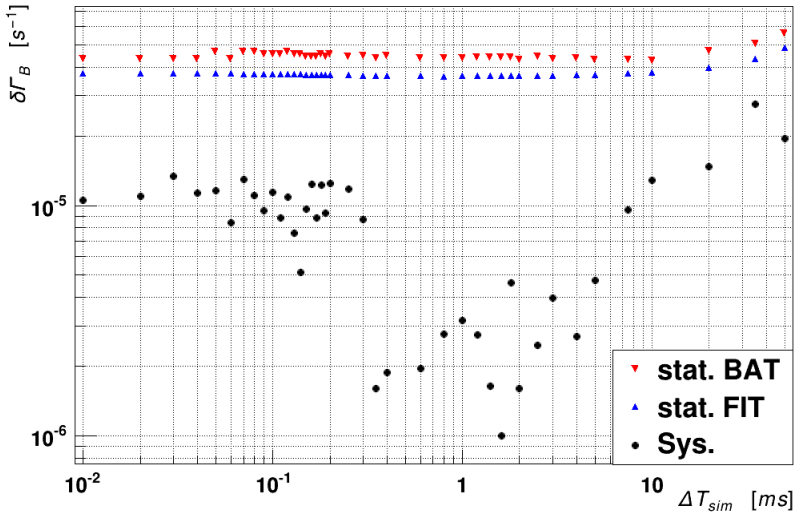

Figure 4.29: The statistical uncertainties on ${\Gamma_B}^{meas}$ obtained with the FIT (blue triangles) and the BAT (red triangles) method are shown. Also shown are the systematic (black circles) uncertainties.

Method	${R_B}^{meas} \cdot 10^{-5}$ [s^{-1}]	${R_B}^{corr} \cdot 10^{-5}$ [s^{-1}]
FIT	(189.6 ± 1.8)	(183.8 ± 1.9)
BAT	(189.7 ± 2.2)	(183.7 ± 2.2)

Table 4.5: Background effective rates before and after the trigger efficiency correction for the FIT and the BAT method.

The FIT method always gives slightly smaller values for the signal than the BAT method and it has smaller statistical uncertainties. The difference between the results is smaller than the statistical uncertainty, i.e. the systematic effects are smaller than the statistical uncertainty. In general, there is good agreement between the results obtained with the two alternative methods.
It is very important to remember that the trigger requirement of through-going muon places the muon-capture-induced events in the background. A future analysis will have to include this contribution in the *signal* component.

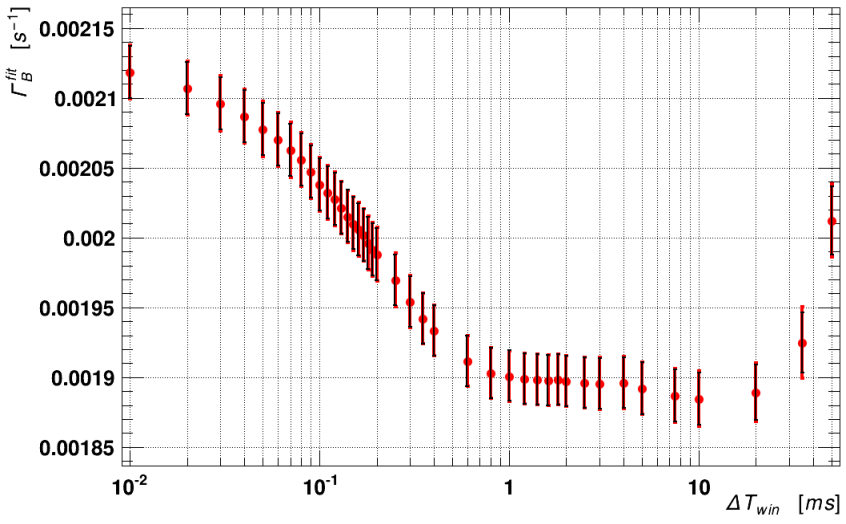

Figure 4.30: The *effective* rate, $\Gamma_B{}^{meas}$, of events observed in the ROI of the *OUTSIDE* spectra as extracted with the FIT method, with the systematic uncertainty added in quadrature. The black lines represent the purely statistical uncertainties, while the red ones correspond to the total uncertainties, i.e. the statistical and the systematic uncertainties added in quadrature.

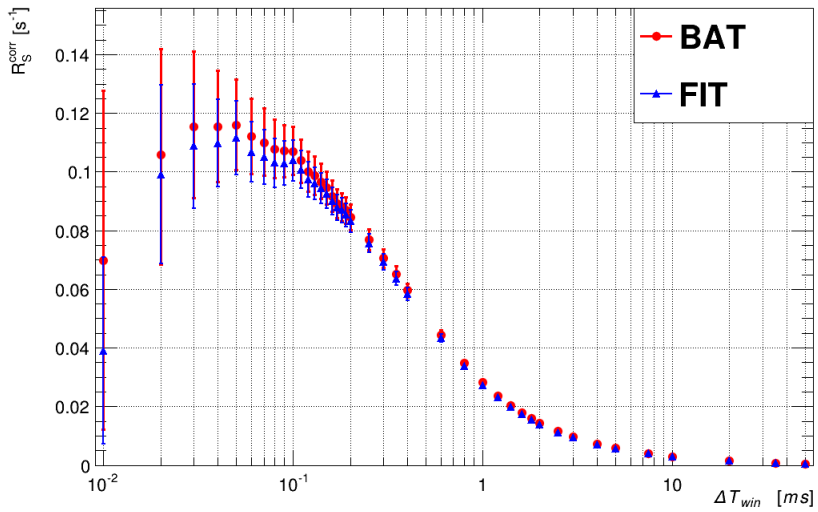

Figure 4.31: The corrected *effective* rate of the signal, $R_S{}^{corr}$, observed with the FIT (blue triangles) and the BAT (red circles) method vs ΔT_{win}. The error bars represent statistical uncertainties only.

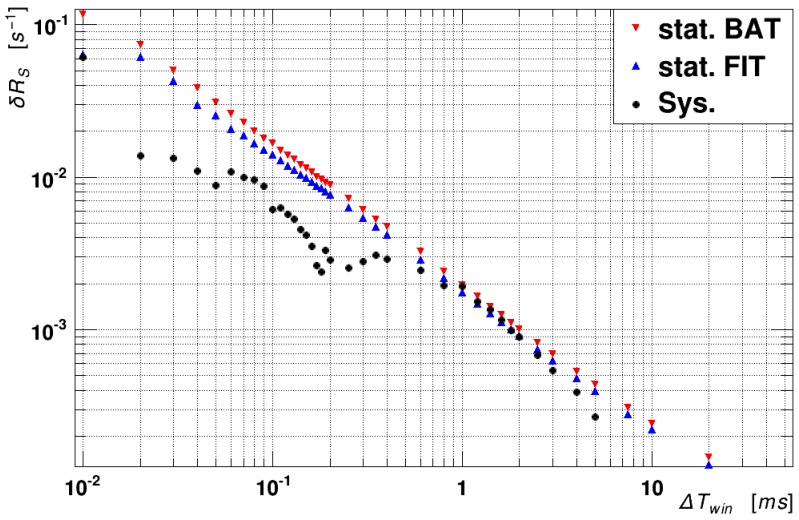

Figure 4.32: The statistical uncertainties on ${R_S}^{corr}$ observed with the FIT (blue triangles) and the BAT (red triangles) method are shown. Also shown are the systematic (black circles) uncertainties.

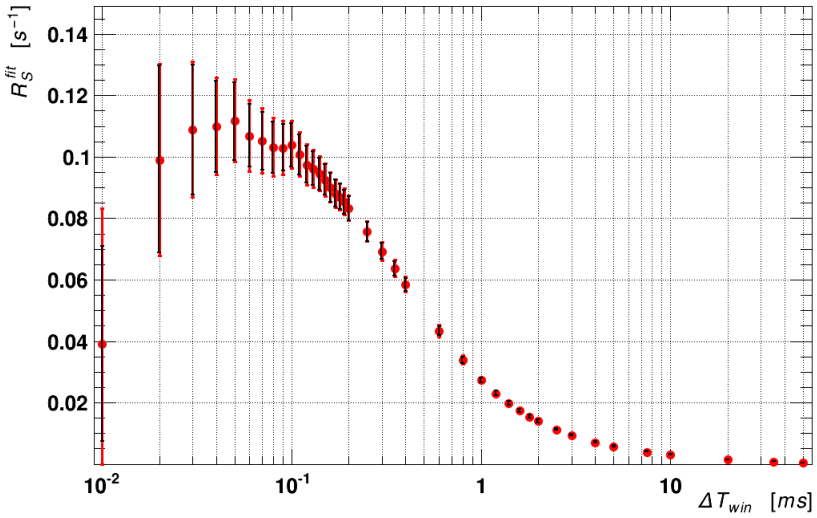

Figure 4.33: The corrected signal *effective* rate, ${R_S}^{corr}$, obtained with the FIT method, with the systematic uncertainty added in quadrature. The black lines represent the purely statistical uncertainties, while the red ones correspond to the total uncertainties, i.e. the statistical and the systematic uncertainties added in quadrature.

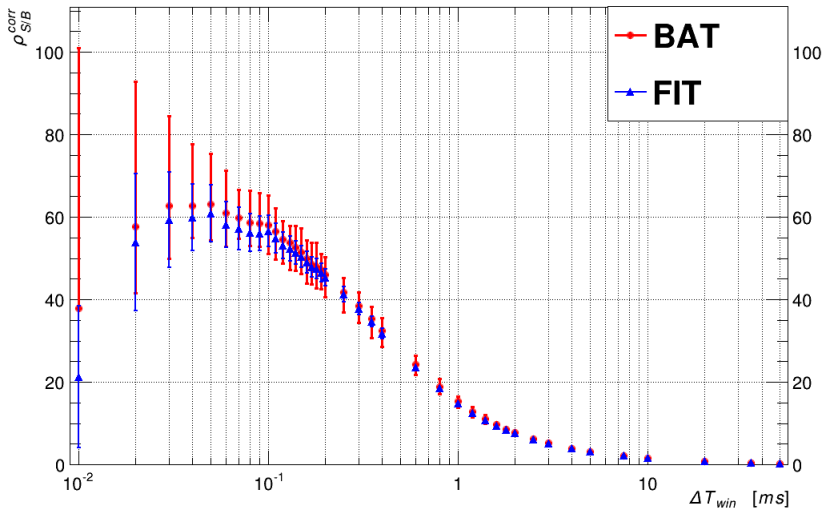

Figure 4.34: The corrected signal-to-background ratio, ${\rho_{S/B}}^{corr}$, observed with the FIT (blue triangles) and the BAT (red circles) method vs ΔT_{win}. The error bars represent statistical uncertainties only.

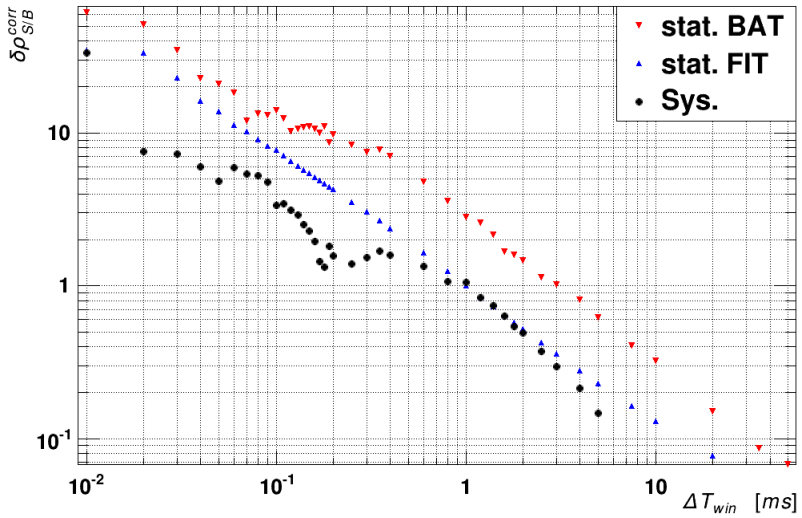

Figure 4.35: The statistical uncertainties on ${\rho_{S/B}}^{corr}$ observed with the FIT (blue triangles) and the BAT (red triangles) method are shown. Also shown are the systematic (black circles) uncertainties.

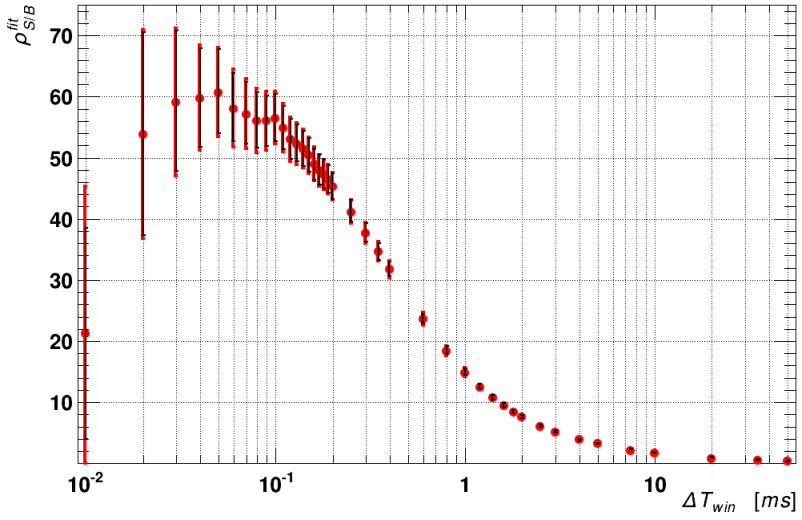

Figure 4.36: The corrected signal-to-background ratio, ${\rho_{S/B}}^{corr}$, observed with the FIT method, with the systematic uncertainty added in quadrature. The black lines represent the purely statistical uncertainties, while the red ones correspond to the total uncertainties, i.e. the statistical and the systematic uncertainties added in quadrature.

Chapter 5

MINIDEX Simulations

In this chapter, the MC techniques used to simulate the events in the MINIDEX apparatus are described in detail. First of all, the simulations to obtain the incoming muon and neutron fluxes at the roof of the shallow underground laboratory are presented. Inside the laboratory, the response of the MINIDEX apparatus was simulated with different physics lists and the results were compared. Furthermore, different input configurations of the particle fluxes incoming at the laboratory roof were investigated. The simulations were divided into two steps: the first step from above ground to the laboratory and the second step inside the laboratory.

5.1 Step 1: from above ground to the roof of the laboratory

The aim of the first step was to obtain the incoming fluxes of cosmogenic muons and neutrons at the roof of the laboratory. This was later used as input to the second step, where the actual simulation of the MINIDEX apparatus was performed.
It was decided to simulate the passage of cosmic muons and neutrons through the laboratory overburden with GEANT4. Other MC packages like MUSUN [177] or MUSIC [151, 236, 237] reduce the burden on the computational resources, but the low depth of the TSUL (≈16 m.w.e.) makes the use of GEANT4 still computationally affordable.
Cosmogenic muons may reach the ground in bundles. However, for this study the arrival of muons was assumed to be statistically uncorrelated. Thus, they were simulated independently.
The simulations were performed within the simulation framework MaGe [217]. This framework is based on GEANT4 [131] and is jointly developed by the GERDA [6] and MAJORANA [45] collaborations. A selection of GEANT4 physics processes is set as the *default* physics list in MaGe.

5.1.1 Geometry

A simplified version of the TSUL overburden was simulated. Specifically, a laboratory hall of volume 5.9 x 5.0 x 3.5 m^3 enclosed in a 35 cm thick concrete shell was implemented. On top of this concrete box a parallelepiped slab of soil with dimensions 8.6 x 7.7 x 9 m^3, was placed. The sides of the concrete box are surrounded by slabs of soil of 1 m thickness. The total overburden corresponds to 16 m.w.e.
Figure 5.1 shows a sketch of the simulated geometry, while Tabs. 5.1, 5.2 and 5.3 report the detailed composition of the materials as used in the simulations for the soil and for the concrete.

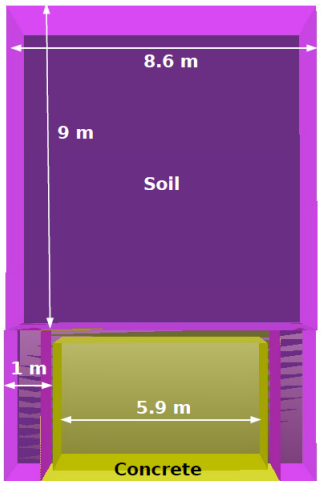

Figure 5.1: Sketch of the simulated overburden of the TSUL.

5.1.2 Inputs

Cosmogenic muons and neutrons, as measured at sea level, were generated. The particles were generated from a plane with an area $A^1_{gen} = 8.6 \,x\, 7.7\, m^2$, placed on top of the laboratory overburden. Both, the energy spectrum and the angular distributions were taken into account for muons and neutrons.
Both, μ^+ and μ^- were generated with identical spectra as measured at sea level by AMS-02 during its commissioning phase at the Kennedy Space Center, Florida [239] (see Fig. 5.2 left). The nominal $cos^2(\theta)$ [148] angular distribution was assumed (see Fig. 5.2 right).
The AMS spectrum was not corrected for the different altitude or latitude of the TSUL.

Material	Mass Fraction
Water	0.200
Limestone ($CaCO_3$)	0.280
$MgCO_3$	0.180
Sand (SiO_2)	0.120
Cellulose ($C_6H_{10}O_5$)	0.040
Lignin ($C_{10}H_{12}O_3$)	0.032
Chitin ($C_8H_{13}NO_5$)	0.004
Fe_2O_3	0.056
Al_2O_3	0.040
SiC	0.048

Table 5.1: Material composition for *Soil*, density = 1.65 g/cm^3

Material	Mass Fraction
Air	0.000022
Portland Cement (see Tab. 5.3)	0.099404
Water	0.044945
Iron	0.264893
Steel	0.264893
Limestone ($CaCO_3$)	0.132446
SiO_2	0.193397

Table 5.2: Material composition for *Concrete*, density = 3.56 g/cm^3. Air was considered as N_2(79%) and O_2(21%).

Material	Mass Fraction
Tricalcium Silicate	0.50
Dicalcium Silicate	0.25
Tricalcium Aluminate	0.10
Tetracalcium Alumin Ferrite	0.10
Gypsum ($CaSO_6H_4$)	0.05

Table 5.3: Material composition for *Portland Cement* [238], density = 3.217 g/cm^3.

Moreover, the fluxes of μ^+ and μ^- were assumed to be identical.

For the cosmogenic neutrons, the energy spectrum on ground measured by Gordon et al. [240] (see Fig. 5.3 left) and a basically isotropic polar-angle distribution as given by A. Nesterenok [241] (see Fig. 5.3 right) were used as input.

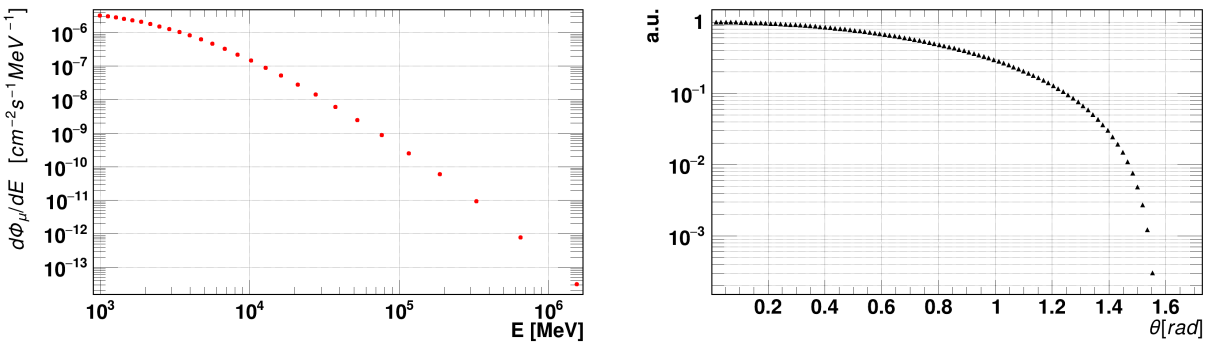

Figure 5.2: Left: muon spectrum on ground as measured by AMS-02 [239]. Right: muon polar-angle distribution on ground.

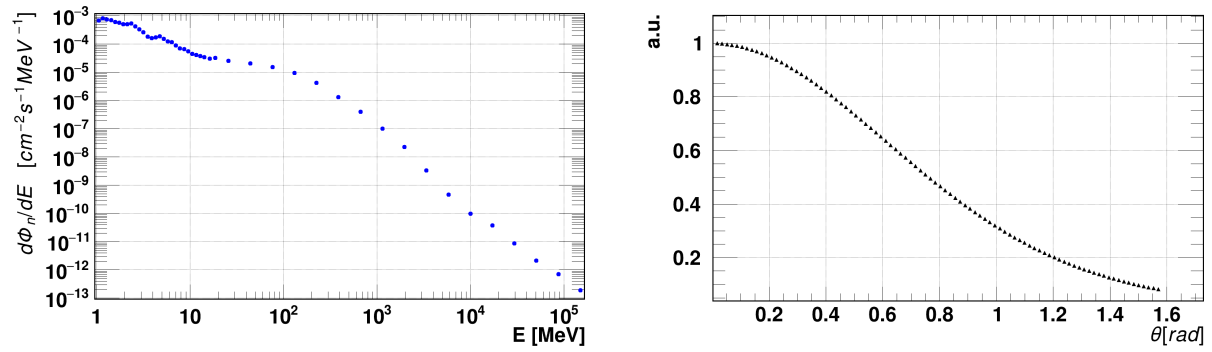

Figure 5.3: Left: Neutron spectrum on ground as measured by Gordon et al. [240]. Right: neutron polar-angle distribution on ground.

The azimuth-angle distribution was assumed to be isotropic for both muons and neutrons. Table 5.4 summarizes the details of this simulation step.

This simulation step was performed with the *FLUX* output scheme described in Sec.4.2.

Geant4 version	9.6.2
MaGe version	May 2014
Output Scheme	*FLUX*
Generation Plane (A^1_{gen}) [m^2]	66.22
Φ_{μ^+}(on ground) [m^{-2} s^{-1}]	37.13 [239]
Φ_{μ^-}(on ground) [m^{-2} s^{-1}]	37.13 [239]
Φ_n(on ground) [m^{-2} s^{-1}]	44.76 [240]
$\frac{d\Phi_\mu}{dE}$(on ground)	[239]
$\frac{d\Phi_n}{dE}$(on ground)	[240]
$\frac{d\Phi_\mu}{d\theta}$(on ground)	$cos^2(\theta)$ [148]
$\frac{d\Phi_n}{d\theta}$(on ground)	isotropic [241]
$\frac{d\Phi_\mu}{d\phi}$(on ground)	isotropic
$\frac{d\Phi_n}{d\phi}$(on ground)	isotropic
Num. of Part. Generated (each type)	$99.99 \cdot 10^6$

Table 5.4: Summary of the inputs for step 1.

5.1.3 Outputs

The interactions of the input particles in the overburden were simulated with GEANT4 and the resulting muons and neutrons penetrating the laboratory roof ($A_{roof} = 5.9\,x\,5\,m^2$) were recorded with their kinetic energies, momenta and positions. The resulting energy spectra and angular distributions were used as inputs to the MINIDEX simulations in step 2.
Figures 5.4 and 5.5 show the energy spectrum (left) and the polar-angle distribution (right) for muons and neutrons, respectively. These particles represent the remnants of the cosmogenic particles incoming at ground level.

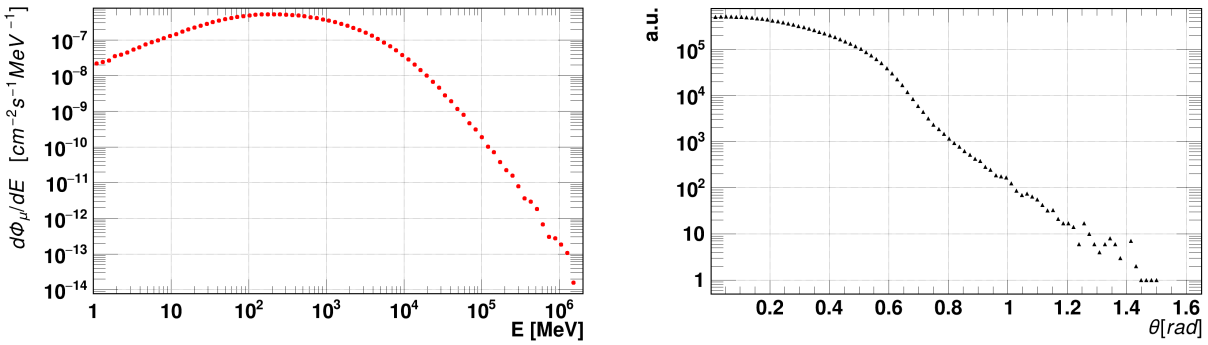

Figure 5.4: Spectrum (left) and polar-angle distribution (right) of muons entering the laboratory from the roof, obtained with step 1 of the simulation.

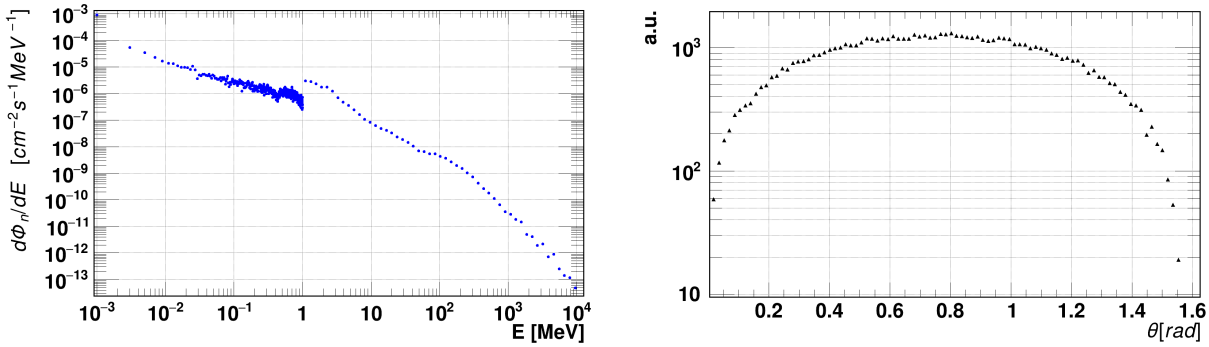

Figure 5.5: Spectrum (left) and polar-angle distribution (right) of cosmogenic neutrons entering the laboratory from the roof, obtained with step 1 of the simulation. The step in the spectrum at 1 MeV simply reflects a different binning used for the two energy regimes, namely below and above 1 MeV.

Given the flux at sea level of a specific particle type, Φ_{IN}, the number of generated particles

at sea level N_{gen} and the area of the generating plane A_{gen}, the corresponding simulated run time RT_{MC} is:

$$RT_{MC} = \frac{N_{gen}}{\Phi_{IN} \cdot A_{gen}} \quad . \tag{5.1}$$

Therefore, the resulting flux Φ_{OUT} is:

$$\Phi_{OUT} = \frac{N_{roof}}{RT_{MC} \cdot A_{roof}} \quad , \tag{5.2}$$

where N_{roof} is the number of a specific type of particle entering the laboratory from the roof surface. Table 5.5 reports the input and the output integral fluxes together with the RT_{MC} for muons and neutrons.

	μ	**n**
Φ_{IN} (on ground) [m^{-2} s^{-1}]	74.26	44.76
RT_{MC} [s]	4.0667 $\cdot 10^4$	3.3737 $\cdot 10^4$
Φ_{OUT} (at roof) [m^{-2} s^{-1}]	16.5766	0.0821575

Table 5.5: Input and output integral fluxes, Φ_{IN} and Φ_{OUT}, for both muons and neutrons, together with the corresponding simulated run time, RT_{MC}. These quantities are treated without uncertainties in this work.

According to the simulations, the muon integral-flux is reduced by a factor of ≈4.5 while the neutron integral-flux is reduced by a factor of ≈545. The much larger reduction of the neutron flux motivates the choice to perform the experiment in a shallow underground laboratory rather than above ground.
Figure 5.6 shows the results of step 1 for the azimuth-angle distribution for muons (left) and neutrons (right) at the inside of the laboratory. These distributions are isotropic within 10%. Hence, they were treated as such in step 2.
It should be noted that, since the simulated fluxes are used as inputs for the MINIDEX simulation (step 2), any inaccuracy in the fluxes due to simulations is propagated into the final results. It would be preferable to have measured values for the fluxes inside the laboratory.

5.2 Step 2

The cosmogenic muon and neutron fluxes at the laboratory roof, together with their energy spectra and angular distributions, as obtained in step 1, were used as input to the second step of the MINIDEX simulations. The geometry implemented for this step includes the whole MINIDEX apparatus with its supporting table and the concrete box described in step 1, which represents the laboratory walls.
In this step, the simulation was performed with two different output schemes:

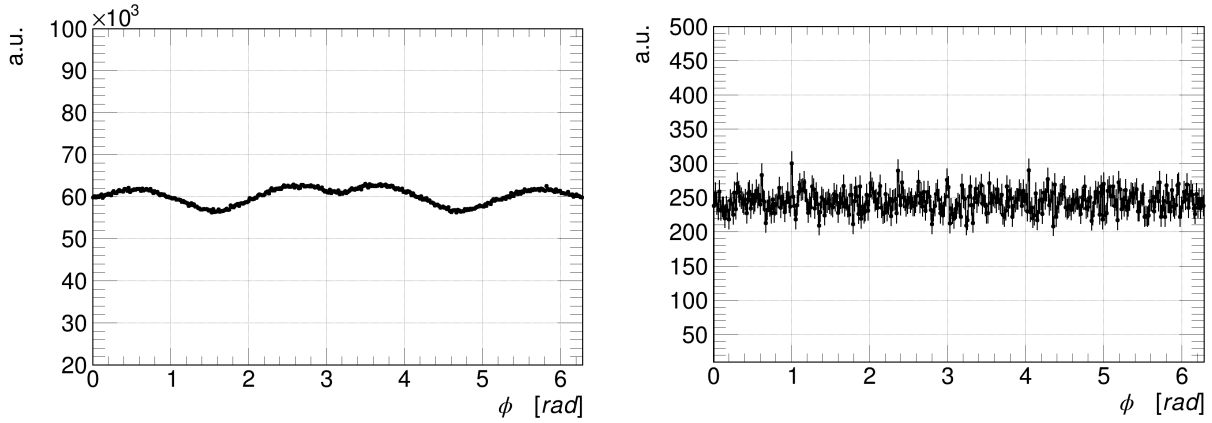

Figure 5.6: The simulated azimuth-angle distribution for cosmogenic muons (left) and neutrons (right) at the laboratory roof, obtained with step 1 of the simulation.

- the already mentioned *FLUX* output scheme;
- the so called *DETECTOR* output scheme.

While in the *FLUX* output scheme, the properties of the particles that cross the boundary between one volume to another are recorded, in the *DETECTOR* output scheme, the *GEANT 4 hits* are recorded for the scintillator panels and for the two HPGe detectors. The *GEANT 4 hits* represent the energy deposited inside an active volume, for which the time[1] and the position[2] is recorded. Hence, with the *DETECTOR* output scheme, the energy spectra as observed with the detectors and their time behavior are obtained. The two output schemes provide complementary information. The *FLUX* output scheme is used to obtain the particle fluxes at different positions within MINIDEX, which are not directly accessible with the experimental data, while the *DETECTOR* output scheme produces the variables that can be directly compared to the experimental data. In the *DETECTOR* output scheme, an energy cutoff of 100 keV was set such that no secondaries were created below 100 keV.
For computational reasons, under the assumption that the incoming particle fluxes do not change between the lab roof and the top of MINIDEX setup, both cosmogenic muons and neutrons were generated from a plane with dimensions $140\,\mathrm{x}\,120\,\mathrm{cm}^2$ (A^2_{gen}), placed 35 cm above the top scintillator panel of MINIDEX.
Although most of the remaining neutrons simulated are muon-induced and an angular correlation between the muons and high energy neutrons exists [106, 179, 178, 194], muons and neutrons were treated as uncorrelated, i.e. they were simulated separately.
As in step 1, the fluxes of μ^+ and μ^- were assumed to be identical and muon bundles were

[1]This is the time when the energy deposition occurred with respect to the beginning of the generated event.

[2]The position is expressed in the coordinate system defined for the simulation.

not considered.
For each output scheme, simulations were performed with two different "physics lists". The first one is the *default* list provided in MaGe and the second one is the modular physics list *Shielding*, which is currently recommended for underground physics by the GEANT4 collaboration [242]. Some details are presented in Sec. 5.3.
Furthermore, simulations were also performed for monoenergetic muons of 7.7 GeV, a value close to the mean energy of the muon spectrum obtained in step 1, and for muons of 0.77 GeV, an energy one order of magnitude lower. This was done to probe the influence of the different parts of the muon spectrum and of the angular distributions. The monoenergetic muons were injected vertically at the center of the MINIDEX top surface.
All the simulations performed in step 2 are based on GEANT4 v. 9.6.4.

Figures 5.7 and 5.8 show selected event displays produced with the *DETECTOR* output scheme. Figure 5.7 shows a through-going muon (left) which does not produce showers and a muon stopped in the apparatus (right). Figure 5.8 shows an event with muon-induced shower and an event with neutron-induced shower.

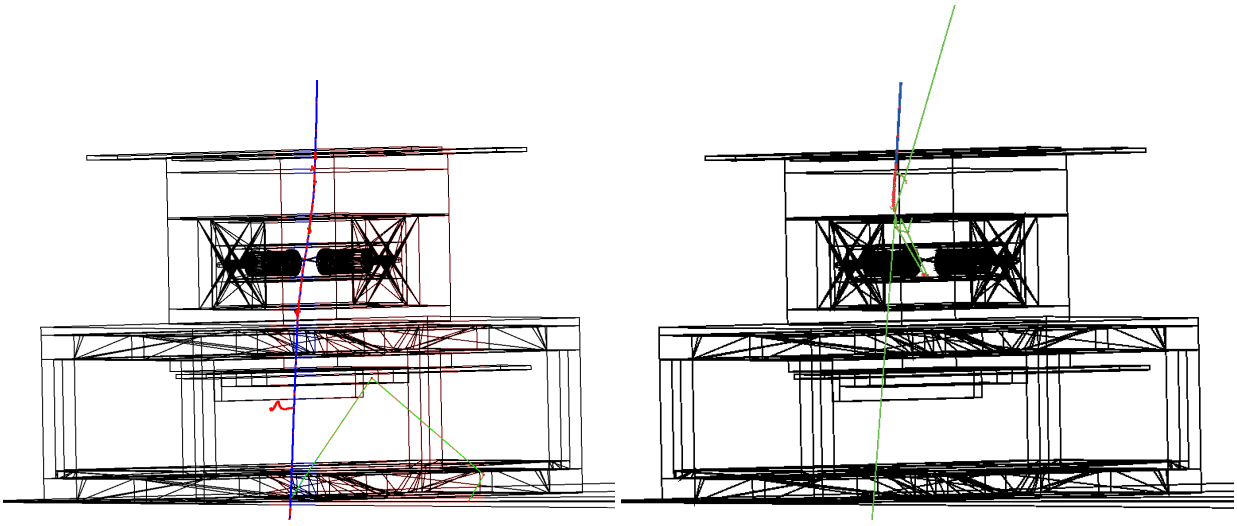

Figure 5.7: Left: a through-going muon which does not produce any shower. Right: a muon is stopped and few secondary particles are produced. Muons are shown in blue and neutral particles in green. Positrons and electrons are shown in red.

No natural radioactive background component was simulated. This will have to be done for future analyses.

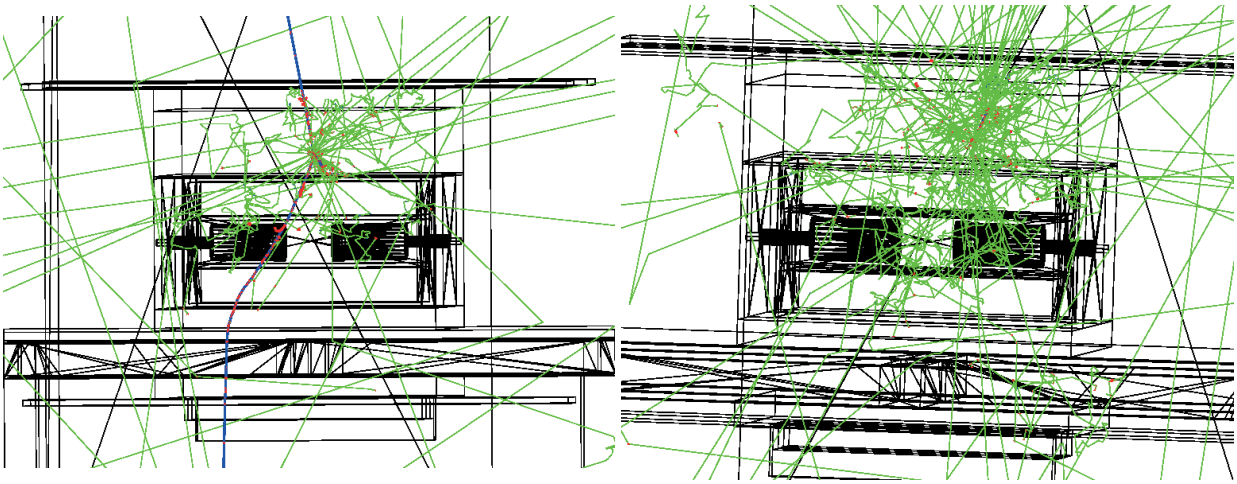

Figure 5.8: Left: muon-induced shower. Right: cosmogenic-neutron-induced shower. The neutrons enters from the top. Muons are shown in blue and neutral particles in green. Positrons and electrons are shown in red.

5.3 Comparison of Physics Lists

In the GEANT4 terminology, a physics list is a collection of physics processes. A physics process is applied to specific types of particles. Different modeling might occur for different energy realms. In the following, the chosen production thresholds, cross sections and energy ranges of the application of individual processes are specified. As previously mentioned, two different physics lists were used for step 2 of the MINIDEX simulations:

- the MaGe (v. May 2014) *default* physics list;
- the GEANT4 reference physics list *Shielding* v. 2.0 .

These two lists represent the best-guess selections of electromagnetic and hadronic physics processes for underground physics made by the developer teams of MaGe [217] and GEANT4 [243], respectively.
This work provides a validation for both the *MaGe default* and the *Shielding* physics lists. The *MaGe default* physics list is mainly based on the QGS[3]P[4]_BERT[5]_HP[6] GEANT4 reference physics list:

- contains all standard electromagnetic processes as implemented in GEANT4;

[3]Quark Gluon String model for collisions of a hadron with a nucleon in the nucleus, valid for hadron energies $\geq$ 20 GeV.

[4]G4Precompound model used for de-excitation of nuclei.

[5]Bertini model [244] for the final state of hadron inelastic scattering, valid for hadron energies $\leq$ 10 GeV.

[6]High Precision neutron model, a data driven model used for the neutron transport from $\leq$ 20 MeV down to thermal energies.

- Bertini-style cascade for hadrons of an initial energy of up to 9.5 GeV;
- QGS model for hadron-nucleus collisions with high energy ($\geq$ 20 GeV);
- Low Energy Parametrized (LEP) models in for hadronic showers in the medium energy range;
- G4Precompound model used for de-excitation of nuclei;
- data driven High Precision neutron package (NeutronHP) for neutron transport below kinetic energies of 20 MeV, down to thermal energies.

The *Shielding* physics list, in comparison, is mainly based on the FTF[7]P_BERT_HP GEANT4 reference physics list:

- contains all standard electromagnetic process as implemented in GEANT4;
- Bertini-style cascade for hadrons of an initial energy of up to 5 GeV;
- FTF model for for hadron-nucleus collisions with high energies ($\geq$ 4 GeV);
- G4Precompound model used for de-excitation of nuclei;
- data driven High Precision neutron package (NeutronHP) for neutrons transportation below 20 MeV, down to thermal energies.

As an example, the relevant differences between the models for inelastic neutron scattering are listed in Tab. 5.6.

Particle	***MaGe default***	***Shielding***
Neutron	QGSP (12 GeV - 100 TeV)	FTFP (4 GeV - 100 TeV)
	Bertini Cascade (19.9 MeV - 9.9 GeV)	Bertini Cascade (19.9 MeV - 5 GeV)
	G4LENeutronInelastic (9.5 GeV - 25 GeV)	-

Table 5.6: Comparison of the models for inelastic neutron scattering between the *MaGe default* and the GEANT4 *Shielding* physics lists. In the overlapping energy-region between two models, a probability which linearly increase (decrease) from 0 to 1 (from 1 to 0) is assigned to the models. The models are then chosen according to that probability.

For more details see [245, 243, 246, 247, 248].

[7]Fritiof string model for hadron-nucleus interactions, valid for hadron energies $\geq$ 5 GeV.

5.4 Comparison between Simulations

In this section, some relevant quantities obtained for the different simulation settings used in step 2 are compared and discussed for both the *FLUX* and *DETECTOR* output scheme. Table 5.7 summarizes the trigger-related information obtained with the *FLUX* output scheme.

Quantity	***MaGe default***	***Shielding***	**Monoenergetic (E_μ = 7.7 GeV)**	**Monoenergetic (E_μ = 0.77 GeV)**
Fluxes Φ $[\mathbf{m^{-2}\ s^{-1}}]$				
μ^+	8.2883	8.2883	-	-
μ^-	8.2883	8.2883	8.2883	8.2883
neutron	0.082158	0.082158	-	-
Generating Plane A^2_{gen} $[\mathbf{m^2}]$	1.68	1.68	-	-
En. Spectra				
μ^+	YES	YES	-	-
μ^-	YES	YES	NO	NO
neutron	YES	YES	-	-
Angular Distributions				
μ^+	YES	YES	-	-
μ^-	YES	YES	NO	NO
neutron	YES	YES	-	-
Number of Gen. Part., N_{gen}				
μ^+	$5.67923{\cdot}10^8$	$5.89211{\cdot}10^8$	-	-
μ^-	$5.73499{\cdot}10^8$	$5.95914{\cdot}10^8$	$9.99052{\cdot}10^8$	$9.97802{\cdot}10^8$
neutron	$4.99876{\cdot}10^8$	$4.96127{\cdot}10^8$	-	-
Number of Triggers, N^{geom}_{trig}				
μ^+	$1.04337{\cdot}10^8$	$1.08336{\cdot}10^8$	-	-
μ^-	$1.05398{\cdot}10^8$	$1.09611{\cdot}10^8$	$9.99049{\cdot}10^8$	$9.97612{\cdot}10^8$
neutron	0	0	-	-
Simulated Runtimes, RT_{MC} [s]				
μ^+	$4.07863{\cdot}10^7$	$4.23151{\cdot}10^7$	-	-
μ^-	$4.11868{\cdot}10^7$	$4.27965{\cdot}10^7$	$39.0403{\cdot}10^7$	$38.9841{\cdot}10^7$
neutron	$3.62164{\cdot}10^9$	$3.59448{\cdot}10^9$	-	-
Predicted Trig. Rates, R^{geom}_{trig} [Hz]				
μ^+	2.56	2.56	-	-
μ^-	2.56	2.56	2.56	2.56
neutron	0	0	-	-

Table 5.7: Trigger-related information for step 2 of the simulation in the *FLUX* output scheme, for different simulation settings.

It should be noted that in the *FLUX* output scheme, the trigger definition is purely geometric (${N_{trig}}^{geom}$), only requiring a muon to go through the top and the bottom scintillator, regardless its energy. In the *monoenergetic* cases, most of the generated muons do provide a geometrical trigger due to the vertical injection directly onto the MINIDEX setup. For *MaGe default* and *shielding*, RT_{MC} was evaluated according to Eq. 5.1, but for the *monoenergetic* cases, RT_{MC} was defined as follows:

$$ {RT_{MC}}^{mono} = \frac{{RT_{MC}}^{default} \cdot {N_{trig}}^{mono}}{{N_{trig}}^{default}} \ . \tag{5.3} $$

In Tab. 5.8 the fraction of geometrical triggers, for which at least one 2.2 MeV gamma reaches one of the HPGe detectors is reported. This is referred to as *successful trigger* fraction. It reflects the probability to produce and geometrically collect at least one 2.2 MeV

Generated Particle	***MaGe default***	***Shielding***	**Monoenergetic (E_μ = 7.7 GeV)**	**Monoenergetic (E_μ = 0.77 GeV)**
μ^+	$1.73{\cdot}10^{-4}$	$8.13 \cdot 10^{-5}$	-	-
μ^-	$1.75{\cdot}10^{-4}$	$8.62{\cdot}10^{-5}$	$2.31{\cdot}10^{-4}$	$1.14{\cdot}10^{-5}$

Table 5.8: Successful trigger fraction obtained with the *FLUX* output scheme, for different simulation settings.

gamma originating from the thermal-capture of a muon-induced neutron in the MINIDEX setup. The *MaGe default* physics list has a higher *successful trigger* fraction compared to the *Shielding* one. Thus, it results in a higher signal rate.
From the comparison between the two *monoenergetic* cases, it is already clear that, for shallow depths, the energy scale of the incoming muons is an important parameter.

Similarly to Tab. 5.7, Tab. 5.9 summarizes the trigger-related information for the *DETECTOR* output scheme.

Quantity	***MaGe default***	***Shielding***	**Monoenergetic (E_μ = 7.7 GeV)**	**Monoenergetic (E_μ = 0.77 GeV)**
Fluxes Φ [$\mathbf{m^{-2}\ s^{-1}}$]				
μ^+	8.2883	8.2883	8.2883	8.2883
μ^-	8.2883	8.2883	8.2883	8.2883
neutron	0.082158	0.082158	0.082158	0.082158
Generating Plane A^2_{gen} [$\mathbf{m^2}$]	1.68	1.68	-	-
En. Spectra				
μ^+	YES	YES	NO	NO
μ^-	YES	YES	NO	NO
neutron	YES	YES	YES	YES
Angular Distributions				
μ^+	YES	YES	NO	NO
μ^-	YES	YES	NO	NO
neutron	YES	YES	YES	YES
Number of Gen. Part., N_{gen}				
μ^+	$9.99852{\cdot}10^8$	$9.98952{\cdot}10^8$	$9.99852{\cdot}10^8$	$9.99802{\cdot}10^8$
μ^-	$9.99852{\cdot}10^8$	$9.99052{\cdot}10^8$	$4.99926{\cdot}10^8$	$9.99852{\cdot}10^8$
neutron	$4.98576{\cdot}10^8$	$4.99426{\cdot}10^8$	$4.98576{\cdot}10^8$	$4.98576{\cdot}10^8$
Number of Triggers, N_{trig}				
μ^+	$1.92365{\cdot}10^8$	$1.92246{\cdot}10^8$	$9.99048{\cdot}10^8$	$9.99669{\cdot}10^8$
μ^-	$1.93079{\cdot}10^8$	$1.92951{\cdot}10^8$	$4.99524{\cdot}10^8$	$9.99717{\cdot}10^8$
neutron	$3.18432{\cdot}10^5$	$3.19371{\cdot}10^5$	$3.18432{\cdot}10^5$	$3.18432{\cdot}10^5$
Simulated Runtimes, RT_{MC} [s]				
μ^+	$7.1806{\cdot}10^7$	$7.17414{\cdot}10^7$	$37.2925{\cdot}10^7$	$37.3156{\cdot}10^7$
μ^-	$7.1806{\cdot}10^7$	$7.17486{\cdot}10^7$	$18.5773{\cdot}10^7$	$37.1794{\cdot}10^7$
neutron	$3.61223{\cdot}10^9$	$3.61838{\cdot}10^9$	$3.61223{\cdot}10^9$	$3.61223{\cdot}10^9$
Predicted Trig. Rates, R_{trig} [Hz]				
μ^+	2.68	2.68	2.68	2.68
μ^-	2.69	2.69	2.69	2.69
neutron	$8.8154{\cdot}10^{-5}$	$8.8263{\cdot}10^{-5}$	$8.8154{\cdot}10^{-5}$	$8.8154{\cdot}10^{-5}$

Table 5.9: Trigger-related information for step 2 of the simulation in the *DETECTOR* output scheme, for different simulation settings.

As the results obtained with the *DETECTOR* output scheme can be directly compared to experimental data, the results obtained in *MaGe default* in step 2 when injecting neutrons were included as background component for the monoenergetic cases. The trigger definition for the *DETECTOR* output scheme was used as given in Sec. 4.6 for the experimental data. With that trigger definition, also neutrons produce a few triggers. However, these neutron-induced triggers are very rare and were neglected in the analysis.
As in the case of the *FLUX* output scheme, most of the generated muons produce a trigger in the monoenergetic cases. The corresponding RT_{MC} were evaluated according to in Eq. 5.3.
The actual trigger rate, R_{trig}, is slightly higher than the geometrical trigger rate, ${R_{trig}}^{geom}$, obtained with the *FLUX* output scheme. Nevertheless, the simulated total, i.e. μ^+ plus μ^-, trigger rate is approximately 2 times lower than the measured one. This reflects the choice of the sizes (A^1_{gen} and A^2_{gen}) of the generating planes and some other aspects of the geometry used in the simulation. The reduced trigger rate in the MC is roughly compatible with the loss of muons as predicted by simple geometric considerations. Further comparisons of data and MC are discussed in Ch. 6.

The *FLUX* output scheme was used to study the flow of particles inside MINIDEX. The following numbers were evaluated:

- **nPb**: number of neutrons at the internal surface of the lead castle going towards the inside of the setup, i.e. towards the HPGe detectors;
- **nW**: number of neutrons at the internal surface of the water container going towards the inside of the setup;
- **nHPGe**: number of incoming neutrons to the HPGe surfaces;
- **2.2MeVgW**: number of 2.2 MeV gammas at the internal surface of the water container going towards the inside of the setup;
- **2.2MeVgHPGe**: number of incoming 2.2 MeV gammas to the HPGe surfaces.

These numbers were normalized to the number of triggers. Table 5.10 reports the results for the different MC settings.
It should be noted that these values were obtained without considering any time window. Furthermore, to evaluate the *averaged* values, a μ^+/μ^- ratio = 1 was assumed.
The results listed in Tab. 5.10 indicate that:

- the neutron yield due to μ^- is larger than due to μ^+, because of neutrons produced in μ^- capture. In the *default* case, it is a factor ≈4 larger, while the *Shielding* MC predicts even a factor of ≈8 larger. This reflects that muon capture at rest is treated differently in the two physics lists. Furthermore, the contribution of muon capture at rest to the total muon-induced neutron flux is substantial. Hence, it will have to be included into a future analysis.

Variable	*MaGe default*	*Shielding*	*default / Shielding*	Monoen. (7.7 GeV)	Monoen. (0.77 GeV)
nPb					
μ^+	$5.31{\cdot}10^{-2}$	$2.39{\cdot}10^{-2}$	2.22	-	-
μ^-	$2.25{\cdot}10^{-1}$	$1.97{\cdot}10^{-1}$	1.14	$7.41{\cdot}10^{-3}$	$3.41{\cdot}10^{-4}$
Average	$1.39{\cdot}10^{-1}$	$1.10{\cdot}10^{-1}$	1.26	-	-
nW					
μ^+	$3.64{\cdot}10^{-3}$	$1.46{\cdot}10^{-3}$	2.5	-	-
μ^-	$1.52{\cdot}10^{-2}$	$1.30{\cdot}10^{-2}$	1.16	$5.54{\cdot}10^{-4}$	$2.46{\cdot}10^{-5}$
Average	$9.40{\cdot}10^{-3}$	$7.25{\cdot}10^{-3}$	1.30	-	-
nW / nPb	0.068	0.066	-	0.075	0.072
nHPGe					
μ^+	$1.79{\cdot}10^{-3}$	$7.09{\cdot}10^{-4}$	2.52	-	-
μ^-	$7.61{\cdot}10^{-3}$	$6.58{\cdot}10^{-3}$	1.16	$3.99{\cdot}10^{-4}$	$1.75{\cdot}10^{-5}$
Average	$4.70{\cdot}10^{-3}$	$3.64{\cdot}10^{-3}$	1.29	-	-
nHPGe / nW	0.5	0.5	-	0.7	0.7
2.2MeVgW					
μ^+	$6.16{\cdot}10^{-4}$	$2.76{\cdot}10^{-4}$	2.23	-	-
μ^-	$2.60{\cdot}10^{-3}$	$2.28{\cdot}10^{-3}$	1.14	$7.86{\cdot}10^{-5}$	$3.63{\cdot}10^{-6}$
Average	$1.61{\cdot}10^{-3}$	$1.28{\cdot}10^{-3}$	1.23	-	-
2.2MeVgW / nPb	0.012	0.012	-	0.011	0.011
2.2MeVgHPGe					
μ^+	$2.47{\cdot}10^{-4}$	$1.11{\cdot}10^{-4}$	2.25	-	-
μ^-	$1.06{\cdot}10^{-3}$	$9.27{\cdot}10^{-4}$	1.14	$5.08{\cdot}10^{-5}$	$2.46{\cdot}10^{-6}$
Average	$6.52{\cdot}10^{-4}$	$5.19{\cdot}10^{-4}$	1.26	-	-
2.2MeVgHPGe / 2.2MeVgW	0.41	0.41	-	0.65	0.68

Table 5.10: Number of particles at the internal surfaces of MINIDEX. The numbers were normalized to the number of triggers. Details are given in the text.

- the *MaGe default* physics list predicts a higher neutron yield than the *Shielding* physics list.
- since the ratios of numbers for the *default* and *Shielding* settings are similar for the different variables, the difference between the two physics lists lies mainly in the neutron yield processes.
- the number of neutrons at the inner surface of the water tank is only ≈7%[8] of the number of neutrons entering from the outside. This demonstrates how efficient

[8]It should be noted that for MINIDEX run I it was not possible to distinguish between neutrons that were generated inside the water from those that were generated inside the lead.

water is in thermalizing and stopping neutrons. However, there is still a significant number of neutrons entering the innermost part of MINIDEX. Future analyses should also look for signatures of direct neutron interactions with the Germanium (mainly inelastic scattering) [249].

- approximately ≈1% of the neutrons entering the water container cause the emission of a 2.2 MeV gamma which passes the inner surface of the water container.
- geometrically, ≈40% of the 2.2 MeV gammas passing through the inner surface of the water container reach the HPGe detectors.
- from the comparison between the two *monoenergetic* cases and the complete *default* simulation, it is clear that including the angular distribution of the incoming muons in step 2 makes a big difference for MINIDEX, because the amount of lead traversed in the center and the side of the setup (see Fig. 4.6 left) is very different.
- the comparison of the simulations of 0.77 GeV and 7.7 GeV *monoenergetic* muons demonstrates that the neutron yield is very sensitive to the muon energy[9]. Therefore, the incoming muon spectrum should not be replaced by a monoenergetic beam for simulations for shallow depths.

The *FLUX* scheme cannot be used to evaluate the number of 2.2 MeV gammas observed in the germanium detectors, because the probability of full absorption has to be taken into account. The *DETECTOR* output scheme was used to calculate the fraction of muon triggers which result in a 2.2 MeV gamma identified in the peak of the spectrum recorded by the germanium detectors. This fraction is of the order of 10^{-5}.

[9]The relative importance of the different processes responsible for neutron production varies with the muon energy.

5.5 Particle Distributions at Different Surfaces of MINIDEX

In this section, the energy spectra obtained with the *FLUX* output scheme for different particles are presented. Also discussed are other quantities, like neutron multiplicity and neutron yield. Unless otherwise specified, the results were obtained with the *MaGe default* settings. Selected results are compared for different simulation settings. The data of MINIDEX run I do not provide a direct access to these quantities.
It is important to point out that, for the quantities presented in this section, no trigger requirements were applied.

5.5.1 Energy Spectra

Figure 5.9 shows the neutron energy spectra at the inner surface of the lead castle, going towards the water container, generated by μ^+, μ^- and neutrons.

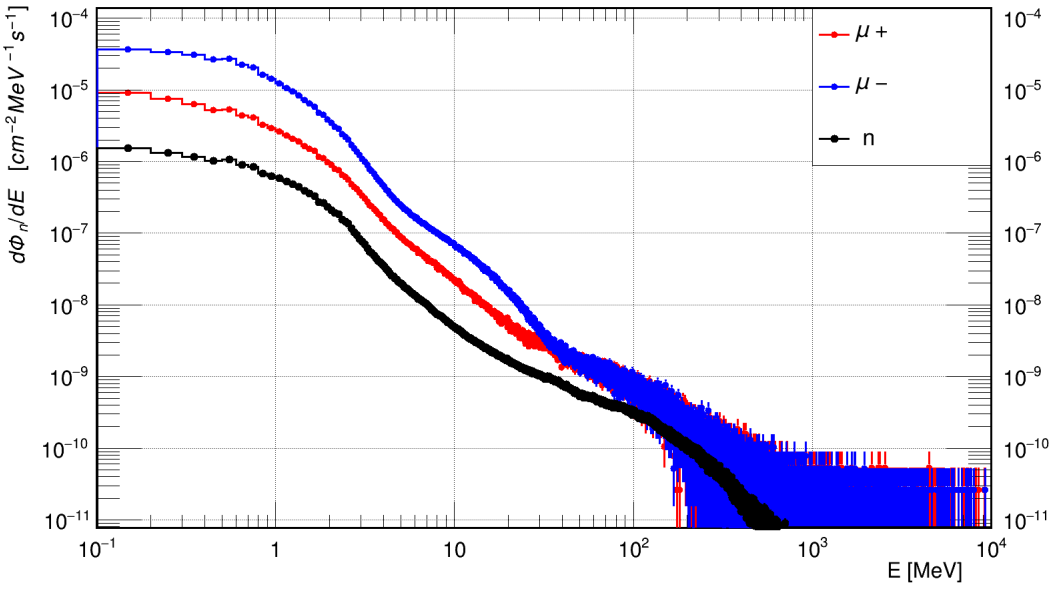

Figure 5.9: The neutron energy spectra at the inner surface of the MINIDEX lead castle, going towards the water container, generated by μ^+, μ^- and neutrons, in red, blue and black, respectively. These spectra were obtained with the *MaGe default* settings.

Similar spectral shapes are observed for the three different types of injected particles. However, the μ^- produce more neutrons than μ^+ below 30 MeV. This is due to muon capture [197], which is only relevant for μ^-.
Figures 5.10 and 5.11 show the gamma energy spectra at the inner water surface going towards the innermost area of MINIDEX and at the outer surface of the HPGe detectors,

respectively. The 2.2 MeV line is clearly visible for all three types of initial particles.

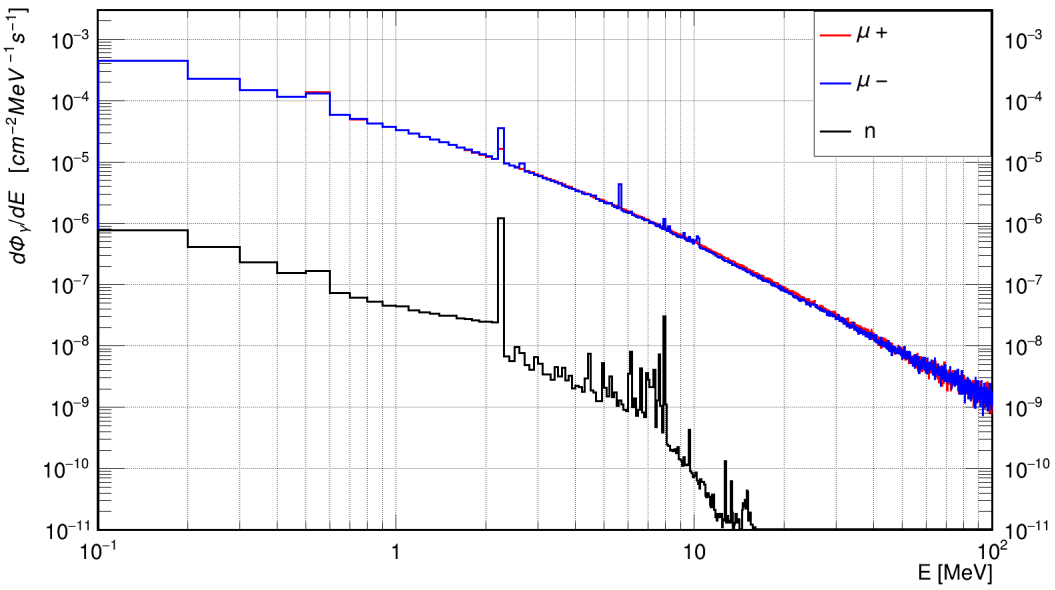

Figure 5.10: Gamma spectra at the inner water surface, going towards the innermost part of MINIDEX. Distributions obtained with *MaGe default* simulation settings.

No difference in shape between μ^+ and μ^- is seen. This indicates that the only difference between the two particles is at the neutron yield level. This is confirmed by a higher number of 2.2 MeV gammas visible in the μ^- case, reflecting the higher number of neutrons produced, see also Tab. 5.10.
The spectra of incoming neutrons at the surface of the HPGe detectors are shown in Fig. 5.12. The difference in intensity between μ^+ and μ^- reflects again the difference in the neutron yield. However, no difference in shape is observed. This is due to the thermalization process inside the water. The contribution from neutrons is small because of the low flux of cosmogenic neutrons. However, at energies around 100 MeV, this contribution is significant.

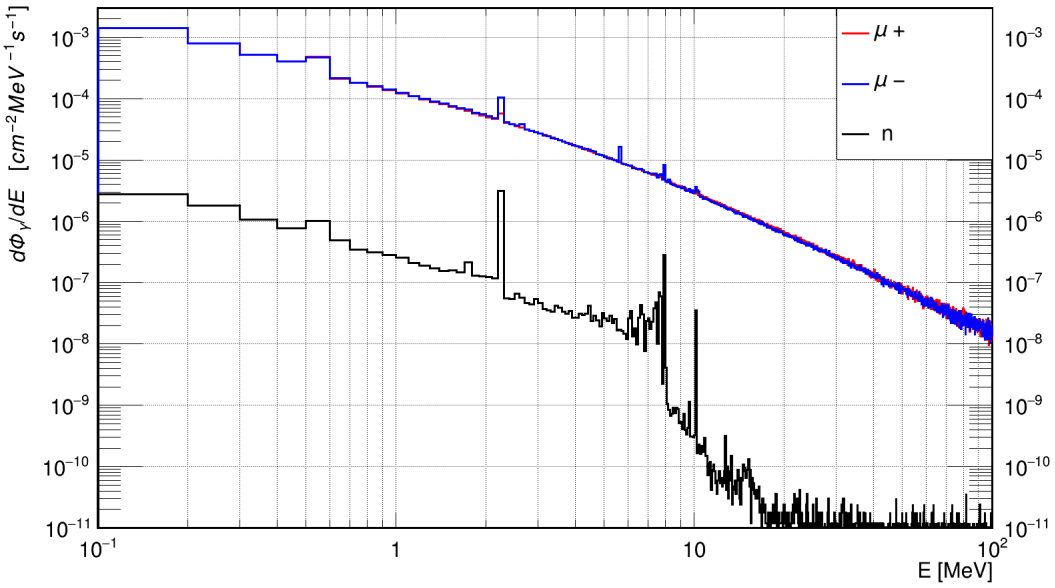

Figure 5.11: Gamma spectra for incoming gammas at the surface of the HPGe detectors. Distributions obtained with *MaGe default* simulation settings.

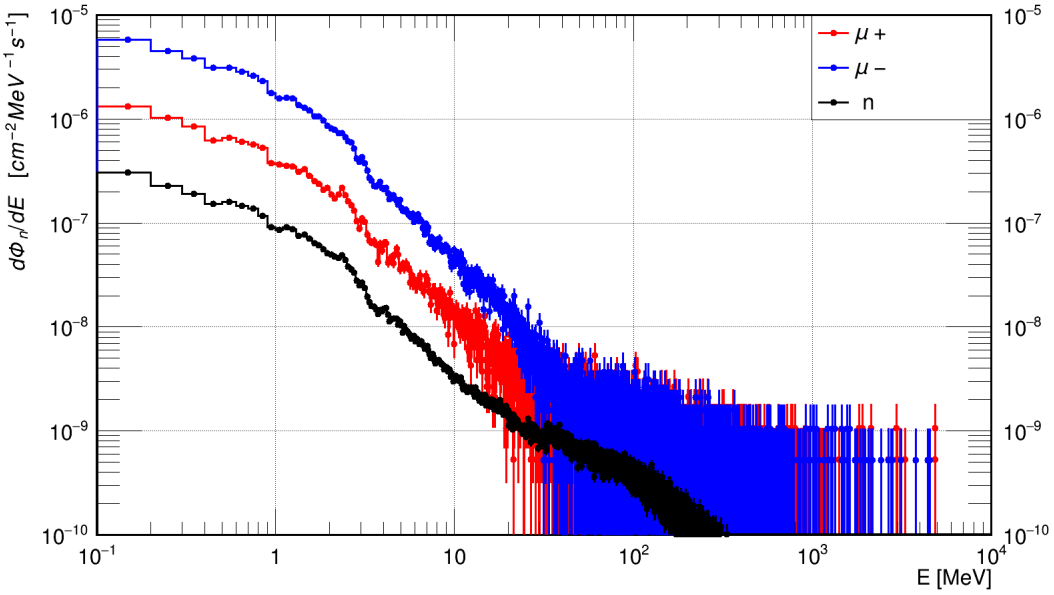

Figure 5.12: The incoming neutron energy spectra at surface of the HPGe detectors for μ^+, μ^- and neutrons, in red, blue and black, respectively. These spectra were obtained with the *MaGe default* settings.

The total neutron spectra at different surfaces, obtained by summing the different components, are compared in Fig. 5.13. As expected, there is no difference in spectral shape between the neutrons at the inner surface of the water tank and at the outer surface of the HPGe detectors. The only differences are due to geometrical effects. The spectral shape of neutrons of the inner surface of the lead castle is different from the one of neutrons emerging from the water. The spectrum of neutron emerging from the inner surface of the lead wall has a low energy plateau due to thermalization in lead and the contribution from μ^- capture. These low-energy neutrons are more likely absorbed than higher-energy neutrons. The water volume is not big enough to thermalize all high-energy neutrons, which effectively makes the spectrum harder.

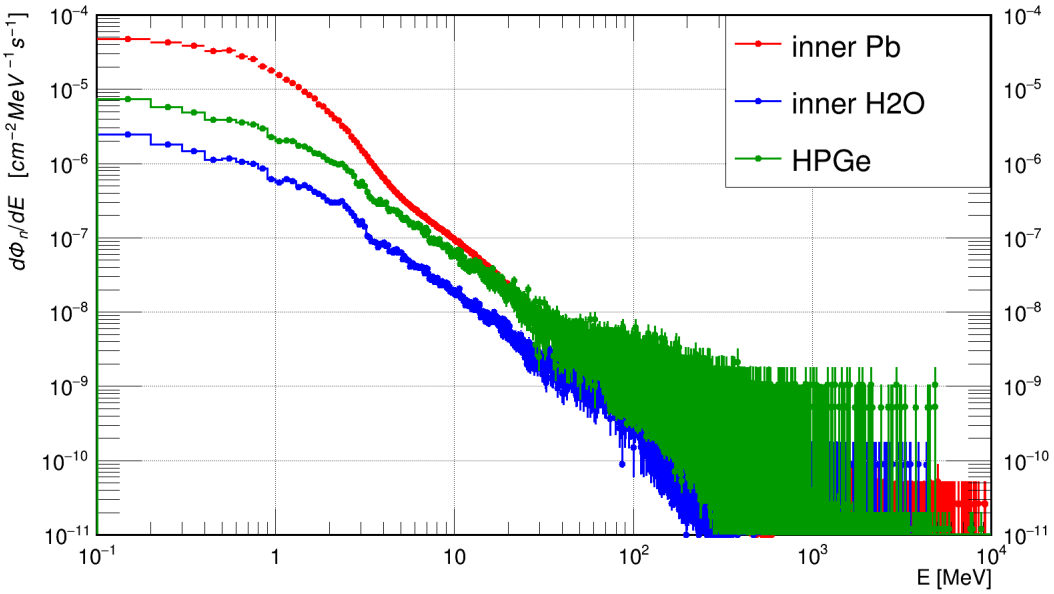

Figure 5.13: Total neutron spectra at the inner surface of the lead, the inner surface of the water and the outer surface of the HPGe detectors. These spectra were obtained with the *MaGe default* settings, summing the individual components from μ^+, μ^- and neutrons.

Correspondingly, Fig. 5.14 shows the total gamma spectra at the same surfaces as selected for the neutron spectra. As expected, due to the neutron thermalization and subsequent thermal-capture by the hydrogen atoms in the water, the 2.2 MeV line arises only after the neutrons have entered the water.

The differences between results obtained with the different simulations settings are illustrated in Figs. 5.15 and 5.16. Specifically, Fig. 5.15 shows a comparison of the neutron spectra at the inner lead surface for neutrons going towards the water container. Consistent with Tab. 5.10, the *MaGe default* physics list results in the production of more

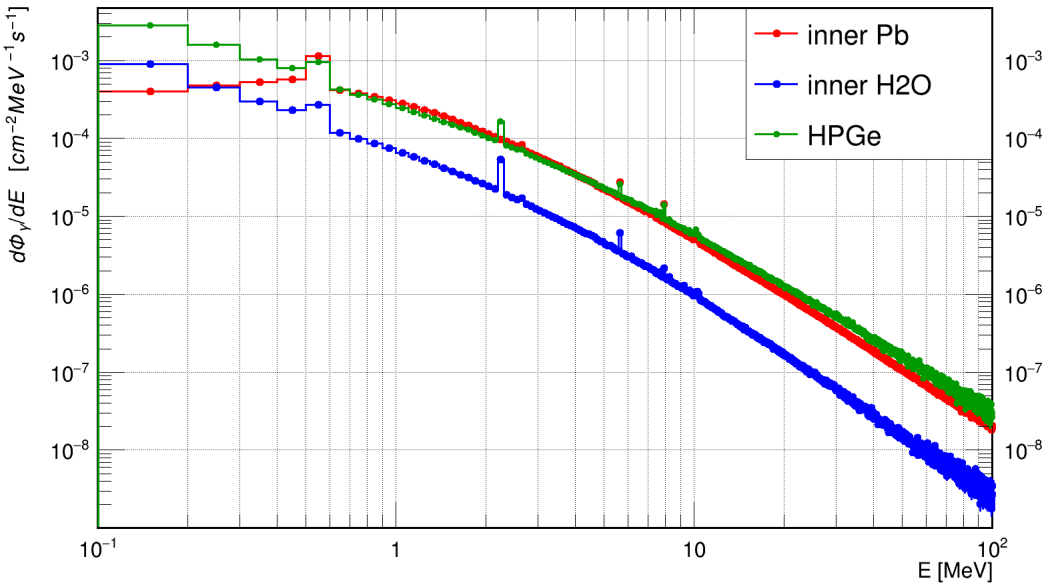

Figure 5.14: Total gamma spectra at the inner surface of the lead, the inner surface of the water and the outer surface of the HPGe detectors. These spectra were obtained with the *MaGe default* settings, summing the individual components from μ^+, μ^- and neutrons.

neutrons than the *Shielding* physics list, especially at high energies. At 40 MeV the difference reaches a factor of 0.7. Above 40 MeV the neutron flux predicted for monoenergetic muons ($E_\mu = 7.7$ GeV), for which the simulation is based on the *MaGe default* physics list, is higher than the one predicted with the *Shielding* physics list. No substantial difference in terms of shape between the complete *MaGe default* simulation and the simulation of monoenergetic muons is observed. The only significant difference is the neutron intensity. As already mentioned, neither the energy spectrum nor the angular distribution of the incoming muons can be neglected at shallow depths. The cutoff in the neutron spectrum in the monoenergetic case with $E_\mu = 0.7$ GeV is due to the limited energy of the incoming muons. The simulation of monoenergetic muons with the actual mean energy of the muons does not predict such a cutoff, but predicts a flux substantially lower than the full spectrum cases at low neutron energies. This is also connected to the simplified generation geometry without angular distribution and a single generation point. Such simplifications are clearly unsuited.

Figure 5.16 shows the different spectra of gammas entering the HPGe detectors. Here, there is no difference in shape between the *MaGe default* and the *Shielding* predictions. The main difference is the higher intensity of 2.2 MeV gammas predicted by *MaGe*. Figures 5.16 and 5.14 indicate the presence of other neutron-induced gamma lines, like the

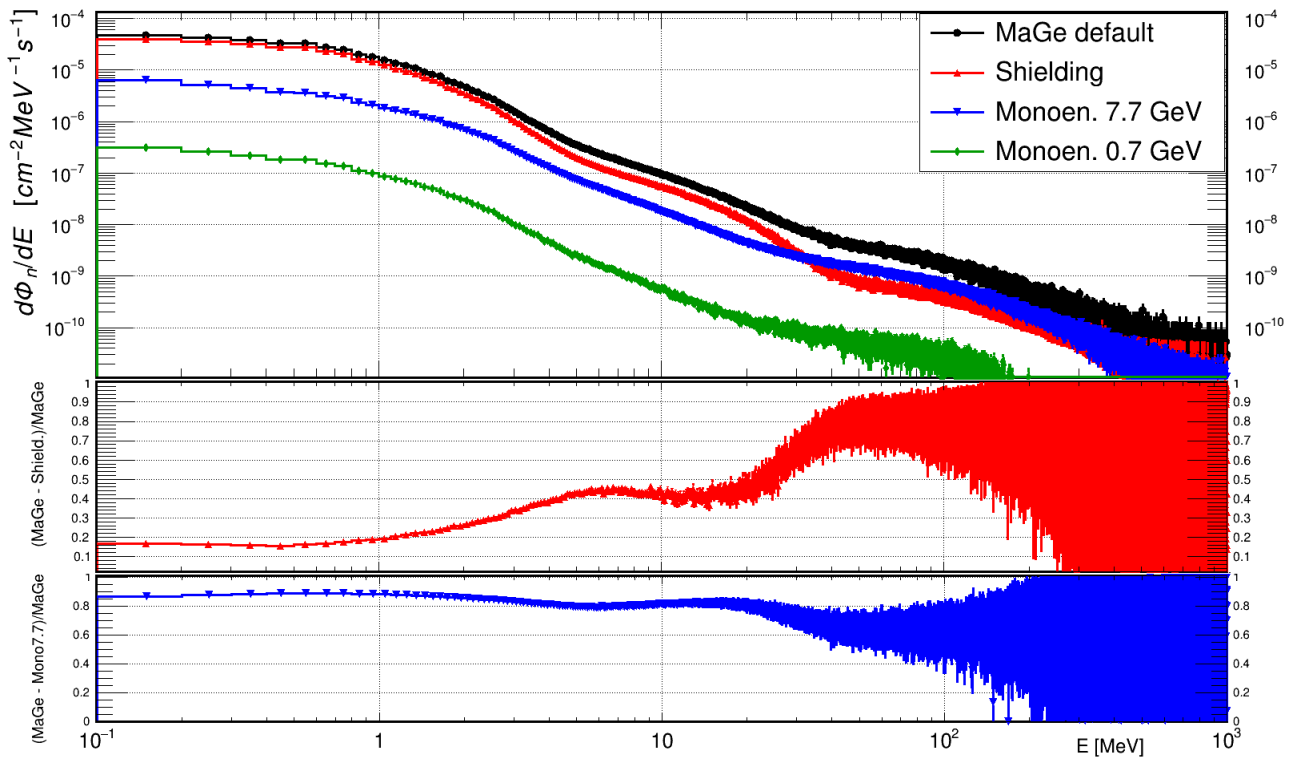

Figure 5.15: Comparison between the total neutron spectra at the inner lead surface as predicted by the *MaGe default* (black), *Shielding* (red), monoenergetic $E_\mu = 7.7\,\text{GeV}$ (blue) and monoenergetic $E_\mu = 0.7$ GeV (green) settings. The relative differences between the *MaGe default* and both the *Shielding* and *monoenergetic* ($E_\mu = 7.7\,\text{GeV}$) predictions are also shown.

gamma line at ≈7.9 MeV, which is due to neutron capture in copper[10], ^{63}Cu(n,γ), [249] and other lines around 10 MeV. They were not considered for the analysis presented in this thesis, however, there are already plans to include them in future analyses.

[10]The copper is present both in the layer between the water container and the uppermost part of the lead castle, and in the cooling finger of the HPGe detectors.

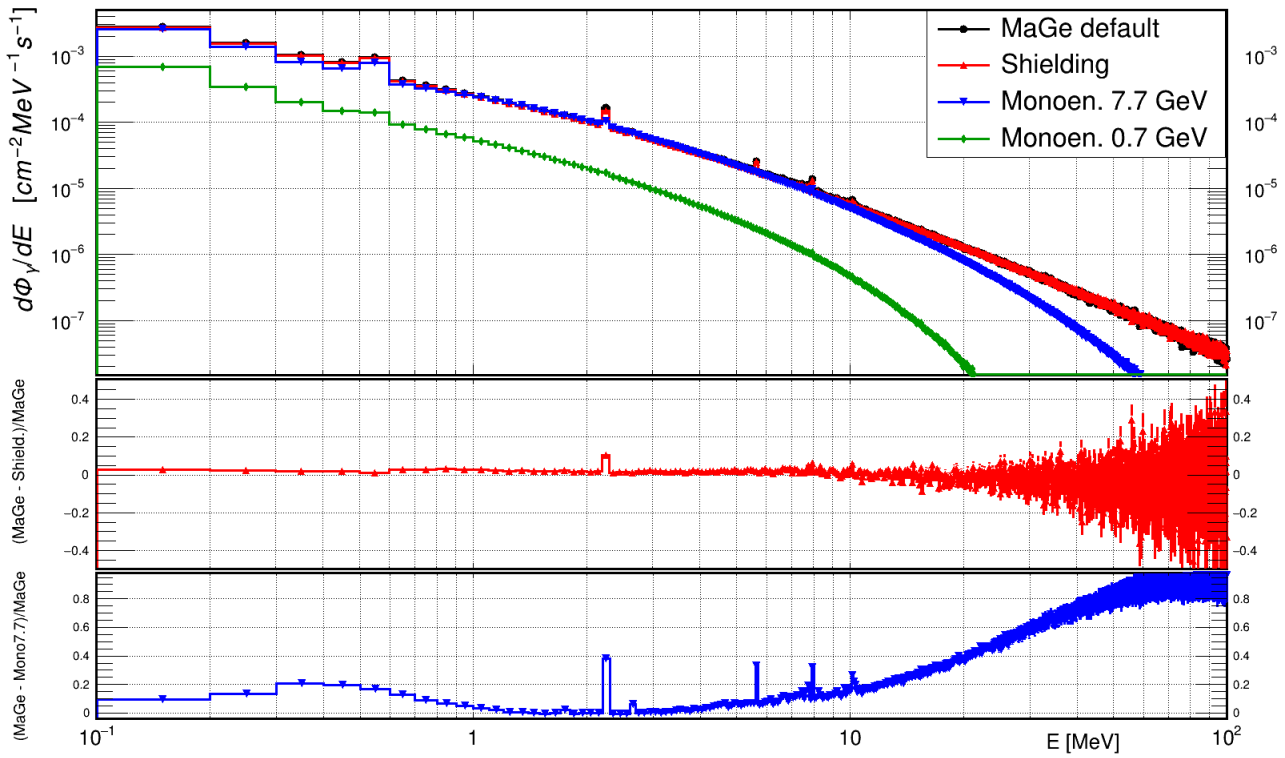

Figure 5.16: Comparison between the total incoming gamma spectra at the outer surface of the HPGe detectors as predicted by *MaGe default* (black), *Shielding* (red), monoenergetic $E_\mu = 7.7$ GeV (blue) and monoenergetic $E_\mu = 0.7$ GeV (green) simulation settings. The relative differences between the *MaGe default* and both the *Shielding* and *monoenergetic* ($E_\mu = 7.7$ GeV) predictions are also shown.

5.5.2 Neutron Multiplicity

A quantity, which is often discussed in the literature is the neutron multiplicity.
Figure 5.17 shows the neutron multiplicity, M, which is defined as the number of neutrons (without any energy requirement) at the inner surface of the lead castle going towards the water container produced in a simulated event, obtained for μ^+ and μ^-. There was no trigger requirement. The distribution depicted in Fig. 5.17 starts at M = 1. The fraction of traversing μ^+ and μ^- with M = 0 is ≈98.5% and ≈99.7%, respectively. The mean multiplicity (for M>0) for μ^+ is ≈5 while it is ≈3.2 for μ^-.

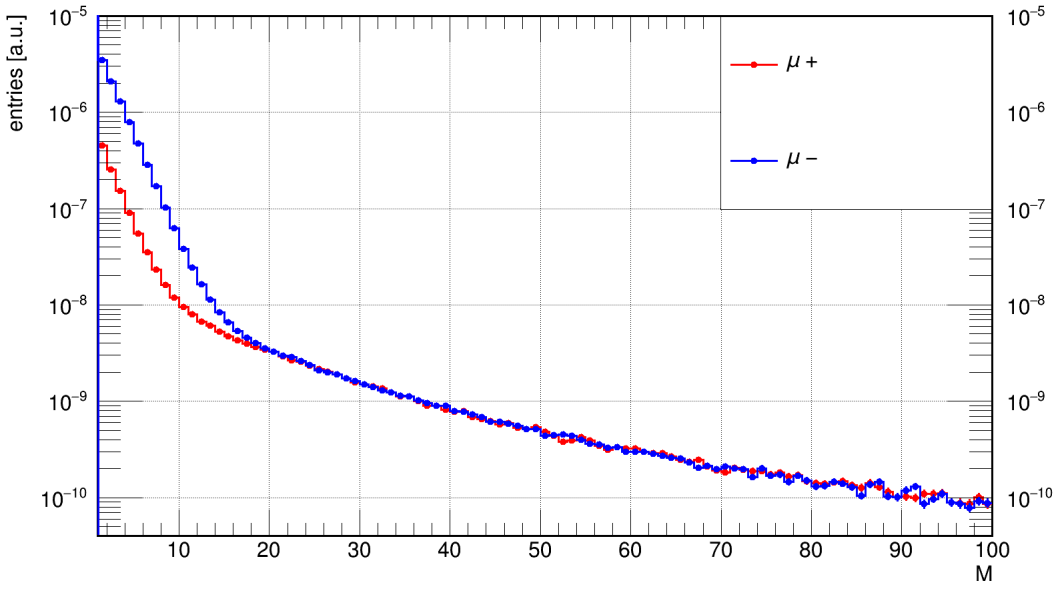

Figure 5.17: Distribution of neutron multiplicity as predicted for μ^+ and μ^-. The distributions were normalized per triggered muon and per area of the surface considered.

The M distributions have two regimes: one for low M (M≤15) and one for high M (M≥15). At M≈15, the distributions change from very steep to a long tail. Beyond that M, the distributions for μ^+ and μ^- are similar, while below, the distribution for μ^- shows extra low-multiplicity events. The extra contribution is most likely due to μ^- capture, see also Fig. 5.9. A detailed study was beyond the scope of this thesis. However, for future analyses, several effects have to be taken into account. The different regimes could be also associated to different geometries, i.e. muons interacting in lead or water. As the two regimes were also observed in the distribution for monoenergetic muons, which are injected onto the center of the top plate, the effect cannot be confined to the lead walls. A detailed study of all the processes involved will have to be done.

Figure 5.18 shows the distribution of neutron multiplicity for all muons for selected neutron energy thresholds.

A very long tail is observed, if no energy cut is applied. There are no events with many

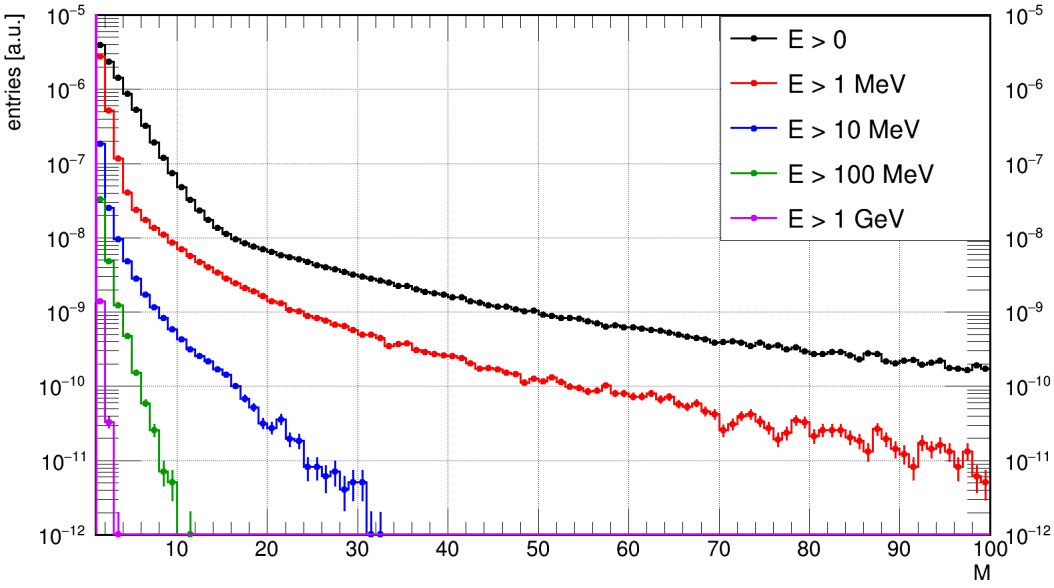

Figure 5.18: Distribution of neutron multiplicity for all neutrons for selected neutron energy thresholds. The distributions were normalized per triggered muon and per area of the surface considered.

high-energy neutrons. However, there are a significant number of events with at least one neutron with an energy above 100 MeV. Future studies should investigate whether these are accompanied by large numbers of low-energy neutrons.

A comparison of the neutron multiplicities as predicted by different simulation settings is depicted in Fig. 5.19. The *MaGe default* prediction differs from the *Shielding* prediction only for high-M events. Furthermore, the cutoff observed in the prediction for the monoenergetic muons with $E_\mu = 0.7\,\mathrm{GeV}$ demonstrates that there is a correlation between events induced by high-energy muons and high-M events. Future studies on high-M events are desirable as well as on the contribution from high-energy muons. The comparison between *MaGe* for muons according to the spectrum and monoenergetic muons indicates that high-energy muons are very important when predicting the total number of neutrons reaching an experiment.

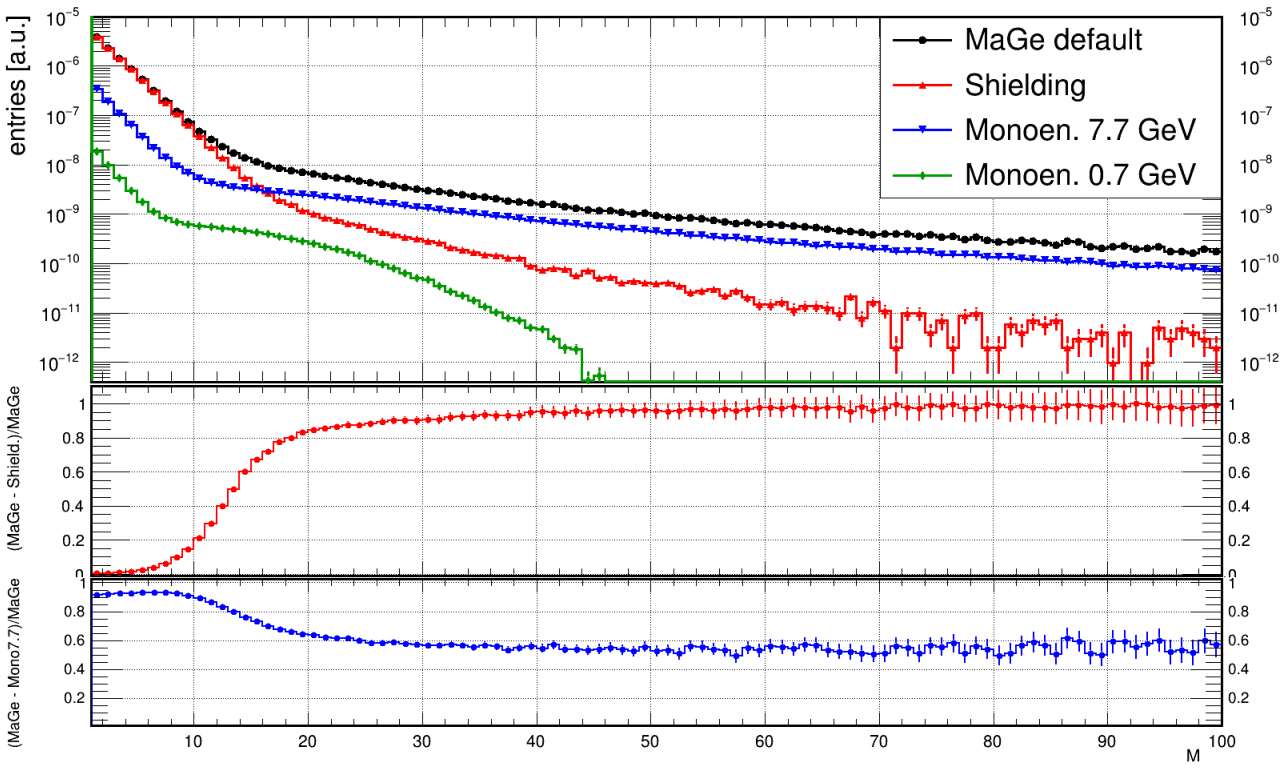

Figure 5.19: Distributions of neutron multiplicity for all muons, without any requirement on the neutron energy, obtained with the different simulation settings. The distributions were normalized per triggered muon and per area of the surface considered. Also shown are the relative differences between *MaGe* and *Shielding* settings and between *MaGe* for muons spectrally distributed and monoenergetic muons.

5.5.3 Neutron Yield

The neutron yield is defined for muons fulfilling the geometrical acceptance requirement as described in Sec. 5.4. According to convention, it is calculated for a material thickness expressed in g/cm^2. In MINIDEX, the surface, which provides the best access to this quantity, is the interface between the lid and the top of the water tank. For this surface, the neutrons emerging from the lid (lead) and entering the water are counted.
The differential yield, dY$_n$/dE, per any triggered muon is shown in Fig. 5.20 for different settings of the simulation.

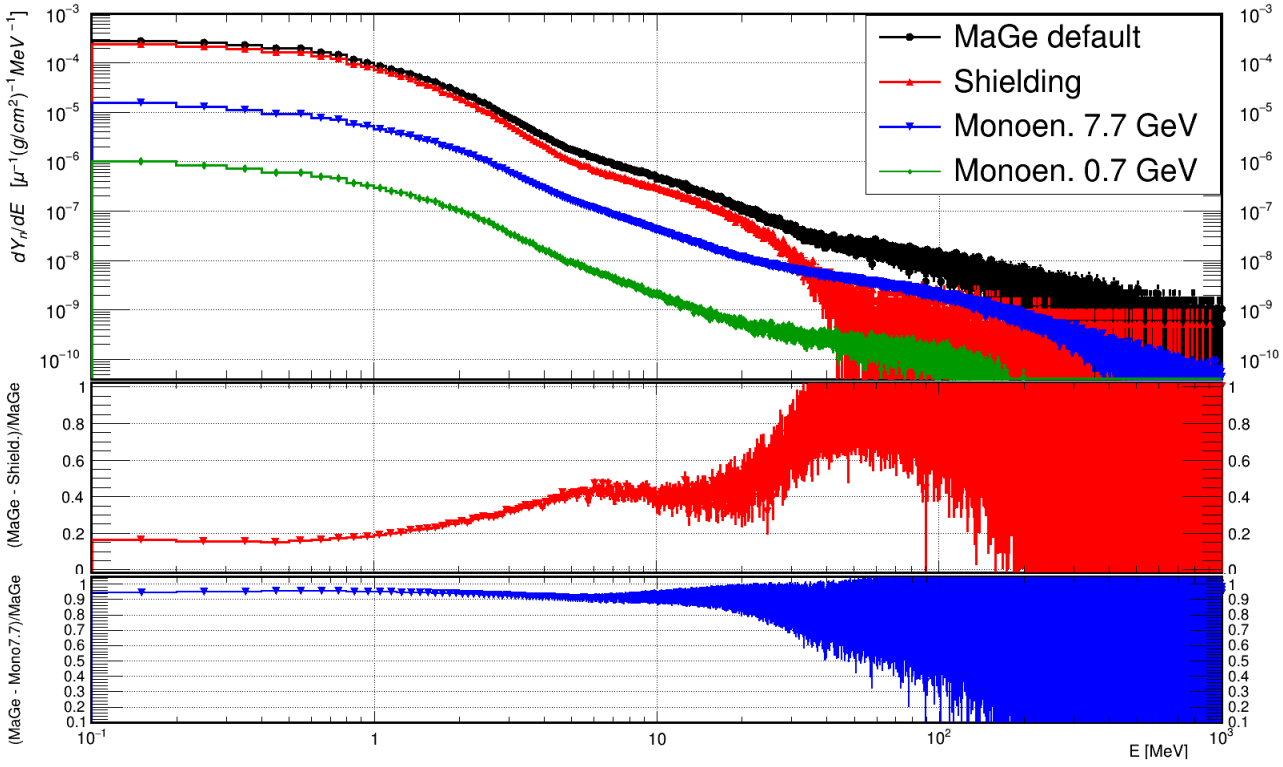

Figure 5.20: Differential neutron yield, dY$_n$/dE, as predicted by the different simulation settings. See text for details.

Correspondingly, Tab. 5.11 reports the integral neutron yield obtained for the different settings.

In agreement with what has been shown so far, the *MaGe default* physics list predicts highest neutron yield. The difference increases at larger neutron energies. The muons considered for Fig. 5.20 and Tab. 5.11 include muons entering from the top of the side lead walls of MINIDEX. This corresponds to the limited trigger abilities of MINIDEX run I. The neutron yield predicted for monoenergetic muons reflects partially that these muons

Variable	*MaGe default*	*Shielding*	Monoen. (7.7 GeV)	Monoen. (0.77 GeV)
$\mathbf{Y}_n$ $[\frac{n}{\mu(g/cm^2)}]$	$4.34{\cdot}10^{-4}$	$3.51{\cdot}10^{-4}$	$2.32{\cdot}10^{-5}$	$1.49{\cdot}10^{-6}$

Table 5.11: Integral neutron yields as predicted by the different simulation settings.

are injected onto the center of the apparatus.
The neutron yield, as aforementioned, was not measured in MINIDEX run I. Further discussions about this important quantity follow in Ch. 7.

5.5.4 Double Counting

An effect which was not been taken into account so far is *double counting*. This effect refers to the fact that neutrons can scatter back and forth through the surface under consideration. These neutrons are therefore counted more than once for that specific surface. To eliminate this effect, one should take the particle out of the simulation stack after the first crossing of the surface. However, it is also possible to use a correction factor for this effect:

$$\frac{IN - OUT}{IN} \quad , \tag{5.4}$$

where:

- IN: number of particles which traverse the surface inwards;
- OUT: number of particles which traverse the surface outwards.

An example of such a correction factor is given in Fig. 5.21 for the neutrons traversing the inner surface of the lead castle inwards as a function of the neutron energy. The correction is large, especially around 1 MeV; it reaches around 75%. This result was obtained for the *MaGe default* physics list. It will have to be investigated whether other physics lists treat this backscattering effect differently.

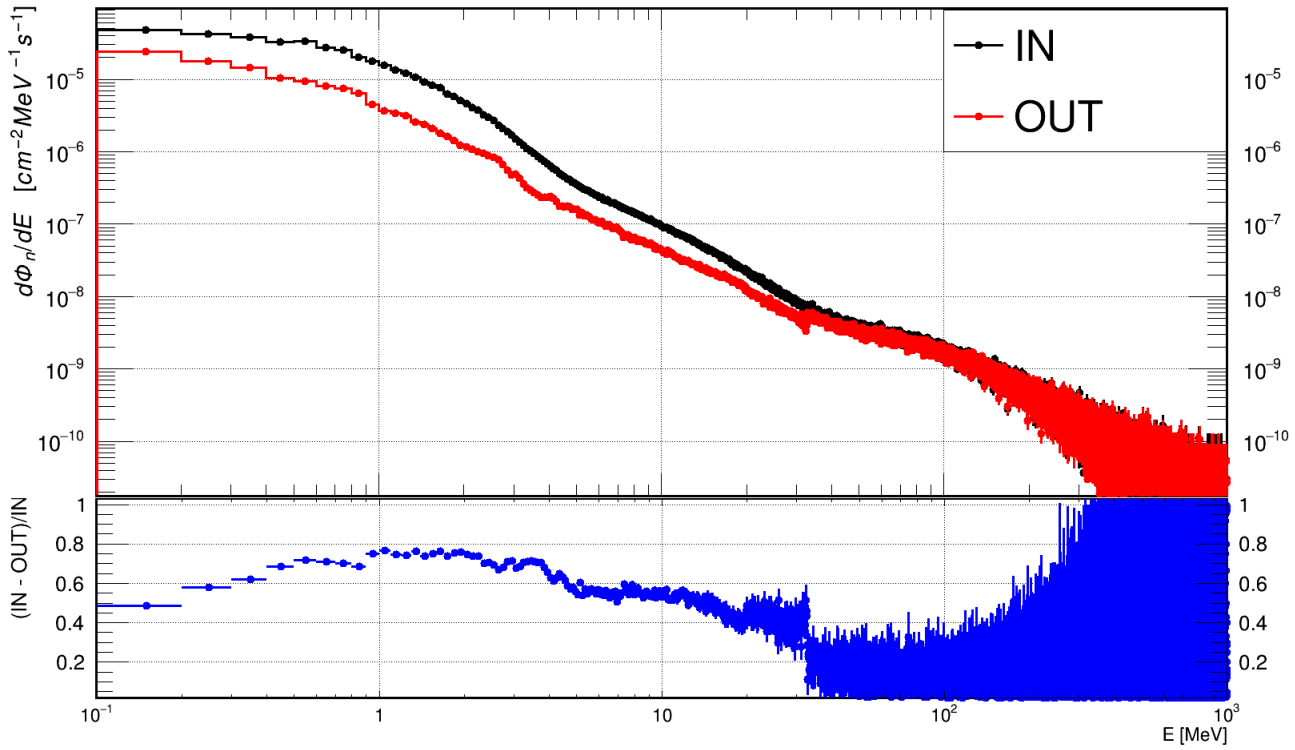

Figure 5.21: Comparison between the spectra of inward (IN) and outward (OUT) going neutrons at the inner surface of the lead castle. The correction factor for double counting, as a function of the neutron energy, is shown at the bottom of the figure.

5.5.5 Edge Effect

The distributions shown so far in Sec. 5.5 might be affected by geometrical effects in the vicinity of the edges of the apparatus. In order to avoid this *edge effect* only neutrons (or particles in general) emerging from the central-half-length[11] of a selected surface have to be considered. In the following, the distributions of selected quantities described in Sec. 5.5 obtained when the edges are considered (*with edge* from now on) are compared to the distributions obtained when the contribution from the edges is removed, i.e. when only the central-half-length of the selected surface is considered (*no edge* from now on).
Figure 5.22 shows the comparison between the neutron energy spectrum at the inner surface of the lead castle as predicted *with edge* and with *no edge*. The spectra are very similar. This demonstrates that the *edge effect* has a very little dependence on the neutron energy.
Figure 5.23 shows the distributions of the neutron multiplicity, as defined in Sec. 5.5.2, as predicted *with edge* and with *no edge*. The distributions were normalized to the actual surface considered and to the triggered muons. The distribution obtained when the contribution from the edges is removed, *no edge*, has a shorter tail. This is most likely due to the fact that near the edges the double counting is enhanced.
For the Figs. 5.22 and 5.23 the total inner surface of the lead castle was considered. For the neutron yield, only the surface underneath the lid is considered. Figure 5.24 shows the differential neutron yields, as defined in Sec. 5.5.3, as predicted *with edge* and with *no edge*. There is a significant difference between the two differential neutron yields, which is reflected in the integral neutron yields. In the literature, the authors often quote the integral neutron yield as predicted with *no edge*.

Table 5.12 reports the integral neutron yield (with *no edge*) for different MC settings. The *MaGe default* simulation predicts an integral neutron yield with *no edge* a factor 4 lower than the integral neutron yield as predicted *with edge*

Variable	***MaGe default***	***Shielding***	**Monoen. (7.7 GeV)**	**Monoen. (0.77 GeV)**
$\mathbf{Y}_n$ $[\frac{n}{\mu(g/cm^2)}]$	$1.14{\cdot}10^{-4}$	$9.18{\cdot}10^{-5}$	$1.39{\cdot}10^{-5}$	$8.77{\cdot}10^{-7}$

Table 5.12: Integral neutron yield as predicted with *no edge* for different simulations settings.

[11] The central-half-length of a surface is the central part with half the width and half the length of that surface.

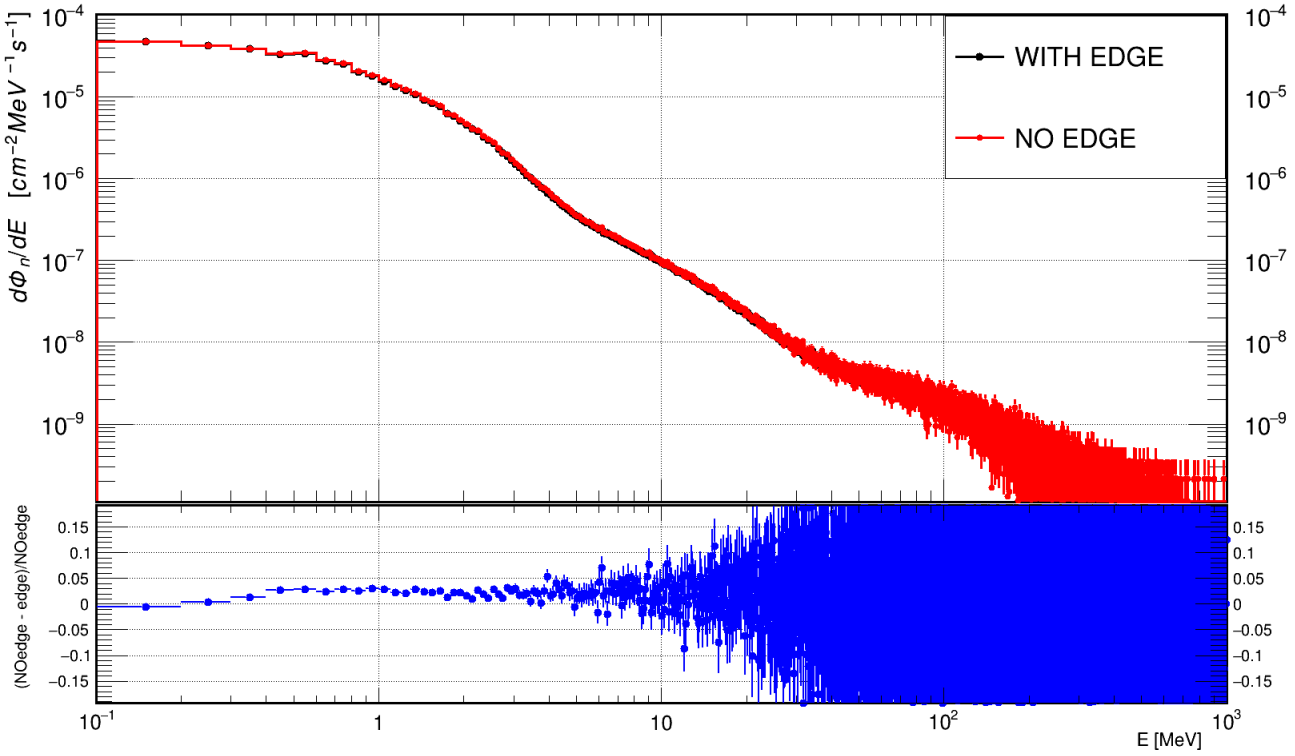

Figure 5.22: Comparison between the neutron energy spectra at the inner surface of the lead castle as predicted *with edge* (black) and with *no edge* (red). Also shown is the relative difference between *no edge* and *with edge*. See text for details.

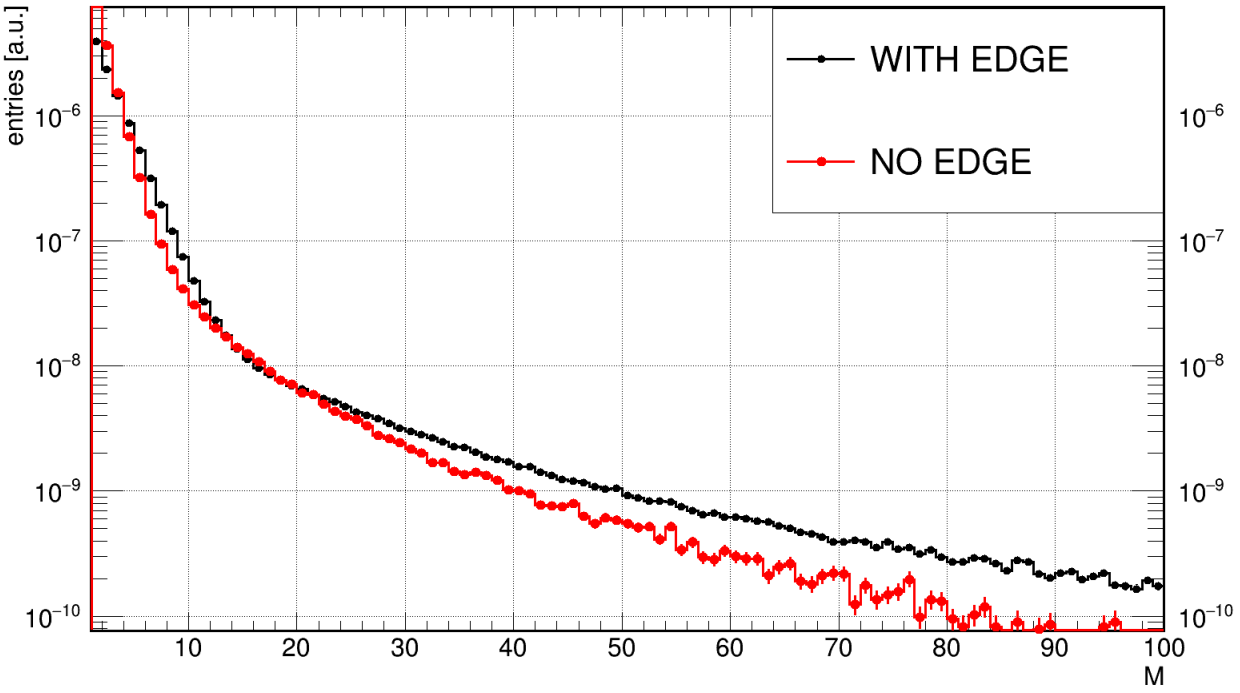

Figure 5.23: Comparison between the neutron multiplicity distributions as predicted *with edge* (black) and with *no edge* (red). The distributions were normalized per triggered muon and per area of the surface considered. See text for details.

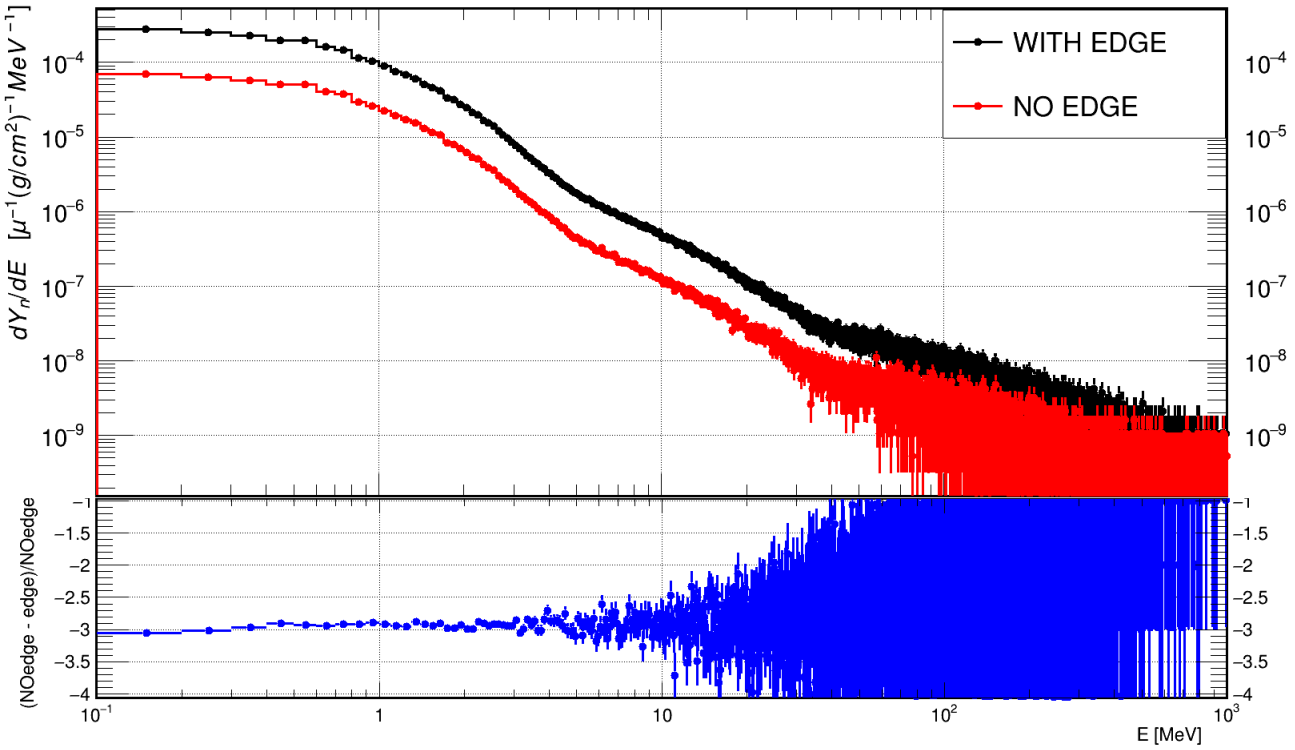

Figure 5.24: Comparison between the differential neutron yields, dY_n/dE, as predicted *with edge* (black) and with *no edge* (red). Also shown is the relative difference between *no edge* and *with edge*. See text for details.

Chapter 6

MINIDEX Results: Comparison of Data and MC

In this chapter, the procedure used to combine the simulation results obtained for the different injected particles is presented. The same procedure is applied to results obtained by all four simulation settings used. The MC results are compared to the MINIDEX run I data.

All the simulation results presented in this chapter were obtained with the *DETECTOR* output scheme and the *MaGe default* physics list, unless otherwise stated.

In the simulations, a 100% detection efficiency was assumed for the scintillators. Hence, the comparisons between data and MC are done after the correction for the inefficiency of the muon trigger was applied to the data.

The energy resolution of the HPGe detectors was taken into account for the simulated HPGe spectra by smearing all energies according to a Gaussian distribution with a constant standard deviation of 1.6 keV. This value corresponds to a FWHM of ≈2.7 keV, which was measured for the peak at 2.2 MeV. Since all the comparisons between data and MC only consider the ROI defined in Sec. 4.6, the choice of a constant FWHM does not influence the results.

Furthermore, the simulated HPGe spectra were shifted by ≈1.5 keV towards lower energies, because the simulated photon peak from the thermal neutron capture in hydrogen, $H(n,\gamma)$, was produced at 2.2246 MeV instead of 2.223 MeV. This feature was already observed by Abt et al. in 2008 [249] and was reported to the GEANT4 Collaboration. The problem is still present in the GEANT4 v. 9.6.4 used for this work.

6.1 Composition of the Total HPGe Spectra

As described in Sec. 4.6, the measured quantities, from which all the results are derived, are Γ_{S+B} and Γ_B, as defined in Eqs. 4.24 and 4.25, respectively. When ΔT_{win} is big enough, all the muon-induced 2.2 MeV gammas are collected in the *INSIDE* spectrum, thus included in Γ_{S+B}. In this case, the *OUTSIDE* spectrum will contain only background events. By construction, in the experimental data, every event which does not provide a trigger signal is considered to be background. The background components are classified as follows:

- **NON-trigger muons**: all muon-induced events which do not provide a trigger signal. A muon might fail to generate a trigger because of geometrical acceptance or too little energy deposited in the scintillators.
- **Cosmogenic Neutrons**: all cosmogenic-neutron-induced events[1].
- **Neutrons from Natural Radioactivity**: all events induced by neutrons from the natural radioactivity, for example neutrons produced by fission and (α,n)-reactions.

All these components are trigger-independent, thus the events are uniformly distributed over time, regardless of any trigger signal.
The signal events are, on the other hand, all the muon-induced events, which are associated with a trigger. This component is referred to in the text as *trigger muons* or simply *signal*. Figure 6.1 shows a comparison between the simulated energy spectra without (blue) and with (red) trigger for the top and the bottom scintillator. The trigger requirement eliminates single hits, but the spectral shape remains the same. Figure 6.2 shows a comparison of the $T_{top} - T_{bot}$ distributions as observed in data (violet) and as predicted by MC (black). The latter distribution contains the individual contributions from μ^+, μ^- and neutrons. Each MC component of the $T_{top} - T_{bot}$ distribution was normalized to the respective RT_{MC}. The relative normalization between data and MC shown in Fig. 6.2 is, however, arbitrary. The width of the peak of the experimental data is limited by the finite time resolution of the DAQ.

Figure 6.3 shows the simulated HPGe spectra for untriggered μ^+ and μ^-. The sum of these two components and their difference is also shown. As seen also in Tab. 5.10, μ^- produce more 2.2 MeV gammas than μ^+. This is consistent with the enhanced neutron yield as shown in Sec. 5.4.
The neutron contribution, together with the total muon contribution, to the HPGe spectrum, without trigger requirements, are shown in Fig. 6.4. The cosmogenic neutron component is more than an order of magnitude smaller than the muon component, even without trigger requirement.
From the independent simulation of μ^+ and μ^-, the events which produce a trigger (*trigger muons*) and the events which do not produce a trigger (*NON-trigger muons*) are selected.

[1] The very rare neutron-induced trigger events were neglected in the MC analysis.

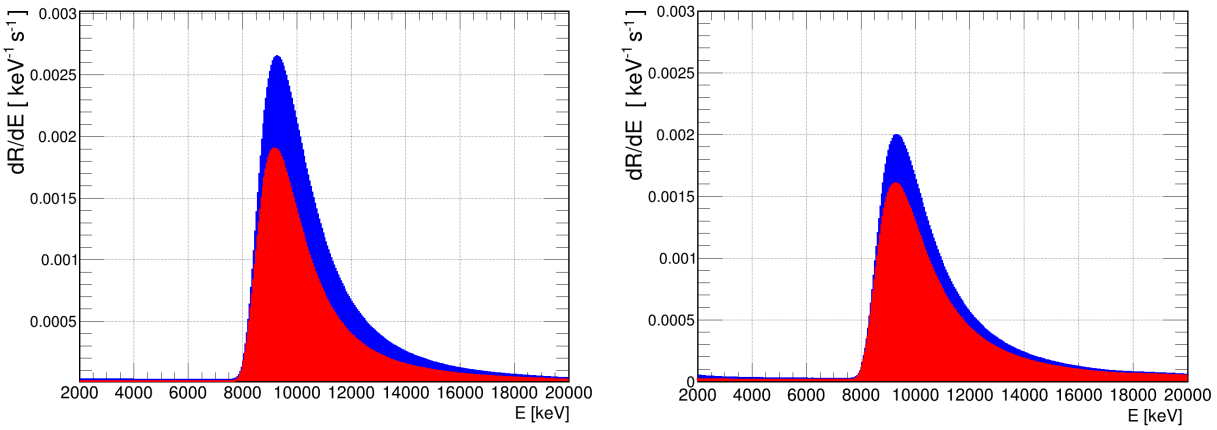

Figure 6.1: Simulated energy spectra without (blue) and with (red) trigger for the upper (left) and lower (right) scintillator panel. These spectra were obtained by summing the individual contributions from μ^+, μ^- and neutrons. Each component was normalized to the respective RT_{MC}.

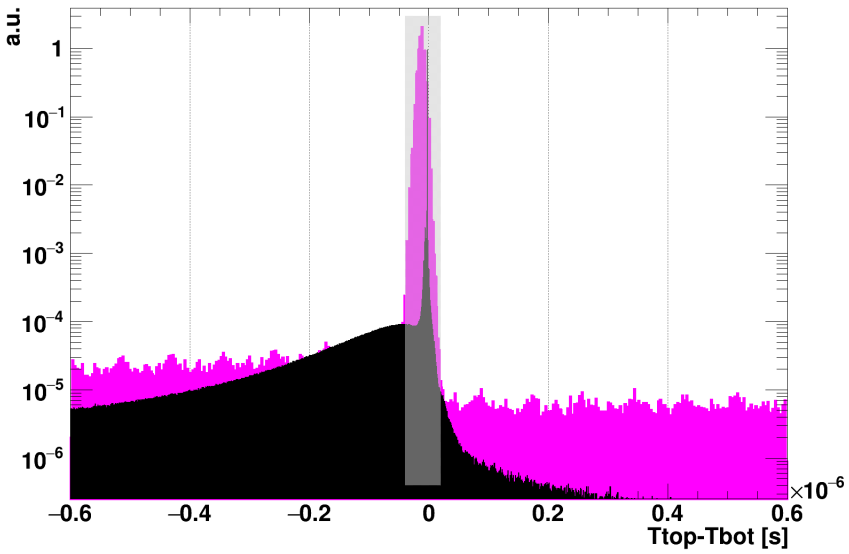

Figure 6.2: Comparison of the distribution of the time difference $T_{top} - T_{bot}$ as observed in data (violet) and predicted by MC (black). The shaded area around the peak was chosen to select trigger events. The simulated distribution was obtained by summing the individual contributions from μ^+, μ^- and neutrons. Each MC component has been normalized to the respective RT_{MC}.

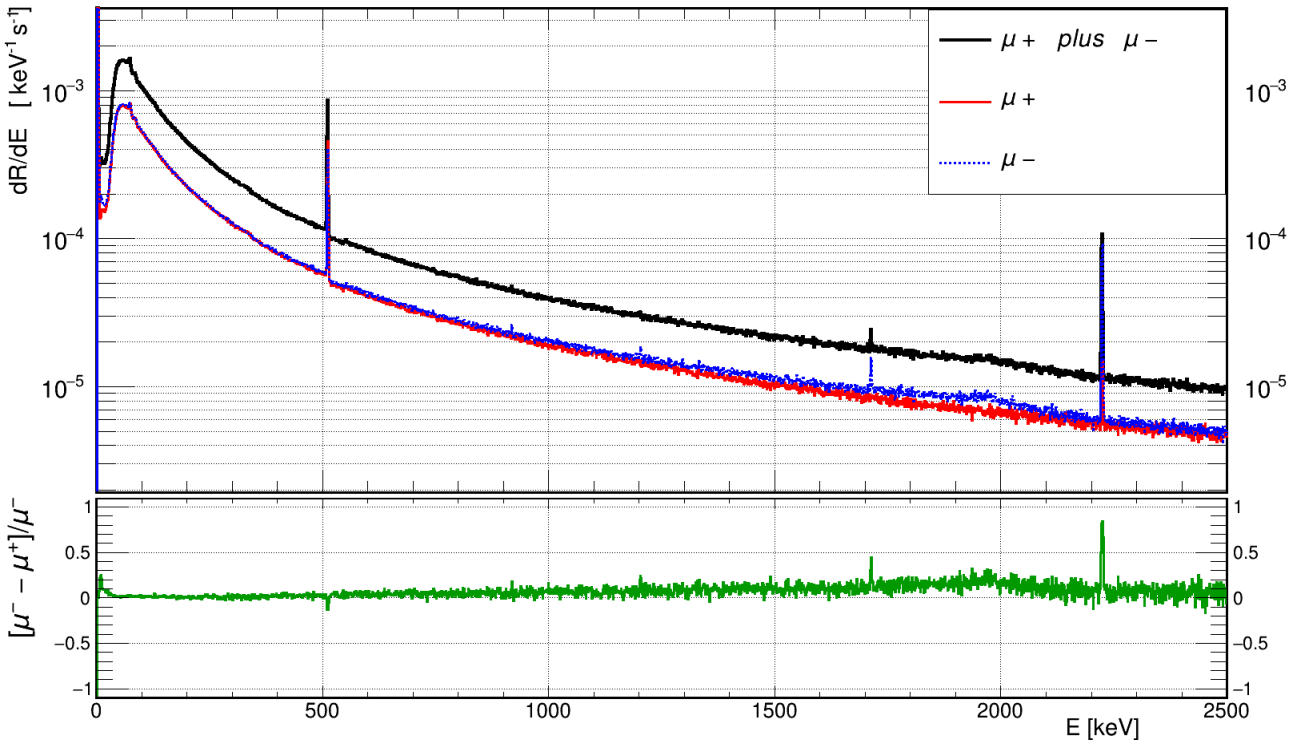

Figure 6.3: Simulated HPGe spectrum obtained for μ^+ (red) and μ^- (blue). Each component was normalized to the respective RT_{MC}. Also shown are the sum from μ^+ and μ^- (black) and their difference (green).

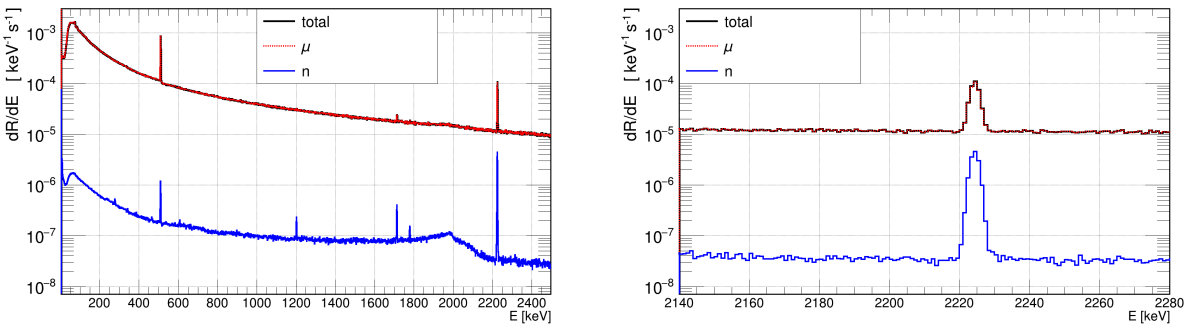

Figure 6.4: Simulated HPGe spectrum obtained for neutrons (blue), all muons (red) and the sum (black). Each component was normalized to the respective RT_{MC}. The ROI is shown separately on the right.

Since the *NON-trigger muons* and *Cosmogenic Neutrons* are trigger independent, the spec-

tra were normalized to ${RT_{MC}}^{\mu}$ and ${RT_{MC}}^{n}$. The *trigger muons* spectra, in contrast, were normalized to ${ET_{inside}}^{sim}$ or ${ET_{outside}}^{sim}$, defined in Eqs. 4.22 and 4.23, for the *INSIDE* and the *OUTSIDE* spectra, respectively. The final spectra used to compare to the experimental Γ_{S+B} and Γ_B were obtained by summing the *trigger muons*, *NON-trigger muons* and *Neutrons* components, as required.
Figure 6.5 shows the different contributions, normalized accordingly, to the *INSIDE* (left) and the *OUTSIDE* (right) HPGe energy spectra for $\Delta T_{win} = 0.17\,\text{ms}$ (top) and $\Delta T_{win} = 4\,\text{ms}$ (bottom). Also shown is the sum of all components.

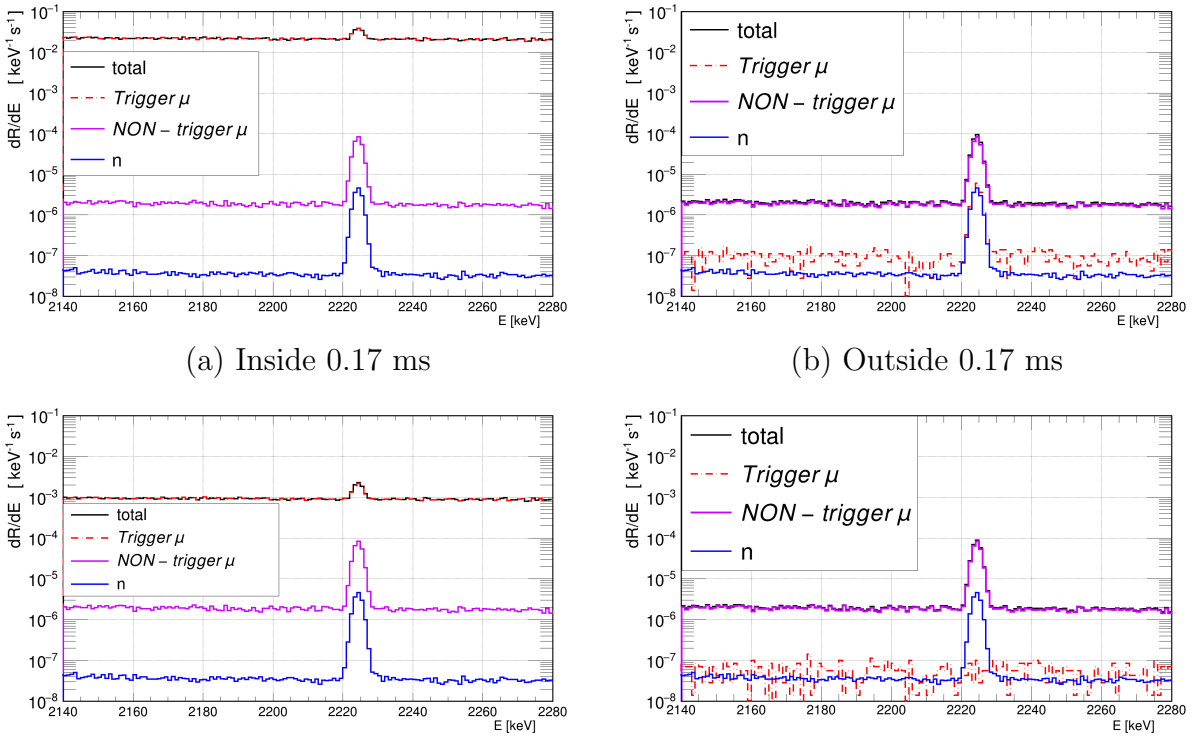

(a) Inside 0.17 ms

(b) Outside 0.17 ms

(c) Inside 4 ms

(d) Outside 4 ms

Figure 6.5: Simulated *INSIDE* (left) and *OUTSIDE* (right) HPGe energy spectra for $\Delta T_{win} = 0.17\,\text{ms}$ (top) and $\Delta T_{win} = 4\,\text{ms}$ (bottom). The individual components *trigger muons* (dotted red), *NON-trigger muons* (solid violet) and *Neutrons* (solid blue), are shown. The sum of all the components is also shown (black)

For $\Delta T_{win} = 0.17\,\text{ms}$, not all the trigger-muon-induced 2.2 MeV gammas are collected in the *INSIDE* spectrum. Accordingly, a fraction of the gammas appear in the outside spectrum. In contrast, there is no contribution to the 2.2 MeV peak due to the *trigger muons* in the *OUTSIDE* spectrum for $\Delta T_{win} = 4$ ms. As expected (see Fig. 4.18), the *OUTSIDE* spectrum for $\Delta T_{win} = 4$ ms only has background contributions.
The sum of the three contributions, also shown in Fig. 6.5, represents the simulated spectrum that can be compared to the experimental data.

6.2 Comparison between data and MC

The comparisons shown in this section have a caveat, because the background due to neutrons from natural radioactivity was not simulated. Therefore, a perfect agreement is not expected. Nevertheless, a comparison of the spectra is instructive.
Figure 6.6 shows the spectra as observed in the data and predicted by MC for $\Delta T_{win} = 0.17$ ms and $\Delta T_{win} = 4$ ms. The MC spectra were obtained with the *MaGe default* physics list. For

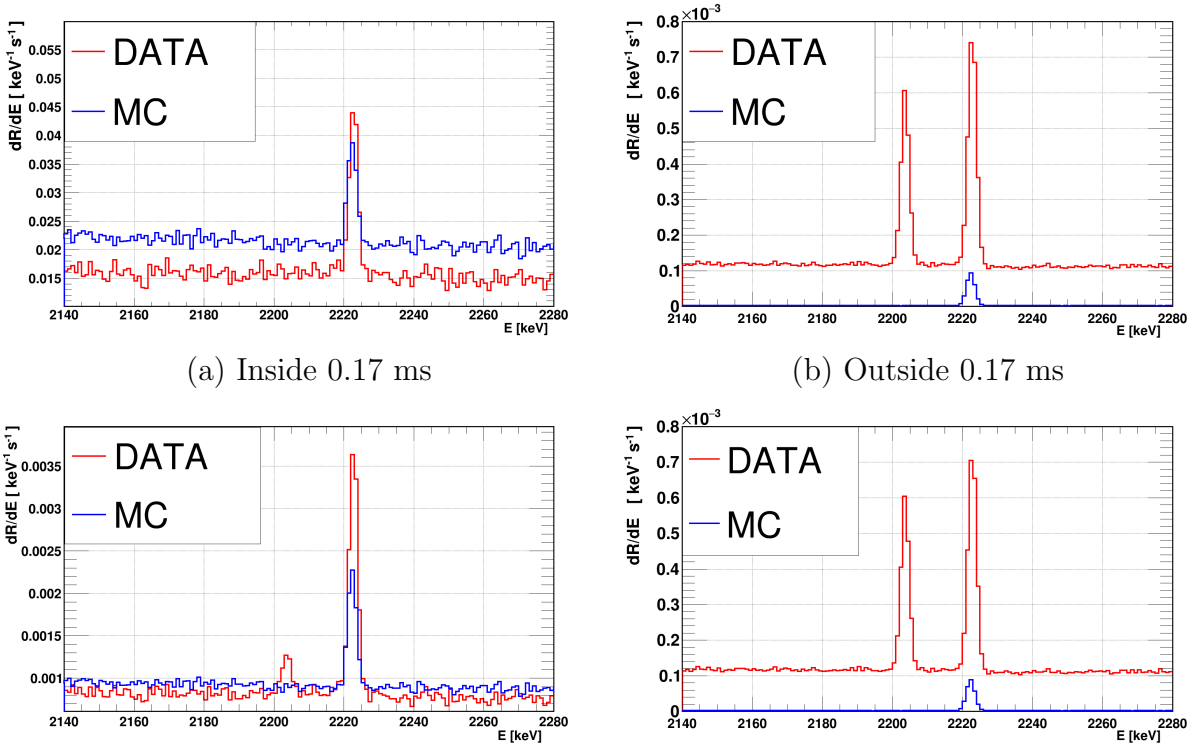

(a) Inside 0.17 ms

(b) Outside 0.17 ms

(c) Inside 4 ms

(d) Outside 4 ms

Figure 6.6: Comparison between data and MC *INSIDE* (left) and *OUTSIDE* (right) HPGe energy spectra for $\Delta T_{win} = 0.17$ ms (top) and $\Delta T_{win} = 4$ ms (bottom).

the small window $\Delta T_{win} = 0.17$ ms, the MC signal is quite similar to the signal observed, see Fig. 6.6 (a). This trend is confirmed for $\Delta T_{win} = 4$ ms, see Fig. 6.6 (c). Figures 6.6 (b) and (d) demonstrate that only a small fraction of the background was simulated. The natural gamma background was also not simulated. Thus, the bismuth peak at 2.204 MeV is also not present in the MC. For short ΔT_{win}, it is not present also in the measured *INSIDE* spectra.
All the signal events are expected to be collected within $\Delta T_{win} \approx 2$ ms. Figure 6.7 (a) shows a comparison between data and MC of the spectra for this ΔT_{win}. The predictions are shown for all four different MC settings. In the experimental data, the background peak due to ^{214}Bi is still not visible within a $\Delta T_{win} = 2$ ms. The signal predicted by the *Shielding* MC is slightly weaker than the signal predicted by the *MaGe default* MC. This is

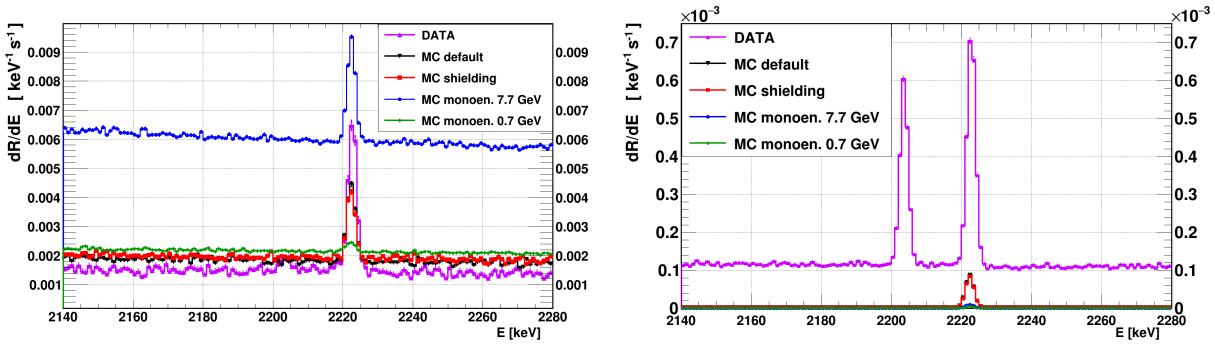

(a) Inside 2 ms (b) Outside 4 ms

Figure 6.7: Simulated total HPGe energy spectra obtained with the different simulation settings compared to data (violet). (a) Inside $\Delta T_{win} = 2\,\text{ms}$. (b) Outside $\Delta T_{win} = 4\,\text{ms}$.

in agreement with the lower neutron yield discussed in Sec. 5.4. The normalization of the simulation of monoenergetic muons is different than for the full MCs. This is suspected to be the reason for the excess of background for the monoenergetic muon spectrum in Fig. 6.7 (a). This issue will have to be investigated. As it is a flat gamma background, it does not affect the actual 2.2 MeV gamma rate from neutron capture. Therefore, it could be ignored in the current analysis.
Figure 6.8 shows a comparison between data and MC for Γ_B, see Eq. 4.25. Only the results obtained with the *MaGe default* and the *Shielding* physics lists are displayed. The result for all four MC settings are available in Appendix D, see Fig. D.1. The experimental values of Γ_B shown in Fig. 6.8 were not corrected for the inefficiency of the scintillators, because the only value which is subject to that correction is $R_B = \Gamma_B|_{\Delta T_{win} = 4\,ms}$, see Sec. 4.6.4. The uncertainties displayed in Figs. 6.8 and 6.9 correspond to the statistical and systematic uncertainties added in quadrature, see Sec. 4.7. All results were obtained with the FIT method. The points were displaced horizontally for better visibility. Some values for small ΔT_{win} are not available due to non-applicability of the FIT method because of too low statistics. As the background from natural radioactivity is not included in the MC, it is not surprising that the overall effective rate is a factor of approximately 10 too low in the MC. The time structure of the simulated background seen in Fig. 6.8 shows that the signal leaks into the background calculation for ΔT_{win} up to $\approx$1 ms. Figure 6.8 also confirms that *MaGe default* predicts a 10% higher background than the *Shielding* MC.

Table 6.1 shows the comparison between data and MC of the *effective* background rates, ${R_B}^{FIT}$, and the *overall* background rates, BR, defined as

$$BR = {R_B}^{FIT} \cdot \frac{ET_{outside}}{RT}\Big|_{\Delta T_{win} = 4\,ms} \quad . \tag{6.1}$$

The predictions of the simulations for monoenergetic muons are much lower than for the full MCs. Such simplifications are clearly not suitable for background predictions.

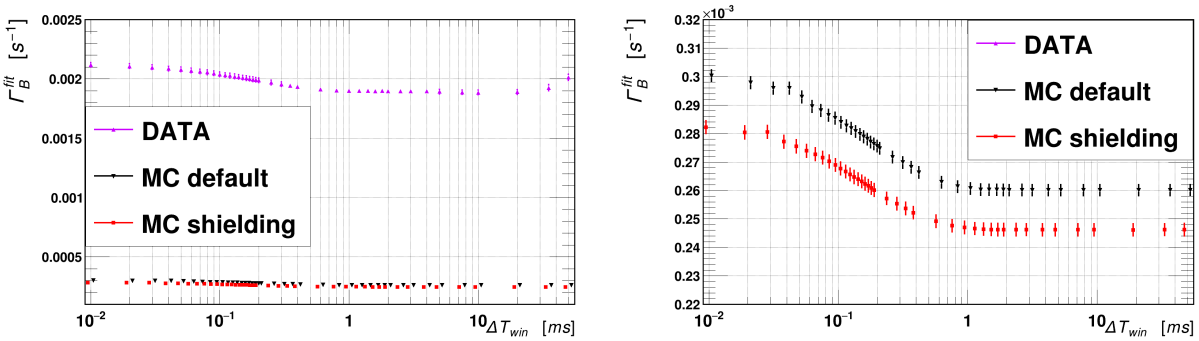

(a) (b)

Figure 6.8: (a) Comparison between data and MC of the *effective* rate, Γ_B, of events observed in the ROI of the *OUTSIDE* spectra vs ΔT_{win}. The results obtained with the *MaGe default* and the *Shielding* physics lists are displayed. (b) MC predictions only.

Sample	${R_B}^{FIT} \cdot 10^{-5}$ [s^{-1}]	$BR \cdot 10^{-5}$ [s^{-1}]
Data	(183.8 ± 1.9)	(176.4 ± 1.8)
MaGe default	(26.1 ± 0.2)	(25.8 ± 0.2)
Shielding	(24.6 ± 0.2)	(24.3 ± 0.2)
Monoen. 7.7 GeV	(2.91 ± 0.03)	(2.88 ± 0.03)
Monoen. 0.7 GeV	(1.49 ± 0.01)	(1.48 ± 0.01)

Table 6.1: *Effective*, ${R_B}^{FIT}$, and *overall*, BR, background rates for data and all four MC settings. Uncertainties are statistical only.

Figure 6.9 shows a comparison between data and MC for R_S, see Eq. 4.27. Figure D.2 in Appendix D provides the result for all four MC settings. The time structure of R_S is similar for data and MC, but some differences are observable. The *Shielding* MC reproduces the time evolution quite well, but has an overall deficit of about a factor of two. The *MaGe default* has a large prompt contribution and predicts an overall larger R_S, but its prediction is too low compared to the data, especially at ΔT_{win} above 100 μs.

Table 6.2 shows the *effective* signal rate, ${R_S}^{FIT}$, for $\Delta T_{win} = 4$ ms for both data and MC.

The values for the experimental data were corrected for the inefficiency of the scintillators. All values were obtained with the FIT method. The MC values were not corrected for the discrepancy of trigger rates between data and MC, see Sec. 5.4. This discrepancy will be taken into account as described in the next section.

It is clear that the simulations do not properly reproduce the 2.2 MeV gamma rates observed in the experimental data. The predicted signal rate is too low. An attempt to compensate for this problem is described in the next section.

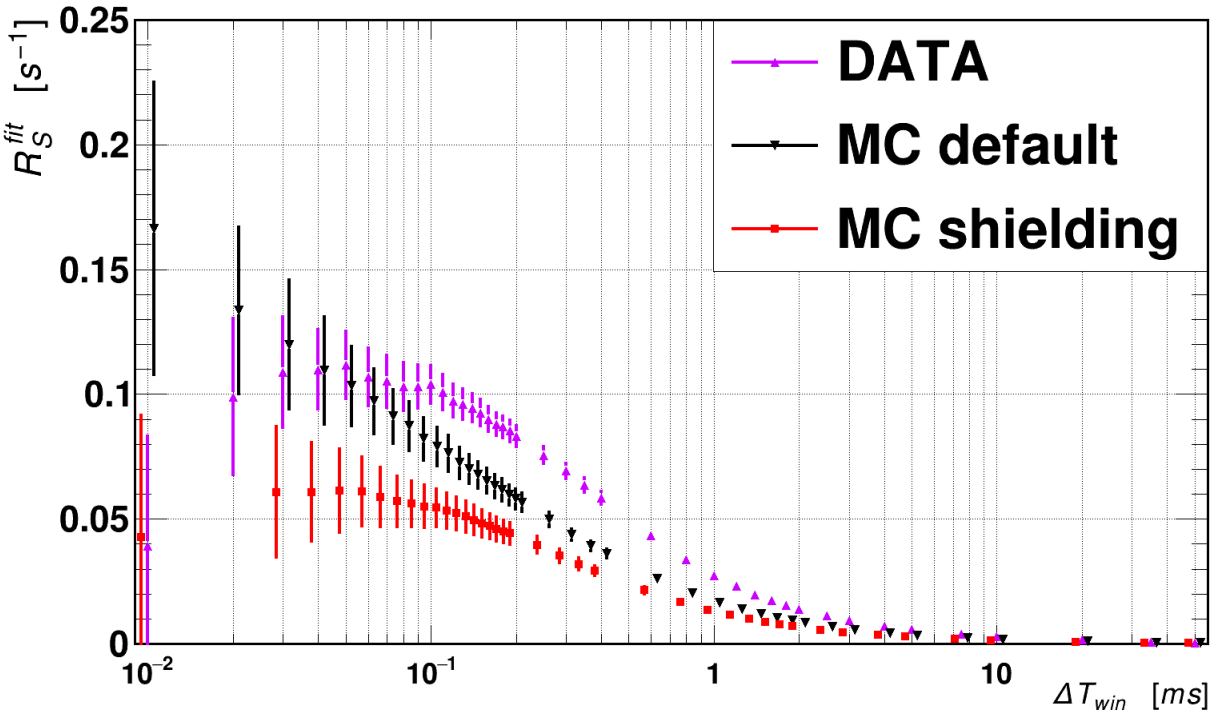

Figure 6.9: Comparison between data and MC of the *effective* signal rate, R_S, vs ΔT_{win}. The results obtained with the *MaGe default* and *Shielding* physics lists are displayed.

Sample	$R_S{}^{FIT}\vert_{\Delta T_{win}=4\,ms} \cdot 10^{-5}$ [$\mathbf{s}^{-1}$]
Data	(702 ± 24)
MaGe default	(418 ± 14)
Shielding	(349 ± 13)
Monoen. 7.7 GeV	(534 ± 12)
Monoen. 0.7 GeV	(58 ± 6)

Table 6.2: *Effective* signal rate, R_S, for $\Delta T_{win} = 4\,\text{ms}$ for data and all four MC settings. Uncertainties are statistical only.

6.3 Adjustment for the Missing MC Component

By construction, the background description in the MC is incomplete. The whole background contribution due to natural radioactivity was not included in the simulation presented in this thesis. For this reason, the simulated 2.2 MeV gamma rates were adjusted with the help of the data.
Under the assumption that the background component to the 2.2 MeV gamma line missing in the MC has the same flat time structure as the background component from *cosmogenic neutrons*, the simulated spectra were adjusted using measured rate information.
In general, for any value of ΔT_{win}, the *INSIDE* spectrum contains the contributions from both the signal and the background. Furthermore, as described in Sec. 4.6, for values of ΔT_{win} big enough, the *OUTSIDE* spectrum is signal-free. The following relations between measured and MC rates of 2.2 MeV gamma rates were used:

$$(\Gamma_{S+B})_i = A_i \cdot \left[(\Gamma_{trigger-\mu}{}^{inside})_i{}^{MC} + (\Gamma_{NONtrig.-\mu}{}^{inside})_i{}^{MC-corr} \right] + B_i \cdot (\Gamma_{neutrons}{}^{inside})_i{}^{MC} \quad (6.2)$$

$$R_B{}^{corr} = A_i \cdot (\Gamma_{NONtrig.-\mu}{}^{outside})_{4\,ms}{}^{MC-corr} + B_i \cdot (\Gamma_{neutrons}{}^{outside})_{4\,ms}{}^{MC} \quad (6.3)$$

where:

- the index i denotes the different ΔT_{win};
- $(\Gamma_{S+B})_i$ represents the effective rate of signal plus background for a certain ΔT_{win}, obtained from the experimental data as defined in Eq. 4.24;
- $R_B{}^{corr}$ represents the corrected effective background rate obtained from the experimental data as defined in Eq. 4.34;
- $(\Gamma_{trigger-\mu}{}^{inside})_i{}^{MC}$ is the simulated effective signal rate inside a certain ΔT_{win};
- $(\Gamma_{NONtrig.-\mu}{}^{inside})_i{}^{MC-corr}$ and $(\Gamma_{NONtrig.-\mu}{}^{outside})_{4\,ms}{}^{MC-corr}$ are the simulated background rates due to *NON trigger muons* inside a certain ΔT_{win} and outside $\Delta T_{win} = 4$ ms, respectively. These rates were corrected for the data-MC discrepancy in terms of trigger rates mentioned in Sec. 5.4, namely:

$$(\Gamma_{NONtrig.-\mu}{}^{inside})_i{}^{MC-corr} = \left[(\Gamma_{NONtrig.-\mu}{}^{inside})_i{}^{MC} \right] \cdot \frac{R_{trig}{}^{data}}{R_{trig}{}^{MC}} \quad (6.4)$$

and

$$(\Gamma_{NONtrig.-\mu}{}^{outside})_{4\,ms}{}^{MC-corr} = \left[(\Gamma_{NONtrig.-\mu}{}^{outside})_{4\,ms}{}^{MC} \right] \cdot \frac{R_{trig}{}^{data}}{R_{trig}{}^{MC}} \quad (6.5)$$

where

$$(\Gamma_{NONtrig.-\mu}) = \frac{N_{peak}{}^{NONtrig.-\mu}}{RT_{MC}{}^{\mu}} \quad (6.6)$$

and

$$\frac{{R_{trig}}^{data}}{{R_{trig}}^{MC}} = 1.89 \tag{6.7}$$

Note, that ${R_{trig}}^{data}$ refers to the measured trigger rate after the correction for the inefficiency of the scintillators.

- $({\Gamma_{neutrons}}^{inside})_i^{MC}$ and $({\Gamma_{neutrons}}^{outside})_{4\,ms}^{MC}$ are the simulated background contributions due to *cosmogenic neutrons* inside a certain ΔT_{win} and outside $\Delta T_{win} = 4$ ms, respectively;

- A_i and B_i are the adjustment factors for the simulated effective rates of the muon-induced and the neutron-induced component, respectively, to account for the incomplete description of the background.

It should be noted that the contribution of the *trigger muons* to the background rate was neglected. This choice was motivated by the lack of signal outside the 4 ms time window as shown Fig. 6.5 (d).
As the background components due to *NON trigger muons* and *cosmogenic neutrons* are trigger independent, the relations

$$\begin{aligned} ({\Gamma_{NONtrig.-\mu}}^{inside})_i^{MC-corr} &= ({\Gamma_{NONtrig.-\mu}}^{outside})_i^{MC-corr} = \\ &= {\Gamma_{NONtrig.-\mu}}^{MC-corr} = const.\ \forall\, i \qquad (6.8) \\ ({\Gamma_{neutrons}}^{inside})_i^{MC} &= ({\Gamma_{neutrons}}^{outside})_i^{MC} = {\Gamma_{neutrons}}^{MC} = const.\ \forall\, i \qquad (6.9) \end{aligned}$$

hold and the system of Eqs. 6.3 can be solved for the adjustment factors A_i and B_i.
All rates were obtained by fitting the spectra in the ROI with a Gaussian plus a first order polynomial (FIT method), considering only the counts under the Gaussian.

Table 6.3 lists selected measured values, for which the MC adjustment described in Eq. 6.3 was performed.

The adjustment factors for different ΔT_{win}, obtained for the different simulation settings, are shown in Fig. 6.10. A complete list of values is reported in Tabs. C.1 and C.2, for A_i and B_i, respectively.
These results indicate:

- in general, the stability of A_i and B_i with respect to the ΔT_{win} quantifies how well the MC reproduces the time evolution of the background in the experimental data. Figure 6.10 indicates that the *MaGe default* and *Shielding* physics lists are doing quite well in this respect.

- The energy scale of the injected muons is relevant.

ΔT_{win} [ms]	Γ_{S+B} [s^{-1}]	$R_B{}^{corr}$ [s^{-1}]
0.01	0.04 ± 0.03	-
0.04	0.11 ± 0.02	-
0.1	0.106 ± 0.007	-
0.4	0.060 ± 0.002	-
1.0	0.0291 ± 0.0009	-
4.0	0.0089 ± 0.0002	$(183.8 \pm 1.9)\cdot 10^{-5}$
10.0	0.0048 ± 0.0001	-

Table 6.3: A sample of measured values involved in MC adjustment. The uncertainties are purely statistical.

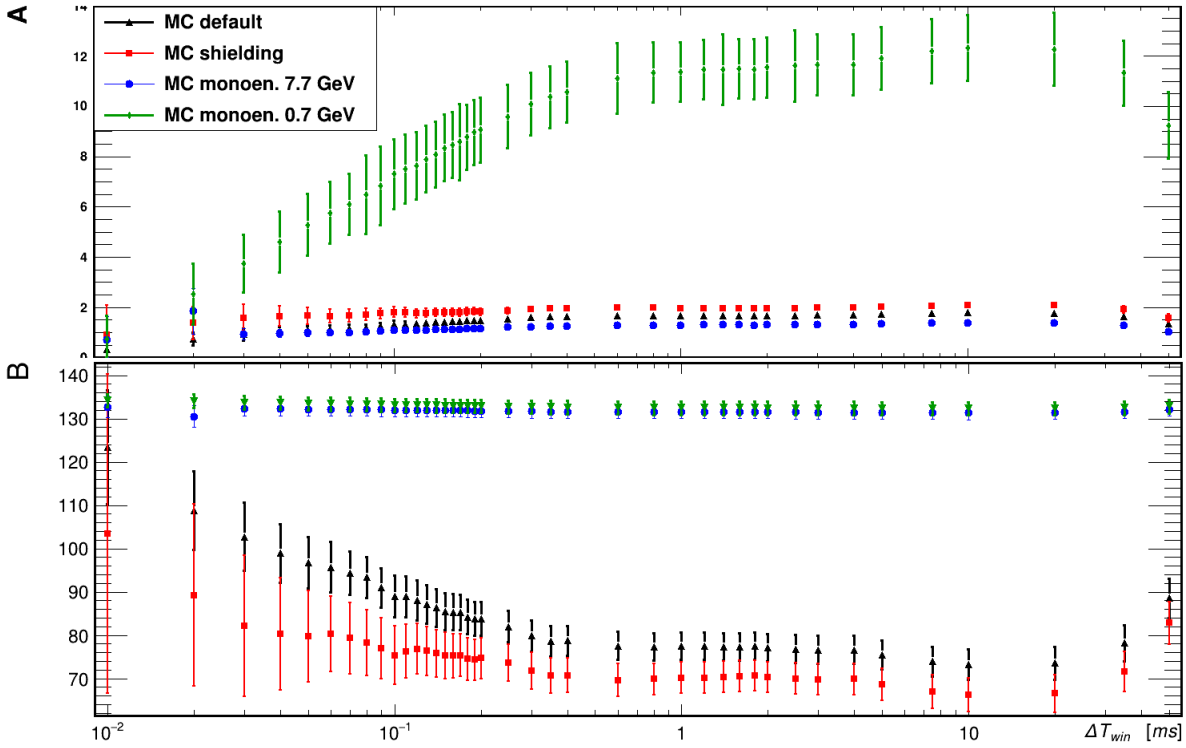

Figure 6.10: Comparison of the adjustment factors vs ΔT_{win} as obtained by the different simulation settings. Uncertainties are statistical only.

- By looking at the results obtained for the monoenergetic cases, it is clear that the angular distribution of the incoming muons has a major impact on the background component due to the *NON trigger muons*. Moreover, the B-values of the simulations for monoenergetic 7.7 GeV and 0.7 GeV muons differ less than the A-values. This

is due to the fact that both simulations for monoenergetic muons include the same neutron component.

- The values of A lie between 1 and 2 for the *MaGe default* and *Shielding* physics lists. This confirms the conclusion that the MC produces less muon-induced 2.2 MeV gammas than observed in the experimental data.
- The *MaGe default* physics list produces more muon-induced 2.2 MeV gammas than the *Shielding* physics list, as previously observed, see Fig. 5.16.
- The values of B are all above 70. This indicates that the missing background component in the simulations is dominant and has to be included in future studies.

It should also be noted that in this analysis, the injected muons and the neutrons are assumed to be uncorrelated. In reality there is a correlation, because most of the neutrons reaching the laboratory roof are muon-induced. This means that the discrepancy between trigger rates for data and MC, for which the muon component was corrected, affects also the neutron component. This correlation is hard to quantify and therefore it was ignored in this first analysis. Its effect is embedded in the B_i factors.
The adjustment factors, although evaluated from the 2.2 MeV gamma rates, were applied bin by bin to the whole simulated spectra. The result can again be compared to the experimental data.
Figure 6.11 shows the predicted energy spectra from Fig. 6.5 after the adjustment just described. The relative contributions of the different components are different after the adjustment. The contribution from the neutrons is now important. Effectively, it is assumed that it looks like the component from natural radioactivity and can absorb it. The sum of these components (black line) is compared to experimental data.
Figure 6.12 shows the comparison between the measured HPGe spectra, *INSIDE* ΔT_{win} = 2 ms (a) and *OUTSIDE* ΔT_{win} = 4 ms (b), and the total simulated spectra after adjustment. The predictions are shown for all four different simulation settings. Since the whole MC spectra are adjusted and not only to the 2.2 MeV rates, the differences in the overall rates between data and MC are enhanced in the *INSIDE* spectra (Fig. 6.12 (a)) and reduced in the *OUTSIDE* spectra (Fig. 6.12 (b)) compared to Fig. 6.7. This indicates that the flat gamma background gets enhanced by a too large factor. As long as only the 2.2 MeV gammas are counted, this has no adverse effect.

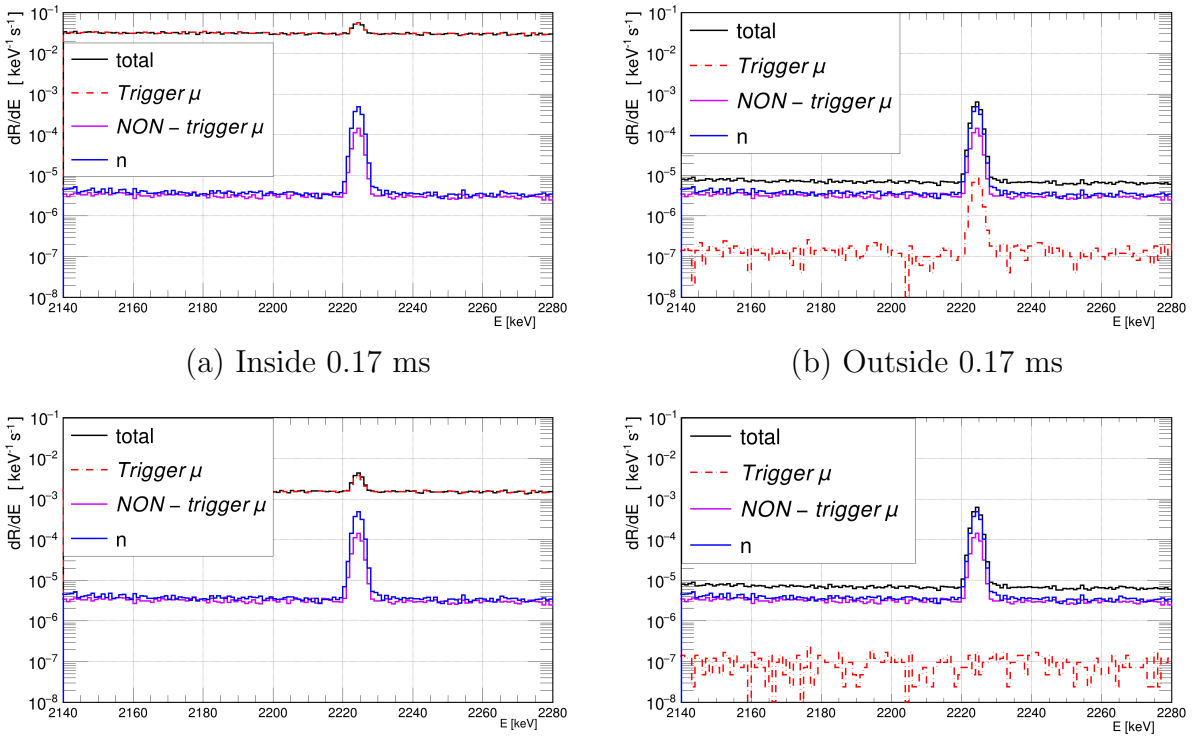

(a) Inside 0.17 ms

(b) Outside 0.17 ms

(c) Inside 4 ms

(d) Outside 4 ms

Figure 6.11: Simulated (adjusted) *INSIDE* (left) and *OUTSIDE* (right) HPGe energy spectra for $\Delta T_{win} = 0.17\,\text{ms}$ (top) and $\Delta T_{win} = 4\,\text{ms}$ (bottom). The individual components, *trigger muons* (dotted red), *NON-trigger muons* (solid violet) and *Neutrons* (solid blue), are shown. The sum of all three components is also shown (black).

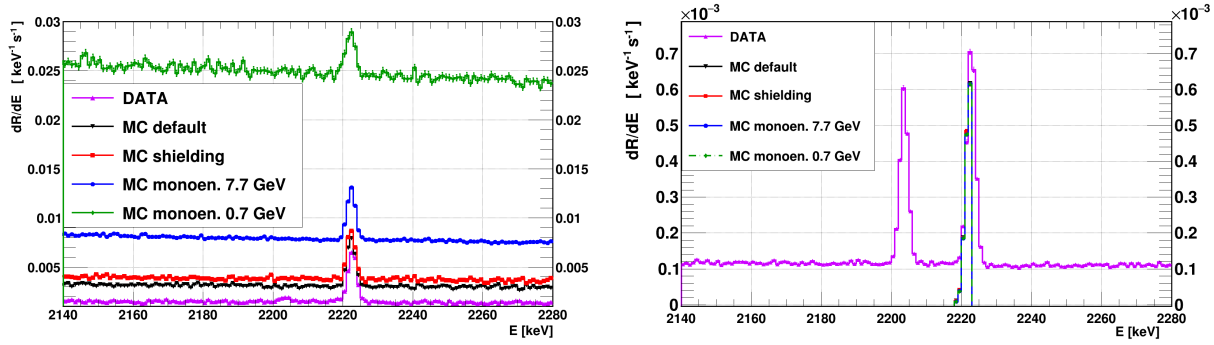

(a) Inside 2 ms

(b) Outside 4 ms

Figure 6.12: Simulated (adjusted) total HPGe energy spectra obtained with the different simulation settings compared to the experimental data (violet). (a) Inside $\Delta T_{win} = 2\,\text{ms}$. (b) Outside $\Delta T_{win} = 4\,\text{ms}$.

6.4 Comparison between the FIT and the BAT Method in MC

The same analysis strategy used for the data was applied to the adjusted total simulated spectra. The results obtained for the *MaGe default* physics list with the BAT and the FIT methods are compared in this section.
Figure 6.13 shows the adjusted *effective* rate of simulated events observed in the *OUTSIDE* spectra (${\Gamma_B}^{default}$) vs ΔT_{win} obtained with the fit and the BAT method. The *effective* rates

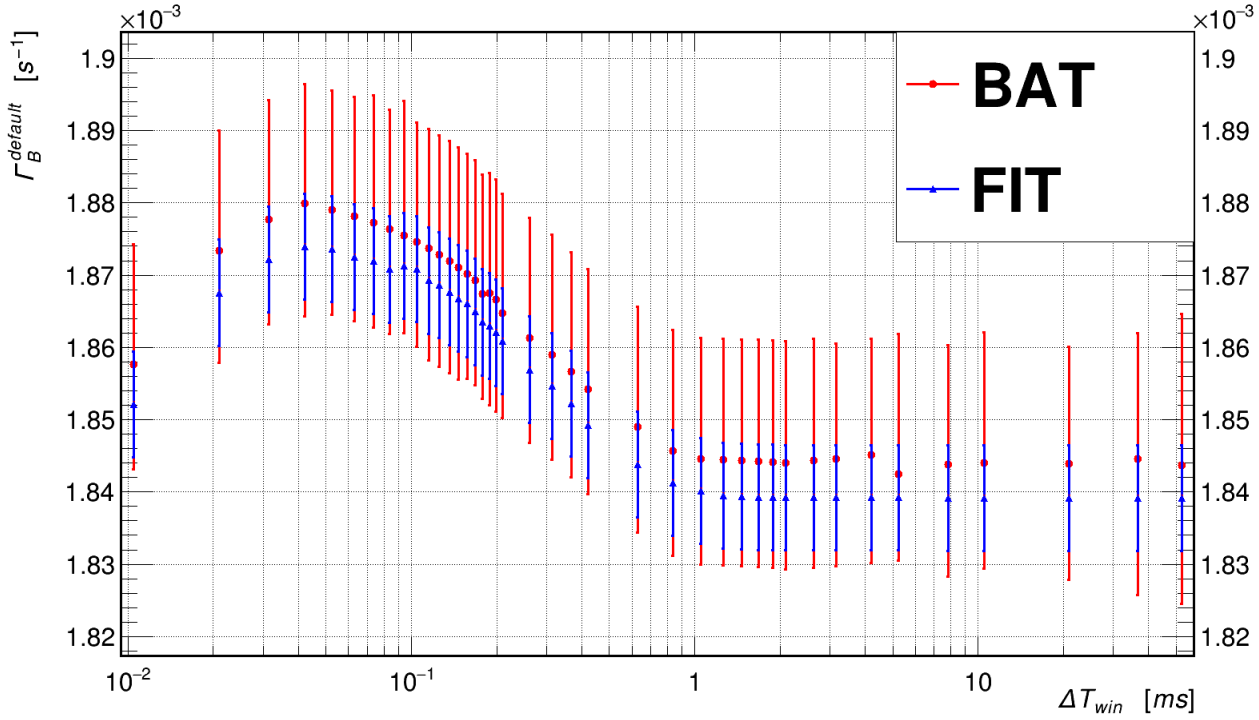

Figure 6.13: The adjusted *effective* rate, ${\Gamma_B}^{default}$, of simulated events observed in the ROI of the *OUTSIDE* spectra, obtained with the FIT (blue triangles) and the BAT (red circles) method vs ΔT_{win}. Uncertainties are statistical as described in Sec. 4.6.

are very consistent within uncertainties, even though the BAT method suggests a slightly higher ${\Gamma_B}^{default}$. By construction, the points are strongly correlated.
Figure 6.14 shows the adjusted simulated *effective* signal rate (${R_S}^{default}$) vs ΔT_{win} obtained with the FIT and the BAT method. The signal *effective* rates are consistent, but in accordance with ${\Gamma_B}^{default}$, ${R_S}^{default}$ is lower for the BAT than for the FIT method.
The signal-to-background ratio obtained with the two methods is shown in Fig. 6.15. The signal-to-background ratio is higher for ΔT_{win} up to 200 μs. For large ΔT_{win} the ratios are very close.

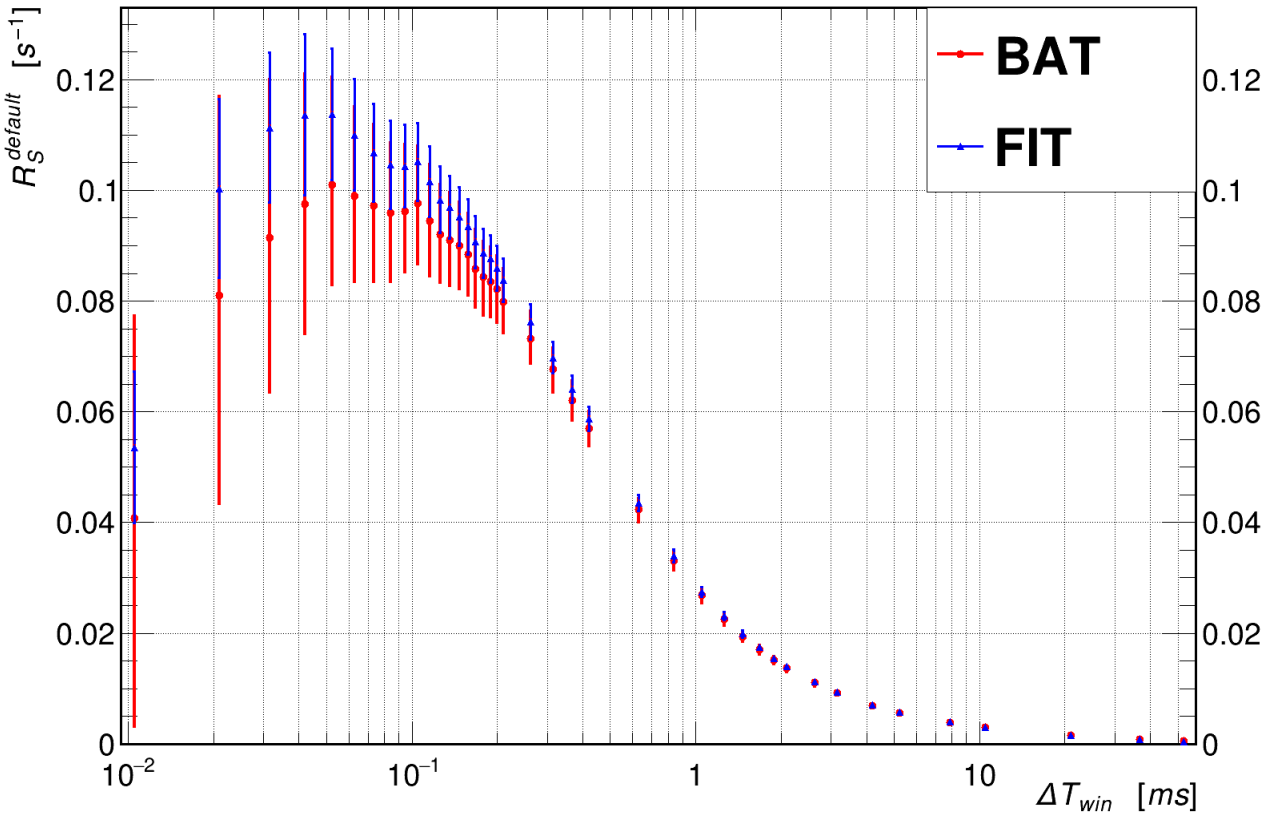

Figure 6.14: The adjusted simulated *effective* signal rate, $R_S{}^{default}$, observed with the FIT (blue triangles) and the BAT (red circles) method vs ΔT_{win}. Uncertainties are statistical as described in Sec. 4.6.

Similarly to Sec. 4.6, the difference between the results obtained with the two methods was taken as the systematic uncertainty, δ^{sys}. A comparison between the systematic and the statistical uncertainties on the signal-to-background ratio is given in Fig. 6.16. The statistical uncertainties are the same depicted in Fig. 6.15, while the systematic values correspond to $2 \cdot \delta^{sys}$. The systematic uncertainties are only important for very small ΔT_{win} where the statistics is low.

In summary, the BAT method expects a higher background and lower signal rate. The signal-to-background ratio is correspondingly lower, especially for ΔT_{win} below 200 μs. The systematic uncertainties observed in the analysis of MC data are higher than for the measurement. For ΔT_{win} below 50 μs they are substantial.

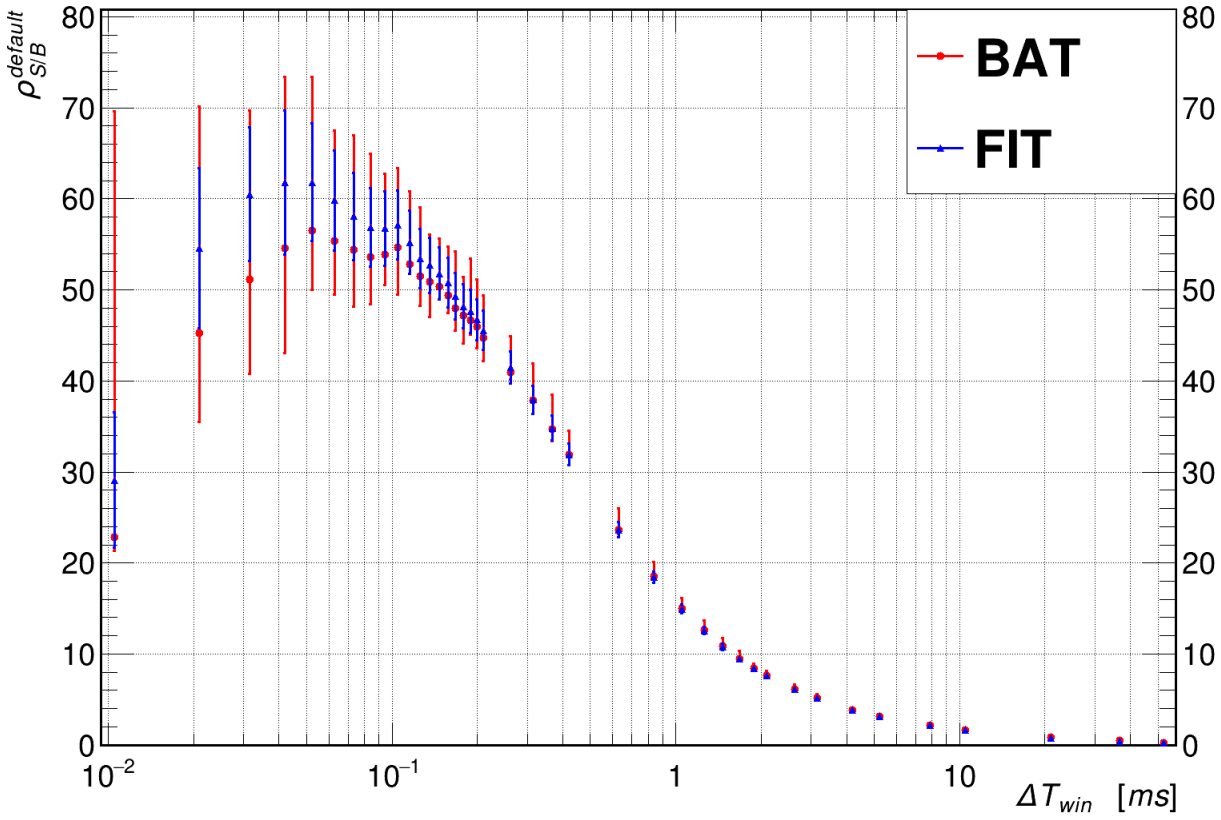

Figure 6.15: The adjusted simulated signal-to-background ratio, ${\rho_{S/B}}^{default}$, observed with the FIT (blue triangles) and the BAT (red circles) method vs ΔT_{win}. Uncertainties are statistical as described in Sec. 4.6.

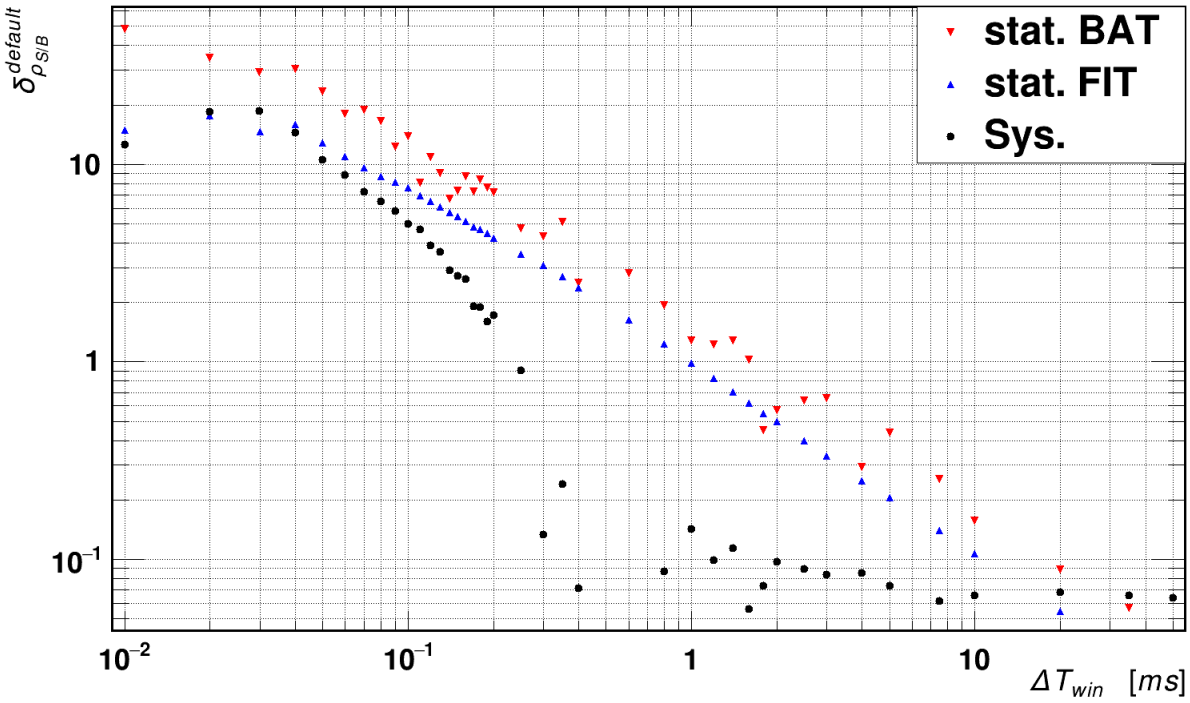

Figure 6.16: Statistical uncertainties on the adjusted ${\rho_{S/B}}^{default}$ as obtained with the FIT (blue triangles) and the BAT (red triangles) method are shown together with systematic uncertainties (black circles).

6.5 Comparison between Adjusted MC and Data

The BAT method relies on the accuracy of the side bands, which are affected by all background components, as described in Sec. 4.6. Therefore, due to the incomplete background description in the MC, the FIT method was chosen as reference to present the comparison of MC and data. Statistical and systematic uncertainties were added in quadrature.
In this section, only the results obtained with the *MaGe default* and the *Shielding* physics lists are shown in comparison to experimental data. The respective comparisons for all four simulation settings are available in Appendix D.
The results for Γ_B, R_S and $\rho_{S/B}$ are shown in Figs. 6.17, 6.18 and 6.19, respectively.

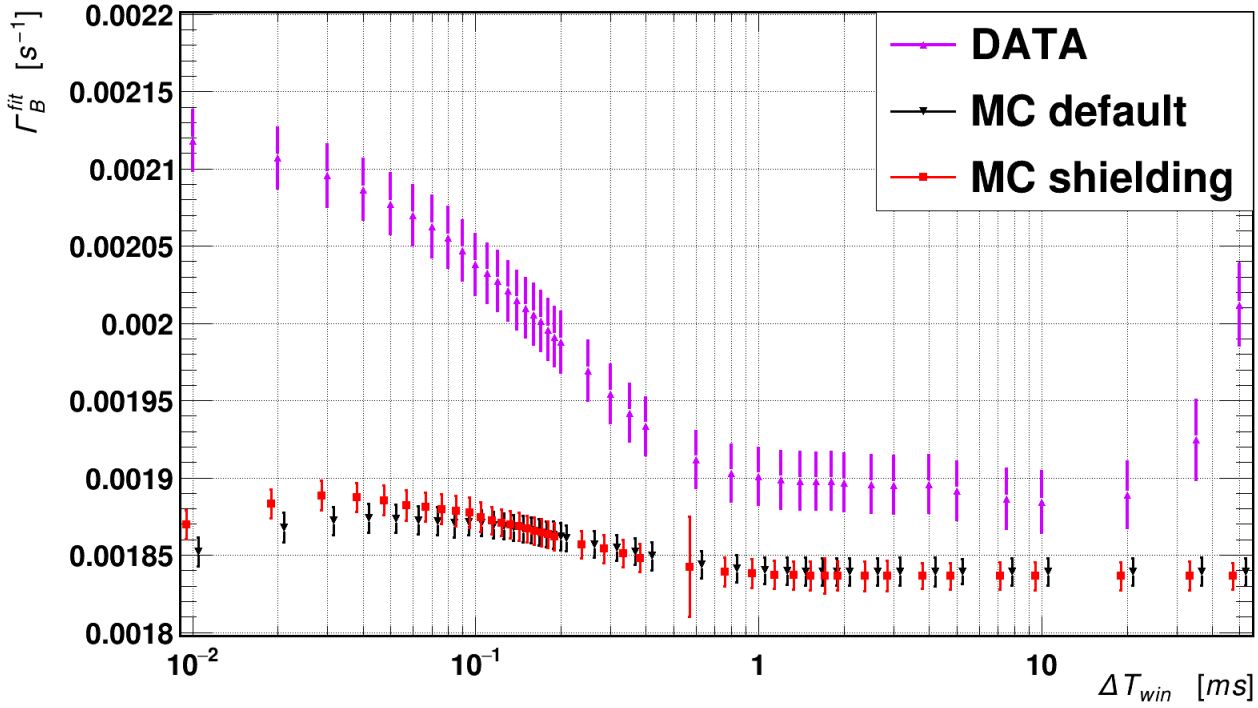

Figure 6.17: Measured and adjusted predicted *effective* rates, Γ_B, vs ΔT_{win}. Only predictions from the *MaGe default* and the *Shielding* physics lists are displayed. The points were displaced horizontally for better visibility. Some values for small ΔT_{win} are not available due to non-applicability of the FIT method because of too low statistics. Uncertainties are statistical and systematic added in quadrature.

As for Fig. 6.8, the measured values of Γ_B shown in Fig. 6.17 were not corrected for the inefficiency of the scintillators. The background-only region, the plateau for ΔT_{win} above 1 ms, is in good agreement between data and MC. The observed rise of Γ_B in the data

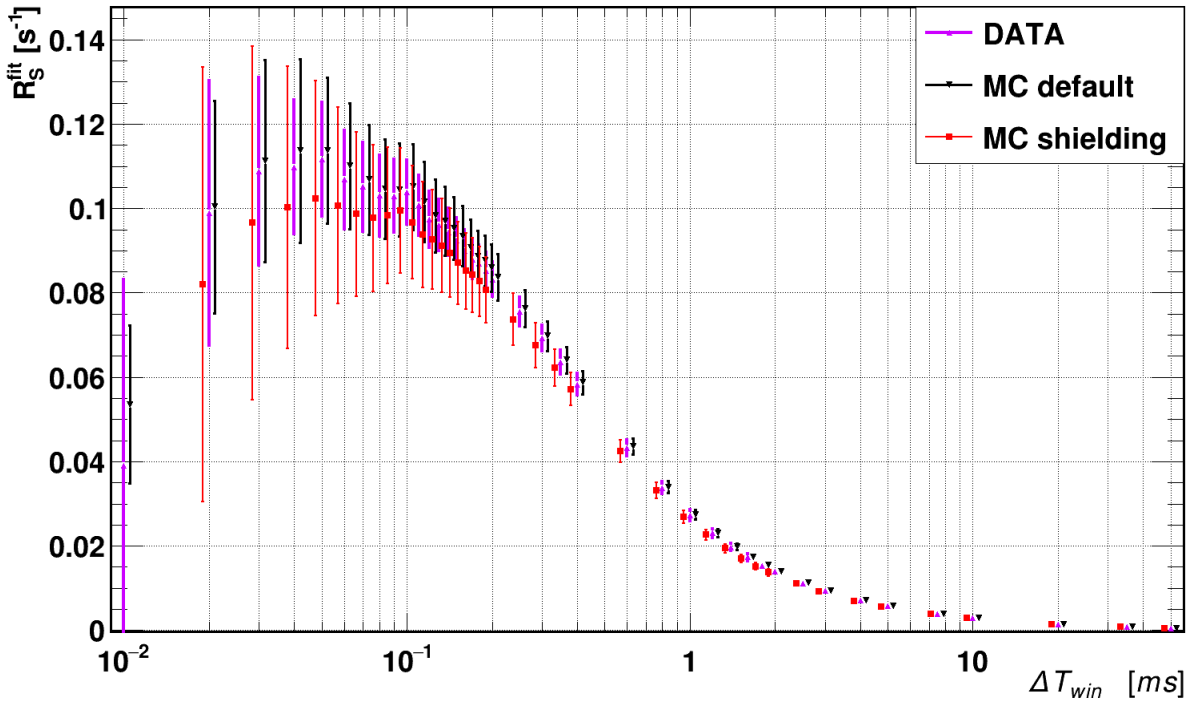

Figure 6.18: Measured and adjusted predicted *effective* signal rate, R_S, vs ΔT_{win}. Only predictions from the *MaGe default* and the *Shielding* physics lists are displayed. The points were displaced horizontally for better visibility. Some values for small ΔT_{win} are not available due to non-applicability of the FIT method because of too low statistics. Uncertainties are statistical and systematic added in quadrature.

towards small ΔT_{win} is not well reproduced by the MC. This is due to the low quality of the fits performed for small ΔT_{win} where the statistics is too low. The absence in the MC of the rise of Γ_B for large ΔT_{win} confirms that the rise observed in the experimental data is related to muon-bundles, which were not described in the MC.
The measurements of ${R_S}^{corr}$ and ${\rho_{S/B}}^{corr}$, shown in Figs. 6.18 and 6.19, were corrected for the inefficiency of the scintillators.

Table 6.4 shows the *effective* background rates, ${R_B}^{FIT-corr}$, for data (corrected for the inefficiency of the scintillators) and adjusted MC.

Table 6.5 shows the *effective* signal rates, ${R_S}^{FIT-corr}$, for $\Delta T_{win} = 4\,\text{ms}$ for both data (corrected for the inefficiency of the scintillators) and adjusted MC.

By construction, measurements and predictions agree after the adjustment of the MC.

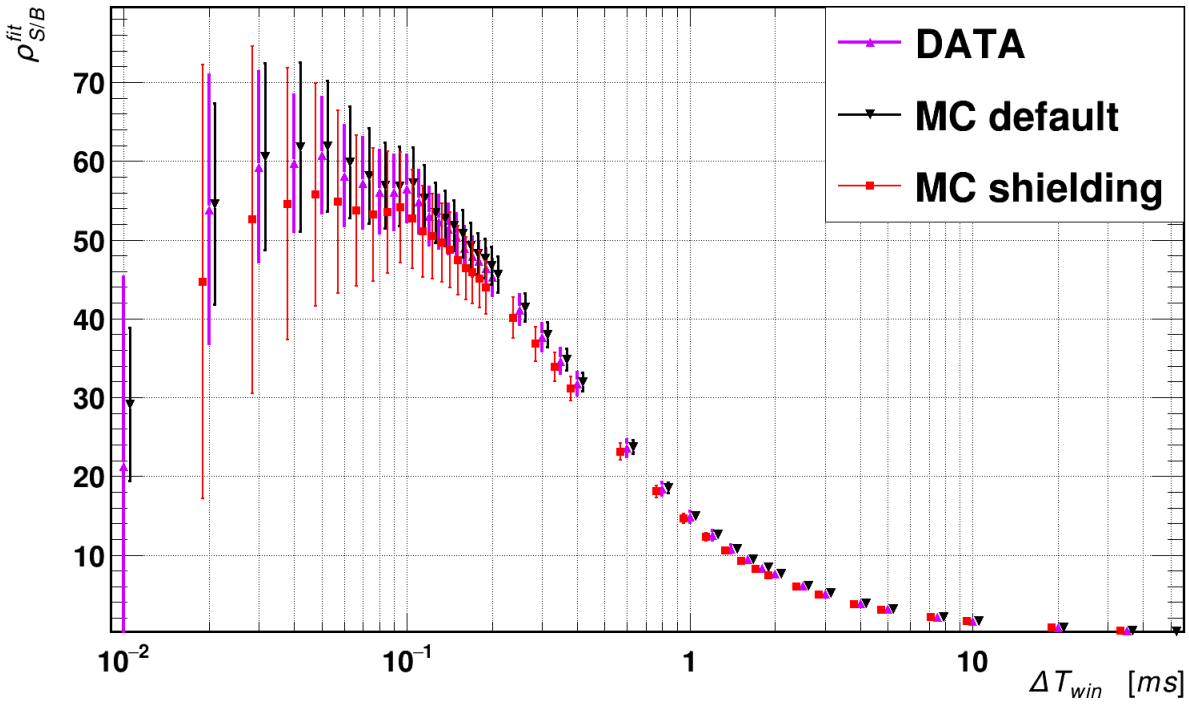

Figure 6.19: Measured and adjusted predicted signal-to-background ratio, $\rho_{S/B}$, vs ΔT_{win}. Only predictions from the *MaGe default* and the *Shielding* physics lists are displayed. The points were displaced horizontally for better visibility. Some values for small ΔT_{win} are not available due to non-applicability of the FIT method because of too low statistics. Uncertainties are statistical and systematic added in quadrature.

Sample	${R_B}^{FIT-corr} \cdot 10^{-5}$ [s^{-1}]
Data	(183.8 ± 1.9)
MaGe default	(183.9 ± 0.7)
Shielding	(183.6 ± 0.7)
Monoen. 7.7 GeV	(184.0 ± 0.8)
Monoen. 0.7 GeV	(184.1 ± 0.8)

Table 6.4: *Effective* background rates obtained with the FIT method as measured and as predicted after the MC adjustment. All four MC settings are listed. The data were corrected for the inefficiency of the scintillators. Uncertainties are statistical only.

The variation of A_i with ΔT_{win}, see Appendix C, shows that the signal development is described within an envelope of approximately 70%. It is important to keep in mind that the

Sample	${R_S}^{FIT-corr}\vert_{\Delta T_{win}=4\,ms} \cdot 10^{-5}$ [$\mathbf{s}^{-1}$]
Data	(702 ± 23)
MaGe default	(706 ± 23)
Shielding	(690 ± 26)
Monoen. 7.7 GeV	(706 ± 15)
Monoen. 0.7 GeV	(675 ± 69)

Table 6.5: *Effective* signal rates, ${R_S}^{FIT-corr}$, for $\Delta T_{win} =$ 4 ms obtained with the FIT method as measured and as predicted after the MC adjustment. All four MC settings are listed. The data were corrected for the inefficiency of the scintillators. Uncertainties are statistical only.

effective signal-rates reported in Tab. 6.5 refers only to events induced by through-going muons which can be triggered.

Figure 6.20 shows the systematic uncertainties of the signal-to-background ratio, ${\delta_{\rho_{S/B}}}^{sys}$, vs ΔT_{win} for data and adjusted MC.

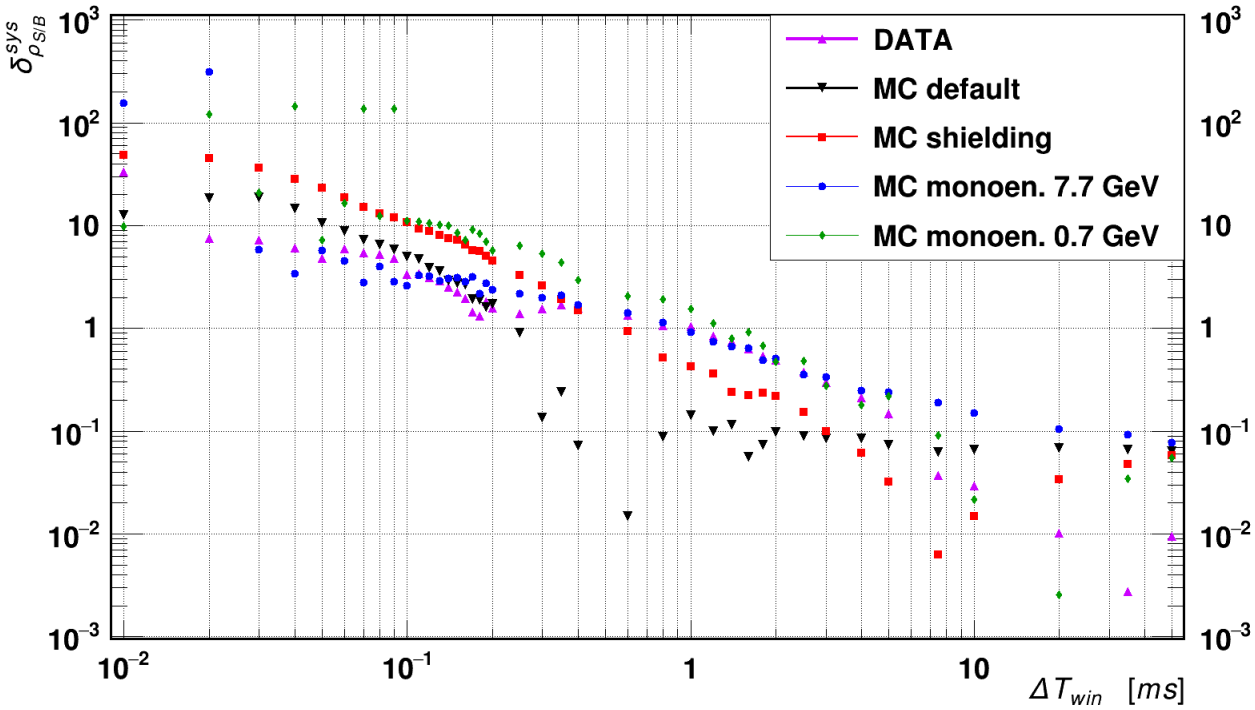

Figure 6.20: Comparison of the systematic uncertainties of the signal-to-background ratio, ${\delta_{\rho_{S/B}}}^{sys}$, vs ΔT_{win}, between data and adjusted MC. The data were corrected for the inefficiency of the scintillators. Some values for small ΔT_{win} are not available due to non-applicability of the FIT method because of too low statistics. All four MC settings are shown.

6.6 Summary of Observations

The main observations are that:

- the data show an overall ≈70% (100%) higher rate of muon-induced events than predicted by the *MaGe default* (*Shielding*) MC, see A_i for $\Delta T_{win} \geq 1\,\text{ms}$ in Appendix C and Tab. 6.2;
- the time until the signal from the muon-induced events is completely collected is well reproduced by the MC, see plateaus of Figs. 4.25, 6.8, D.3 and numbers for A_i for ΔT_{win} above 1 ms;
- the MCs predict a faster time evolution as observed in the data. This is especially observed for the *MaGe default* MC, see A_i for $\Delta T_{win} < 200\,\mu\text{s}$ in Appendix C
- the *Shielding* MC reproduces the time evolution of the muon-induced signal better than the *MaGe default* MC, see Fig. 6.9 and the stability of the values A_i in Appendix C;
- the background contribution from natural radioactivity is ≈78 (70) times higher than the background from cosmogenic sources as predicted by the *MaGe default* (*Shielding*) MC, see B_i for $\Delta T_{win} \geq 1\,\text{ms}$ in Appendix C.

Chapter 7

Summary and Outlook

In low-background experiments, such as direct dark matter and neutrinoless double-beta-decay experiments, neutrons, either muon-induced or from natural radioactivity represent a serious source of background. Detailed and reliable Monte Carlo simulations are crucial to predict this background, which is needed to estimate the sensitivity of such experiments, especially for deep underground locations.
The MINIDEX setup is a table-top apparatus aimed to measure muon-induced neutrons in high-Z materials via neutron thermal capture in hydrogen. Its simplicity helps to keep the systematics at a minimum, although its signal-to-background ratio strongly depends on its geometry. The target material chosen for MINIDEX run I is lead, since it represents one of the most common shielding materials used in low-background experiments. Furthermore, as discussed in Ch. 3, the results related to neutron production in lead are still controversial in the literature. This controversy concerns both experimental results and MC studies.
The lead castle of MINIDEX surrounds a volume of water, which is used to thermalize and capture the neutrons on hydrogen resulting in the emission of 2.2 MeV gammas. The gammas are detected with two HPGe detectors, placed in the innermost part of the setup. Two scintillator panels, placed on top and at the bottom of the lead castle, are used to identify through-going muons. All the different detectors are recorded independently allowing for a parallel measurement of the signal and the background. MINIDEX is located in the Tübingen Shallow Underground Lab. Its first run, MINIDEX run I, started the data-taking on July 15, 2015.
Although it was a simple apparatus, the MINIDEX run I setup was already a valuable facility for MC validation for neutron production and transport in lead. It has provided benchmark data to validate GEANT4 simulations. The analysis strategy adopted, which was presented in Ch. 4, provides a clear distinction between signal and background. Moreover, it allows to probe the time evolution of the events.
The data of the first 113 days of data-taking of MINIDEX run I were analyzed and the results were discussed. In Ch. 5, a detailed description of the MC simulations used to predict the behavior of the MINIDEX setup was reported. Different physics lists were probed and the respective results were compared. In Ch. 6 the experimental results were compared to predictions from the simulations. The similarities and differences between data and MC

were discussed.
In this chapter the main results of the analysis are summarized. In addition, some problems with the current MC implementation are discussed. In the end, the future plans for MINIDEX will be presented.

7.1 The Muon-Induced Neutron Signal

In the first 113 days of data-taking of MINIDEX run I, $7.98745 \cdot 10^7$ triggered events were recorded. This translates, after the correction for the inefficiency of the scintillator panels, to a trigger rate of ${R_{trig}}^{DATA-corr} = 10.15$ Hz. The overall signal (muon-induced 2.2 MeV gammas) detection probability of the MINIDEX apparatus is of the order of $\approx 10^{-5}$ (2.2 MeV gammas/trigger-muon).

The measured *effective* rate of events induced by through-going muons for a signal window (ΔT_{win}) of 4 ms is

$$ {R_S}^{FIT}|_{\Delta T_{win}=4\,ms} = (702 \pm 24) \cdot 10^{-5}\ \mathrm{s}^{-1} \tag{7.1} $$

while the measured *effective* background rate is:

$$ {R_B}^{FIT}|_{\Delta T_{win}=4\,ms} = (183.8 \pm 1.9) \cdot 10^{-5}\ \mathrm{s}^{-1}\ . \tag{7.2} $$

This amounts to a signal-to-background ratio of approximately 4. The largest signal-to-background ratios of around 55 were measured for ΔT_{win} between 20 and 100 μs.
Simulation studies were carried out with GEANT4 9.6 interfaced to the MaGe simulation framework. Cosmic muons and cosmogenic neutrons were propagated from ground level to the roof of the Tübingen ,TSUL, laboratory where MINIDEX is located. For this, a simplified geometry of the TSUL overburden was implemented. The muons and neutrons recorded at the laboratory roof were subsequently used as input to the simulation of the response of the MINIDEX run I. The simulated muon flux at the laboratory roof is:

$$ \Phi_\mu = 16.58\,\mathrm{m}^{-2}\,\mathrm{s}^{-1}\ . \tag{7.3} $$

The resulting trigger rate is ${R_{trig}}^{SIM} = 5.37$ Hz. There is a factor of $\approx$1.8 difference between the measured and the simulated trigger rate. This discrepancy between data and MC, however, reflects the choice of the size of the generation plane at the surface and the simplified description of the geometry of the laboratory overburden.
The two physics lists that were probed in the analysis presented in this thesis are:

- the *MaGe default* physics list;
- the *Shielding* physics list.

These physics lists are the recommendations of the GERDA-Majorana and the GEANT4 collaborations, respectively. No difference was found between the two physics lists in

terms of predicted trigger rate, but the predicted neutron yield was found to be different. The *MaGe default* physics list predicts an overall factor of ≈1.3 more neutrons than the *Shielding* one. The prediction for the neutron yield via muon-capture is ≈2 times higher in the *MaGe default* physics list. However, in MINIDEX run I the neutrons produced via muon-capture are part of the background. For μ^+, the mean neutron multiplicity predicted by the simulation is ≈5, whereas for μ^-, it is ≈3.2. The difference is most likely due to the muon-capture events.
The neutron yield obtained with the *MaGe default* physics list is:

$$Y_n \;=\; 1.14 \cdot 10^{-4}\, \frac{n}{\mu(g/cm^2)} \;. \tag{7.4}$$

When MC was compared to data, an underproduction of the MC of muon-induced neutrons, and thus of muon-induced 2.2 MeV gammas, was found. This underproduction was already observed in the past, as discussed in Ch. 3. There is factor of approximately 1.7 between data and MC concerning the muon-induced component, see Tab. 6.2 and Appendix C. The MC correctly predicts the time, after which the muon-induced signal is collected completely. However, a detailed study of the time evolution indicates that the signals builds up faster in the MC. This is less pronounced for the *Shielding* than for the *MaGe* physics list. In terms of rates, the *MaGe default* physics list reproduces the experimental data better than the *Shielding* physics list. Nevertheless, it still needs to be improved. Detailed studies of the different models used by this physics list are necessary.
Since in the background model, the natural radioactivity component was missing, the MC components were adjusted to the data. Under the assumption that in the ROI, the neutron background from natural radioactivity has the same shape as the background from cosmogenic sources, this allows to estimate the relative strength of the missing component. It was found that natural radioactivity is about 75 times more important than cosmogenic neutrons in the TSUL.
In general, at shallow depths, the muon energy spectrum should not be replaced by a monoenergetic muon beam. Furthermore, the muon and neutron angular distribution represent a relevant input parameter to be included in the MC description. Neglecting either spectral or angular distributions leads to invalid MC predictions.

7.2 Background Composition

The background in MINIDEX run I can be separated according to its origin:

- the contribution of 2.2 MeV gammas due to neutrons produced in muon captures was considered as part of the background for MINIDEX run I. This component could experimentally be included in the *signal-like* events with full coverage of the MINIDEX lead castle with plastic scintillators. From the difference between the predicted μ^-- and μ^+-induced 2.2 MeV gamma fluxes shown in Fig. 5.11, the contribution of the events induced by muon capture to the measured background can be roughly estimated, if it is assumed that the entire difference originated from μ^- capture[1]. The result of this rough estimate is a background rate of

$$BR_{\mu-capture} \approx 45 \cdot 10^{-5}\ \mathrm{s}^{-1} \quad , \tag{7.5}$$

  which corresponds to ≈25% of the total background rate measured in MINIDEX run I.

- A complete coverage of the lead castle with scintillators would also drastically reduce the *NON triggering muons* background component. Geometric arguments provide a rough estimate to the background rate due to the *geometrically NON triggering muons*:

$$BR_{geom-NON-trig.-\mu} \approx 10 \cdot 10^{-5}\ \mathrm{s}^{-1} \ , \tag{7.6}$$

  which corresponds to ≈6% of the total background rate measured in MINIDEX run I.

In total, about 1/3 of the background events in MINIDEX run I are due to untriggered muons, which either cross the setup at shallow angles or undergo muon capture. The rest of the background to the 2.2 MeV gamma peak is due to cosmogenic neutrons and, even more important, to neutrons from natural radioactivity. The latter was shown to be dominant by a factor of around 75 in a fit to the data.

[1] This assumption is reasonable, as all other processes are the same for μ^- and μ^+.

7.3 MC Issues

In the following, a summary of known deficits in the MC description, which might have affected the predictions used in this analysis, is given:

- a detailed description of the geometry of the TSUL overburden is missing. The information was not available at the time of implementation.
- The generation plane at ground level was chosen to just cover the lab. After the implementation of the full geometry, it will be appropriately enlarged. The plane can also be replaced with a hemisphere. This will remove any geometrical issue concerning the incoming particle fluxes at the roof of the laboratory.
- The muon flux at sea level used as input of Step 1 of the simulation was neither corrected for the latitude nor for the altitude of the TSUL location.
- The fluxes of μ^+ and μ^- were assumed to be identical. A refined ratio of these two component should be used in the future.
- A measurement of the muon energy spectra inside the laboratory would be the best crosscheck for step 1 of the MINIDEX simulations. This will however not be feasible in the foreseeable future.
- Muon bundles were not considered in the MC.
- The background from natural radioactivity was not included in the description of the background in the MC. From the results presented here, it is clear that this background component is substantial. It will be included in future studies. Currently, a study to determine the uranium and thorium concentration in the walls of the laboratory is ongoing.
- In general, various particles produced by the interactions of muons in the overburden of an experiment can contribute to the neutron background. Such processes were also not included in the MC. For example, Fig. 7.1 shows the simulated gamma (a) energy, (b) polar-angle and (c) azimuthal-angle distributions at the laboratory roof. These gammas result from cosmic muon and neutron interactions in the lab overburden. They can interact in the laboratory and even in MINIDEX via photonuclear disintegration and themselves create neutrons.
- Cosmogenic muons and neutrons were assumed to be uncorrelated. However, it has been shown that there is a correlation, especially for neutrons above 10 MeV [106, 250, 194]. Figure 7.2 shows the azimuthal-angle distribution for muons, neutrons and gammas at the laboratory roof. The fluxes were normalized to 1. As expected for Bremsstrahlung (see also [179]), there is an angular correlation between muons and gammas.

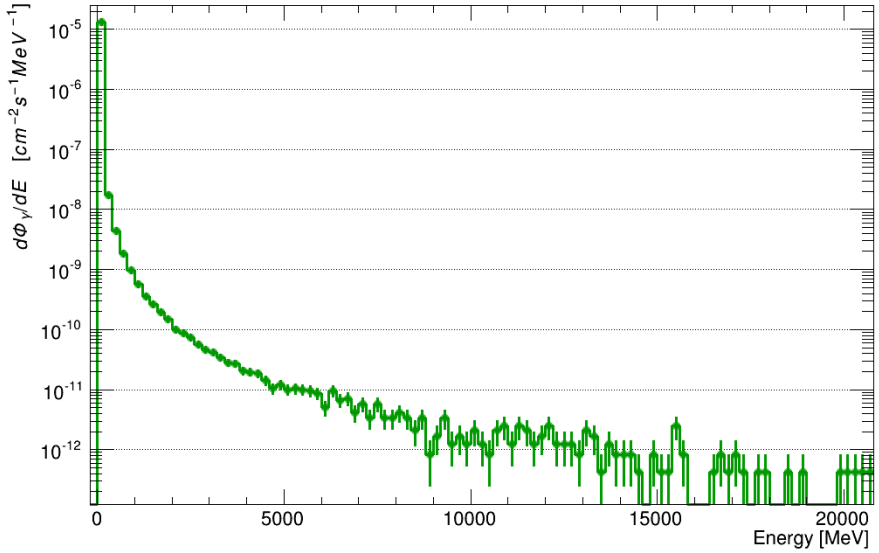

(a)

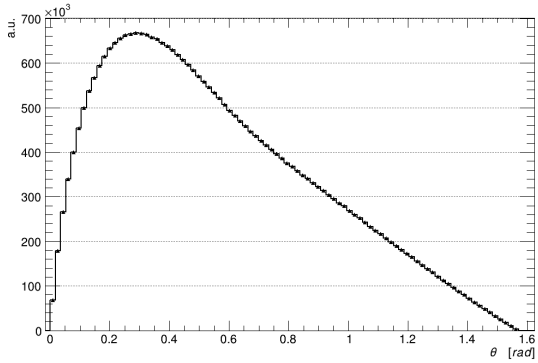

(b)

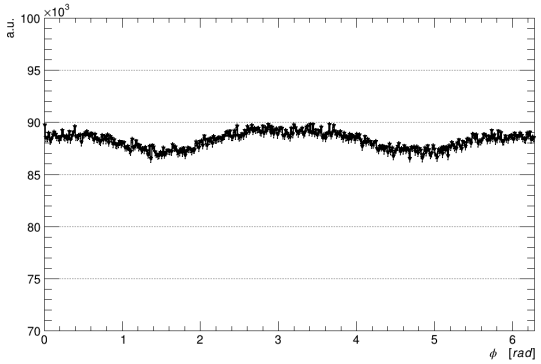

(c)

Figure 7.1: Simulated gamma (a) energy, (b) polar-angle and (c) azimuthal-angle distributions at the laboratory roof.

- The MC did not include particle fluxes entering the laboratory from the side walls. It should be noted that the choice of the generation plane in step 1 would have an even larger impact on these fluxes than on those at the roof.

All these MC issues will have to be addressed in the future. The goal is to tune the MC processes, such that the MC predictions become more reliable. Work on improving the inputs to the MC has started. This will certainly result in an improvement of the accuracy of the MC predictions. Moreover, a detailed study of the contributions of the different physics processes responsible for the neutron yield in the MC will improve the understanding and the interpretation of the data. Eventually, a customized physics list should be built.

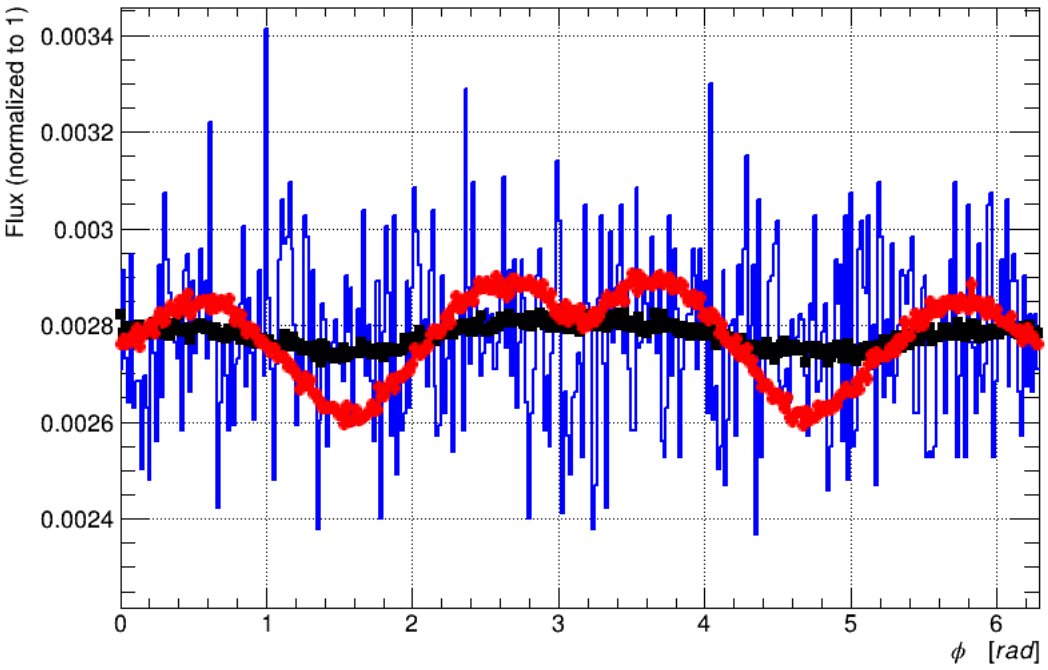

Figure 7.2: Simulated azimuthal-angle distributions at the laboratory roof for muons (red), neutrons (blue) and gammas (black). The fluxes were normalized to 1.

The MC studies presented here were done with GEANT4 based packages. For the future, comparisons with FLUKA predictions are also foreseen. The MINIDEX geometry and TSUL environment have been already implemented in FLUKA [251].

7.4 Neutron Yield

As discussed in Ch. 3, one of the most debated issues in the low-background physics community concerns the neutron yield. In the literature, there are even multiple definitions of the neutron yield. This quantity is, in general, difficult to measure, especially for high-Z materials. Moreover, the neutron yield is very sensitive to the geometry of the experiments. MC based techniques were developed in order to remove the geometry dependence of the neutron yield [135, 134]. However, these techniques have introduced a dependence on the simulation packages used. Therefore, a direct comparison between results obtained by different experiments is not straight forward possible and the results are still under debate. In Tab. 7.1 selected measurements of neutron yield at different depths using liquid scintillators are reported.

Reference	**Depth [km.w.e]**	$< E_\mu >$ **[GeV]**	Y_n **[n/(μ g cm^{-2})]**
Hertenberger [173]	0 .02	13	$(2 \pm 0.7) \cdot 10^{-5}$
Bezrukov [189]	0 .025	14.7	$(4.7 \pm 0.5) \cdot 10^{-5}$
Boehm [174]	0 .032	16.5	$(3.6 \pm 0.31) \cdot 10^{-5}$
Bezrukov [189]	0 .316	55	$(1.21 \pm 0.12) \cdot 10^{-4}$
Blyth [207]	0 .611	120	$(1.19 \pm 0.08(stat.) \pm 0.21(syst.)) \cdot 10^{-4}$
Enikeev [208]	0 .75	120	$(2.15 \pm 0.15) \cdot 10^{-4}$
KamLAND [128]	2.7	260 ± 8	$(2.8 \pm 0.3) \cdot 10^{-4}$
Lindote [181]	2.85	260	$(1.31 \pm 0.06) \cdot 10^{-3}$
Reichhart [134]	2.85	260	$(5.78\ ^{+0.21}_{-0.28}) \cdot 10^{-3}$
LVD-1999 [172]	3.1	270	$(1.5 \pm 0.4) \cdot 10^{-4}$
LVD-2013 [183]	3.1	280	$(2.9 \pm 0.6) \cdot 10^{-4}$
Borexino [209]	3.8 [252]	270 [146]	$(3.10 \pm 0.11) \cdot 10^{-4}$
LSD [171]	5.2	385	$(5.3\ ^{+0.95}_{-1.02}) \cdot 10^{-4}$

Table 7.1: Measurements of muon-induced neutron yield performed with liquid scintillators at different underground sites. For each site, the equivalent vertical depth relative to a flat overburden and the mean muon energy $< E_\mu >$ are reported.

From Tab. 7.1, it can be seen that there are inconsistencies. The two LVD measurements [172, 183] are clearly inconsistent. It should be also noted that the inconsistent results of Lindote [181] and Reichhart [134], which refer to ZEPLIN-II and ZEPLIN-III, respectively, were performed with liquid scintillators, but according to simulations, lead was the main source of the measured neutrons rather than the liquid scintillator material. Although liquid scintillators are the most common technique used to measure muon-induced neutrons, there are also measurements based on other techniques, see for example [176, 253, 254, 255]. Inconsistencies were also observed between different simulation packages and their different

versions, as discussed in Ch. 3.
There have been multiple attempts to parametrize Y_n as a function of the mean muon energy[2] [135, 178, 181, 119, 132, 167, 256], using the measured values of Y_n. However, these parametrizations are highly controversial in the community.
The setup of MINIDEX run I was not optimized to measure the neutron yield. However, a prediction of Y_n was given in Sec. 5.5.3. Due to its simplicity, MINIDEX can be easily moved to different locations. This will allow to have measurements of the neutron yield in lead at different depths, i.e. for different mean energies of the incoming muons, that can be directly compared to each other. This will remove any ambiguity on the definition of the neutron yield and a coherent parametrization of Y_n as a function of the mean muon energy will become possible. For this reason, some future locations are currently being discussed.
It is worth mentioning that the analysis technique presented in this thesis can be applied to MINIDEX data from both deeper and shallower locations than TSUL. However, due to the limited size of the MINIDEX setup, measurements at deep sites ($>$ 100 m.w.e.) are not feasible. The possibility to irradiate MINIDEX with a muon beam with a tunable energy at CERN is currently also discussed. This would allow to study the interactions of high-energy muons.
Future plans also include the possibility to probe different materials, such as copper, polyethylene, steel and concrete. These materials are also commonly used in low-background experiments.
The capability of MINIDEX to measure neutron yields was enhanced by adding a fast neutron detector for MINIDEX run II.

7.5 MINIDEX run II

MINIDEX run II started January 21, 2016, two days after the end of MINIDEX run I. The very short shutdown was used to upgrade the setup. The scintillator panels were replaced. New scintillators, produced again by Saint-Gobain Crystals [221], of the same size (65 x 75 x 5 cm^3) and made of the same material (BC-408) were installed. These have a much higher efficiency of $\epsilon \geq 99\%$ each. The efficiency is drastically improved because the PMTs are now placed outside the volume of the panels and not embedded anymore (see Fig. 7.3) and because the manufacturing process was properly controlled.
In addition, four more scintillator panels were added to the system. Their size is 65 x 20 x 5 cm^3 and they also have high efficiency, $\epsilon \geq 99\%$ each. Two of them are positioned on top and two of them at the bottom of the setup as shown in Fig. 7.4. These new scintillators allow to determine the topology of through-going muons. Specifically, it is now possible to distinguish between muons which pass through only lead or also through water. In MINIDEX run I, it was not possible to make such a distinction. MINIDEX run II can, thus, provide a clean sample of muons only crossing lead.

[2]Different depths correspond to different mean muon energies.

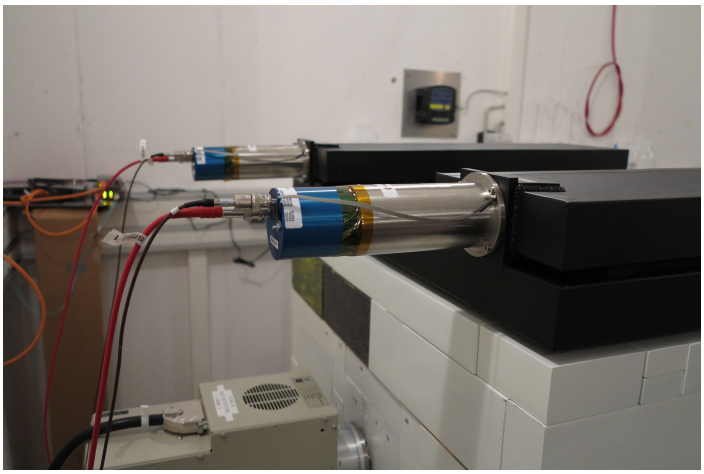

Figure 7.3: The new plastic scintillator panels. The PMTs are mounted outside the panel volumes.

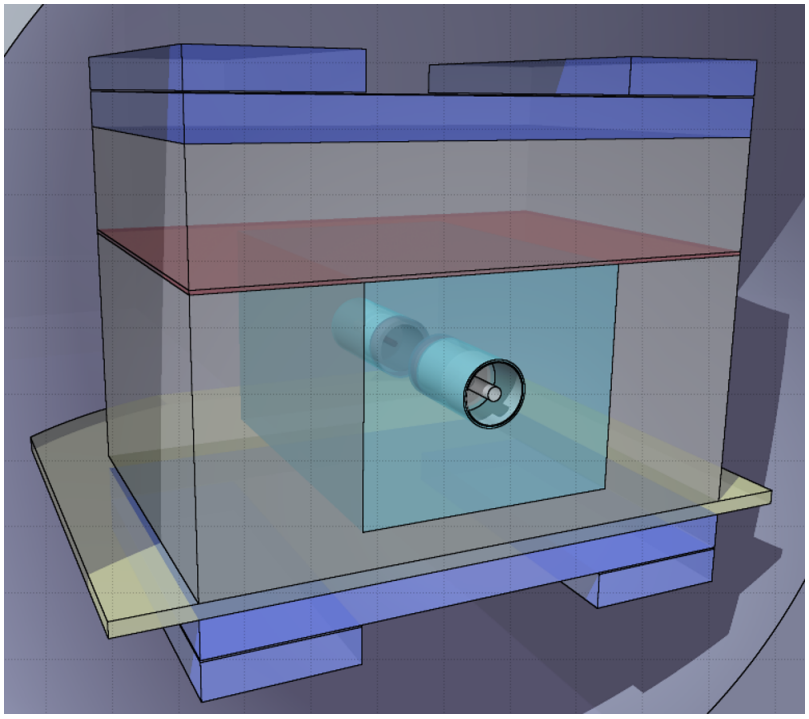

Figure 7.4: Sketch illustrating the MINIDEX run II geometry [251]. Four smaller scintillators above and below the lead walls were added to the system compared to MINIDEX run I.

The possible trigger configurations, depicted in Fig. 7.5, of MINIDEX run II are:

- **MAIN** trigger: similarly to MINIDEX run I, only the big panels are required to provide a signal within a time difference of 60 ns. It is requested for all sub-triggers.
- **Side** sub-trigger: muons which have crossed only one of the lead walls of MINIDEX. These muons represent a clean sample of interactions in lead.
- **Central** sub-trigger: muons which have gone through the central part of MINIDEX without firing the new four small panels.
- **Fully Diagonal** sub-trigger: muons which have crossed MINIDEX diagonally, by firing either the top-left and bottom-right or the top-right and bottom-left panels.
- **Partially Diagonal** sub-trigger: muons which have fired only one of the small panels.

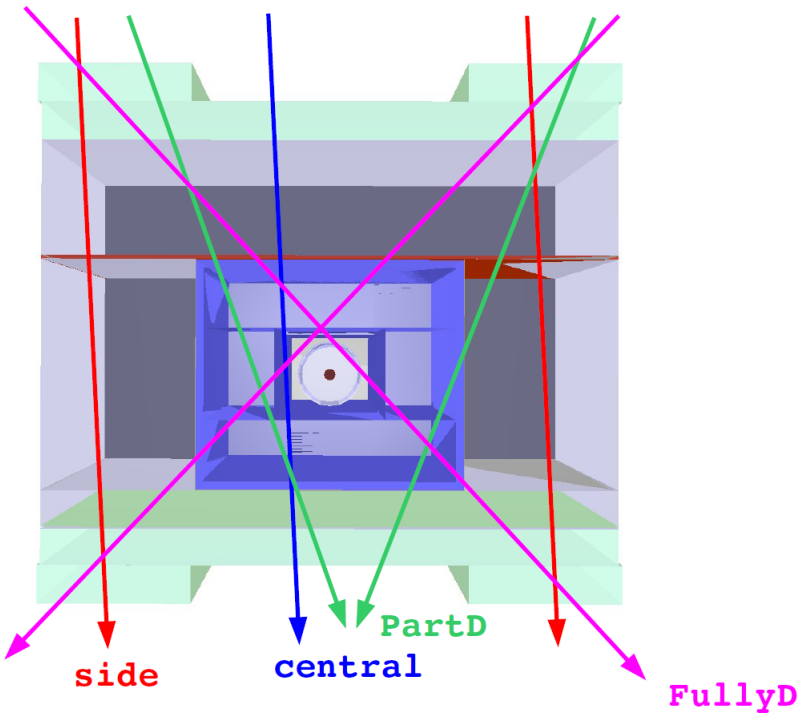

Figure 7.5: Sketch illustrating the MINIDEX run II trigger configurations.

Figure 7.6 shows the simulated HPGe energy spectra, normalized to RT, for the different trigger configurations. These spectra were obtained using the *MaGe default* physics list.

The overall probabilities to detect 2.2 MeV muon-induced gammas, i.e. the number of counts under the 2.2 MeV Gaussian peak divided by the number of *MAIN* triggers for the different trigger configurations are:

- **MAIN** trigger: $\approx 1.2 \cdot 10^{-5}$, as MINIDEX run I;
- **Side** sub-trigger: $\approx 3.7 \cdot 10^{-6}$; .
- **Central** sub-trigger: $\approx 4.7 \cdot 10^{-6}$;
- **Fully Diagonal** sub-trigger: $\approx 1.4 \cdot 10^{-6}$;
- **Partially Diagonal** sub-trigger: $\approx 1.9 \cdot 10^{-6}$.

The lead-water sample, *Central*, is more efficient than the pure lead sample, *Side*. The *self absorption* of neutrons inside the lead is responsible for this.

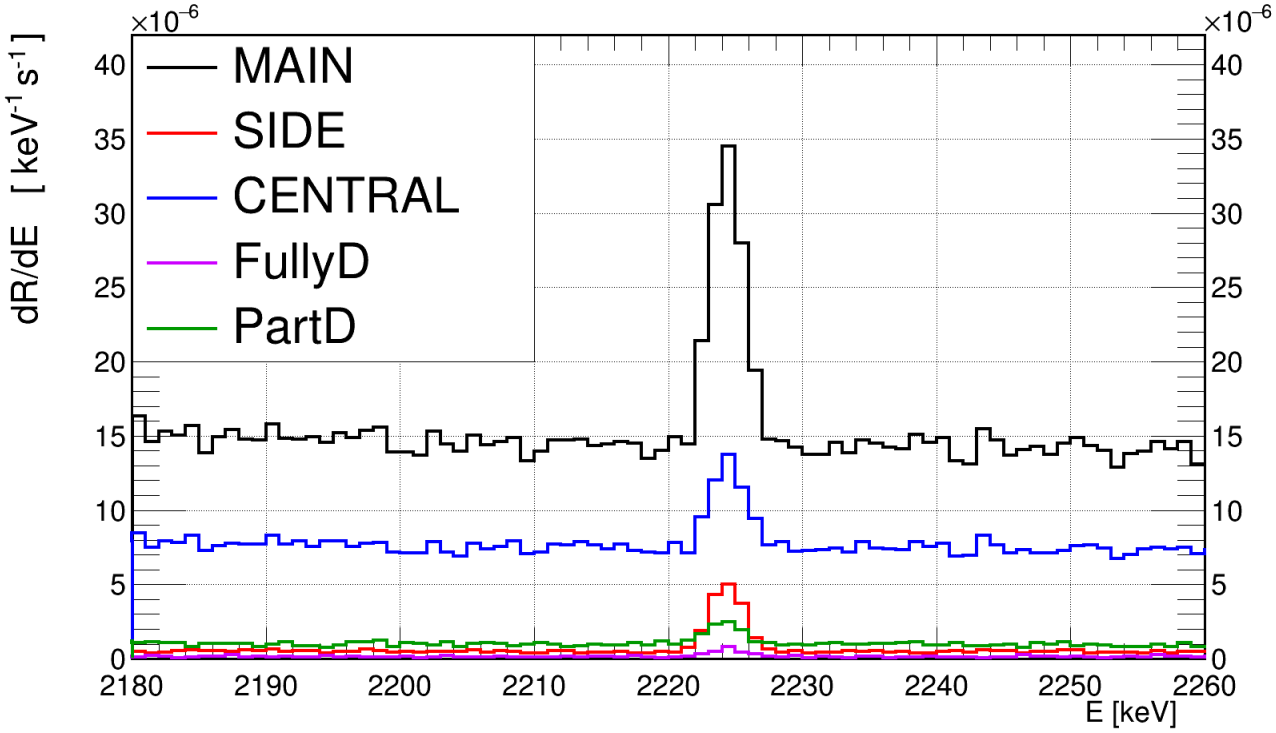

Figure 7.6: The simulated HPGe spectra for the different trigger configurations of MINIDEX run II. These spectra were obtained with the *MaGe default* physics list.

The small scintillators can also be used to identify muon bundles by looking for events when both top or bottom small panels fire within the trigger window. A study of such events will be included in the analysis of MINIDEX run II. Furthermore, possibilities to

identify muon-capture events are currently under investigation.
In addition to these extra scintillator panels, MINIDEX run II is equipped with a fast neutron detector placed on the side of the lead castle as shown in Fig. 7.7.

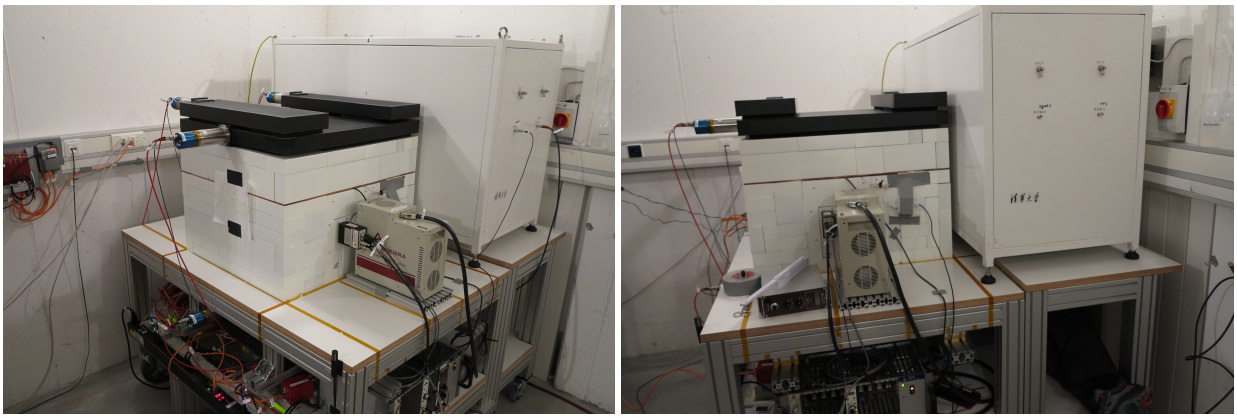

Figure 7.7: The MINIDEX run II apparatus at TSUL. The additional scintillators on top and the neutron detector, placed next to the lead castle, are clearly visible.

This neutron detector, provided by the Tsinghua University, consists of a quartz glass cylinder, 4 mm thick and 40 cm long and with a diameter of 30 cm. It is filled with ≈28 l of organic liquid scintillator (EJ-335) doped with gadolinium (Gd) to a level of 0.05%. The two ends of the cylinder are each equipped with an 8 inch PMT, Hamamatsu R5912-20. The neutrons slow down in the liquid scintillator, which provides an initial light signal. The Gd is responsible for the thermal capture of neutrons; the arising gammas are also collected in the PMTs. The cylinder is wrapped with black tape and, together with the two PMTs, is enclosed in a steel container. This container is 2 mm thick and has outer dimensions of $129.5 \times 57 \times 93.5\,\mathrm{cm}^3$. The cylinder placed inside the steel container is shown in Fig. 7.8.
The neutron detector is capable to distinguish interacting gammas from neutron-induced gammas by means of pulse-shape discrimination techniques. The energy range of neutrons that can be detected spans from thermal neutrons to fast neutrons (tens of MeV).
The neutron detector is recorded independently like all components of MINIDEX. It provides an independent measurement of muon-induced neutrons as well as of the background. It provides also a measurement of the neutron energy spectrum, neutron multiplicity and neutron yield. The latter quantities will be compared to those predicted by the MC and those deduced from the main part of MINIDEX.

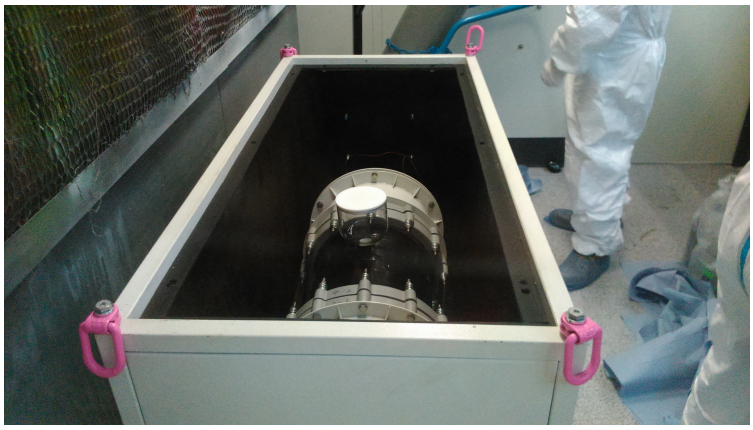

Figure 7.8: The neutron detector of MINIDEX run II. The glass cylinder wrapped with black tape and the steel container are visible.

7.6 Long Term Plans

MINIDEX is foreseen to run for many years in different locations and with different configurations. Detailed plans already exist for two further runs.

MINIDEX run III

The amount of lead between the scintillator panels of MINIDEX will be increased. This will increase the mean energy of the triggering muons and allow to study the influence of muon energy on the production of neutrons and neutron multiplicity.

MINIDEX run IV

The neutron detector will be integrated without the steel box inside an enlarged lead castle. In this way, the measurement of the muon-induced neutrons by the neutron detector will be affected by fewer systematic uncertainties.

7.7 Achievements

The goals of the work presented here were to design, build and commission an apparatus to measure muon-induced neutron from a high-Z target. These goals were reached and exceeded. MINIDEX run I was very successful. It established the feasibility of the experiment and provided first data, which already give a handle on neutron production and can help to improve the Monte Carlo programs used to make predictions for future experiments.

Appendix A

Hadronic Shower Development in Rock

In order to determine the distance from a cavity up to which interactions have to be simulated, a study of the development of hadronic showers in rock was performed with GEANT4, version 9.4. This study was performed with the *FLUX* output scheme, described in Sec. 4.2.
The showers were generated at the center of a layered rock sphere. The difference in radius between each sub-sphere, called *step*, is 200 mm. The properties of the particles (like kinetic energy, momentum, position and particle type) created in the showers were recorded when crossing a sub-sphere. To save computing time, the showers were generated with protons as initial particles, instead of muons. This choice is legitimate because, as far as the spatial extensions are concerned, no big differences are expected for hadronic showers with the same energy for different initial particles.
Figure A.1 shows an example of such a shower.
The following quantities were investigated:

- the distance, V, from the interaction point in the longitudinal direction of the initial particle, after which the sum of the kinetic energies of the shower particles taken into account drops below 10 MeV;
- the lateral distance, L, from the barycenter of the hadronic shower, after which the sum of the kinetic energies of the particles taken into account drops below 10 MeV;

These quantities were also studied for different particle types, referred to as shower component. Figure A.2 shows the sum of the kinetic energies of all the particles (left) and only neutrons (right), arising from hadronic showers initiated by 1 GeV protons vs step. From these figures of merit, the distance V can be inferred as marked by the red lines. Figure A.3 shows, in comparison, the case for the lateral distance L vs step for all particles (left) and only neutrons (right) in the case of 10 GeV protons. The maximum value of L characterizes the lateral extension of the shower, given the definition as stated above. Hadronic showers extend laterally for several meters in rock, especially the neutron component, which, therefore, contribute to the irreducible background in a deep underground

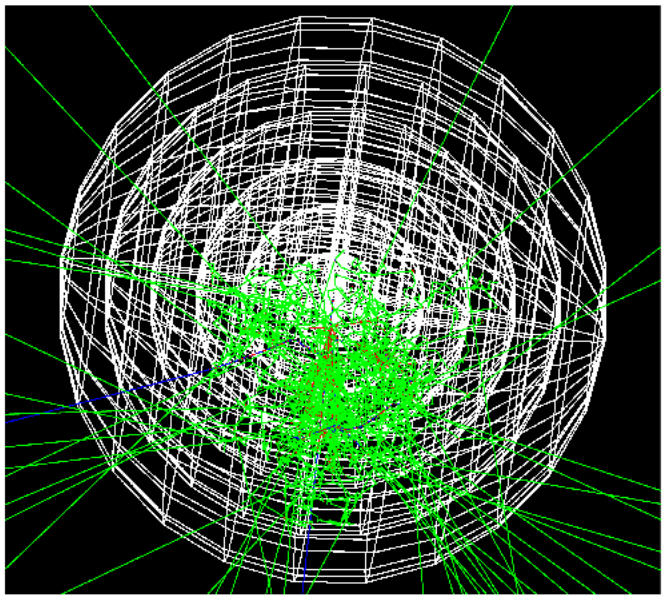

Figure A.1: Event display of a hadronic shower originating from the center of a rock sphere. The initial particle is a proton of 10 GeV coming from the top.

experiment.

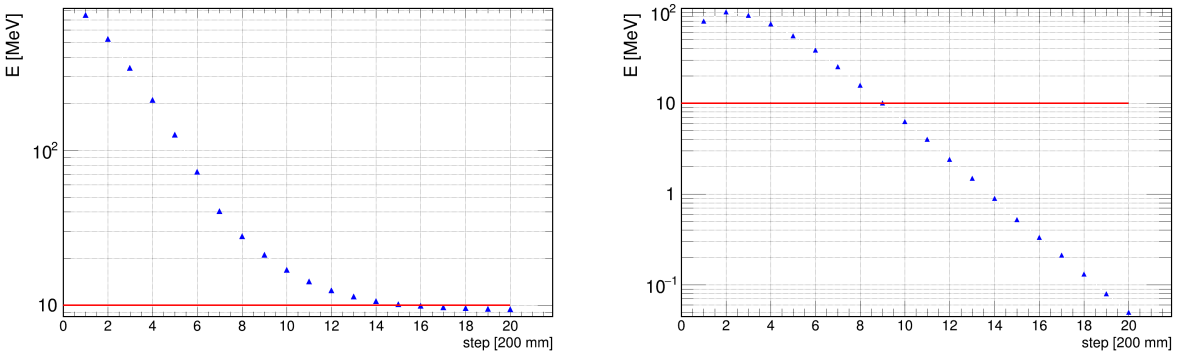

Figure A.2: Sum of the kinetic energy of all particles (left) and only neutrons (right), arising from hadronic showers initiated by 1 GeV protons vs step. The red lines mark the threshold used for the definition of the distance V.

Clearly, these distances, V and L, depend on the energy of the initial particle. This is demonstrated in Fig. A.4. The lateral extension depends on the number of neutrons created in the shower, which depends on the energy of the initial particle. V and L depend also on the particle type. As a hadronic shower develops, the particle composition changes. In

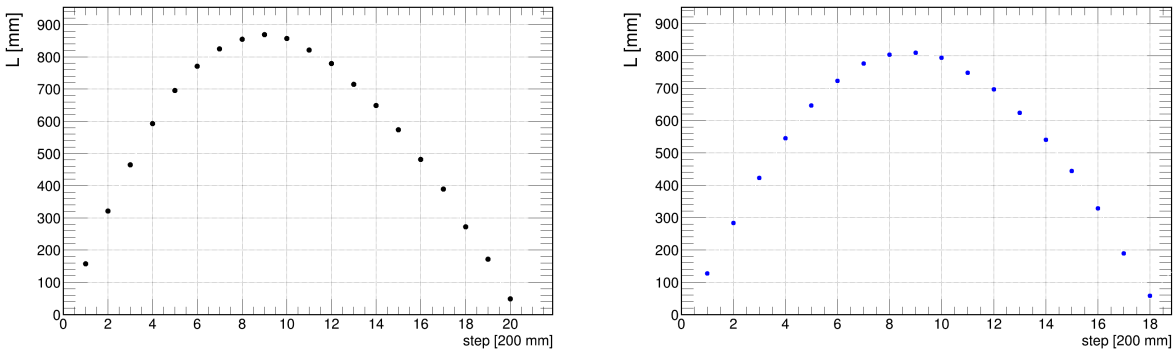

Figure A.3: Lateral distance, L, for all particles (left) and only neutrons (right) for 10 GeV protons vs step. The maximum value of L characterizes the lateral extension of the shower.

its late stage, most of the energy is carried by the neutrons (and unobservable neutrinos). This is demonstrated in Fig. A.5.

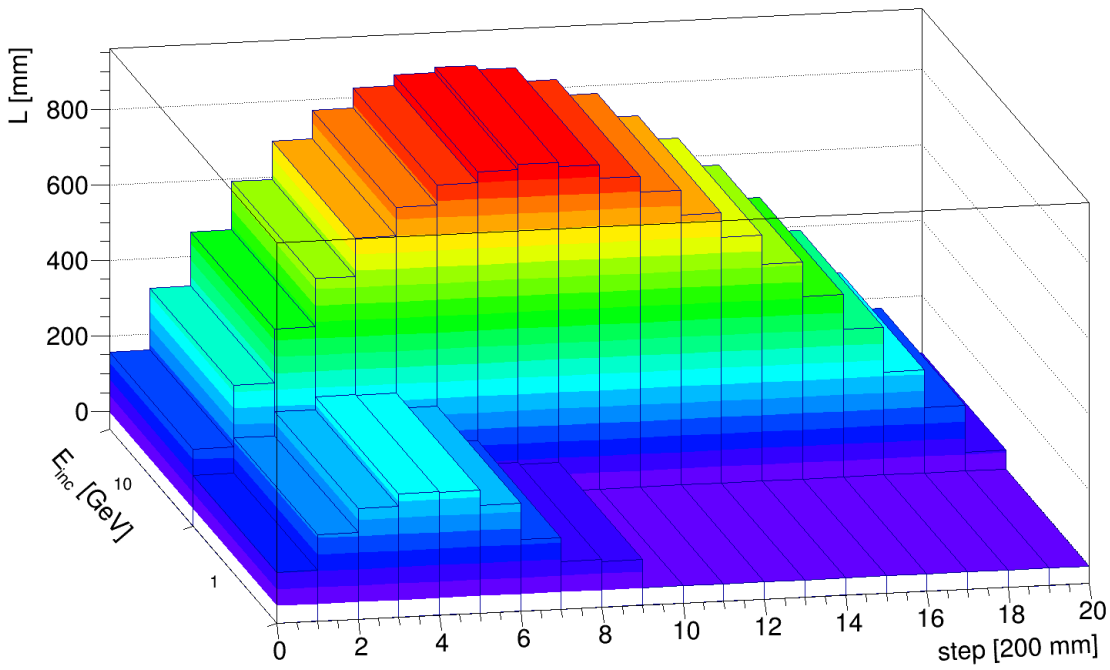

Figure A.4: Comparison of the lateral distance L vs step for 10 GeV and 1 GeV protons, for all particles.

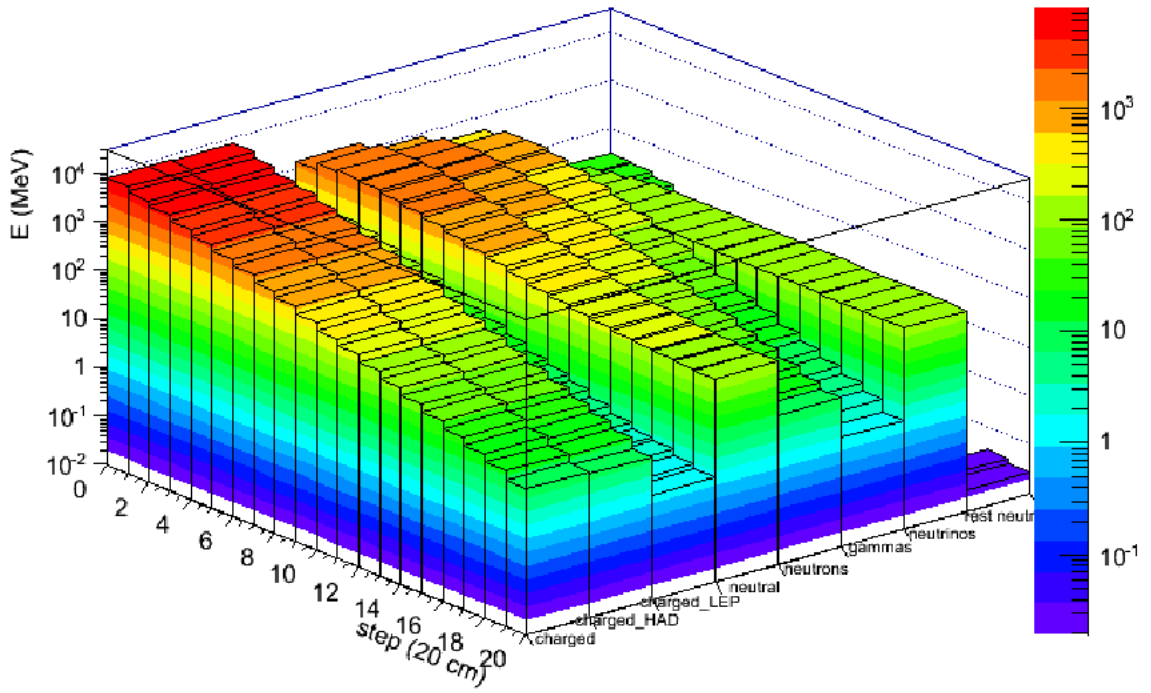

Figure A.5: Particle number distribution, weighted with the kinetic energy of the particles, vs step, for 10 GeV protons. A comparison between different components of the shower is given.

Appendix B

Uncertainty Propagation

In this appendix, the uncertainty propagation as used in the analysis of data from MINIDEX run I and the corresponding MC is briefly described.

B.1 FIT Method

In the case of the results obtained with the FIT method, all the statistical uncertainties were treated as uncorrelated. As stated in the main text, this is a clear simplification. The uncertainty on the number, N_{peak}, of counts in the peak, δN_{peak}, is given by the uncertainty on the fit parameter and is assumed to be Gaussian-distributed. The number of measured triggers, ${N_{trig}}^{meas}$, as well as the run time RT and the time windows, ΔT_{win}, are assumed to have no uncertainties.
The general propagation rule used to propagate the statistical uncertainties of any function $f(x_1, ..., x_n)$ is given by Eq. B.1

$$\delta f = \sqrt{\sum_{i=1}^{n} (\frac{\partial f}{\partial x_i} \cdot \delta x_i)^2} \tag{B.1}$$

where x_i are random uncorrelated variables with uncertainties δx_i.
Equation B.1 was applied to evaluate the uncertainties on all quantities such as R_S, R_B and $\rho_{S/B}$.

B.2 BAT Method

The case of the BAT method is slightly more complicated because, in principle, the statistical uncertainty, δN_{peak}, is not Gaussian distributed. Specifically, the marginalized posterior probability distribution $P(\Gamma_{peak}|n_{CB}, n_T)$ given in Eq. 4.19 is used to determine an asymmetric interval as an estimate of the statistical uncertainty on N_{peak}. To propagate the statistical uncertainties to any function $c = f(a+b)$, where a and b are variables distributed according to general probability distribution functions $P_A(a)$ and $P_B(b)$, respectively, the

probability distribution $P_C(c)$ has to be evaluated numerically. This was done employing the *Law of Total Probability* [257] was applied:

$$P_C(c) = \sum_{a \in \Omega_A} P_B(c-a) \cdot P_A(a) \tag{B.2}$$

where Ω_A is the range of the variable a.
Once the probability distribution function $P_C(c)$ was obtained, the smallest interval containing the 68% probability of $P_C(c)$ was assigned as the statistical uncertainty of the most probable value (mode), c_{mode}, of $P_C(c)$.
This method was applied to the variables Γ_{S+B} , Γ_B (thus R_B) and R_S. To finally obtain the probability distribution function of the signal-to-background ratio $P(\rho_{S/B})$ the following formula was used to generate each single entry $(P(\rho_{S/B})_i)$ of that distribution:

$$(P(\rho_{S/B})_i) = \frac{(R_S)_i \cdot (P(R_S)_i)}{(R_B)_i \cdot (P(R_B)_i)} \quad , \tag{B.3}$$

where $(R_S)_i$ and $(R_B)_i$ are uniformly sampled in their ranges, Ω_{R_S} and Ω_{R_B}, respectively. Examples of the probability distributions for Γ_{peak}^{inside}, R_B, R_S and $\rho_{S/B}$ for $\Delta T_{win} = 2$ ms are shown in Figs. B.1, B.2, B.3 and B.4, respectively. It should be noted that these distributions are not normalized.

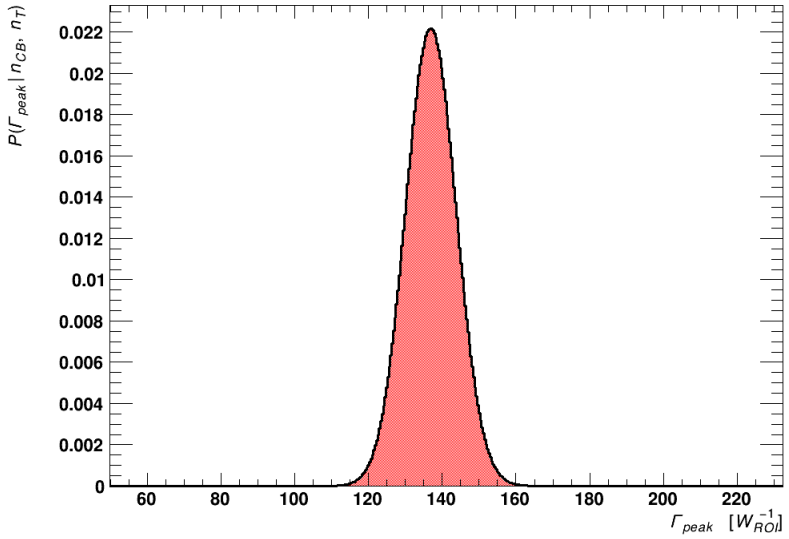

Figure B.1: Probability distribution obtained from BAT for Γ_{peak}^{inside} for the $\Delta T_{win} = 0.2\,\text{ms}$.

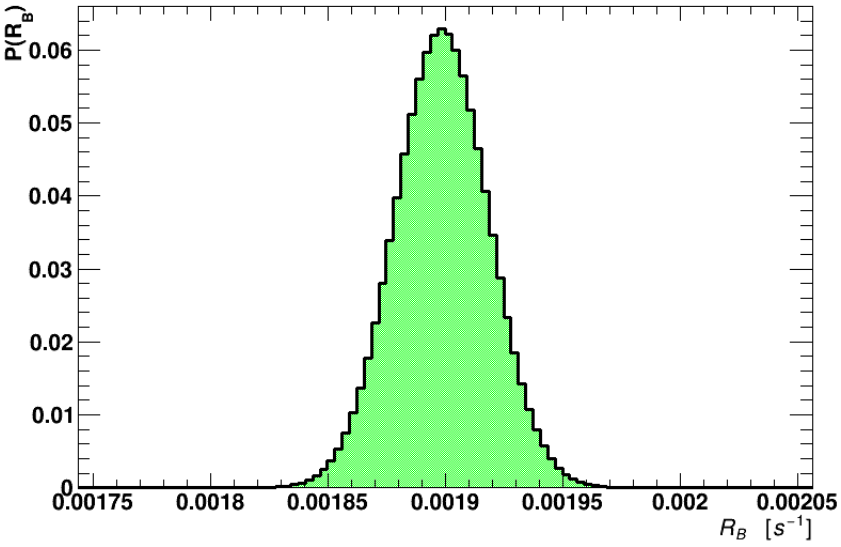

Figure B.2: Probability distribution evaluated with Eq. B.2 for R_B.

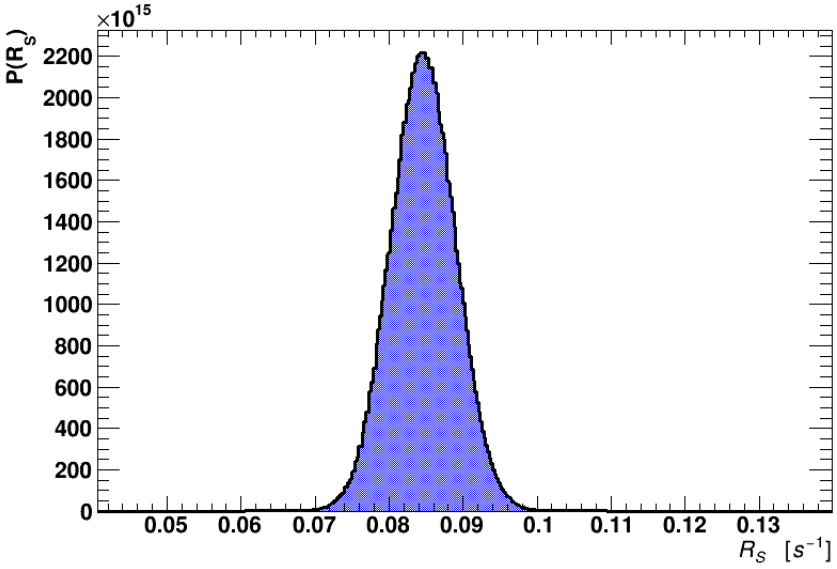

Figure B.3: Probability distribution evaluated with Eq. B.2 for R_S for the $\Delta T_{win} = 2\,\text{ms}$..

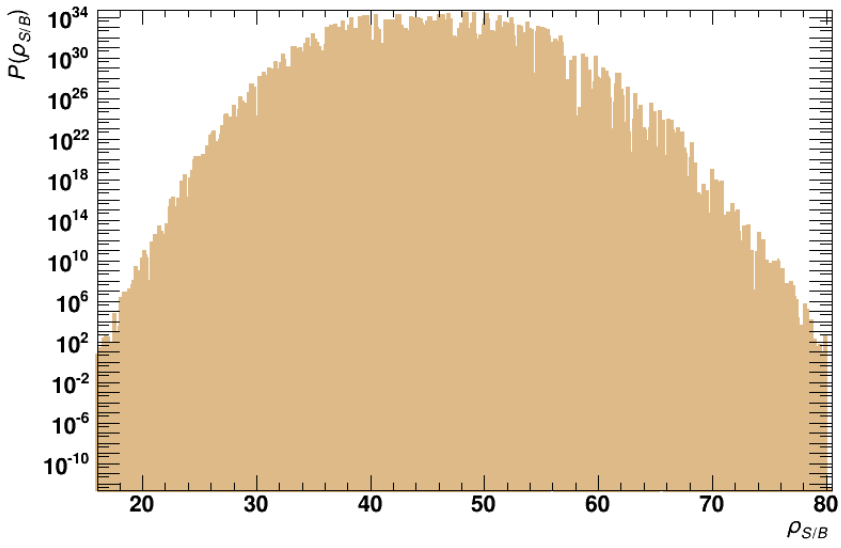

Figure B.4: Probability distribution evaluated with Eq. B.3 for R_S for the $\Delta T_{win} = 2\,\text{ms}$.

Appendix C

Adjustment Factors A and B

A complete set of values for the adjustment factors A and B as defined in Sec. 6.3 is given for the four different simulation settings. The factors are stable between $\Delta T_{win} = 1\,\text{ms}$ and $4\,\text{ms}$.

ΔT_{win} [ms]	***MaGe default***	***Shielding***	**Monoen. (7.7 GeV)**	**Monoen. (0.77 GeV)**
0.01	0.32 ± 0.38	0.92 ± 1.20	0.72 ± 0.93	0.75 ± 0.92
0.02	0.75 ± 0.26	1.37 ± 0.66	1.85 ± 0.90	2.54 ± 1.20
0.03	0.93 ± 0.23	1.60 ± 0.51	0.94 ± 0.22	3.74 ± 1.15
0.04	1.04 ± 0.19	1.65 ± 0.40	0.98 ± 0.17	4.61 ± 1.20
0.05	1.10 ± 0.17	1.67 ± 0.33	1.00 ± 0.14	5.29 ± 1.23
0.06	1.13 ± 0.17	1.65 ± 0.27	1.00 ± 0.13	5.77 ± 1.24
0.07	1.17 ± 0.14	1.68 ± 0.26	1.01 ± 0.11	6.10 ± 1.21
0.08	1.20 ± 0.13	1.71 ± 0.24	1.02 ± 0.10	6.48 ± 1.56
0.09	1.27 ± 0.13	1.75 ± 0.22	1.06 ± 0.10	6.85 ± 1.57
0.10	1.33 ± 0.14	1.81 ± 0.21	1.11 ± 0.10	7.31 ± 1.39
0.11	1.33 ± 0.13	1.78 ± 0.19	1.11 ± 0.09	7.51 ± 1.36
0.12	1.36 ± 0.13	1.76 ± 0.18	1.10 ± 0.09	7.65 ± 1.34
0.13	1.39 ± 0.12	1.78 ± 0.17	1.11 ± 0.08	7.90 ± 1.33
0.14	1.41 ± 0.12	1.79 ± 0.17	1.12 ± 0.08	8.09 ± 1.31
0.15	1.43 ± 0.16	1.81 ± 0.16	1.13 ± 0.08	8.34 ± 1.32
0.16	1.44 ± 0.11	1.81 ± 0.16	1.13 ± 0.07	8.46 ± 1.31
0.17	1.44 ± 0.11	1.81 ± 0.15	1.13 ± 0.07	8.58 ± 1.51
0.18	1.47 ± 0.11	1.83 ± 0.15	1.15 ± 0.07	8.78 ± 1.29
0.19	1.48 ± 0.11	1.84 ± 0.14	1.16 ± 0.07	8.96 ± 1.29
0.20	1.48 ± 0.10	1.83 ± 0.14	1.16 ± 0.07	9.06 ± 1.28
0.25	1.54 ± 0.10	1.86 ± 0.13	1.20 ± 0.06	9.60 ± 1.25
0.30	1.60 ± 0.10	1.92 ± 0.13	1.23 ± 0.06	10.08 ± 1.25
0.35	1.63 ± 0.09	1.95 ± 0.12	1.25 ± 0.06	10.38 ± 1.23
0.40	1.63 ± 0.09	1.95 ± 0.12	1.26 ± 0.06	10.56 ± 1.21
0.60	1.67 ± 0.09	1.99 ± 0.11	1.29 ± 0.05	11.12 ± 1.40
0.80	1.67 ± 0.08	1.98 ± 0.11	1.31 ± 0.05	11.35 ± 1.20
1.00	1.66 ± 0.08	1.97 ± 0.10	1.30 ± 0.05	11.36 ± 1.18
1.20	1.67 ± 0.08	1.97 ± 0.10	1.31 ± 0.05	11.46 ± 1.19
1.40	1.67 ± 0.08	1.96 ± 0.10	1.31 ± 0.05	11.47 ± 1.40
1.60	1.67 ± 0.08	1.96 ± 0.10	1.31 ± 0.05	11.50 ± 1.20
1.80	1.67 ± 0.08	1.95 ± 0.10	1.31 ± 0.05	11.48 ± 1.19
2.00	1.68 ± 0.08	1.96 ± 0.10	1.31 ± 0.05	11.54 ± 1.20
2.50	1.69 ± 0.08	1.97 ± 0.10	1.32 ± 0.05	11.61 ± 1.42
3.00	1.69 ± 0.08	1.98 ± 0.10	1.32 ± 0.06	11.65 ± 1.21
4.00	1.69 ± 0.08	1.98 ± 0.11	1.32 ± 0.06	11.65 ± 1.22
5.00	1.73 ± 0.09	2.02 ± 0.11	1.35 ± 0.06	11.88 ± 1.24
7.50	1.77 ± 0.09	2.07 ± 0.11	1.39 ± 0.06	12.20 ± 1.28
10.00	1.79 ± 0.09	2.09 ± 0.12	1.40 ± 0.06	12.33 ± 1.30
20.00	1.79 ± 0.10	2.09 ± 0.13	1.39 ± 0.07	12.27 ± 1.46
35.00	1.65 ± 0.12	1.92 ± 0.14	1.29 ± 0.08	11.33 ± 1.30
50.00	1.34 ± 0.13	1.57 ± 0.15	1.08 ± 0.09	9.24 ± 1.33

Table C.1: Values obtained for each ΔT_{win} for the adjustment factors A_i.

ΔT_{win} [ms]	***MaGe default***	***Shielding***	**Monoen. (7.7 GeV)**	**Monoen. (0.77 GeV)**
0.01	123 ± 13	104 ± 37	133 ± 3	134 ± 2
0.02	109 ± 9	89 ± 21	130 ± 2	134 ± 2
0.03	103 ± 8	82 ± 16	132 ± 2	134 ± 2
0.04	99 ± 7	80 ± 13	132 ± 2	134 ± 2
0.05	97 ± 6	80 ± 11	132 ± 2	134 ± 2
0.06	96 ± 6	80 ± 9	132 ± 2	133 ± 2
0.07	94 ± 5	79 ± 8	132 ± 2	133 ± 2
0.08	93 ± 5	78 ± 8	132 ± 2	133 ± 2
0.09	91 ± 5	77 ± 7	132 ± 2	133 ± 2
0.10	89 ± 5	75 ± 7	132 ± 2	133 ± 2
0.11	89 ± 5	76 ± 6	132 ± 2	133 ± 2
0.12	88 ± 5	77 ± 6	132 ± 2	133 ± 2
0.13	87 ± 4	76 ± 6	132 ± 2	133 ± 2
0.14	86 ± 4	76 ± 5	132 ± 2	133 ± 2
0.15	86 ± 4	75 ± 5	132 ± 2	133 ± 2
0.16	85 ± 4	75 ± 5	132 ± 2	133 ± 2
0.17	85 ± 4	75 ± 5	132 ± 2	133 ± 2
0.18	84 ± 4	75 ± 5	132 ± 2	133 ± 2
0.19	84 ± 4	74 ± 5	132 ± 2	133 ± 2
0.20	84 ± 4	75 ± 5	132 ± 2	133 ± 2
0.25	82 ± 4	74 ± 4	132 ± 2	133 ± 2
0.30	80 ± 4	72 ± 4	132 ± 2	133 ± 2
0.35	79 ± 4	71 ± 4	132 ± 2	133 ± 2
0.40	79 ± 3	71 ± 4	132 ± 2	133 ± 2
0.60	78 ± 3	70 ± 4	132 ± 2	133 ± 2
0.80	77 ± 3	70 ± 4	132 ± 2	133 ± 2
1.00	78 ± 3	70 ± 4	132 ± 2	133 ± 2
1.20	78 ± 3	70 ± 4	132 ± 2	132 ± 2
1.40	77 ± 3	70 ± 4	132 ± 2	132 ± 2
1.60	77 ± 3	71 ± 4	132 ± 2	132 ± 2
1.80	78 ± 3	71 ± 4	132 ± 2	132 ± 2
2.00	77 ± 3	70 ± 4	132 ± 2	132 ± 2
2.50	77 ± 3	70 ± 4	132 ± 2	132 ± 2
3.00	77 ± 3	70 ± 4	132 ± 2	132 ± 2
4.00	77 ± 3	70 ± 4	132 ± 2	132 ± 2
5.00	76 ± 3	69 ± 4	131 ± 2	132 ± 2
7.50	74 ± 3	67 ± 4	131 ± 2	132 ± 2
10.00	73 ± 4	66 ± 4	131 ± 2	132 ± 2
20.00	74 ± 4	67 ± 4	131 ± 2	132 ± 2
35.00	78 ± 4	72 ± 5	132 ± 2	133 ± 2
50.00	89 ± 5	83 ± 5	132 ± 2	133 ± 2

Table C.2: Values obtained for each ΔT_{win} for the adjustment factors B_i.

Appendix D

Comparison between Data and MC (All Settings)

Selected comparisons between data and MC from Ch. 6 are provided for all four MC settings.

Figure D.1 corresponds to Fig. 6.8 with all MC settings.

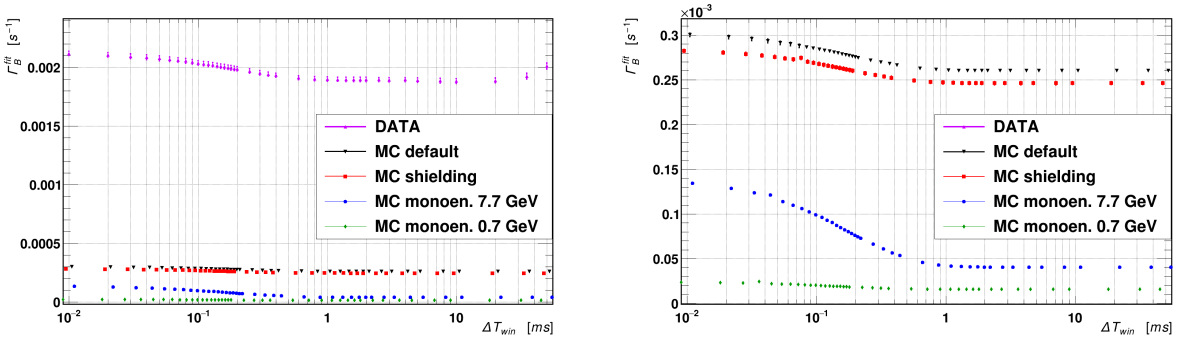

(a) (b)

Figure D.1: (a) Comparison between data and MC of the *effective* rate, Γ_B, of events observed in the ROI of the *OUTSIDE* spectra vs ΔT_{win}. (b) MC predictions only. The points were displaced horizontally for better visibility. Some values for small ΔT_{win} are not available due to non-applicability of the FIT method because of too low statistics. Uncertainties are statistical and systematic added in quadrature.

Figure D.2 corresponds to Fig. 6.9.

Figures D.3, D.4 and D.5 correspond to Figs.6.17, 6.18 and 6.19, respectively.

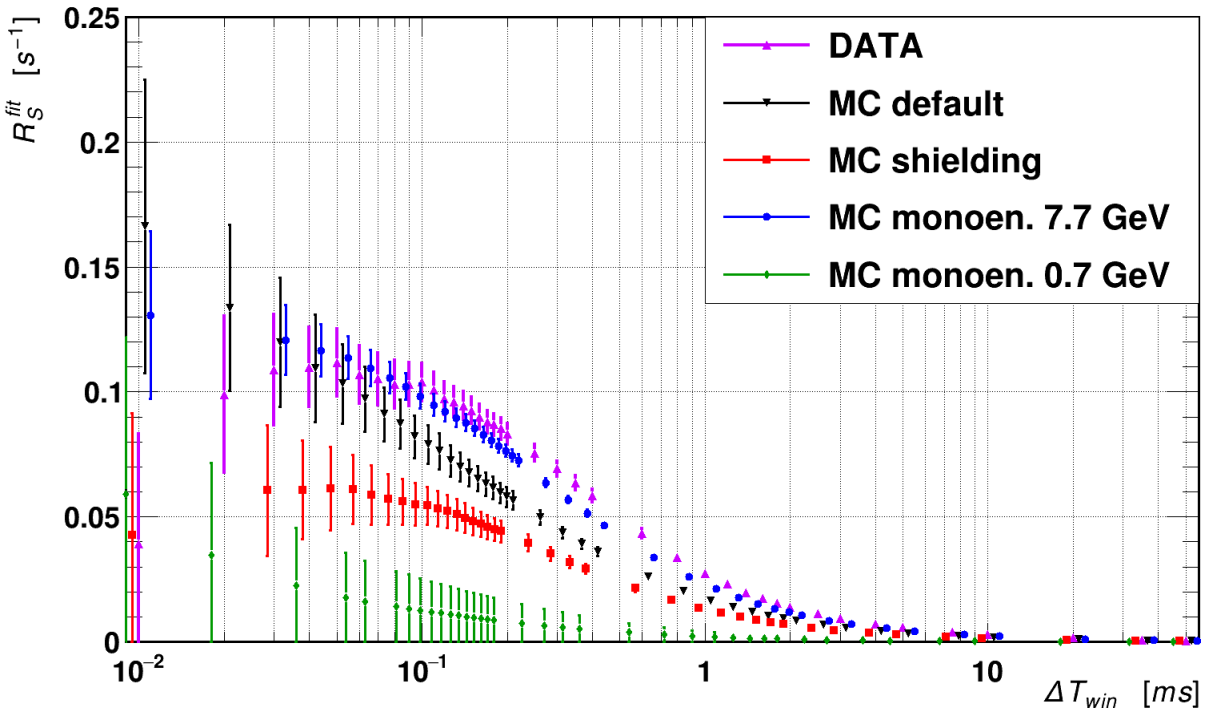

Figure D.2: Comparison between data and MC of the *effective* signal rate, R_S, vs ΔT_{win}. The points were displaced horizontally for better visibility. Some values for small ΔT_{win} are not available due to non-applicability of the FIT method because of too low statistics. Uncertainties are statistical and systematic added in quadrature.

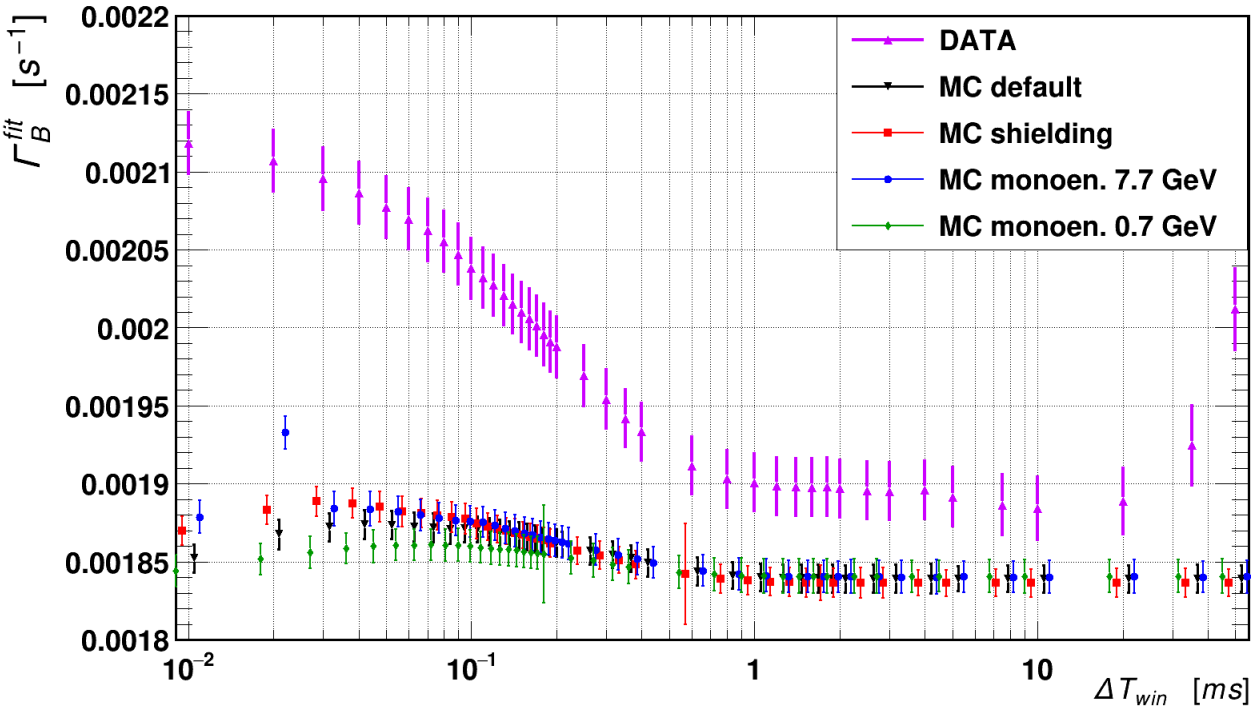

Figure D.3: Comparison between data and MC of the *effective* rate, Γ_B, vs ΔT_{win}, after MC adjustment to account for the missing background component. The points were displaced horizontally for better visibility. Some values for small ΔT_{win} are not available due to non-applicability of the FIT method because of too low statistics. Uncertainties are statistical and systematic added in quadrature.

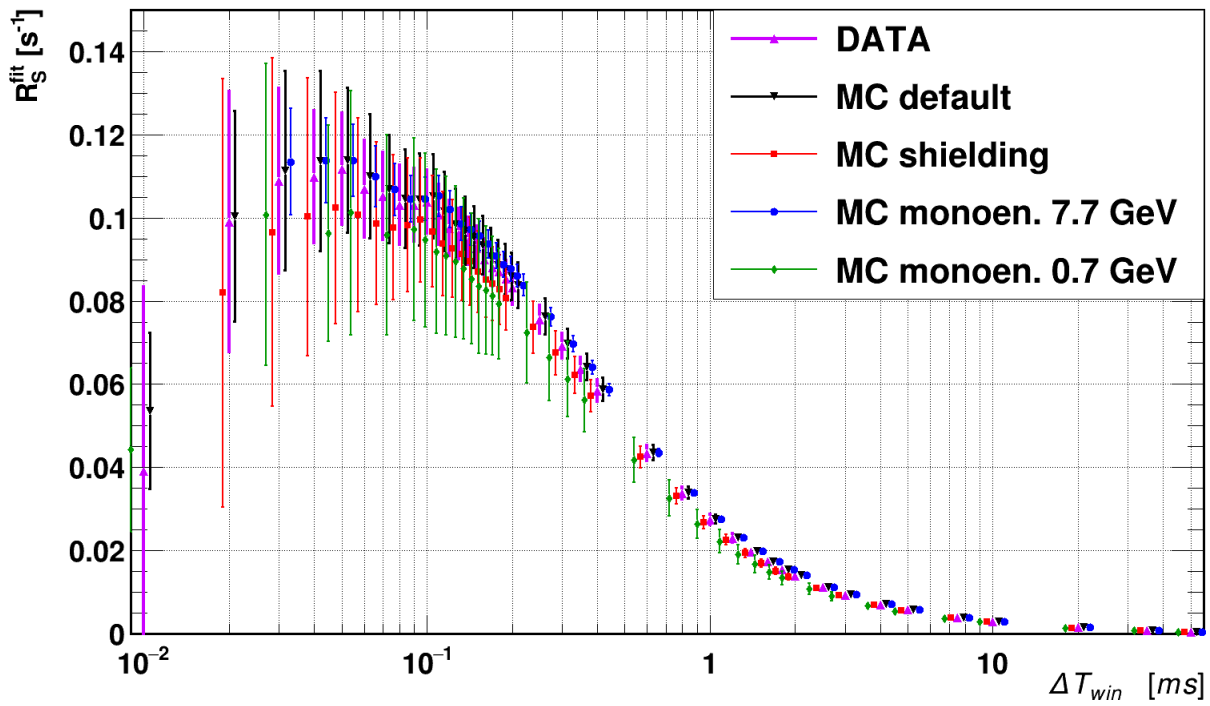

Figure D.4: Comparison between data and MC of the *effective* signal rate, R_S, vs ΔT_{win}, after MC adjustment to account for the missing background component. The points were displaced horizontally for better visibility. Some values for small ΔT_{win} are not available due to non-applicability of the FIT method because of too low statistics. Uncertainties are statistical and systematic added in quadrature.

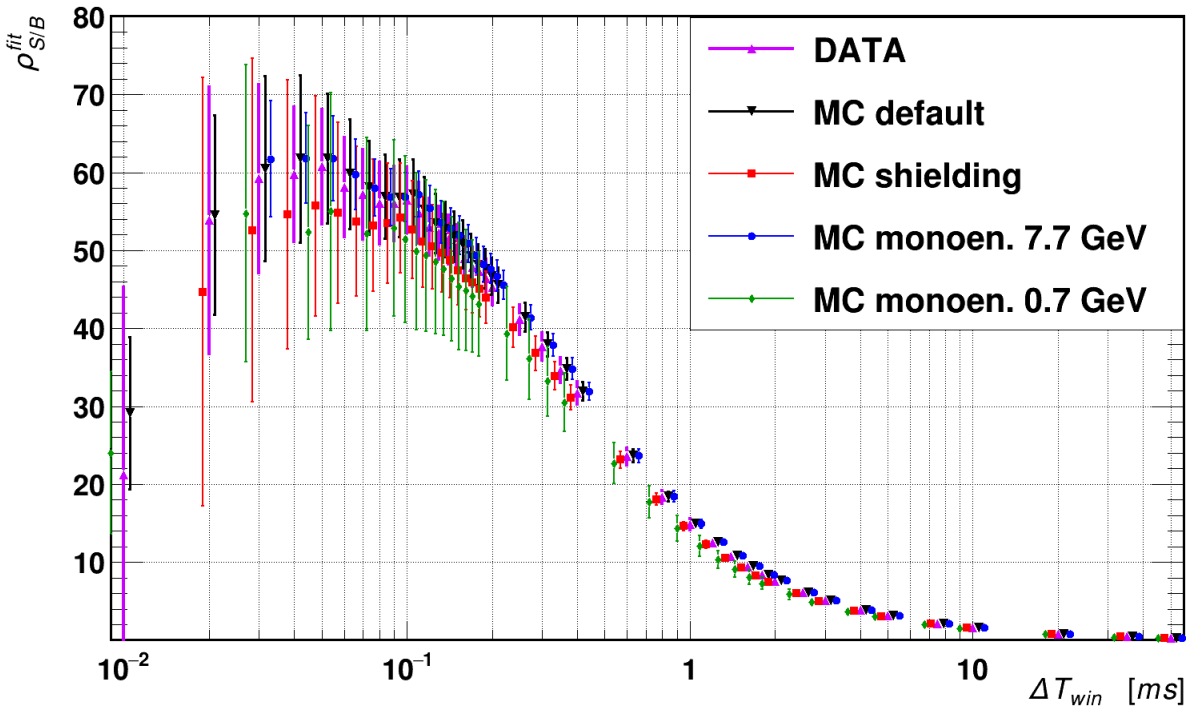

Figure D.5: Comparison between data and MC of the signal-to-background ratio, $\rho_{S/B}$, vs ΔT_{win}, after MC adjustment to account for the missing background component. The points were displaced horizontally for better visibility. Some values for small ΔT_{win} are not available due to non-applicability of the FIT method because of too low statistics. Uncertainties are statistical and systematic added in quadrature.

Bibliography

[1] ATLAS Collaboration, *Observation of a new particle in the search for the Standard Model Higgs boson with the ATLAS detector at the LHC*, Phys.Lett. B716 (2012) 1-29

[2] CMS Collaboration, *Observation of a new boson at a mass of 125 GeV with the CMS experiment at the LHC*, Phys. Lett. B 716 (2012) 30

[3] E. Andreaotti et al., *^{130}Te neutrinoless double-beta decay with CUORICINO*, Astropart. Phys. 34, 822 (2011)

[4] H. V. Klapdor-Kleingrothaus et al., *Latest results from the Heidelberg-Moscow double beta decay experiment*, Eur. Phys. J. A 12, 147 (2001)

[5] K. Alfonso et al., CUORE Collaboration, *Search for Neutrinoless Double-Beta Decay of ^{130}Te with CUORE-0*, Phys. Rev. Lett. 115 (2015)

[6] The GERDA Collaboration, Eur. Phys. J. C 73 (2013) 2330 DOI: 10.1140/epjc/s10052-013-2330-0

[7] R. Bernabei et al., Eur. Phys. J. C67 (2010) 39-49

[8] The CoGeNT Collaboration, Phys. Rev. D 88, 012002 (2013)

[9] F. Reines and C. L. Cowan Jr, Nature 178 (1956) 446

[10] R. Davis Jr., Phys. Rev. 97 (1955) 766

[11] R. Davis Jr., Bull. American Phys. Soc., Washington Meeting (1956) 219

[12] K. S. Hirata et al, Kamiokande Collaboration, Phys. Rev. Lett. 63 (1989) 16

[13] T. Kajita, M. Koshiba and A. Suzuki, *On the origin of the Kamiokande experiment and neutrino astrophysics*, Eur. Phys. J. H, Springer-Verlag, 2012, 37. 33-73

[14] A. I. Abazov et al., SAGE Collaboration, Phys. Rev. Lett. 67 (1991) 3332

[15] P. Anselmann et al, Gallex Collaboration, Phys. Lett. B, 285, (1992) 376

[16] B. T. Cleveland et al., *Measurement of the Solar Electron Neutrino Flux with the Homestake Chlorine Detector*, Astrophys. J. 496, 1998

[17] T. J. Haines et al, IMB Collaboration, Phys. Rev. Lett. 57 (1986)

[18] K. S. Hirata et al, Kamiokande Collaboration, Phys. Lett. B 205 (1988) 416

[19] Y. Fukuda et al., Kamiokande Collaboration, Phys. Lett. B 335, (1994) 237

[20] Y. Fukuda et al., Kamiokande Collaboration, Phys. Rev. Lett. 81, (1998) 1562

[21] M. Goldhaber et al, Phys. Rev. 109 (1958) 1015

[22] Y. Fukuda et al., Kamiokande Collaboration, Phys. Rev. Lett. 86 (2001) 5651

[23] Q. R. Ahmad et al, SNO Collaboration, Phys. Rev. Lett. 87 (2001) 071301

[24] T. Araki et al., KamLAND Collaboration, Phys. Rev. Lett. 90 (2003) 021802

[25] M. Apollonio et al., Chooz Collaboration, Eur. Phys. J. C 27 (2003) 331

[26] F. Ardellier et al., *Double Chooz, A Search for the Neutrino Mixing Angle theta-13*, arXiv:hep-ex/0606025

[27] M. H. Ahn et al., K2K Collaboration, Phys. Rev. D 74 (2006) 072003

[28] B. Armbruster et al., KARMEN Collaboration, Phys. Rev. Lett. 90 (2003) 181804

[29] S. Dodelson, A. Melchiorri, A. Slosar, Phys. Rev. Lett. 97 (2006) 04301

[30] F. P. An et al., Daya Bay Collaboration, *Measurement of the Reactor Antineutrino Flux and Spectrum at Daya Bay*, Phys. Rev. Lett. 116 (2016) 061801

[31] S.-B. Kim et al., RENO Collaboration, *Observation of Reactor Electron Antineutrino Disappearance in the RENO Experiment*, Phys. Rev. Lett. 108 (2012) 191802

[32] F. Pupilli et al., OPERA Collaboration, *Recent results of the OPERA experiment*, arXiv:1401.6776

[33] K. Abe et al., T2K Collaboration, *Upper bound on neutrino mass based on T2K neutrino timing measurements*, Phys. Rev. D 93 (2016) 012006

[34] P. Adamson et al., *First measurement of electron neutrino appearance in NOvA*, arXiv:1601.05022

[35] S. T. Petcov, Adv. High Energy Phys. 2013, 852987

[36] S. M. Bilenky and C. Giunti, Int. J. Mod. Phys. A 30 (2015) 1530001

[37] M. Agostini et al., GERDA Collaboration, *Measurement of the half-life of the two-neutrino double beta decay of Ge-76 with the Gerda experiment*, J. Phys. G: Nucl. Part. Phys. 40 (2013) 035110

[38] S. Dell'Oro, S. Marcocci, M. Viel and F. Vissani, *Neutrinoless double beta decay: 2015 review*, arXiv:1601.07512

[39] P. B. Pal, *Dirac, Majorana and Weyl fermions*, arXiv:1006.1718

[40] V. Gribov and B. Pontecorco, *Neutrino astronomy and lepton charge*, Phys. Lett. B 28 (1969) 493

[41] F. Capozzi et al., Phys. Rev. D 89 (2014) 093018

[42] P. A. R. Ade et al., Planck Collaboration, (2015) arXiv:1502.01589

[43] S. Dell'Orso, S. Marcocci, M. Viel and F. Vissani, J. Cosm. Astropart. Phys. 2015, 023 (2015)

[44] R. Saakyan, Ann. Rev. Nucl. Part. Sci. 63, (2013) 503

[45] The Majorana Collaboration, Phys. of Atom. Nucl. Vol. 67, Issue 11 , pp 2002-2010, DOI: 10.1134/1.1825519

[46] D. R. Artusa et al., CUORE Collaboration, Adv. High Energy Phys. 2015, (2015) 879871

[47] L. Pattavina, (2015), Presentation at TAUP 2015, Turin, Italy

[48] I. H. Kim, (2015), Presentation at TAUP 2015, Turin, Italy

[49] A. Gando et al, KamLAND-Zen Collaboration, Phys. Rev. Lett. 110, 062502 (2013)

[50] S. Andringa et al., SNO+ Collabotation, 2015, arXiv:1508.05759

[51] J. B. Albert et al., EXO Collaboration, Nature 510, (2014) 229

[52] J. J. Gomez-Cadenas et al., NEXT Collaboration, Adv. High Energy Phys. 2014, 907067

[53] I. Ostrovskiy, (2015), Presentation at TAUP 2015, Turin, Italy

[54] X. Ji, , (2015), Presentation BLV 2015, Amherst, MA, USA

[55] R. Arnold et al., NEMO Collaboration, Phys. Rev. D 89 (2014) 111101

[56] R. Arnold et al., NEMO Collaboration, Phys. Rev. D 92 (2015) 072011

[57] K. Zuber, *Neutrino Physics*, Published in 2004 by Taylor and Francis Group

[58] M. Agostin et al., GERDA Collaboration, *Results on Neutrinoless Double-β Decay of ^{76}Ge from Phase I of the GERDA Experiment*, Phys. Rev. Lett 111 (2013) 122503

[59] F. Zwicky., *Spectral displacement of extra galactic nebulae*, Helv. Phys. Acta, 6:110, 1933.

[60] Y. Mellier, *Cosmological applications of gravitational lensing*, astro-ph/9901116, 1999.

[61] R. Adam et al., PLANCK Collaboration, *Planck 2015 results. I. Overview of products and scientific results*, arXiv:1502.01582v1

[62] Schramm D.N, Turner N.S, Rev. Mod. Phys., 70:303-318 (1998)

[63] D. Caraffini, *Anti-proton Flux Detection and Indirect Search for Dark Matter with the AMS-02 Experiment*, PhD Thesis, 2004

[64] S. Dodelson, E. Gates, M. S. Turner, *Cold Dark Matter Models*, Science 274 (1996) 69-75
DOI: 10.1126/science.274.5284.69

[65] L. Baudis, *Direct dark matter detection: The next decade*, Dark Universe 1 (2012) 94-108

[66] D. Bauer et al., *Dark Matter in the Coming Decade: Complementary Paths to Discovery and Beyond*, arXiv:1305.1605v2

[67] D. Bauer et al., *Snowmass CF1 Summary: WIMP Dark Matter Direct Detection*, arXiv:1310.8327v2

[68] K. Maki, T. Mitsui and S. Otrio, 1996, Phys. Rev. Lett. 76 3474.

[69] A. D. Dolgov and S. H. Hansen, *Massive sterile neutrinos as warm dark matter*, Astropart. Phys. 16 (2002) 339-344

[70] G. Raffelt, *Axions*, Space Sci. Rev. 100 (2002) 153-158

[71] G. Jungman, M. Kamionkowski and K. Griest, 1996, Phys. Rep. 267, 195.

[72] G. Bertone, D. Hooper and J. Silk, 2005, Phys. Rep. 405, 279

[73] M. Kuhlen et al., *Numerical simulations of the dark universe: State of the art and the next decade*, Dark Universe 1 (2012) 50-93

[74] S. A. Mailik et al., *Interplay and Characterization of Dark Matter Searches at Colliders and in Direct Detection Experiments*, arXiv:1409.4075v3

[75] The ATLAS Collaboration, *Search for new phenomena in final states with an energetic jet and large missing transverse momentum in pp collision at* $\sqrt{s} = 8$ *TeV with the ATLAS detector*, arXiv:1502.01518v1

[76] Z. Ahmed et al., *Dark matter search results from the CDMS-II esperiment*, Science 327 (2010) 1619-1621

[77] G. Angloher et al., *Results from 730 kg days of the CRESST-II dark matter search*, Eur. Phys. J. C72 (2012) 1971

[78] E. Armengaud et al., *Final results of the EDELWEISS-II WIMP search using a 4-kg array of cryogenic germanium detectors with interleaved electrodes*, Phys. Lett. B 702 (2011) 329-335

[79] K.-J. Kang et al., *Introduction to the CDEX experiment*, Front. Phys. 8 (2013) 412

[80] E. Aprile et al., *The XENON100 dark matter experiment*, Astropart. Phys. 35 (2012) 573-590

[81] D. Akerib et al., The Large Underground Xenon (LUX) experiment, Nucl. Inst. and Meth. in Phys. Res. A 704 (2013) 111-126

[82] T. Alexander et al., DarkSide Collaboration, *Light Yield in DarkSide-10: A prototype two-phase argon TPC for dark matter searches*, Astropart. Phys. 49 (2013) 44

[83] R. Bernabei et al., *New results from DAMA/LIBRA*, Eur. Phys. J. C67 (2010) 39-49

[84] J. Amare et al., *Low energy events in NaI(Tl) scintillators. ANSIS status and prospects*, PoS IDM 2010 (2011) 020

[85] S. Archambault et al., *Constraints on low-mass WIMP interactions on* ^{19}F *from PICASSO*, Phys. Lett. B711 (2012) 153-161

[86] M. Felizardo et al., *Recent results from the SIMPLE dark matter search*, J. Phys. Conf. Ser. 375 (2012) 012011

[87] E. Daw et al., DRIFT Collaboration, *The DRIFT Dark Matter Experiments*, arXiv:1110.0222

[88] G. Heusser, *Low-Radioactivity Background Techniques*, Annu. Rev. Nucl. Part. Sci. 45:543 (1995)

[89] A. Caldwell, K. Kröninger, *Signal discovery in sparse spectra: A Bayesian analysis*, Phys. Rev. D 74 (2006), 092003

[90] F. Alessandria et al., *Sensitivity and Discovery Potential of CUORE to Neutrinoless Double-Beta Decay*, arXiv:1109.0494

[91] J. A. Formaggio and C. J. Martoff, *Backgrounds to Sensitive Experiments Underground*, Annu. Rev. Nucl. Part. Sci. 54, 361 (2004)

[92] R. Heaton, Nucl. Instrum. Meth. A 276:529 (1989)

[93] R. Heaton, Nucl. Geophys. 4:499 (1990)

[94] V. Chazal et al., Astropart. Phys. 9:163 (1998)

[95] H. Wulandari et al., *Neutron Flux at the Gran Sasso underground laboratory revisited*, Astropart. Phys. 22 (2004), 313-322

[96] V. A. Kudryavtsev et al., *Neutron- and muon-induced background in underground physics experiment*, European Phys. J. A, 36 (2008) 171-180

[97] M. J. Carson et al., *Neutron background in large-scale xenon detectors for dark matter searches*, Astropart. Phys. 21 (2004), 667-687

[98] A. Rindi et al., Nucl. Instrum. Meth. A 272 (1988) 871

[99] P. Belli et al., Nuovo Cim. A101:959 (1989)

[100] F. Arneodo et al., Nuovo Cim. A112:819 (1999)

[101] J.N. Abdurashitov et al., physics/0001007 (2000)

[102] R. Aleksan et al., Nucl. Instrum. Meth. A 274 (1989) 203

[103] E. Bellotti et al., INFN/TC-85/19, October 1985

[104] M. Cribier et al., Astropart. Phys. 4 (1995), 23

[105] The CDEX Collaboration, Front. Phys., 2013, 8(4):412-437

[106] D.-M. Mei and A. Hime, *Muon-Induced Background Study for Underground Laboratories*, Phys. Rev. D 73, (2006) 053004

[107] J. S. OConnel and F. J. Schima, Phys. Rev. D 38, 2277 (1988)

[108] B. Heisinger et al., Earth Plant. Sci. Lett. 200, 345 (2002)

[109] S. Tanaka et al., Proc. of 8th Int. Conf. on Radiation Shielding, Arlington, April 24-28, 1994. Vol. 2, pp.965-971, Ameircan Nuclear Society Inc. (1994)

[110] T. Fukahori, Proc. of the Specialists Meeting on High Energy Nuclear Data, Tokai, October 3-4, 1991, JAERIM 92-039, pp. 114-122 (1992)

[111] A. M. Hillas, *Cosmic Rays: Recent Progress and some Current Questions*, arXiv:astro-ph/0607109

[112] Tibor J. Dunai, *Cosmogenic Nuclides: Principles, Concepts and Applications in the Earth Surface Sciences*, Cambridge University Press (2010)

[113] D. Bastieri et al., MAGIC Collaboration, *The MAGIC Experiment and Its First Results*, arXiv:astro-ph/0503534

[114] M. Aguilar et al., AMS Collaboration, *First Result from the Alpha Magnetic Spectrometer on the International Space Station: Precision Measurement of the Positron Fraction in Primary Cosmic Rays of 0.5350 GeV*, Phys. Rev. Lett. 110 (2013) 141102

[115] P. Picozza et al., *PAMELA: A Payload for Antimatter Matter Exploration and Light-nuclei Astrophysics*, Astropart. Phys. 27 (2007) 296-315

[116] J. Abraham et al., AUGER Collaboration, *Properties and performance of the prototype instrument for the Pierre Auger Observatory*, Nucl. Instrum. Meth. A 523 (2004) 50-95

[117] K. Yoshimura et al., *BESS-Polar experiment: Progress and future prospects*, Adv. in Space Res. 42 (2008) 1664-1669

[118] T.K. Gaisser, *Cosmic Rays and Particle Physics*, Cambridge, UK: Cambridge University Press (1990), p.71

[119] H. M. Araújo et al., Nucl. Instrum. Meth. A 545 (2005), 398.

[120] R. Bernabei et al., Phys. Lett. B 280, 23 (2000)

[121] R. Bernabei et al., DAMA Collaboration, *First results from DAMA/LIBRA and the combined results with DAMA/NaI*, Eur. Phys. J. C56, 333 (2008)

[122] T. Schwetz and J. Zupan, JCAP 1108, 008 (2011)

[123] J. H. Davis, *Fitting the annual modulation in DAMA with neutrons from muons and neutrinos*, arXiv:1407.1052

[124] F. Boehm et al., Phys. Rev. Lett. 84, 3764 (2000)

[125] F. Boehm et al., Phys. Rev. D 62, 072002 (2000)

[126] E. Aprile et al., *Dark Matter Result from 225 Live Days of XENON100 Data*, Phys. Rev. Lett. 109 (2012) 181301

[127] P. Alivisatos et al., *KamLAND: a Liquid Scintillator Anti Neutrino Detector at the Kamioka site*, Report No. Stanford-HEP-98-03, Tohoku-RCNS-98-15

[128] S. Abe et al., *Production of radioactive isotopes through cosmic muon spallation in KamLAND*, Phys. Rev. C 81 (2010)

[129] D. S. Akerib et al., The LZ Collaboration, *LUX-ZEPLIN (LZ) Conceptual Design Report*, arXiv:1509.02910

[130] A. Fassò, A. Ferrari and P.R. Sala in: *Proceedings of MonteCarlo 2000 Conference*, (Lisbon, October 23-26, 2000), Ed. A. Kling, F. Barao, M. Nakagawa, L. Távora, P. Vaz (Springer-Verlag, Berlin, 2001).

[131] Geant4 Collaboration, Nucl. Instrum. Meth. A 506 (2003), 250.

[132] A. Empl et al, *A Fluka study of underground cosmogenic neutron production*, JCAP08 (2014) 064

[133] M. Aglietta et al., Proc. 26th Int. Conf. Cosmic Rays, Salt Lake City, Vol. 2 (1999) 44; hep-ex/9905047

[134] L. Reichhart et al., *Measuremnt and simulation of the muon-induced neutron yield in lead*, Astropart. Phys. 47 (2013) 67-76

[135] H. Kluck, *Measurement of the cosmic-induced neutron yield at the Modane underground laboratory*, Ph.D. Thesis, Institut für Experimentelle Kernphysik, Karlsruhe, 2013

[136] D.S. Akerib et al, CDMS Collab., *First Results from the Cryogenic Dark Matter Search in the Soudan Underground Laboratory*, Phys. Rev. Lett 93, 211301 (2004)

[137] R. Brun et. al, *GEANT 3*, CERN DD/EE/84-1, 1987

[138] Q. Yue et al., *Measurement of cosmic ray flux in the China JinPing underground laboratory*, Chinese Physics C 37 (8): 086001

[139] C. Castagnoli et al., Nuovo Cimento 35, 969 (1965)

[140] P. H. Barrett et al., Rev. Mod. Phys. 24, 133 (1952)

[141] S. Miyake et al., Nuovo Cimento 32, 1505 (1964)

[142] M. Ambrosio et al., Phys. Rev. D 52, 3793 (1995)

[143] M. Aglietta et al., Phys. Rev. D 58, 092005 (1998)

[144] P. Adamson et al., (MINOS Collab.), Phys. Rev. D 81, 012001 (2010)

[145] M. Ambrosio et al., (the MACRO Collab.), *Measurement of the energy spectrum of underground muons at Gran Sasso with a transition radiation detector*, Astropart. Phys. 10: 11-20, 1999

[146] M. Ambrosio et al., (the MACRO Collab.), *Measurement of the residual energy of muons in the Gran Sasso Underground Laboratories*, Astropart. Phys. 19, 313 (2003)

[147] P. Lipari and T. Stanev, Phys. Rev. D 44, 3543 (1991)

[148] Particle Data Group, Review of Particle Physics, volume 15,Number 1-4 (2000)

[149] Particle Data Group, Phys. Letter B 592, 230 (2004)

[150] D. E. Groom et al., Atomic Data and Nuclear Data Tables 78, 183 (2001)

[151] P. Antonioli, C. Ghetti, E.V. Korolkova, et al., Astropart. Phys. 7 , 357 (1997)

[152] G. Battistoni et al., *FLUKA as a new high energy cosmic ray generator*, Nucl. Instrum. Meth. A (2011), 626-627

[153] E. V. Bugaev et al., *Atmospheric muon flux at sea level, underground, and underwater*, Phys. Rev. D 58, 054001 (1998)

[154] F.E. Gray et al., *Cosmic ray muon flux at Sanford Underground Laboratory at Homestake*, Nucl. Instrum. Meth. A 638 (2011), 63-66

[155] E.I. Esch et al., Nucl. Instr. and Meth. A 538 (2005) 516 astro-ph/0408486

[156] S.M. Kasahara et al., Phys. Rev. D, 1997, 55:5282

[157] K. Eguchi, et al., Phys. Rev. Lett. 90 (2003) 021802 hep-ex/0212021

[158] M. Robinson, et al., Nucl. Instr. and Meth. A 511 (2003) 347 hep-ex/0306014

[159] M. Cribier et al., Astropart. Phys. 6, 129 (1997)

[160] C. Berger, et al., Phys. Rev. D 40 (1989) 2163

[161] B. Aharmim, et al. (SNO Collab.), Phys. Rev. D 80 (2009) 012001 arXiv:0902.2776

[162] M. Aglietta et al., Astropart. Phys. 3:311 (1995)

[163] M. Crouch, Proc. Int. Cosmic Ray Conf., 20th, Moscow 6:165 (1987)

[164] M. Andreev Yu et al., Proc. Int. Cosmic Ray Conf., 20th, Moscow 6:165 (1987)

[165] K. Hagiwara et al., Phys. Rev. D 66:010001 (2002)

[166] J. Delorme et al., Phys. Rev. C 52, 2222 (1995)

[167] O.G. Ryazhskaya and G.T. Zatsepin, Izv. Akad. Nauk SSSR, Ser. Fiz. 29, 1946 (1965); in Proceedings of the IX International Conference on Cosmic Rays, London, 1965, Vol. 21, p.987

[168] J.C. Barton, in Proceedings of the 19th International Conference on Cosmic Rays, La Jolla, 1985, edited by F. C. Jones Physical Society, London, 1985), p. 98.

[169] O.C. Allkofer and R.D. Andresen, Nucl. Phys. B 8, 402 (1968)

[170] D.H. Perkins, *Calculation of neutron background in Soudan* 1990.

[171] M. Aglietta et al., Nuovo Cimento Soc. Ital. Fis., C 12, 467 (1989)

[172] M. Aglietta et al., in Proceedings of the 26th International Cosmic Ray Conference, Salt Lake City, 1999, edited by D. Kieda, M. Salamon, and B. Dingus, Vol. 2, p. 44, hep-ex/9905047

[173] R. Hertenberger, M. Chen, and B.L. Dougherty, Phys. Rev. C 52, 3449 (1995)

[174] F. Boehm et al., *Neutron production by cosmic-ray muons at shallow depth*, Phys. Rev. D 62, 092005 (2000)

[175] J. Rapp, Ph.D. thesis, University of Karlsruhe, 1996

[176] T. Langford et al., *Fast neutron detection with a segmented spectrometer*, Nucl. Instrum. Meth. A 771 (2015), 78-87

[177] V.A. Kudryavtsev, N.J. Spooner and J.E. McMillan, Nucl. Instrum. Meth. A 505 (2003)

[178] Y.F. Wang et al., *Predicting neutron production from cosmic-ray muons*, Phys. Rev. D 62, 013012 (2000)

[179] C. Zhang and D.-M. Mei, *Measuring Muon-Induced Neutrons with Liquid Scintillation Detector at Soudane Mine*, Phys. Rev. D 90, 122003

[180] M. G. Marino et al., *Validation of spallation neutron production and propagation within Geant4*, Nucl. Instrum. Meth. A 582 (2007), 611-620

[181] A. Lindote et al., *Simulation of neutrons produced by high-energy muons underground*, Astropart. Phys. 31 (2009), 366-375

[182] H. Wulandari et al., *Neutron Background Studies for the CRESST Dark Matter Experiment*, hep-ex/0401032

[183] R. Persiani et al., the LVD Collaboration, *Measure of the muon-induced neutron yield in liquid scintillator and steinless steel at LNGS with the LVDexperiment*, AIP Conf. Proc. 1549, 235 (2013)

[184] International Atomic Energy Agency (IAEA): Photonuclear Data Library, *https://www-nds.iaea.org/photonuclear/*, Retreived 25/11/2015

[185] P. C. Stein et al., *Dependence on Atomic Number of the Nuclear Photoeffect at High Energies*, Phys. Rev. 119 (1960) 348

[186] B.L. Berman and S.C. Fultz, *Measurerments of the giant dipole resonance with monoenergetic photons*, Rev. Mod. Phys. 47, (1975) 713

[187] J.S. Levinger, Phys. Rev. 84:43 (1951)

[188] M.B. Chadwick et al., Phys. Rev. C 44:814, (1991)

[189] L.B. Bezrukov et al., Sov. J. Nucl. Phys. 17:51 (1973)

[190] L.B. Bezrukov and E.V. Bugaev, Sov. J. Nucl. Phys. 33:635 (1981)

[191] E. Fermi, Physik Z. 29:315 (1924)

[192] C.F. Weizsäcker, Physik Z. 88:612 (1934)

[193] E.J. Williams et al., Kgl. Dan. Vidensk. Selsk. Mat. Fys. Medd. XIII:4 (1935)

[194] M. Horn, *Simulations of the muon-induced neutron background of the EDELWEISS-II experiment for Dark Matter search*, Ph.D. Thesis, Institut für Experimentelle Kernphysik, Karlsruhe, 2007

[195] K. Ebert and J. Meyer-Ter-Vehn, *Radiative pion and muon capture on* ^{208}Pb, Phys. Lett. B 77, (1978) 24:28

[196] J. Bernstein, *Radiative Muon Capture*, Phys. Rev. 115, 694 (1959)

[197] D.F. Measday, *The nuclear physics of muon capture*, Phys. Rep. 354, (2001) 243-409

[198] E.H.S. Burhop, High Energy Physics, Vol. III, Academic Press, New York, 1969, p. 109

[199] S. Devons, L. Duerdoth, Adv. Nucl. Phys. 2 (1969) 295

[200] C.S. Wu, L. Wilets, Annu. Rev. Nucl. Sci. 19 (1969) 527

[201] J. Hüfner, F. Scheck, C.S. Wu, Muon Physics, Vol. I, Academic Press, New York, 1977

[202] S. Charalambus, Nucl. Phys. A, 166:145 (1971)

[203] H. Biloken et al., J. Geophys. Res. 94:12145 (1989)

[204] T. Suzuki et al., Phys. Rev. C 35:2212 (1987)

[205] B. MacDonald et al., Phys. Rev. B, 139:1253 (1965)

[206] A. Empl, private communication

[207] S. C. Blyth et al., *Measurement of Cosmic-ray Muons and Muon-induced Neutrons in the Aberdeen Tunnel Underground Laboratory*, arXiv:1509.09038

[208] R. I. Enikeev et al., Sov. J. Nucl. Phys. 46, 1492 (1987)

[209] G. Bellini et al., the BOREXINO Collaboration, *Cosmogenic Backgrounds in Borexino at 3800 m water-equivalent depth*, JCAP 08 (2013)

[210] V. Chazal, et al., Nucl. Inst. and Meth. A 490 (2002) 334, hep-ex/0102028

[211] S. Taniguchi et al., Nucl. Inst. and Meth. A 503 (2003) 595

[212] S. Roeslera et al., Nucl. Inst. and Meth. A 503 (2003) 606

[213] H. M. Araújo et al., *Measurements of neutrons produced by high-energy muons at the Boulby Underground Laboratory*, Astropart. Phys. 29, (2008) 471-481

[214] A. F. Khalchukov et al., Il Nuovo Cimento 6 C, 320 (1983)

[215] A. Empl et al., *Study of Cosmogenic Neutron Backgrounds at LNGS*, arXiv:1210.2708

[216] L. Pandola et al., *Neutron- and muon-induced background in underground physics experiment*, ILIAS 4th Annual Meeting, Chambery, 2007

[217] M. Bauer et al., *MaGe: a Monte Carlo framework for the Gerda and Majorana double beta decay experiments*, J. Phys. Conf. Ser. 39, (2006) 362

[218] Geant4 9.6 Release Notes, *http://geant4.cern.ch/support/ReleaseNotes4.9.6.html*, Retreived 03/11/2015

[219] J. Kopecky, *Atlas of Neutron Capture Cross Sections*, International Nuclear Data Commitee, April 1997

[220] B. C. Rastin, J. Phys. G 10, p. 1609 (1984)

[221] *http://www.crystals.saint-gobain.com*, Retreived on 26-01-2016

[222] *http://www.et-enterprises.com/*, Retreived on 26-01-2016

[223] M. Paterno, *Calculating Efficiencies and Their Uncertainties*, 2003
http://home.fnal.gov/ paterno/images/effic.pdf, Retreived on 26-01-2016

[224] G. D'Agostini, *Bayesian Reasoning in Data Analysis*, World Scientific Publishing Company, Singapore, 2003

[225] *http://www.canberra.com/products/detectors/germanium-detectors.asp*, Retreived on 27-01-2016

[226] *http://www.canberra.com/products/detectors/pdf/XtRa-detectors-C40024.pdf*, Retreived on 25-02-2016

[227] *http://www.struck.de/sis3316.html*, Retreived on 27-01-2016

[228] *http://www.supermicro.com/products/system/1u/5018/SYS-5018D-MTF.cfm*, Retreived on 27-01-2016

[229] I. Abt et al., *The GALATEA Test-Facility for High Purity Germanium Detectors*, Nucl. Instrum. Meth. A 782 (2015), 56-62
Online monitoring available at: *https://www.mpp.mpg.de/∼palermo/monitor/*

[230] *https://en.wikipedia.org/wiki/Resistance_thermometer*, Retreived on 01-02-2016

[231] *http://www.vegetronix.com/Products/AquaPlumb/*, Retreived on 01-02-2016

[232] A. Caldwell, D. Kollar, and K. Kroninger, *BAT: The Bayesian Analysis Toolkit*, Comput. Phys. Commun. 180 (2009) 2197-2209

[233] N. Becerici Schmidt, *Results on Neutrinoless Double Beta Decay Search in GERDA: Background Modeling and Limit Setting*, PhD Thesis, 2014

[234] M. Agostini et al., GERDA Collaboration, *The background in the* $0\nu\beta\beta$ *experiment Gerda*, Eur. Phys. J. C 74 (2014) 2764

[235] J. Abdallah, et al., DELPHI Collaboration, *Study of multi-muon bundles in cosmic ray showers detected with the DELPHI detector at LEP*, Astropart. Phys.28 (2007) 273-286

[236] V. A. Kudryavtsev et al., Phys. Lett. B 471 (1999) 251

[237] V. A. Kudryavtsev et al., Phys. Lett. B 494 (2000) 175

[238] *http://matse1.matse.illinois.edu/concrete/prin.html*, Retreived on 09-06-2016

[239] M. Duranti, *Measurement Of The Atmospheric Muon Flux On Ground With The AMS-02 Detector*, PhD Thesis, 2011

[240] Gordon et al, *Measurement of the Flux and Energy Spectrum of Cosmic-Ray Induced Neutrons on the Ground*,IEEE Transactions on Nucl. Sci., Vol. 51, No. 6, December 2004

[241] A. Nesterenok, *From Numerical Calculations Of Cosmic Ray Cascade In The Earth's Atmosphere – Results For Nuclear Spectra*, Nucl. Instrum. Meth. B 295 (2013) 99-106

[242] *http://geant4.cern.ch/support/proc_mod_catalog/physics_lists/useCases.shtml*, Retreived on 17-02-2016

[243] *http://geant4.web.cern.ch/geant4/support/proc_mod_catalog/physics_lists/physicsLists.shtml*, Retreived on 18-02-2016

[244] *http://geant4.cern.ch/support/proc_mod_catalog/models/hadronic/BertiniCascade.html*, Retreived on 08-06-2016

[245] M. Boswell et al., *MaGe: a Geant4-based Monte Carlo Application Framework for Low-background Germanium Experiments*, IEEE Trans.Nucl.Sci.58:1212-1220,201

[246] *http://www.slac.stanford.edu/comp/physics/geant4/slac_physics_lists/shielding/physlistdoc.html*, Retreived on 18-02-2016

[247] *http://geant4.web.cern.ch/geant4/G4UsersDocuments/UsersGuides/PhysicsReferenceManual/html/* Retreived on 18-02-2016

[248] *http://geant4.web.cern.ch/geant4/UserDocumentation/UsersGuides/ForApplicationDeveloper/html/* Retreived on 18-02-2016

[249] I. Abt et al., *Neutron Interactions as Seen by A Segmented Germanium Detector*, Eur. Phys. J., A 36:139-149,2008

[250] Y.-F. Wang et al., Phys. Rev. D 64, 013012 (2001)

[251] A. Empl et al., *MINIDEX simulations with FLUKA*, in preparation

[252] G. Bellini et al., the BOREXINO Collaboration, *Muon and Cosmogenic Neutron Detection in Borexino*, 2011 JINST 6 P05005

[253] B. Schmidt et al, *Muon-induced background in the EDELWEISS dark matter search*, Astropart. Phys. 44, 28 (2013)

[254] L. Bergamasco et al., Il Nuovo Cimento 13A, N.2 (1973) 403

[255] G. V. Gorshkov et al., Sov. J. Nucl. Phys. 18, 57 (1974)

[256] A. Empl et al., *FLUKA: Predictive power for cosmogenic backgrounds*, Low-Radiation Techniques 2015, Seattle. AIP Conference Proceedings 1672, 090001 (2015)

[257] A. Papoulis, *Probability, Random Variables, and Stochastic Processes*, 2nd ed. New York: McGraw-Hill, pp. 37-38, 1984.

List of Figures

List of Tables

Acknowledgments

As many people contributed in one way or another to accomplish my PhD, I would like to spend couple of words to thank them.

First of all, I would like to thank my supervisor at the Ludwig-Maximilians-Universität München, Prof. Dr. Jochen Schieck. I would also like to thank the second referee of my thesis, Prof. Dr. Otmar Biebel as well as the members of the committee, Dr. Georg Raffelt and Prof. Dr. Katia Parodi.

I am very thankful to the whole GERDA/GeDet group at the Max-Planck-Institut für Physik for letting me to pursue my PhD in this group. In particular, I would like to thank my day-to-day supervisor who guided me towards this important objective, Dr. Iris Abt. Many thanks also to Dr. Bela Majorovits for helping me over my stay in the group.

My special gratitude goes also to Dr. Oliver Schulz for all the time, sometimes very fun, spent working together in the labs. I have learnt a lot with you Oli, also when you drove me crazy. I am also glad for the friendship that grew over these years.

Many thanks to the MINIDEX team members, former and present, for the strong support in this project. Without them all the achievements would have not been possible. A very special thank goes to the first members of the MINIDEX team, my students Sergio, Jonny and, above all, Costanza. Being your supervisor was a great experience and I wish you have learnt as much as I did during the time spent together. Thanks also to the Tübingen colleagues for hosting MINIDEX, especially Igor who is always helping us.
A big thanks goes to my friend and colleague Lucia for sharing the burden of GALATEA and most importantly, for the last 11 years spent side-by-side to achieve exciting goals over our physics career. A great thank goes also to Chris and Dimi for all the fun time together at work and outside. The three of you made my PhD time definitely better. It would have not been the same without you. I would like to thank also Dr. Xiang Liu for his unlimited willingness to help and for all the fun football-nights. I will definitely miss you guys.

Many thanks to the former members of the group such as Hans, Burcin and Neslie for all the support and the fun time together.
I would also thank the IT department of the Max-Planck-Institut für Physik for all the times I needed his technical support. And I would like to thank Dr. Anton Empl for the extremely fruitful discussions and the work together for MINIDEX.

But all of this would have not been possible without my parents, which have always strongly supported my Physics career and my studies in general. I owe them the awareness of the importance of an high-quality education. Moreover, I cannot not to mention all my friends which I got over the last 4+ years in Munich. I wish to thank you all guys. The Stefanos which have already left Munich for new adventures. The ladies creek Fabiana, Daniela, Anna and Julia which are luckily still here. And, of course, my accomplices Enrico and Alessandro. Thank you guys for all the great time. None of this would have been bearable without you.

In the end, I feel to thank also myself, cause I made it!!